Department of Meteorology

Use of Operational Weather Radars for Understanding Indian Monsoon Convection and Evaluating Convection-Permitting Models

Alexander John Doyle

A thesis submitted for the degree of Doctor of Philosophy

July 2022

Declaration

I confirm that this is my own work and the use of all material from other sources has been properly and fully acknowledged.

Alexander John Doyle

Abstract

The Indian summer monsoon can be described as a convectively coupled phenomenon – a factor that complicates modelling and forecasting. Interactions between the large-scale monsoon circulation and local convective systems are two-way and non-linear, but these relationships are not well documented. Based on data collected during the 2016 INCOMPASS field campaign, this thesis enhances our ability to objectively analyse monsoon storms using operational weather radars and provides insight into the complex relationships between these storms and the large-scale. The impressive potential for radar-based model evaluation for the region is also demonstrated.

Firstly, an existing calibration technique is applied to the operational radar data for the first time and shown to lead to improved rainfall estimates. Next, the calibrated radars are used to gain further understanding of how monsoon onset and other aspects of variability during the 2016 monsoon season regulate convection. Storms most frequently reach heights of around 6–8 km for all locations. Intraseasonal variability during the monsoon affects the regional patterns of storm heights, especially for western and central India, and also modulates the diurnal cycle of storm occurrence for all regions. Over land, the horizontal area of storms peaks in the afternoon and evening, and typically in the early morning over the surrounding ocean, consistent with the diurnal cycle of precipitation. These results confirm that Indian monsoon convective regimes are partly regulated by the large-scale environment within which they are embedded.

Finally, radar-derived storms are compared to those simulated by convection-permitting models over India for the first time. The model is found to simulate too much shallow convection; modelled storms are also often too wide and intense, and are largest around the freezing level, higher than observed. Some of these biases have been found before for other regions, and potential reasons for the major discrepancies are discussed.

Acknowledgements

First of all, I would like to thank my two supervisors – Andy Turner and Thorwald Stein – for making this project possible and truly excelling in all things PhD supervision. Encouragement and constructive criticism were always handed out in carefully considered doses, and my work always felt valued and important, even during a global pandemic and one very long paper-review process. I get the impression this is no mean feat! To Andy, for always being audibly excited when a new figure appeared in a meeting and for having a *very* keen eye for detail, and to Thorwald, for repeatedly saving me from radar-related disaster and always encouraging me to be independent.

I am also grateful to my Monitoring Committee members – Chris Westbrook and Ted Shepherd – for very useful perspective and stimulating discussion. I have fond memories of the seven meetings we had during my PhD, and again, this is apparently no mean feat. I am also thankful to Jennifer Fletcher and Doug Parker in Leeds, for being so curious about my work and having such confidence in my ability to be a proper scientist early in my PhD. To the Department of Meteorology as a whole, I will miss you greatly. There are so many aspects to what makes it a truly great department that I can't name them all. I hope to be able to visit often in the future. Thanks in particular to those who stuck by me on Lyle 5 until the bitter end, you know who you are!

Finally, thank you to my family and extended family, and all those who have lived with me at various stages over the last three and a half years. Thank you for believing in me, showing genuine interest in my little specific contribution to the field of meteorology, and for always making me laugh.

This thesis is dedicated to my brother Joseph Francis Pender, who always sought the fullest God-given potential in those he knew.

Table of Contents

List of Tables

List of Figures

Chapter 1

Introduction

1.1 Indian monsoon convection

1.1.1 The Indian summer monsoon

The Indian summer monsoon (ISM) is responsible for one of the largest modes of seasonal variability in wind direction and precipitation seen worldwide, providing more than 80% of the annual rainfall of India. Therefore, the monsoon has pronounced importance for India's vast population and economy, which rely upon the monsoon rains (e.g., Gadgil and Gadgil, 2006). Additionally, the ISM is inherently complex, owing to the extreme nature of its associated rainfall totals combined with substantial multi-scale spatiotemporal variability (e.g., Krishnamurti and Bhalme, 1976). For these reasons, the ISM is one of the most frequently studied phenomena in the atmospheric sciences, with significant potential for further improvement in our physical understanding and forecast skill in the region (e.g., Rao et al., 2019).

The ISM is understood to develop as a result of the reversal of the large-scale meridional temperature gradient over the Indian subcontinent, following the hot spring months in which a sharp land-sea temperature gradient develops between India and the surrounding Indian Ocean (Webster et al., 1998; Xavier et al., 2007). In particular, elevated heating of the extensive Tibetan Plateau (with a mean elevation above 4.5 km) has been cited as a key driver through thermal and mechanical forcing (Flohn, 1968; Li and Yanai, 1996; Wu et al.,

2007, 2012). This elevated heating leads to the northward migration of high pressure and the mid-latitude jet, which leads to an easterly jet developing in the upper troposphere centred at around 8 km (Koteswaram, 1958). Low pressure then builds over India, resulting in a quasi-reversal of the winds in the equatorial lower troposphere over the Indian Ocean and the establishment of the ISM circulation. Furthermore, the Himalayas act to separate the dry and stable air to the north from the moist and unstable ISM circulation (Molnar et al., 2010; Turner et al., 2020). Monsoons have also been thought of as a global phenomenon associated simply with the seasonal migration of the inter-tropical convergence zone (Charney, 1969), which is a discussion that is ongoing today (e.g., Gadgil, 2018). For example, Trenberth et al. (2000) noted that monsoons globally can be defined from the standpoint of the large-scale overturning in divergent winds in the atmosphere that varies with the seasons. Nonetheless, the unique geography and topography of India and its surrounding regions results in the ISM being the most potent monsoon system on Earth.

Once the Indian monsoon circulation is established (median onset date at Kerala is 1 June; Pai et al., 2020), the monsoon rains progress gradually from the south to the far north-west of India, reaching their climatological peak around mid-July. This movement is quasi-perpendicular to the low-level winds (at around 1.5 km elevation), and directly opposed to the mid-level winds (at 5.0 km elevation) and, as discussed by Parker et al. (2016), cannot be explained solely by moisture advection and convergence. Furthermore, Volonté et al. (2020) found the propagation of the northern limit of the ISM to be a non-steady process. It also is well-known to have substantial interannual variability, associated with, for example, the strength of Tibetan Plateau heating and the land-sea temperature contrast (Li and Yanai, 1996), or the El Niño Southern Oscillation (Xavier et al., 2007). Evidently, the ways in which the monsoon interacts with its surroundings are multi-factor and multi-timescale, and so these interactions are key to understand in order to increase forecast skill in the region. This thesis will focus on one of these ways that the monsoon interacts with the large-scale atmosphere around it: monsoon convection.

1.1.2 Importance of convection during the monsoon

In meteorology, moist cumulus convection refers specifically to the density-gradient driven process of warm, moist air rising vertically in the atmosphere, before cooling, thus forming cumulonimbus clouds which are associated with heavy precipitation at the surface. As convection is the fundamental process by which thunderstorms are formed, it is now common practice to use convection as a noun to describe thunderstorms, with the assumption that convective processes are occurring. Therefore, throughout this thesis, convection and thunderstorms will be used interchangeably to refer to such storm clouds.

Due to moisture-laden winds from the equatorial Indian Ocean and ample surface heating, convection is a frequent occurrence during the ISM. The importance of studying this convection becomes especially apparent through the realisation that monsoon convection has relevance beyond its own life-cycle. Chiefly, Parker et al. (2016) noted that the advance of the ISM is intrinsically linked with that of moist convection, which gradually builds in height, and penetrates into the background mid-level dry air (advected from desert regions in the north-west). This is visualised in their schematic of Figure 1.1. At the start of the monsoon season (1 June; panels a and c), convection is typically shallow and non-precipitating, except for the far south-east where monsoon onset is occurring. Further north, although the lower tropospheric winds are already monsoonal (from the Arabian Sea), the mid-level winds continue to advect dry air from the north-west that is highly stable with low equivalent potential temperature. In advance of the northern limit of the monsoon, shallow and congestus convection frequently detrains around the freezing level (Menon et al., 2018), thus acting to moisten the mid-level environment, causing the mid-level wedge of dry air to become shallower in vertical extent and retreat further north-westwards. By 15 July, Figures 1.1b and d display how the monsoon circulation dominates at low-levels and mid-levels, with the dry air confined to Pakistan, and deep convection penetrating well above the freezing level with associated heavy precipitation at the surface.

The hypothesis of Parker et al. (2016) makes sense of the advance of the monsoon propagating non-steadily directly against the mid-level flow, as it is the convection-induced retreat

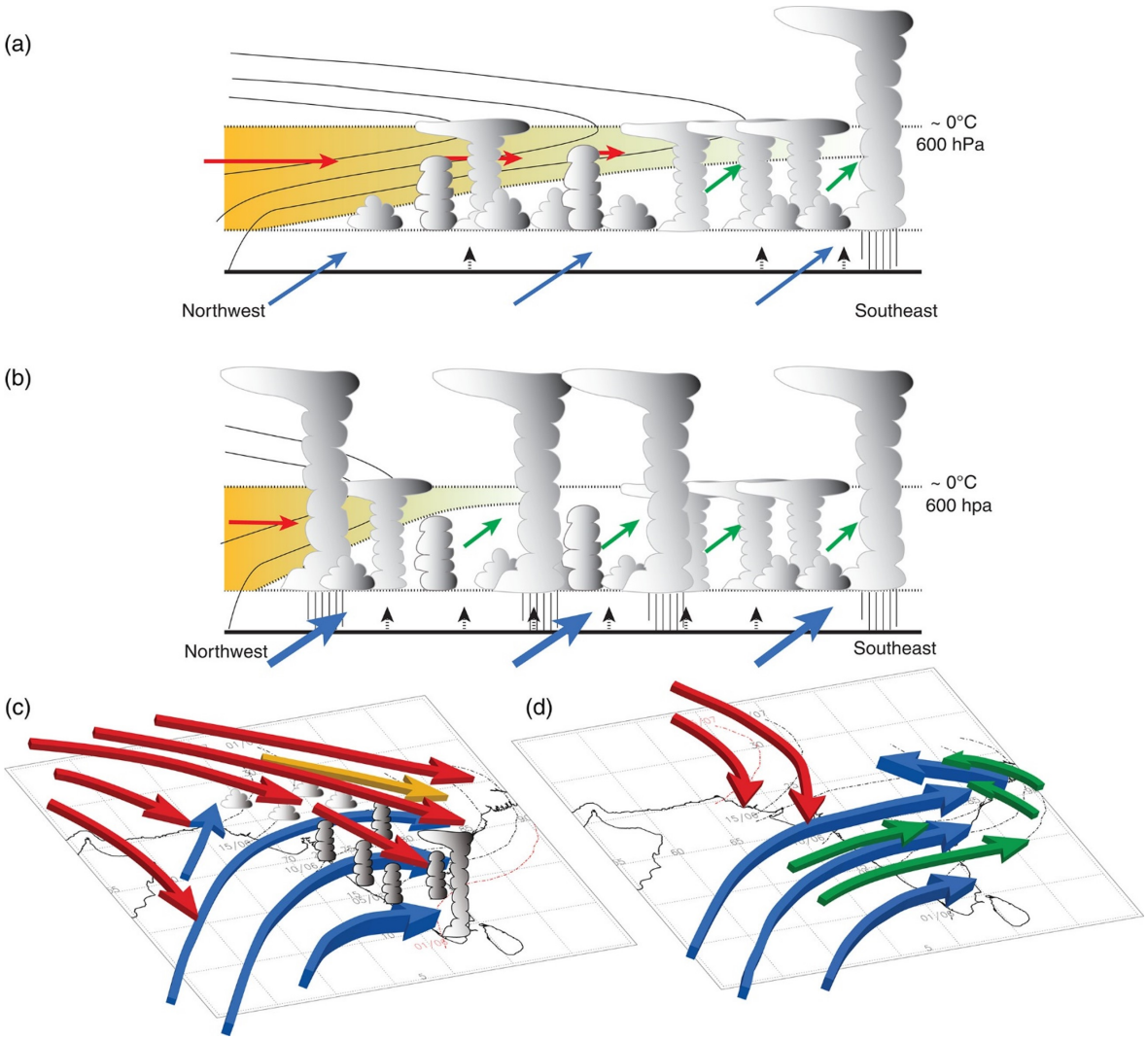

Figure 1.1: Schematic diagram showing equivalent potential temperature (θ_e, fine contours), horizontal wind vectors, and convective heights. Regions with high static stability are shaded orange. Panels (a) and (c) show a cross-sectional and 3-D view respectively for a date around 1 June, and panels (b) and (d) for 15 July. From Parker et al. (2016).

of this mid-level dry air that drives the northern limit of the monsoon forwards. As a result, there is clear motivation for understanding what controls the development of convection. However, understanding monsoon convection is intrinsically complex because the monsoon circulation (and associated rainfall) is a convectively coupled phenomenon; convection occurs on multiple spatial scales, and its relationship with the large-scale circulation is two-way and non-linear, e.g., as seen by Louf et al. (2019a) for northern Australia during the Austral monsoon. Furthermore, atmospheric convection is predictable on timescales of only a few hours (Lorenz, 1969). Turner et al. (2020) noted that to better understand variability

in monsoon rainfall, one must approach the two-way interaction between convection and large-scale forcing from both angles. Obtaining more detailed high-resolution observations of convection during the Indian monsoon – of which there is a notable historical lack – will allow for the design of better parameterisation schemes. Furthermore, the provision and use of these observations in real-time would allow for their assimilation into numerical weather prediction models, potentially enhancing forecast skill.

1.1.3 Known characteristics of Indian monsoon convection

Many early works in monsoon convection used weather station data, specifically the number of thunderstorm days as monthly means, in order to understand storm frequency in different regions (Williams, 1961; Portig, 1963). Whilst such works were limited by the spatial availability and reliability of these station observations, it became evident that monsoon convection is especially prevalent in north-eastern parts of India, as well as the western coast (i.e., the Western Ghats region). Early radar studies and aircraft observations also showed that the heights of storms in the tropics were capable of exceeding the height of the tropical tropopause (at about 16 km), reaching maximum heights of almost 20 km in north-eastern India (Krishna Rao, 1961).

Since the dawn of the satellite era, understanding of monsoon convection has been primarily driven by the use of space-borne radars aboard the Tropical Rainfall Measurement Mission (TRMM), and its successor (Global Precipitation Measurement, GPM). Romatschke and Houze (2011) focused specifically on the South Asian monsoon, and found the Western Ghats and north-eastern India to exhibit the highest precipitation totals during the monsoon season (Figure 1.2), owing to the aforementioned frequency of convection in these regions. They referred to two main reasons for this: persistent onshore coastal winds, and their positions upstream from mountainous regions. A high proportion of rainfall for much of north-eastern India is classified as stratiform (Figure 1.2e), as well as parts of the eastern coast at latitudes of around 20°N. This is possibly due to the precipitation footprint of large mesoscale systems such as monsoon depressions in these regions (Virts and Houze, 2016),

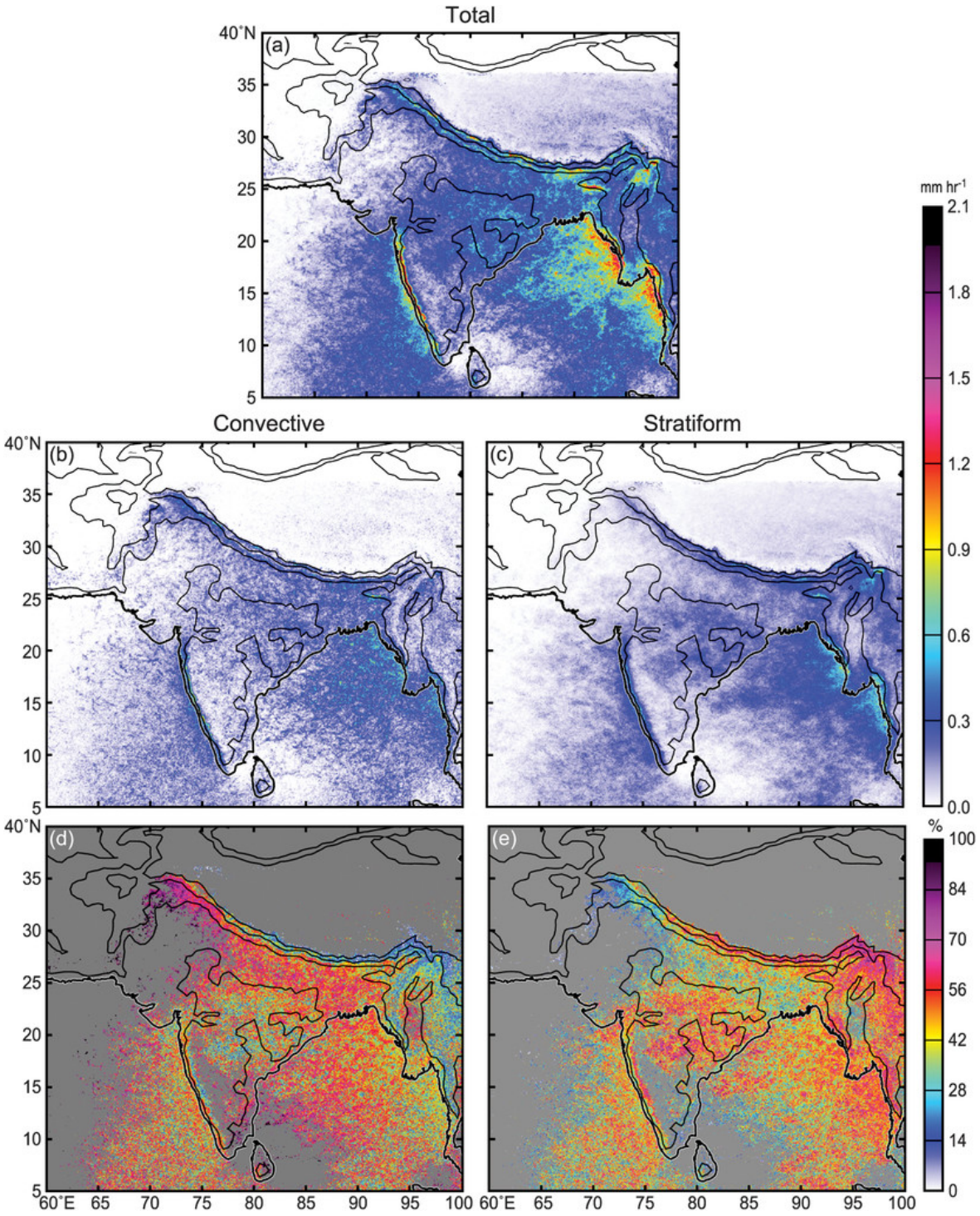

Figure 1.2: Climatology of monsoon precipitation (a, total; b, convective; and c, stratiform) using TRMM. Percentages of rainfall classified as convective (panel d) or stratiform (panel e) are shown for all areas with rainfall exceeding 0.15 mm hr^{-1}. From Romatschke and Houze (2011).

and this is reflected in the precipitation totals in Figure 1.2a. Nonetheless, Figure 1.2 shows that, typically, large stratiform regions are collocated with areas of extreme convection (Ro-

matschke et al., 2010; Romatschke and Houze, 2011). Indeed, the similar rainfall patterns in Figure 1.2b–c provide assurance that the study of Indian monsoon convection has relevance too for the large-scale conditions associated with broader stratiform regions that can bring sustained rainfall. However, Romatschke and Houze (2011) noted the exception of the Western Ghats region, which seems to exhibit frequent non-extreme convection with no associated stratiform region, although this is not too obvious in Figure 1.2. The foot of the Himalayas, despite being non-coastal, displays another relative maximum in precipitation, again upstream of steep orography. Nocturnal northerly katabatic winds from the Himalayas converging with the moist background monsoon circulation is a likely contributor to this maximum, in addition to the afternoon peak associated with the solar cycle (Hunt et al., 2022). This region also exhibits a high percentage of rainfall classified as convective (Figure 1.2d).

Further patterns evident in Figure 1.2 are that, downstream from the Western Ghats (south-eastern India), there is a rain shadow region with less convective activity. North-western India sees lower relative rainfall totals, with the monsoon a less persistent influence in this region, and there is perhaps less frequent propagation of intense convective systems into this area. Instead, the region seems to rely on isolated convective cells (Figures 1.2b and d).

The diurnal cycle of monsoon convection is also of great interest, as it is known to be the principle mode (along with seasonality) that regulates convective variability in the tropics (e.g., Yang and Slingo, 2001). Yang and Slingo (2001) found that tropical convection over land can be most frequently explained by the solar cycle and associated low-level atmospheric heating. Over the ocean, the diurnal cycle of convection is known to be more complex with a weaker mid-morning peak evident, possibly from initially land-based convection propagating out from the coastlines. Despite the infrequent overpasses of TRMM in any particular grid-box, many years of data have also allowed a satellite-based analysis of the diurnal cycle of convection in a regional sense across India (e.g., Romatschke et al., 2010; Qie et al., 2014). They found a diurnal maximum in convection during the afternoon and evening over land with a weaker maximum around midday over the ocean, in-keeping with Yang and Slingo (2001). More recently, Shige and Kummerow (2016) studied precipitation-top heights (PTHs) over the Western Ghats region during the ISM and related variation in PTH

to its large-scale environment, specifically to low-level static stability. PTH is defined as the maximum height of 0.5 mm hr^{-1} rainfall rates in any precipitating region. They found that PTHs decreased systematically as low-level stability increased, and found stability to be a more influential parameter compared to low-level and mid-level humidity in regulating PTH. Intraseasonal variability during the monsoon, associated with the Boreal summer intraseasonal oscillation (BSISO), has also been the focus of much research from a local precipitation and cloud standpoint. Specifically, it has been found that precipitation and the organisation of convection significantly increases in central, northern, and western parts of India associated with monsoon active periods (e.g., Krishnamurthy and Shukla, 2000, 2007; Rajeevan et al., 2010; Saha et al., 2014; Rao et al., 2016).

1.1.4 Modelling ISM convection

There are several notable model inaccuracies in present-day simulations of the ISM, which might be better diagnosed if we were to improve our understanding of monsoon convection in observations. For example, the monsoon is typically too dry in CMIP-class models (Coupled Model Intercomparison Project; e.g., Sperber et al., 2013) over central parts of India (frequently described as the monsoon core zone). This bias is coupled to that of the large-scale monsoon circulation, specifically the 850 hPa winds being too weak (Sperber et al., 2013). Convection-permitting simulations have been shown to be excessively wet in the north and north-east, and too dry over the Western Ghats (Willetts et al., 2017). Furthermore, monsoon onset is consistently too late in coupled models (Levine and Turner, 2012; Levine et al., 2013; Sperber et al., 2013), suggesting that models do not represent the convectively driven onset of the monsoon well. Moreover, model simulations struggle to accurately capture variability in convection within the monsoon season, such as the diurnal cycle (Willetts et al., 2017) and active and break periods (Jayakumar et al., 2020). For instance, global models with parameterised convection tend to have a peak in convective activity too early in the day (Willetts et al., 2017), and whilst overall more realistic, perhaps slightly too late and intense in convection-permitting models. Additionally, monsoon active periods are known to

be inherently less predictable than break spells (Goswami and Xavier, 2003; Taraphdar et al., 2010), which has ramifications for model skill. The transition of convection from shallow to deep is also a profound problem for parameterisations (Mapes and Zuidema, 1996), due to the feedback between mid-level detrainment of cumulus congestus clouds moistening the mid-troposphere and further convective growth. It remains unclear how convection-permitting models of different resolutions cope with this transition during the monsoon.

Ultimately, to evaluate our understanding of monsoon convection against that of theory and convection-permitting models, current information on the characteristics of ISM convective storms is insufficiently resolved. In order to capture further insight into monsoon convection, a network of ground-based weather radars is used, and is introduced in the following section.

1.2 Monitoring convection with radars

This section provides background with respect to using ground-based weather radars for analysing convection. As mentioned previously, there exists a historical lack of observations of convection over India, despite the highlighted importance of convection as a coupled component of the monsoon itself. Ground-based weather radar data provide high-resolution measurements of precipitation at a high sampling frequency, observing large swathes of Earth's lower atmosphere. Assuming a negligible effect from interruptions to data provision (e.g., due to radar maintenance), these radars are consistently observing the local precipitation state around them, gradually building a climatology of rainfall regimes where they exist. Due to the prevalence and multi-scale complexity of convection in the tropics, such observational measurements are becoming increasingly valuable as more radars begin to be used in tropical regions for nowcasting, rainfall prediction and flood warning purposes.

Particularly during the 2010–2020 decade, ground-based weather radars have been assembled in locations beyond the more established networks of Europe and North America, especially those regions susceptible to extreme rainfall. As shown in Figure 1.3, radar networks now encompass much of populated China, India, South Africa, Australia, Indonesia, and Brazil (Saltikoff et al., 2019), as well as more recently Nepal (Talchabhadel et al., 2021).

Additionally, existing radar networks within countries and administrative regions continue to be developed and expanded, notably in India (e.g., Roy et al., 2019) and Australia, where a long-term archive of operational radar data has recently been developed and made available for research purposes (Soderholm et al., 2019). Previous studies have often taken advantage of research-grade radars such as CAMRa (The Chilbolton Advanced Meteorological Radar; Goddard et al., 1994) or CPOL (C-Band Polarimetric Radar System; Keenan et al., 1998) in Darwin, Australia. These radars are specifically operated for research purposes, and so typically have very high spatiotemporal resolution and tailored scanning strategies, as well as dual-polarisation functionality. However, they are difficult to finance, especially in developing regions that are less likely to have the scientific funds available, and are often restricted to when field campaigns are in operation. Therefore, exploring the potential use of operational radars in understanding local hydrometeor fields and model evaluation is especially important owing to the relatively few research-grade radars in tropical regions. For these reasons, the proven ability to robustly measure the morphology of clouds and convection using operational radars is very advantageous to the scientific community.

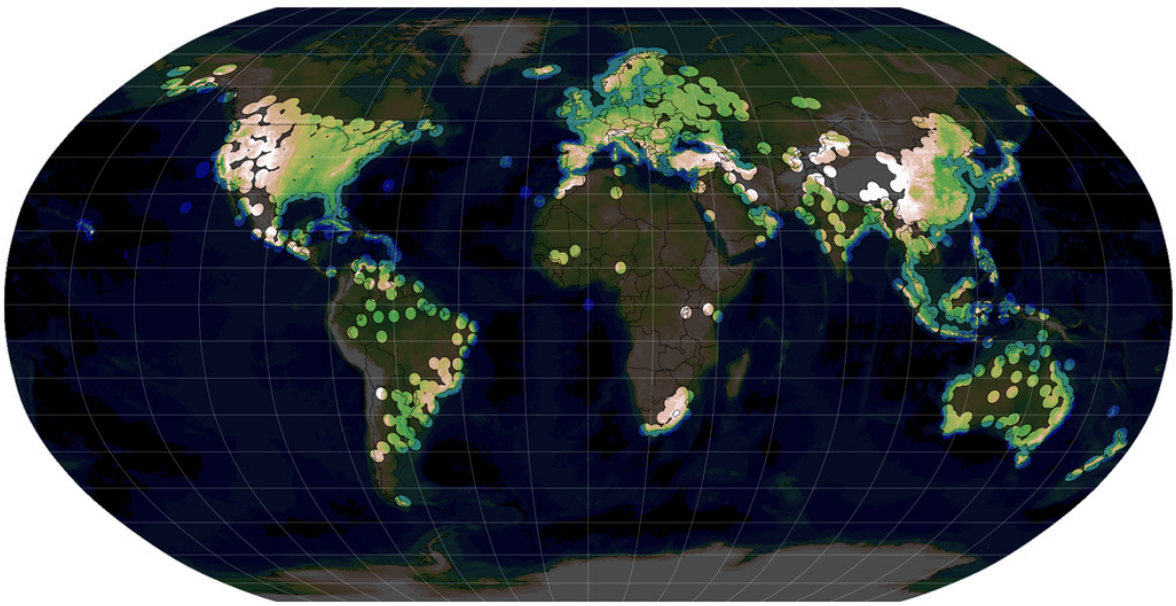

Figure 1.3: A recent (2019) worldwide distribution map of ground-based weather radar sites (illuminated regions), assuming coverage within a radius of 200 km. From Saltikoff et al. (2019), primarily utilising the World Meteorological Organization radar database (http://wrd.mgm.gov.tr/).

1.2.1 Radar reflectivity

The original use for radar technology in the second world war was for the detection of enemy aircraft. The potential for this technology to also observe hydrometeors was noted soon afterwards, leading to the development of weather radars. Today, the primary operational use for these radars is to monitor precipitation, for capabilities related to nowcasting and flood forecasting. Traditional weather radars operate at microwave wavelengths around 10 cm for an S-band radar (or 5 cm for a C-band radar), thus observing rain drops and other hydrometeors within the Rayleigh scattering regime. Therefore, the weather radar does not directly measure rainfall rate, but simply remotely observes atmospheric particles through a scattered microwave pulse return. From the amplitude of this return, one can calculate the radar reflectivity factor (Z), which gives us information on the average diameter (D) and number of particles (n) for each range-gate where the radar dish is pointing.

$$Z = \sum_{i=1}^{n} D_i^6 \tag{1.1}$$

Equation 1.1 makes evident the importance of the diameter of particles for determining the magnitude of the reflectivity, whose native units are $\mathrm{mm}^6\ \mathrm{m}^{-3}$. Typically radar reflectivity is independent of wavelength if the hydrometeor's maximum diameter is much smaller than the radar wavelength and the scattering is described by the Rayleigh approximation. For most weather radars, this will typically be the case, except for very large hydrometeors, such as hail aggregates. As the diameter of particles can vary substantially in the real atmosphere, this is frequently converted to dimensionless logarithmic units of decibels relative to Z (dBZ), and is given by:

$$Z_{dBZ} = 10 \log_{10} Z. \tag{1.2}$$

Fortunately, it is widely accepted that convective parts of clouds are typically associated with larger diameter hydrometeors compared to surrounding stratiform rains (e.g., Tokay and Short, 1996), owing to riming and accretion growth processes dominating in the intense

updraft regions of convective cells. As a result, reflectivity is an inherently useful parameter for the identification (and subsequent analysis) of convection with radars. Specific details on how radar reflectivity is used to classify convection are given in Chapter 2.

1.2.2 Radars used in this study

The India Meteorological Department (IMD) maintains a network of operational ground-based Doppler weather radars (Viswanathan et al., 1997; Roy Bhowmik et al., 2011), with the current network map as of January 2022 shown in Figure 1.4. The network initially was primarily coastal in nature to allow for the tracking and nowcasting of monsoon depressions, for which it is still used today. However, the number of radars has continued to expand in the 2010–2020 decade, resulting in good coverage spanning most Indian regions. The network is primarily S-band with a minority of C-band and X-band radars, some with dual-polarisation capabilities (e.g., for hydrometeor classification). All radars also have Doppler functionality for measuring particle velocities. For the purposes of this thesis however, only radar reflectivity is utilised.

Following the INCOMPASS field campaign of 2016 (Interaction of Convective Organisation with Monsoon Precipitation, Atmosphere, Surface and Sea, Turner et al., 2020), radar data from 17 network radars – the majority operating at S-band (frequencies of 3 GHz) – were provided for the entire 2016 monsoon season (May 15–September 30), and constitute the primary source of data for this thesis. These 17 radars are highlighted in Figure 1.4. Further specifications of these radars are given in Chapter 2, where a thorough description of the radar scanning strategy is given.

1.2.3 Previous use of ground-based weather radars

It is well known that ground-based weather radar observations provide useful information for observing and tracking mesoscale features concomitant with precipitation. Indeed, its versatility for analysis regarding various applications of meteorology was noted whilst weather radars were still in their relative infancy (e.g., Atlas, 1964; Battan, 1973; Smith et al., 1974;

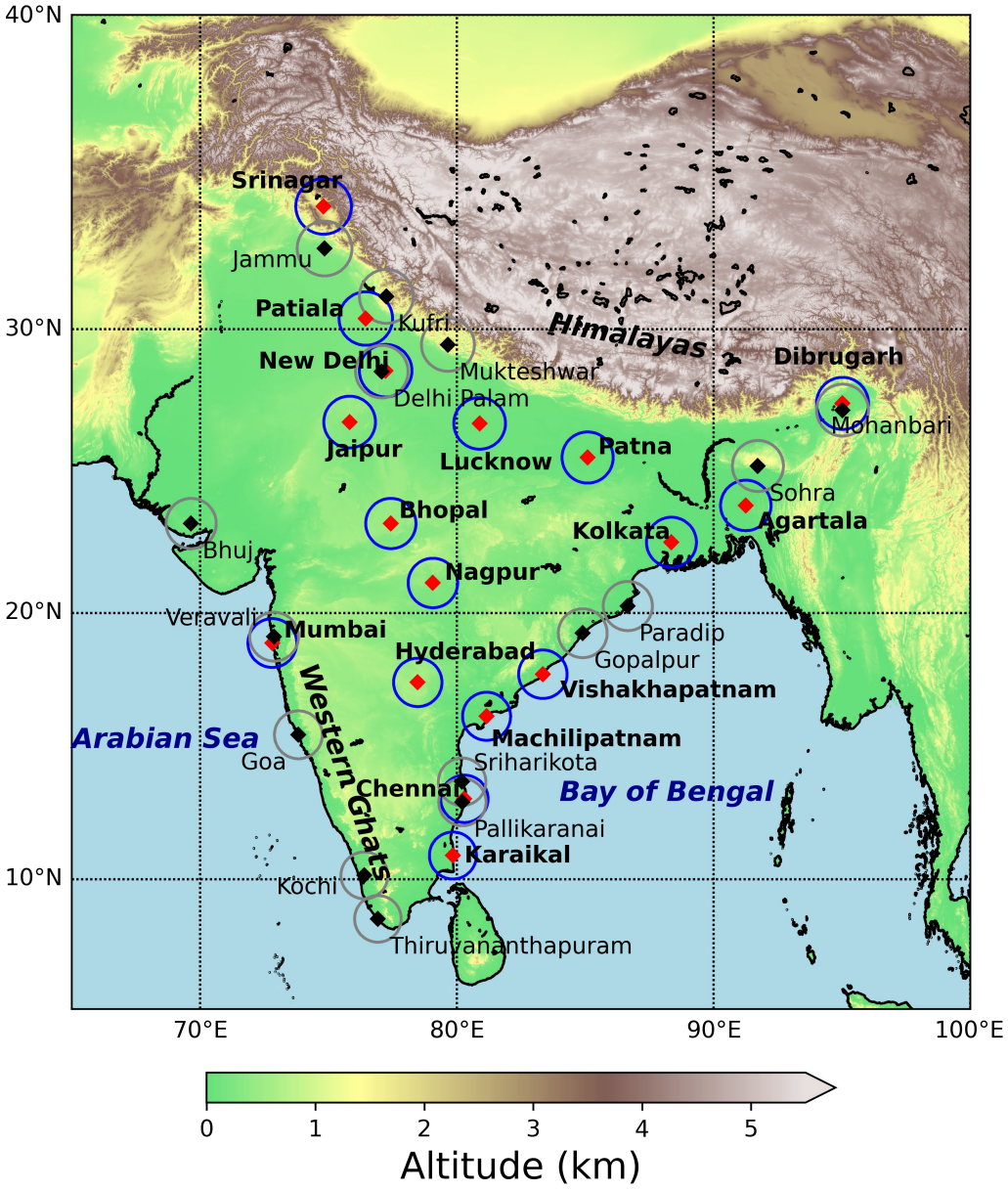

Figure 1.4: Current map of IMD radar locations (as of March 2022), as shown at https://mausam.imd.gov.in/imd_latest/contents/index_radar.php, overlayed on top of Indian orography, with major geographical features labelled. The 17 radar sites available for use in this thesis following INCOMPASS 2016 are highlighted in red with blue rings and bold font. The IMD continues to expand the network.

Browning, 1978). However, early attempts at objective determination of clouds were restricted by the multi-dimensional nature of weather radar reflectivity data (range, azimuth, elevation, echo intensity, and time; Boardman and Smith, 1974) and thus, the shear volume of processing required, combined with less powerful computers at the time. Nonetheless, many attempts at objectively analysing clouds and convection have been trialled over time, by inspecting

patterns in radar reflectivity echoes (e.g., Donaldson, 1961; Asai et al., 1977; Rosenfeld, 1987; Lakshmanan et al., 2013).

In particular, radar-derived echo-top height (ETH) is of key importance for understanding local cloud fields as it is indicative of storm severity (Donaldson, 1964). For a typical Plan Position Indicator (PPI) radar scanning strategy, pulses are emitted at multiple elevation angles, providing data coverage at different heights in the atmosphere. Conventionally, ETH is defined as the maximum height of the minimum detectable echo (Donaldson, 1964; Lakshmanan et al., 2013), and in practice the maximum height of some standard value of reflectivity is taken. The limitations of such a quantitative analysis were noted early on, for reasons such as radar resolution, beam broadening, and side lobes (e.g., Atlas, 1964; Donaldson, 1964). Additionally, there are only as many data points as there are elevation angles for PPI scanning, i.e., a continuous vertical profile of reflectivity can only be estimated through interpolation or some other method. Naturally, due to the nature of radar sampling, no 'perfect' method exists. However, vast improvements in the quality and accuracy of computing ETH and other cloud statistics with radar have been made over time. Indeed, satellite observations have shown that 10 dBZ ETH derived by ground-based radars for tropical congestus convection is negatively biased (i.e., too low) by less than 2 km compared to the visually observed cloud-top height (Casey et al., 2012), and this holds for the 0 dBZ ETH threshold for deep convection (Kumar et al., 2013a). Such quantitative assurances allow for greater confidence in the ETH parameter and its applications for understanding storms. It is also justified to consider ETH as a useful parameter in its own right, thus negating the non-zero errors with respect to true cloud top, though utmost care should be taken to ensure ETH values are self-consistent as a function of range from the radar, height, and time. Further information on the method employed for robust calculation of ETH and other statistics using Indian operational radars is provided in Chapter 2.

More recently, progress in the communal development of open-source radar-related software has enabled the automation of some quality control and processing of radar measurements such as ETH. The Wradlib library for Python (Heistermann et al., 2013) has broad capabilities, from more basic operations such as the conversion of reflectivity to rainfall, or

quality control procedures such as clutter removal, to more complex georeferencing facilities. Additionally, the PyArt library for Python (Helmus and Collis, 2016) offers a similar collection of user-friendly algorithms and utilities, as well as simple routines for radar data visualisation, and is compatible with a variety of radar data formats. A frequently desirable technique in radar meteorology (for analysing a vertical profile of reflectivity and calculation of ETH) is the construction of a constant altitude plan position indicator (CAPPI), a horizontal cross-section of data at a constant altitude. This allows for the analysis of reflectivity or velocity data on a discrete vertical level (East and Dore, 1957; Marshall and Gordon, 1957). The Thunderstorm Identification, Tracking, Analysis and Nowcasting (TITAN) system (Dixon and Wiener, 1993), which identifies storms using a series of vertically stacked CAPPIs, computes a large number of storm diagnostic properties, and has been utilised in many radar studies since using both operational and research-grade radars. Radar meteorologists and forecasters can spend significant time and resources on radar quality control and common approaches such as 3-D grid construction, especially in a research context. Thus, the past and continued development of such analysis tools has profound positive ramifications for the accessibility of radar forecasting and research. However, the limitation of such tools is that one is largely constrained by their fixed methodology. Weather radars with lower resolution specifications (such as a smaller number of elevation angles or larger beamwidths) may require a fine-tuned method due to a higher likelihood of spatial artefacts developing during the regridding process (e.g., Zhang et al., 2005; Collis et al., 2010). As a result, a tailored approach toward radar processing is undertaken in this thesis, whilst using some of the aforementioned processing tools, such as Wradlib.

For the operational radars to provide accurate and consistent reflectivity data and be useful as a comparison for models, they must also be calibrated to within a high degree of accuracy. Consequentially, the development of calibration procedures has been a long-standing pursuit in radar meteorology. Recently, Louf et al. (2019b) developed a two-step approach towards weather radar calibration using ground clutter to evaluate consistency, before being calibrated against GPM using the volume-matching method of Warren et al. (2018). In order to ensure consistent and accurate reflectivity retrievals here, this method is applied for the first time to

the IMD radars, and is described in detail in Chapter 3.

1.2.4 Radar-derived convection and the large-scale environment

Recently, with the advancement of regional high-resolution models, it has become increasingly desirable to understand the placement of convection within the large-scale circulation. One of the most widely used data sources for such work in recent years is the CPOL research radar in Darwin, northern Australia (Keenan et al., 1998). More than 17 years of largely uninterrupted data from the site has been used to build a climatology of convection (e.g., Jackson et al., 2018), with the primary aim of better understanding the relationship between convection and the large-scale in the tropics. Kumar et al. (2013b) stressed the importance of large-scale dynamical conditions in determining local convection, with a strong influence attributed also to orographic effects. Kumar et al. (2013a) demonstrated the existence of four cumulus modes of tropical convection, with an additional overshooting top mode as well as the shallow, congestus, and deep modes detailed by Johnson et al. (1999). The existence of these four cumulus modes has importance for model representations of convection through parameterisation, that often distinguish between shallow and deep convection only (Arakawa and Schubert, 1974; Davies et al., 2013). Furthermore, Kumar et al. (2013a) discovered that the transition between congestus and deep modes is strongly related to mesoscale and synoptic-scale dynamical forcing as opposed to simple thermodynamic principles. However, Peters et al. (2013) and Louf et al. (2019a) noted that establishing reasonable causal relationships between tropical convection and the large-scale environment remains challenging due to the non-linear interactions involved. In spite of this, by describing the relationship between convection and the large-scale in greater detail, valuable additional insight into convective behaviour is gained (Louf et al., 2019a), thus providing a testbed for high-resolution simulations of convection, which is a principal motive for this thesis.

For India specifically, the use of ground-based weather radars for the analysis of ISM convection remains a very novel pursuit owing to the relatively recent implementation of the operational radar network. Utsav et al. (2017) used an X-band radar in the Western Ghats

to analyse statistical patterns in convection. Most relevantly, they found that congestus cells were most frequent on the windward side of the Western Ghats mountains, with deep cells more prevalent on the leeward side. Furthermore, they found a lead-lag relationship between congestus and deep cells, suggesting that moistening of the mid-levels by congestus allows for the subsequent formation of deep convection, and this is consistent with Parker et al. (2016). Following this, Utsav et al. (2019) proceeded to examine variability in convection as seen by the X-band radar between monsoon active and break periods, showing differing characteristics in local convection and the amplitude of its diurnal cycle with respect to this intraseasonal variability. Specifically, they found an increased frequency of deeper storms, as well as a smaller amplitude in the diurnal cycle of ETH, during active (wet) periods. Finally, Jha et al. (2021) analysed convection derived from an S-band IMD radar at Kolkata in the monsoon trough region, comparing to long-term reanalysis datasets. They noted the importance of large-scale dynamic forcing such as static stability for regulating the characteristics of storms around Kolkata. So far, Indian radar studies have focused on individual sites and regions, and so this thesis goes further by comprehensively analysing statistical characteristics of convection across multiple network radars for an entire season, allowing a direct comparison of monsoon cloud regimes in different climate regions.

1.2.5 Use of radars for model evaluation

Model development is presently a rapidly progressing field. Regional convection-permitting models have been shown to greatly improve the diurnal cycle and overall representation of convection compared to general circulation models that use parameterised convection (e.g., Jones and Randall, 2011; Clark et al., 2016; Martin et al., 2017; Crook et al., 2019; Kendon et al., 2021). Furthermore, convection-permitting models continue to be run at ever-higher resolutions. Therefore, many studies have focused on exploring the value of very high-definition models (i.e., horizontal resolution $\leq$ 1 km), given the significant computational expense involved in running them (Weisman et al., 1997; Bryan et al., 2003; Lean et al., 2008; Stein et al., 2014, 2015b). Moreover, these models are tested under many different configurations as

new schemes become available, and as such it can be an overwhelming task to consider what model is best to run. Therefore, it is expedient to evaluate these models on a regular basis, whenever necessary. Indeed, weather radars are one of the few observational sources of data of sufficient resolution and areal coverage to hypothetically keep up with the current pace of model advancements. Therefore, radars are an indispensable tool for better understanding the representation of convection in models. Additionally, due to the aforementioned increasingly high density in the global network of radars, radar-based evaluation can be performed and repeated in more regions, as long as data are made available.

Whilst radars have been used to evaluate models for some time for constraining precipitation estimates, it is only recently that the potential for a wide array of operational radars to evaluate models whenever necessary has been recognised. Formative testbeds in the evaluation of modelled tropical convection using operational radars have been established in recent years. For example, Keat et al. (2019) and Stein et al. (2019) used a network of 11 C-band South African operational radars for evaluation of tropical convection, noting the ability of 3-D radar composites to evaluate the vertical structure and life-cycles of modelled convection.

However, evaluation work of this nature has yet to be performed for India. Therefore, this thesis consists of two major components: robust observation and analysis of convection with Indian operational radars, and secondly, use of this information as a testbed for the evaluation of convection-permitting models. The ability to perform such an analysis has wide-ranging benefits for improving our understanding of modelled convection, particularly in tropical regions.

1.3 Thesis outline

Considering the lack of historical observations of convection over the Indian region outlined above, and its importance as a coupled component of the monsoon, this thesis will focus on developing novel and robust observations of monsoon convection across multiple regions of India using a network of radars. As stated in Section 1.1.1, the ISM is also innately complex, exhibiting several major timescales of variability associated with the diurnal cycle,

active and break periods, and the progression of the monsoon and its onset. A better understanding of the relationships between local convective regimes and this multi-scale variability will enhance predictability and provide a testbed for model evaluation. Finally, as mentioned in Section 1.1.4, it is largely unclear how accurately high-resolution models with explicit convection represent convection over different regions of India. Therefore, this thesis describes how radar observations can be used to compare to convection simulated in high-resolution models, before presenting a radar-based evaluation of modelled convection. Therefore, this work showcases radars as a powerful tool for evaluation of convection-permitting models in India and elsewhere. The research questions addressed by this thesis are summarised as follows:

- To what extent can we develop a robust method toward using IMD Doppler weather radars for identifying convection and evaluating convection-permitting models?
- What relationships exist between radar-derived convection, monsoon onset, and the large-scale circulation during the 2016 monsoon season across multiple regions of India?
- How well do convection-permitting models simulate different aspects of convection compared to the radar observations during the 2016 ISM? What might explain specific biases in modelled convection?

In Chapter 2, the IMD radar network and frequently used large-scale data are described, and the preeminent processing applied to the radars to observe convection is detailed. In Chapter 3, the calibration of radar reflectivity for the Indian operational radars is demonstrated. Chapter 4 is comprised of a paper published in the journal *Weather* (Doyle et al., 2021a), and using the calibrated radar reflectivity data, presents how convection and rainfall develop at 12 sites across India during the 2016 monsoon onset and progression. Chapter 5 – published in *JGR: Atmospheres* (Doyle et al., 2021b) – then provides a detailed assessment of how Indian monsoon convection interacts with large-scale variability such as the diurnal cycle and monsoon active and break periods. In Chapter 6, the IMD weather radars are used to

evaluate convection simulated by convection-permitting models. Finally, the major outcomes and implications of the thesis and thoughts for future work are summarised in Chapter 7.

Chapter 2

Data and methods

This chapter describes the primary sources of data used in this thesis, as well as the processing performed upon the radar data for analysis of convection. More specific and specialised data and methods can be found within the method sections of the individual chapters to which they are relevant.

2.1 Indian ground-based Doppler weather radars

The INCOMPASS field campaign of 2016 resulted in the provision of archived weather radar data from 17 IMD operational ground-based radars (Viswanathan et al., 1997). Data was made available for the entire 2016 monsoon season, spanning 139 days from 15 May to 30 September 2016. Whilst these radars are all part of the same network, their properties are not all homogeneous. For example, of the 17 radars made available, Srinagar is the only one operating at X-band (3 cm wavelength), emitting higher frequency beams compared to the other radars. X-band radar scans are significantly more prone to signal attenuation in convective regions (e.g., Hitschfeld and Marshall, 1954; Serafin, 1990). Furthermore, Srinagar has a higher pulse repetition frequency, which means its maximum unambiguous range is reduced below 100 km. Due to the importance for robust comparisons of convection between radars in this work, the Srinagar radar is not employed for analysis.

Important specifications of the 16 remaining radars are shown in Table 2.1. Of these 16 radars, Mumbai is the only radar available on the west coast. Otherwise, however, there

is good spatial coverage of different regions of India represented by these radars. Many of the radars are coastal and thus near sea-level, but some of the inland sites are at higher elevations, such as Hyderabad and Bhopal at 560 m and 570 m respectively. Table 2.1 shows that all Doppler radars are S-band (approximate 10 cm wavelength) except New Delhi and Jaipur which are C-band (approximate 5 cm wavelength) dual-polarisation radars. The dual-polarisation capabilities are not used in this thesis except when utilised as part of the calibration procedure detailed in Chapter 3. C-band radars experience more attenuation in rain compared to S-band radars, and this effect is quantified later in this section. Otherwise, there are small differences in the angular resolution of the radars shown by the beam-widths. The majority of radars operate with a gate-size of 500 m. Vishakhapatnam has the coarsest range resolution with a gate-size of 1000 m, and Patna and Karaikal the highest resolution at 250 m. The 16 remaining Doppler radars all have a maximum pulse repetition frequency (PRF) of 600 Hz, except Nagpur where the PRF is 400 Hz, resulting in a greater maximum unambiguous range.

The IMD radar scanning strategy (Roy Bhowmik et al., 2011) is to operate in PPI display mode, with polar coordinates of elevation, range, and azimuth. This PPI mode has the antenna at the centre of the display, with height and range increasing radially away from it, dependent on the elevation angle of the radar. Each radar volume scan takes approximately 7 minutes, and repeats every 10 minutes, consisting of 10 elevation angles (θ_{el} ={0.2°, 1.0°, 2.0°, 3.0°, 4.5°, 6.0°, 9.0°, 12.0°, 16.0°, 21.0°}). The radar elevation angles making up a single volume scan are shown in Figure 2.1, out to a range of 150 km. Figure 2.1 shows how the coverage becomes sparser at higher altitudes in this scanning regime, with more continuous sampling provided by the first 4 elevation angles.

Some quality control procedures are performed upon the archived radar data automatically by the IMD. This includes the removal of ground clutter and anomalous propagation echoes in the reflectivity data by specialist software, and is described in more detail in Roy Bhowmik et al. (2011). Moreover, for the purposes of deriving accurate ETH estimates that can be cross-compared between radars, it is crucial to have accurately calibrated readings of reflectivity, which is detailed for the IMD radars in Chapter 3.

Table 2.1: Relevant positional and diagnostic information pertaining to the network of 16 IMD radars used in this thesis. The right-most column shows the total number of complete radar volume scans (consisting of ten elevation angles) available for each radar over the 2016 monsoon season.

Location	Lat. (°N)	Lon. (°E)	Alt. AMSL (m)	Gate size (m)	Beam width (°)	Wave-length (cm)	Total volume scans
New Delhi (DEMS)*	28.59	77.22	253	300	0.95	5.3	17087
Mumbai (VABB)	18.90	72.81	100	300	1.00	10.9	3553†
Bhopal (VABP)	23.24	77.42	570	500	0.93	10.4	13546
Nagpur (VANP)*	21.10	79.06	335	500	0.93	10.4	10701
Agartala (VEAT)	23.89	91.25	35	500	0.93	11.0	14710
Kolkata (VECC)	22.57	88.35	35	500	1.00	10.4	13018
Dibrugarh (VEMN)	27.47	95.02	132	500	0.93	10.6	4314
Patna (VEPT)	25.58	85.09	67	250	0.97	10.4	17207
Vishakhapatnam (VEVZ)	17.75	83.35	35	1000	1.00	10.4	16497
Patiala (VICH)	30.36	76.45	277	500	0.93	10.5	16453
Jaipur (VIJP)*	26.82	75.82	399	300	0.95	5.3	5566‡
Lucknow (VILK)	26.77	80.88	143	500	0.97	10.4	6914
Hyderabad (VOHY)	17.45	78.47	560	500	0.93	10.5	10211‡
Karaikal (VOKL)	10.91	79.84	20	250	0.93	10.7	4987
Chennai (VOMM)	13.07	80.29	35	500	1.00	10.4	17839
Machilipatnam (VOMP)	16.18	81.15	35	500	1.00	10.4	18589

*These radars have a minimum elevation angle of 0.5° as opposed to 0.2°. All other elevation angles are the same as given in the text.
†Frequent periods of missing data after 27 June.
‡Data from 1 July onwards only.

The right-most column in Table 2.1 shows that the total number of radar volumes (i.e., a complete set of 10 elevation angle scans) varies greatly between sites. If there were zero missing data through the season from 15 May through 30 September, i.e., a radar volume every 10 minutes, this would equate to 19872 volume scans. The number of available radar scans for each day through the season is shown in Figure 2.2 for each site. Dibrugarh (VEMN) is not shown here as following radar calibration in Chapter 3, it is not used further in this thesis, and has large amounts of missing data. Firstly, two locations (Hyderabad and Jaipur in panels a and b respectively) only have data available from 1 July 2016. Secondly, days with few

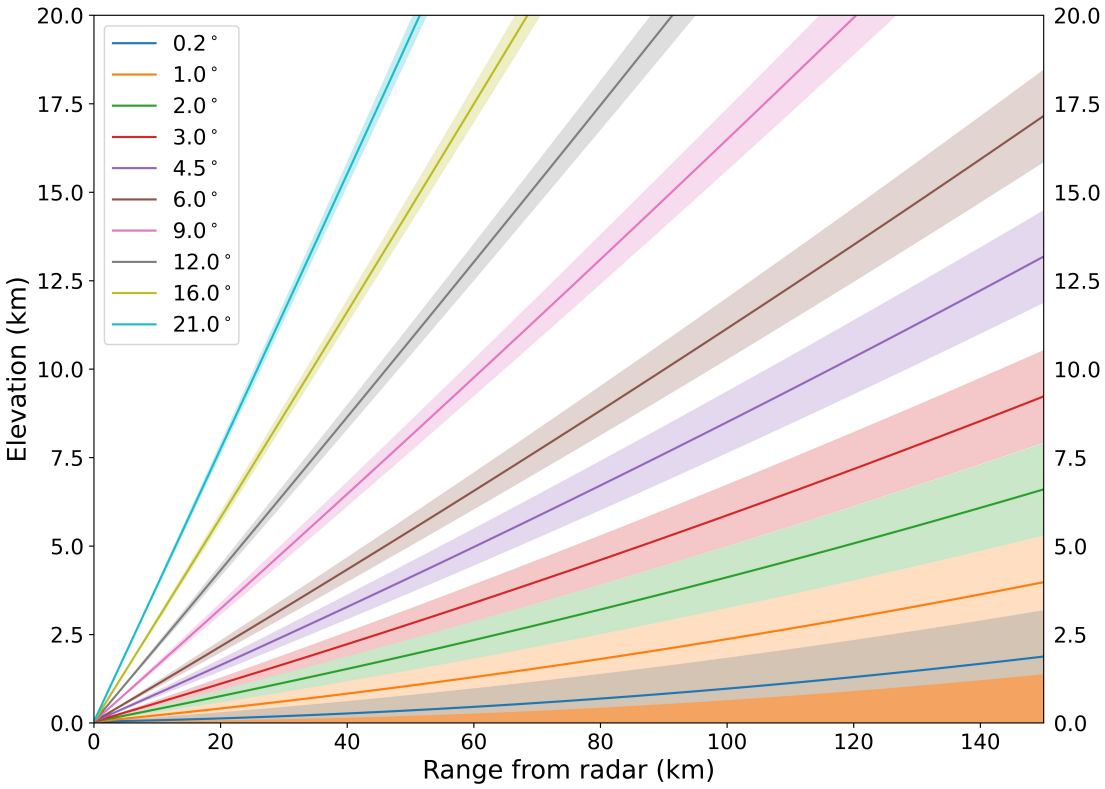

Figure 2.1: Height above ground level (assumed flat) of each IMD radar elevation angle as a function of range from the radar. The solid line is the centre of the beam, and accompanying shaded regions represent a beam-width of 1°. These 10 elevation angles make up an IMD radar volume scan. Areas at (or below) ground level are shaded light brown.

radar scans are common-place within the archived data, most notably for Mumbai (VABB) and Karaikal (VOKL). Lucknow (VILK) and Jaipur (VIJP) also have lengthy periods of few daily radar scans. Whilst the frequencies and distributions of these data are still sufficient for understanding the average characteristics of 2016 monsoon convection, caution must be applied when relating cloud characteristics over the diurnal cycle or active and break periods, and when comparing between radar sites, owing to the differences in sampling.

2.2 Processing of radars

The procedure for the identification of convective regions with this radar network is explained in this section. Firstly, details of the re-gridding of the radar data are given, then the classification of convection is described, and finally the statistical storm characteristics obtained from this approach are specified.

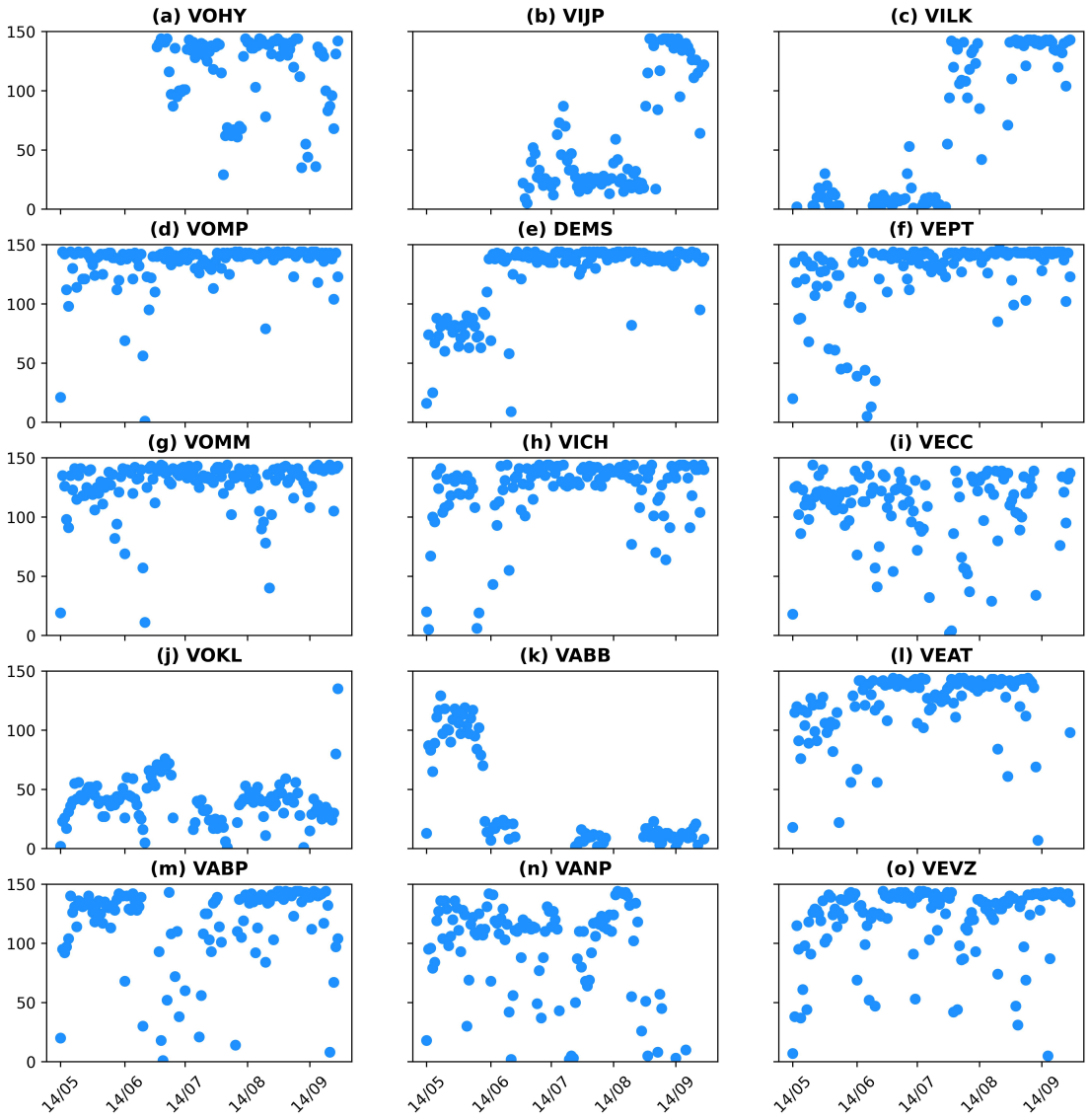

Figure 2.2: Daily number of complete radar volume scans through the 2016 monsoon season for each site (a–o) shown in Table 2.1, except for Dibrugarh. A radar volume scan every 10 minutes equates to a daily total of 144 volumes.

2.2.1 Construction of a 3-D grid

The primary method surrounds the construction of a vertical profile of reflectivity in Cartesian coordinates, transformed from its native polar coordinates, utilising CAPPIs. In a storm, a radar pulse – travelling at the speed of light (c) – samples many hydrometeors distributed within a single sample volume. The size of this sample volume increases with range due to beam broadening and is dependent too on the pulse width (τ). As the horizontal and vertical beam-widths of the IMD radars are equivalent (i.e., a cylindrical beam with diameter θ), the

sample volume (β) as a function of range (R) from the radar can be given by

$$\beta = \frac{\pi \cdot R^2 \cdot c\tau \cdot \theta^2}{8}. \tag{2.1}$$

This means that for a standard τ of 1.0 μs and if θ is 1° (converted to radians), then β is 0.057 km^3 at 40 km and 0.355 km^3 at 100 km. This equates to a volume more than 6 $\times$ larger at 100 km compared to 40 km, thus reiterating the need for carefully considered interpolation onto a 3-D Cartesian grid to reduce any biases in radar-derived convection.

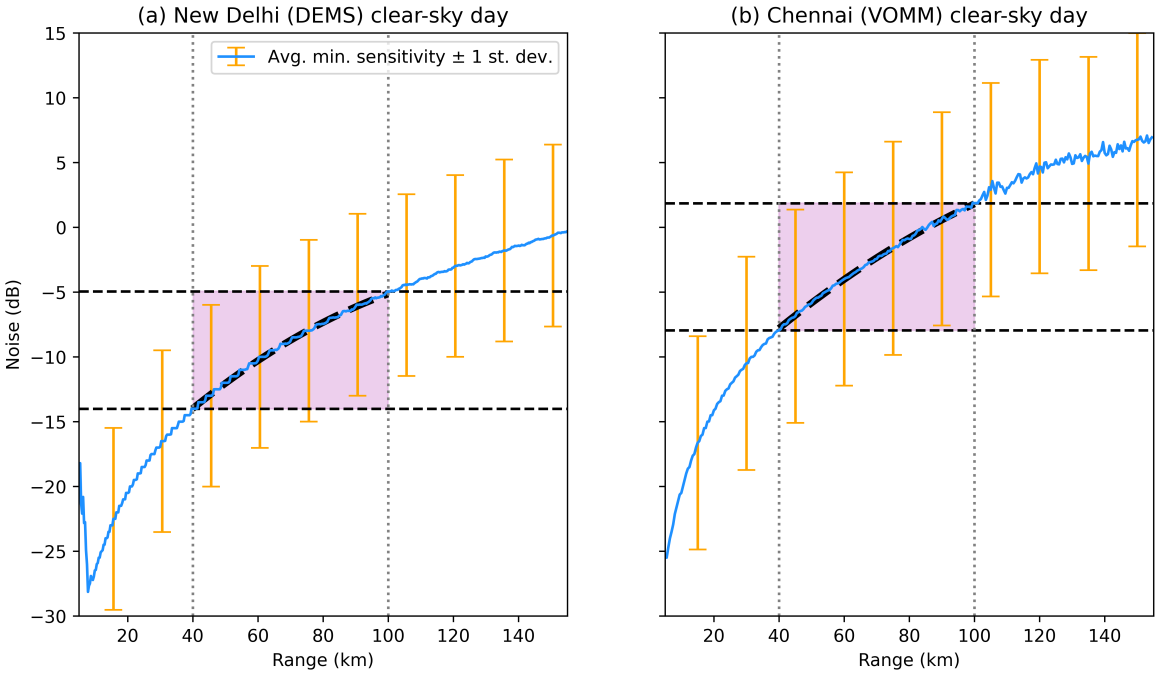

Figure 2.3: Minimum sensitivity of calibrated reflectivity for (a) the New Delhi C-band radar, and (b) the Chennai S-band radar, as a function of range from the radar, for all radar volumes during a clear-sky day (15 May 2016 in both cases). The blue line shows the average noise floor and the orange error bars represent the standard deviation. Dotted vertical lines show the domain boundaries of the 3-D grid, and dashed horizontal lines show the average minimum sensitivity at ranges of 40 km and 100 km. Thus, the shaded region is the relevant region for the 3-D grid, and the thick dashed black line within is the quadratic polynomial fitted to these data.

The 3-D grid is constructed using the Wradlib module for Python (Heistermann et al., 2013). The Cartesian grid consists of 28 vertical levels at 0.5 km resolution from a base of 2 km, chosen to be above any clutter near the surface but below the freezing level so as to avoid brightband effects (usually at around 5 km over India during the Boreal summer;

Harris Jr et al., 2000). Only reflectivity data within a range of 40–100 km from the radar are considered. This is partly due to beam broadening effects, that as described above, means the resolution becomes coarser with range. Secondly, the noise floor (i.e., the minimum signal the radar can measure) increases with range, as shown in Figure 2.3. The radar sensitivity also varies by radar, as it depends on the wavelength, angular and range resolutions of the radar. As shown in Figure 2.3, the minimum sensitivity of the C-band New Delhi radar at 100 km is around −5 dB. For the S-band Chennai radar, it is a little higher at around 2 dB. In order to estimate the approximate height of convective cells (described later), and gain information on cell size and morphology, it is important that the minimum sensitivity of the radars are not too high such that cloud edges/tops are being missed. All minimum sensitivities will be given in later chapters after the radar reflectivities are corrected for any calibration errors. Finally, the 40 km inner boundary was necessary to avoid the 'cone of silence' due to constraints in the steepest elevation angles. Large cumulonimbus towers may exceed 16 km during the monsoon season (Krishna Rao, 1961). However, the largest elevation angle in the IMD radar scanning strategy is 21°. The upper edge of this approximately 1° circular beam will intersect the 16 km level when it is a horizontal distance of around 40 km from the radar. Any further restrictions in the size of the horizontal domain in order to capture higher clouds would reduce the number of sampled cells and because only one season of data is available, the size of the horizontal domain was prioritised.

The horizontal resolution of the grid should ideally be high enough to retain original features observed by the radar that constitute convective cells, and it is useful to recall that one key advantage of the radars is that they have superior horizontal resolution to satellite observations. It is found that a horizontal resolution of around 1 km × 1 km performs well at retaining original features in the original PPI scans. Re-gridding the radar data to a higher resolution than this increases computational time, and was found to result in an over-abundance of very small-scale features that don't represent true convection (not shown).

Interpolation of reflectivity is carried out in dBZ following the recommended procedure for deriving ETH by Warren and Protat (2019). One problem with interpolation in logarithmic dBZ units is that regions with no measureable reflectivity must have a minimum reflectivity

value inserted, as neglecting these data would lead to erroneously high reflectivity values in the case where a small pocket of high reflectivity is surrounded by a large non-precipitating region. Referring back to Figure 2.3, the black polynomial between 40 km and 100 km is used to take a minimum noise value at each range gate (for each radar). Assuming that the sub-noise floor reflectivity values are randomly distributed within the bounds where the minimum possible value is 0 mm^6 m^{-3}, and the maximum is the sensitivity represented by the polynomial in Figure 2.3 (approximately 0 dB = 1 mm^6 m^{-3} at 100 km), then an appropriate estimate would be to take the mid-point of 0.5 mm^6 m^{-3} as the missing value. This approximately equates to −3 dB, which is 3 dB less than the minimum sensitivity given by the polynomial. Therefore, for each undefined reflectivity at each range, 3 dB subtracted from the range-dependent noise value (given by the polynomial in Figure 2.3) is inserted. A unique polynomial is fitted to each radar based on its range-distribution of minimum sensitivity. Whilst this procedure may seem slightly crude, it is preferable to directly inserting the minimum sensitivity for all undefined reflectivities, and allows for the desired interpolation in logarithmic units.

Once noise has been inserted at each range, the raw reflectivity data can be interpolated onto the 3-D Cartesian grid. At each elevation, for each Cartesian pixel, all grid points within 3 km are located, and an average of all these values are taken, weighted by the inverse square of its Euclidean distance from the Cartesian pixel. This distance of 3 km was chosen as a trade-off between a smooth Cartesian grid of reflectivity and the retention of original features, and was tested on the Chennai S-band radar with a 500 m gate-size, in order to be applicable to radars with slightly higher and lower range resolutions (see Table 2.1). Whilst Wradlib was used to construct the Cartesian 3-D grid, its CAPPI algorithm introduced significant artificial annular ring features at regular intervals around the radar above and including the brightband region. These occur as a result of increasingly large spatial gaps between sweeps (Figure 2.1) and the effects of melting precipitation (e.g., Zhang et al., 2005). Instead, the vertical profile (0.5 km grid) is calculated by linearly interpolating vertically across all elevation scans for each Cartesian pixel, removing most of the annular ring artefacts. Some spurious radar artefacts remain present in the 3-D reflectivity field after CAPPI construction, especially at

higher altitudes. These artefacts are not expected to greatly influence the results, given the subsequent processing of the data.

2.2.2 Identifying convection with reflectivity

With a high-resolution 3-D Cartesian reflectivity field now available, convective regions can be objectively identified. There are many ways to approach this exercise, but the key assumption is that convection has relatively high reflectivity compared to its surroundings.

This thesis utilises the frequently adopted Steiner algorithm of Steiner et al. (1995). The algorithm simply considers the horizontal 2-D reflectivity field below the freezing level, usually the base CAPPI (at 2 km height here), to find convection. These convective regions are then extrapolated upwards throughout the vertical domain, which is a fair assumption in tropical regions with low vertical wind shear (2–12 km vertical shear during the ISM is $< 10^{-3}$ s^{-1} over India; not shown). Furthermore, as noted by Kumar et al. (2013a), where tilting of convective columns does occur, it is mitigated through the use of storm-average properties such as cell-top height (CTH; defined below). Therefore, more complex algorithms using the 3-D structure of the hydrometeor field (e.g., Rosenfeld et al., 1995; Biggerstaff and Listemaa, 2000) or neural networks (Anagnostou, 2004), are considered nonessential and not implemented here. The Steiner algorithm is summarised below in 4 steps, with further details in Steiner et al. (1995).

1. Any reflectivity pixel $\geq$ 40 dBZ is automatically considered convective.

2. Any pixel greater than a background state by the reflectivity difference depicted in Figure 7 of Steiner et al. (1995) is convective.

3. Each convective pixel has a convective radius of a certain size as a function of intensity.

4. A cell then is any connected set of convective pixels (using 4-connectivity), and hence is termed a cell here, as a typical cumulonimbus cloud would have convective and stratiform segments.

The Steiner algorithm has a few advantages for the purposes of this work. Firstly, it was originally formulated using high-resolution radar data for the Austral monsoon, and so it is likely to be well-suited too for the ISM. Secondly, it is a superior choice for capturing different stages of convective development, especially smaller cells, compared to analysis tools based on simple reflectivity, volume, and lifetime thresholds. Nonetheless, as discussed by Biggerstaff and Listemaa (2000), it displays a couple of limitations. The algorithm frequently misclassifies forward portions of convective lines as stratiform, as well as being too conservative in the size of the precipitating background radius of convective cells. Secondly, intense portions of stratiform rain regions associated with mesoscale disturbances can be misclassified as convective rainfall. However, the Steiner algorithm has been shown to work well by Steiner et al. (1995), and Biggerstaff and Listemaa (2000) noted that it exhibits sufficient accuracy across multiple convective regimes. This knowledge, alongside its widespread use within similar studies using CPOL (e.g., May and Ballinger, 2007; Kumar et al., 2013a,b), provides reassurance that it is a sage choice of procedure for the statistical analysis presented here.

Applying the Steiner algorithm to the base CAPPI targets precipitating convection in particular. Indeed, the visual cloud base may be higher than 2 km. Dry and elevated convection may not be detected, however, due to very moist lower-troposphere conditions during the ISM, the environmental characteristics favouring these types of convection are uncommon. Therefore, the identified convection is considered to be representative of the existing local convective state. The only additions implemented on top of the original method are that, firstly, any cell intersecting the inner or outer edges of the 40–100 km domain is not considered, in order to always sample entire cells. Secondly, only cells with a surface area (at 2 km height) of at least 4 pixels (i.e., 4 km^2 for 1 km grid spacing) are retained for analysis. Cells smaller than this do not often represent true convection.

2.2.3 Deriving storm characteristics

Following the application of the Steiner algorithm, the total storm size is calculated simply as the area of a cell (any set of contiguous pixels) at 2 km. With increasing height, the size of the storm above the ETH threshold reduces as the height converges to that of the maximum cell height (see below). Storm intensity (i.e., precipitation rate) is then related to the reflectivity values within each cell at each CAPPI level. Finally, the endeavour of calculating storm characteristics such as ETH and CTH can be undertaken.

To calculate radar-derived ETH, that is to say, the highest observed altitude of reflectivity for each column, a threshold for what constitutes a meteorological value must be applied (Z_{min}). The choice of threshold must be greater than the noise level at 100 km (the outer-edge of the domain) after calibration. Searching upwards from 2 km, the pixel nearest in value to Z_{min} in the vertical column is taken as the ETH, with the condition that there must be retrievals greater than Z_{min} at each 0.5 km level in the vertical column below the ETH, similarly to Kumar et al. (2013a). Appendix A specifically discusses the biases involved with calculating ETH, owing to the spatial gaps between radar sweeps, and more information is also given in Section 5.2.2.

Next, CTH is defined as the maximum ETH in a convective cell (Kumar et al., 2013a). As ETH values are likely biased low owing to the need for Z_{min} to be sufficiently above the radar sensitivity, extracting the maximum ETH in each cell brings CTH closer to the true cloud top. Figure 2.4 summarises the processing steps taken to obtain statistical information on storms from the original radar input in polar coordinates.

An example of a radar reflectivity mosaic at a height of 2 km is shown in Figure 2.5a, with domain boundaries of 40 km and 100 km from the location of the radar shown by the dashed radial lines. Several storms identified from the Steiner algorithm can be seen within contoured regions. Some high reflectivities near the domain edges do not have any associated convective region due to the requirement for the entire storm to be contained within the domain for sampling purposes. A vertical cross-section of this reflectivity (see white dashed line in Figure 2.5a) is then shown in Figure 2.5b, with the two black lines denoting the boundaries

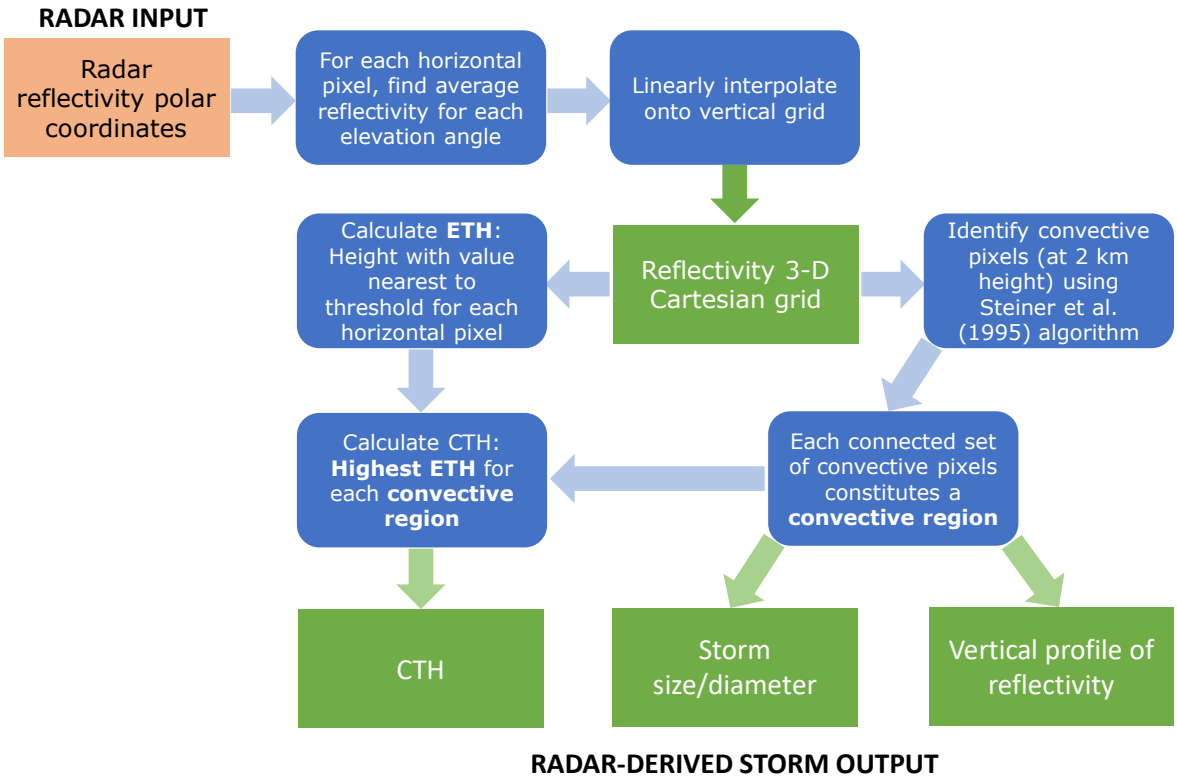

Figure 2.4: Flowchart summarising the procedure for obtaining statistics of radar-derived convection from radar reflectivity in polar coordinates (i.e., a PPI scan).

of the convective region this transect passes through. The red dashed line is that of the CTH, i.e., the maximum 5 dBZ ETH in this cell, which is at 12 km in this case. It is important to recall that this storm is just the convective part of a wider precipitating thunderstorm region, with each convective pixel at 2 km extrapolated upwards through the vertical column.

Finally, no attenuation corrections are deemed necessary to apply here. Quantifying the effect of attenuation (Serafin, 1990) in heavy precipitation (e.g., 25 mm hr^{-1}) for a temperature of 18°C, attenuation is 0.124 dB km^{-1} for a C-band wavelength of 5 cm and 0.007 dB km^{-1} for an S-band wavelength of 10 cm. Therefore, S-band radars are largely unaffected by along-path attenuation through rain (Seliga et al., 1981; Testud et al., 2000). Whilst intense convective storms with hail may have an impact, such storms are assumed to constitute a small proportion of the large, final sample. Also, though two C-band radars are used, the outer domain boundary is a non-extensive 100 km, reducing the opportunity for significant along-path attenuation to occur. Finally, as ETH is aggregated into single CTH values for each convective cell, any attenuation that does occur will not greatly impact the statistical

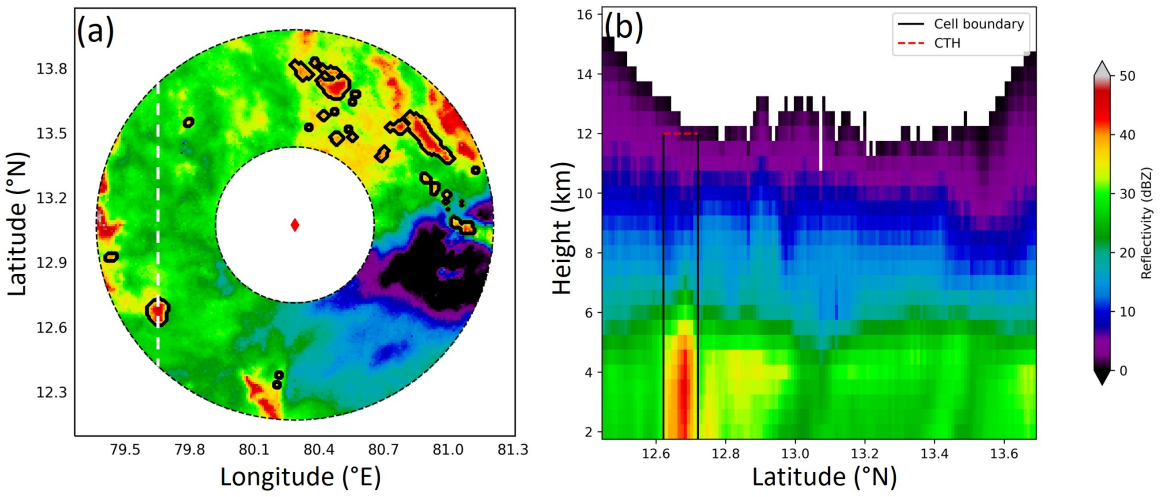

Figure 2.5: (a) An example radar reflectivity mosaic at 2 km (from the Chennai radar) with contoured regions showing the boundaries of convective cells identified with the Steiner algorithm. (b) A vertical cross-section of reflectivity at a longitude of 79.63°E (the white dashed line in panel a), with black markers denoting the boundaries of the convective cell, and the horizontal red dashed line representing the CTH of this storm, using an ETH threshold of 5 dBZ.

analysis of storm properties.

2.3 Large-scale data overview

One of the chief aims of this thesis is to show the relationship between local convection, associated precipitation, and the large-scale environment. Therefore, this section introduces the recurring datasets used for this purpose, assessing the respective advantages and limitations of each. The convection-permitting model data used is introduced in Chapter 6.

2.3.1 GPM IMERG

The Integrated Multi-Satellite Retrievals for GPM product (GPM IMERG; Huffman et al., 2020) provides half-hourly robust precipitation estimates at $0.1° \times 0.1°$ horizontal resolution. Version V06B of the IMERG product is used here. It is a level 3 product based on measurements from a constellation of satellites, combining data from passive microwave and infrared sensors (Da Silva et al., 2021). The IMERG rainfall estimates are finally nudged towards rainfall gauges using the Global Precipitation Climatology Centre monthly rainfall

estimates (Schneider et al., 2008). In this thesis, GPM IMERG data corresponding to the period of radar data available (15 May–30 September 2016) are used over the wider South Asian monsoon region at 30-minute sampling frequency.

For large-scale spatial analysis of precipitation, GPM IMERG is a useful product due to its complete coverage of tropical regions that may have sparse rain gauge observations. It has been shown to improve the representation of monsoon rainfall and its variability compared to its predecessor TRMM, and also the Global Satellite Mapping of Precipitation product (Prakash et al., 2018). However, it is not exempt from errors. For example, it has been found to exhibit spatial sampling errors in regions with less rain gauge data and areas with high intragrid spatial variability in extreme precipitation (Da Silva et al., 2021), and over the complex orography of north-eastern India (Prakash et al., 2018). Nonetheless, its high-resolution twice-hourly measurements are a clear advantage for analysis of convective variability and the diurnal cycle, where existing rain-gauge datasets over India such as APHRODITE operate at daily resolution (Yatagai et al., 2012). Finally, it has been found to depict the diurnal cycle of tropical rainfall broadly well (Tan et al., 2019), and so the author commends it for use as a statistical and evaluative tool in studying tropical precipitation and its drivers.

2.3.2 ERA5

Reanalyses assimilate observations in four-dimensional space from a broad range of sources to provide a global picture of past and present weather and climate. Gaps in the data are filled by numerical weather prediction models. Version 5 of the re-analysis from the European Centre for Medium-Range Weather Forecasting (ERA5; Hersbach et al., 2020) is one such product, freely available for download and use, and has a horizontal resolution of 0.25°, with data every hour. Four-dimensional ERA5 data span 137 model levels in the vertical, approximately 70 of these below 16 km in a standard atmosphere.

The use of ERA5 here is motivated through its transparency, high skill, and ease-of-access. Furthermore, its hourly sampling frequency means its variables can be related to

the diurnal cycle of convection, similarly to GPM IMERG. ERA5 also provides an extensive selection of variables that are invaluable for use over data sparse regions in particular. For this thesis, dynamical and thermodynamical multi-level fields of relative humidity, horizontal and vertical winds, and temperature are considered due to their known importance for monsoon variability and convection. Moreover, these variables compare well to IMD observations, with ERA5 exhibiting small errors compared to other reanalyses in horizontal winds (Olauson, 2018). Furthermore, ERA5 has small biases in temperature compared to other reanalysis products and its predecessor ERA-Interim, although it has been found to display a small cold bias during the monsoon (e.g., Mahto and Mishra, 2019).

Recently, a high-resolution (12 km) regional re-analysis of the South Asian region (Indian Monsoon Data Assimilation and Analysis; IMDAA) has been made available and is found to compare well to ERA5 (Rani et al., 2021), with hourly and 3-hourly products available. Future work in the Indian region might consider the use of this product.

2.3.3 Radiosonde soundings

Twice daily (00 and 12 UTC) atmospheric soundings are available in the near vicinity (<25 km) of all 16 sites in Table 2.1. As India Standard Time (IST) is 5 and a half hours ahead of Coordinated Universal Time (UTC), these soundings are released once in the early morning at 0530 IST and once in the late afternoon at 1730 IST. Details and coordinates of each sounding site used are shown in Table 2.2, with distance from the equivalent radar site given. All sites are within 25 km of the radar site except Jaipur (VIJP), where the radiosonde site is positioned further away to the south-east. These data were freely downloaded from the University of Wyoming Atmospheric Soundings web-page (http://weather.uwyo.edu/upperair/sounding.html). Soundings are especially useful for analyses of vertical profiles of temperature, moisture, and horizontal wind, as they sample at very high resolution throughout the troposphere.

Table 2.2: Information and coordinates for each radiosonde station, where the right-most column shows the distance (km) to the corresponding radar site.

Station ID	Station Number	Lat. (°N)	Lon. (°N)	Alt. (m)	Dist. to Radar (km)
VIDD	42182	28.58	77.20	216	2 (DEMS)
VABB	43003	19.11	72.85	14	24
VABP	42667	23.28	77.35	523	8
VANP	42867	21.10	79.05	310	1
VEAT	42724	23.88	91.25	16	1
VECC	42809	22.65	88.45	6	14
VEMN	42314	27.48	95.01	111	1
VEPT	42492	25.60	85.10	60	2
VEVZ	43150	17.70	83.30	66	8
VICH	42101	30.33	76.46	251	3
VIJO	42339	26.30	73.01	224	285 (VIJP)
VILK	42369	26.75	80.88	128	2
VOHY	43128	17.45	78.46	545	1
VOKL	43346	10.91	79.83	7	1
VOMM	43279	13.00	80.18	16	14
VOMP	43185	16.20	81.15	3	2

Chapter 3

Calibration of Indian Doppler weather radars

3.1 Introduction

As was discussed in Chapter 1, ground-based weather radars have been instrumental in numerous advances in meteorology, from nowcasting severe thunderstorms to providing long-term rainfall measurements at high spatiotemporal resolution. Post-processed radar measurements, such as rainfall rate retrievals or vertically integrated liquid, have supported operational forecasters as well as Numerical Weather Prediction (NWP) verification studies for years. Research-grade radars (typically operating at very high resolution for research purposes) such as CAMRa and CPOL have been used to obtain vertical information on cloud hydrometeor distribution (e.g., Thurai et al., 2010) and the statistical morphology of convection (e.g., Kumar et al., 2013a; Stein et al., 2014; Jackson et al., 2018) for many years now. More recently, cloud hydrometeor distributions obtained from operational ground weather radars have also been successfully applied to inform and constrain NWP models on the 3-D structure of precipitating clouds, e.g., South Africa (Stein et al., 2019), and the UK (Stein et al., 2020). Provided that the data are accessible for research, the wide distribution of today's radar networks allow NWP model evaluation studies to consider regions that vastly differ in precipitation climatologies, rather than tune a model to the weather that dominates

a specific region. However, regional heterogeneity in radar operational strategies such as scan schedule and radar diagnostic parameters, as well as diversity in radar wavelengths and antenna sizes and lack of support for quality control can hinder such studies.

The usefulness of radars as tools for these applications can only be fully realised if radar reflectivity is accurately calibrated. Radar reflectivity is proportional to the returned power received by the radar from a target, with the radar constant determining the proportionality factor. However, the radar constant is notoriously difficult to determine, as it is a combination of properties such as wavelength, beamwidth, pulse width, transmitted power, and receiver gain (e.g., Atlas and Mossop, 1960; Probert-Jones, 1962), which can vary over time owing to radar degradation or maintenance of the hardware (Louf et al., 2019b). Calibration is a particularly necessary consideration for archived operational radar data such as the IMD radars, where calibration changes may not be as carefully monitored as with research-grade radars, and because of the importance of accurate cross-comparisons between different radars within the network. Whilst many calibration techniques have been developed over the years (ref. Atlas, 2002), it is clearly desirable for an easily repeatable and widely applicable procedure to be employed for continuous monitoring of radar calibrations, as more radar data is continually being created and archived. In this vein, Vaccarono et al. (2016) and Louf et al. (2019b) noted that by combining different calibration techniques through an integrated approach, then additional information on calibration changes can be obtained and evaluated on a seasonal basis.

Rinehart (1978), followed by Louf et al. (2019b), demonstrated that the calibration of an individual radar can be monitored over time using ground clutter, allowing calibration to a single relative value over a season. This is because the most persistent and robust ground clutter signal should remain constant over time. Following Schwaller and Morris (2011) and Warren et al. (2018), Louf et al. (2019b) showed that subsequent calibration against the GPM dual-precipitation radar allows for absolute calibration of the ground-based radar of interest, provided sufficient GPM overpasses are available for the calibration to converge. Louf et al. (2019b) performed their calibration study on a long-term data set for the research-grade CPOL radar at Darwin, Australia, and their algorithms are publicly available on Github

(https://github.com/vlouf/matchproj-python). In this chapter, the application of these techniques to a single season of operational weather radar data from the network of Indian Doppler radars is described. The accuracy, robustness and suitability of the calibration for the Indian network is discussed, as well as its potential wider usability. In addition, a simple verification procedure using synop rainfall measurements is undertaken, and any caveats in the application of this method to operational radars are outlined. This chapter also aims to demonstrate that this level of quality control is accessible, (even when an organisation or project may only have limited personnel to support such work).

In the remainder of this technical chapter, the respective methods for relative and absolute calibration of ground-based weather radar data are outlined in Section 3.2. The application of the procedures upon the IMD weather radar data in 2016 is then presented in Section 3.3; the first time this has been applied to operational radar data. A verification against IMD synop data is also provided. Discussion pertaining to this work and its associated conclusions are given in Section 3.4.

3.2 Data and methods

Here, an overview of the two-stage calibration method as comprehensively described in Louf et al. (2019b) is provided, with sufficient detail for reasons of scientific repeatability.

3.2.1 Relative Calibration Adjustment

The first stage of the calibration method involves adjusting radar measurements within a season if they differ greatly from a baseline for that season, and is termed Relative Calibration Adjustment (RCA; Silberstein et al., 2008; Wolff et al., 2015). This is done using ground clutter. The suitability of ground clutter for monitoring the relative calibration of a radar stems from the fact that ground clutter (associated with buildings, trees and other surface features) are primarily stationary features with constant scattering properties, and so if the radar calibration remains constant, its ground clutter reflectivity readings will remain quasi-constant. However, meteorological signals in the near-vicinity of the radar site as well as

more temporary sources of clutter may disturb this relationship. Therefore, it is important to consider multiple radar scans to evaluate robust clutter pixels. Rainfall can also increase the variability in the measured returns close to the radar that are used for finding clutter (Louf et al., 2019b). Therefore, ground clutter needs to be determined from clear-sky (precipitation-free) data. Here, similarly to Wolff et al. (2015), one clear-sky day is chosen. In order to create a robust clutter map, it is decided this day must have at least 50 radar volumes available. The clear-sky day is selected as having zero rainfall in the vicinity of the radar domain, and infra-red satellite imagery from the Kalpana satellite is used to visually confirm a day with clear-sky conditions.

After choosing a suitable day, clutter is determined from the raw reflectivity within a close radius of the radar, which must be greater than 40 dBZ for at least 95% of radar volumes in that period, meaning only the most robust clutter artefacts are used for the calibration (Silberstein et al., 2008). This is important as it lends weight to the assumption that any variability in this clutter is a change in calibration. Louf et al. (2019b) also explored the cross-correlation ratio, available from dual-polarisation radars. Non-meteorological objects that constitute clutter are complex features that will typically result in a small correlation between the horizontal and vertically oriented radar pulses. Therefore, where dual-polarisation quantities are available, high values of the cross-correlation ratio (above 0.6; Louf et al., 2019b) can be removed as they may not be robust clutter.

The choice of the radius within which clutter is located is ideally as small as possible whilst observing a significant amount of clutter. Louf et al. (2019b) chose 10 km owing to a large amount of clutter in the vicinity of the CPOL radar in Darwin. For the Indian Doppler radar network, a smaller amount of clutter was observed for many radars, and so this radius was extended to 15 km so as to sample more clutter. The amount of derived clutter is naturally related to the range and azimuthal resolution of the radar. Research-grade radars such as CPOL will have more clutter owing to a higher number of samples to choose from within a small radius and that the small beamwidths and range-gates will robustly observe physically smaller artificial clutter.

The lowest elevation angle is used (0.2° or 0.5° for the Indian Doppler radars) to obtain

the most ground clutter, as a larger amount of clutter allows for a more robust interpretation of its variability. Silberstein et al. (2008) noted that even very small changes in the elevation angle affect the distribution of clutter, thus bringing unwanted noise into the subsequent radar calibration. Whilst any changes in elevation angle must thus be accounted for, noise from slight day-to-day variations can be isolated from any significant calibration changes of interest. A clutter mask is then obtained (Figure 3.1c), where every pixel defined as clutter is used to monitor the calibration through the season. Applying the clutter mask to one season is a fair assumption owing to a constant scanning pattern of the radar during this period, as well as persistent clutter artefacts. Nonetheless, it is worth repeating this procedure across multiple clear-sky days in order to be assured that the choice of day does not significantly change the clutter map. To test this here, a clutter map was produced from all the May radar data. This reduced the amount of clutter by around 5%, but the locations of clutter were otherwise largely unchanged, and the subsequent RCA was very similar in terms of the clutter distribution. Finally, over multiple seasons, it is important to repeat the process of clutter mask calculation, as surface features registered as clutter in one season may not be present the next, and scanning strategies such as elevation angle may change (Louf et al., 2019b). However, this does not apply here as we are using just one season of data. A list of clear-sky days and number of clutter points for each radar are given in Section 3.3.

Figure 3.1a–c summarises the process for finding clutter: the raw, unfiltered reflectivity (total power) within 15 km of the radar for the clear-sky day is obtained (the average over the day is shown in Figure 3.1a). The frequency with which a pixel exceeds 40 dBZ during the day is calculated (Figure 3.1b). Finally, those pixels that meet the 95% threshold make up the clutter mask (Figure 3.1c).

To be assured that any change in ground clutter is associated with a change in calibration, the 95th percentile of the ground clutter reflectivity distribution (CDF_{95}) is taken for each radar timestamp, following the recommendation of Silberstein et al. (2008). Furthermore, reflectivities associated with precipitation are typically substantially lower than CDF_{95} such that it has little impact on the RCA technique (quantitatively shown in Louf et al., 2019b). CDF_{95} is then compared to an established clutter reflectivity baseline (Z_{ref}). The value of

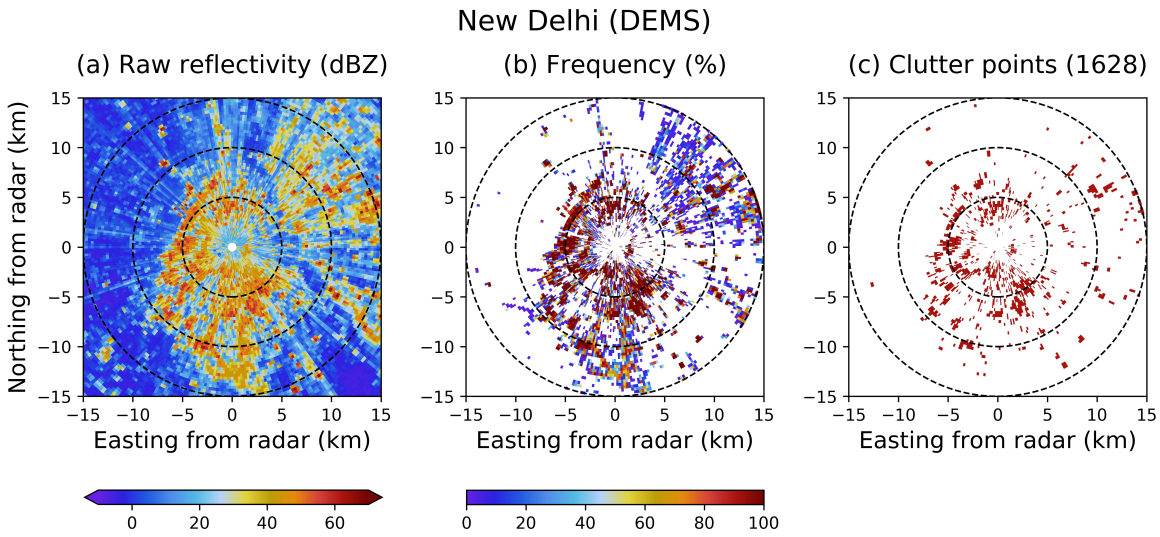

Figure 3.1: The process of obtaining a clutter mask using a clear-sky day (15 May 2016) for the New Delhi radar. (a) The mean raw reflectivity (total power) across every radar volume during the day, (b) the frequency at which a pixel within 15 km is greater than 40 dBZ, and (c) the mean total power of the clutter mask. Only pixels that meet the requirement of being greater than 40 dBZ for at least 95% of radar volumes are shown, and the total number is labelled.

Z_{ref} is obtained for a single season with no prior information. The RCA process aims to determine step-changes in the calibration of a radar. Therefore, it is not prudent to take the mean of the CDF_{95} distribution over the season, as if there is a single, large step-change in the radar calibration, the mean will not represent either the former or latter calibration states. Instead, the modal value of the CDF_{95} distribution (rounded to one decimal place) is used for Z_{ref}. It is worth noting that Z_{ref} merely acts as a relative calibration baseline, and as explained later, this entire baseline is corrected toward the GPM dual-precipitation radar.

Finally, variability in the CDF_{95} distribution is corrected toward the baseline. To simplify this process and smooth the RCA offset, daily means in CDF_{95} for each day over the season are calculated, such that a daily RCA offset is obtained: $RCA_{offset}(dB) = Z_{ref} - \overline{CDF_{95}}$, where RCA_{offset} is the offset used to correct to the baseline (Wolff et al., 2015). Whilst Louf et al. (2019b) obtained accuracy in the RCA to within 0.5 dB for CPOL, offset correction is only applied for $RCA_{offset} > 1.0$ dB here, chosen as substantial variability is seen in CDF_{95} of a magnitude less than this value for the Indian radars. Research using radars for applications such as rainfall estimation (e.g., Smith et al., 1996; Fulton et al., 1998; Ulbrich

and Lee, 1999; Vivekanandan et al., 2003), and model evaluation (e.g., Stein et al., 2020), have indicated calibration accuracy to within ± 0.5 dB acceptable. However, for the IMD operational network, accuracy to within 1.0 dB is as high as can be achieved in the subsequent absolute calibration with GPM (Louf et al., 2019b). As an example, at a reflectivity of 30 dBZ (2.73 mm hr^{-1} using the Marshall-Palmer reflectivity-rainfall relationship; Marshall and Palmer, 1948), a 1 dB difference equates to a 0.4 mm hr^{-1} change in resulting rainfall rate. For analysis of convection, the peakedness criteria of the Steiner algorithm (Section 2.2) is not found to be very sensitive to a 1 dB change for locating convective regions (not shown). Testing a few volume scans with the calibration offset applied nominally, and then again offset by ± 1 dB, a mean absolute error in ETH of approximately 0.5 km is found, and the number and size of storms also varies by a small amount. These errors are somewhat negligible compared to the errors associated with radar resolution on ETH (ref. Appendix A). Further detail on the RCA process applied specifically to the Indian Doppler radars is presented in Section 3.3.

3.2.2 Absolute calibration with GPM

The second stage in calibrating the radars is the correction of Z_{ref} toward the GPM dual-precipitation radar (DPR), chosen as a reliable, external source of reflectivity data. In theory, any spaceborne radar with robust reflectivity measurements for the ground radar region can be used. GPM DPR is chosen due to frequent overpasses and furthermore, substantial amounts of cross-validation of these measurements with radars display high correlations (Biswas and Chandrasekar, 2018). The Cartesian coordinates for each radar pixel are calculated, and where the swath of GPM falls within the spatial domain of any ground radar sweep, a volume matching scheme is applied to compare the reflectivities, following the procedure of Schwaller and Morris (2011), adapted by Warren et al. (2018). All available elevation angles are used for this comparison (10 for the Indian Doppler radars). Figure 2 of Schwaller and Morris (2011) visualises this intersection between satellite and ground radars, where all spaceborne radar gates contained within the swath of the ground radar are averaged. Of

course, this relies on satellite overpasses over the position of the ground radar occurring at the same time as sufficient rainfall in order to compare the respective reflectivities, as well as ground radar data being available at this time, which with many operational radar networks is not a given.

GPM operates in low-Earth orbit, and its dual frequency radar operates at Ku- and Ka-bands (13.6 GHz and 35.5 GHz respectively). The ground radar C- and S-band frequencies are converted to the native Ku-band reflectivity of the spaceborne radar using a fourth-order polynomial derived by Cao et al. (2013), with different empirical coefficients depending on the type of precipitation. This polynomial was adapted by Louf et al. (2019b) for C-band radars, applicable only for liquid precipitation in the tropics, and is accurate to within 0.5 dB for reflectivities less than 30 dBZ, and 1.0 dB for reflectivities greater than 30 dBZ (Louf et al., 2019b). The minimum sensitivity of GPM is approximately 14 dBZ (Louf et al., 2019b). Following the identification of a volume match and the reflectivity conversion outlined above, the DPR reflectivities can then be directly cross-compared to the radar reflectivites within the relevant swath, and is described with relation to IMD network radars in Section 3.3.2.

Applying this method and its parameters (ref. Table 3.1) across an entire radar network can result in a highly variable number of volume matches – in the case of the Indian Doppler radars, between 0 and 19 volume matches were found during the 139 day season. Of course, if only one or a few radars are considered, parameters can be fine-tuned in order to obtain an appreciable number of volume matches, whilst ensuring the accuracy of the calibration itself through sensitivity studies. When applied across many radars, fine-tuning of parameters becomes increasingly time consuming, and defeats the purpose of applying automated calibration procedures frequently upon entire radar networks. However, even in a radar network with identical scanning strategies, a radar in a drier region would still be susceptible to fewer volume matches than a radar in a wet region, as there would be fewer potential volume matches owing to fewer reflectivities meeting the minimum sensitivity threshold. Therefore, some quality control is inevitable and is discussed in Section 3.3.

The entire calibration procedures of Warren et al. (2018) and Louf et al. (2019b) are summarised briefly below:

1. Find persistent ground clutter within a close radius (here 15 km) of the radar (Figure 3.1), defined as any pixel that has a reflectivity greater than 40 dBZ for at least 95% of a week of clear-sky data. Only the lowest elevation angle is used for this analysis.

2. These fixed echoes are analysed statistically over the season to monitor relative radar calibration. The assumption is any variation in ground clutter reflectivity is caused by a change in radar calibration. This is done by comparing the 95th percentile of the ground clutter reflectivity distribution with an established clutter reflectivity baseline.

3. All variability for the season is corrected toward the clutter reflectivity baseline. A threshold of 1.0 dB in the relative calibration adjustment (RCA) offset is applied to define a calibration change.

4. The baseline is compared to an external, robust reference of reflectivity in the form of the GPM dual-precipitation radar. A volume matching scheme (Warren et al., 2018) is applied, determining the RCA offset to agree with GPM.

3.3 Application of calibration procedure

The application of the procedure described in Section 3.2 upon the Indian Doppler radars (Section 2.1) is presented here, with emphasis given to the difficulties encountered in the various aspects of the RCA and GPM volume matching respectively.

3.3.1 RCA technique applied to India radar data

There are a couple of caveats to be aware of when applying the RCA technique to the Indian Doppler radars (which are likely to be applicable too for other radar networks).

A calibration correction is required when there is a change in the relationship between reflectivity and returned power from a target. Sometimes a calibration change can be clear in the clutter distribution. However, for many sites there remains substantial high-frequency variability in the clutter time-series which makes it more difficult to ascertain changes in calibration. The following steps act to reduce some of this variability, leaving only reliable

reflectivity readings and thus calibration changes. Files with missing or erroneous reflectivity readings substantially displaced from the rest of the distribution should be discarded in advance or identified during the RCA process, as these could result from heavy rain at the radar site resulting in attenuation. There are various ways one could achieve this. Here, outliers in the distribution of CDF_{95}, defined as any point more than 3 standard deviations from the mean, were removed.

Recalling that an RCA correction is applied for $CDF_{95} \geq 1.0$, there may be a period of several consecutive days where some days exhibit CDF_{95} slightly greater than the correction threshold (1.0 dB) and some days slightly less than 1.0 dB. In order to consider whether this period of time should be adjusted to a baseline, the mean CDF_{95} of the entire period is considered, as opposed to correcting each day individually. Only if the absolute value of this mean exceeds 1.0 dB is the period adjusted to the RCA baseline. A time period is any selection of days within which there is no day-to-day absolute change in the RCA offset exceeding 1.0 dB. Operationally, due to uncertainty in the RCA values, this procedure is more likely to identify the systematic changes in radar calibration, as recommended by Wolff et al. (2015).

An additional potential difficulty to be aware of is that quality control procedures such as clutter removal are often automatically applied to the radar data. In the case of the Indian Doppler radars, 5 radars did not have the total power data pre-clutter removal available (VECC, VEVZ, VOHY, VOMM, and VOMP). The majority of the Bhopal (VABP) radar scans are also missing the total power. Whilst some clutter artefacts may still remain after this process, making it possible to still proceed with the analysis, confidence in the robustness of the RCA is of course greatly reduced. As a result, a simple sensitivity test was performed to ascertain how many clutter points are required to monitor the stability of the radar calibration. To do this, a 'good' radar is chosen with plentiful clutter. New Delhi is selected (ref. Figure 3.1) with 1628 clutter points within a 15 km radius of the radar site. A random subsample of these clutter points is taken at lots of different values from as low as 2 clutter pixels, up to the total number of 1628 pixels.

Figure 3.2 shows the results of this sensitivity test. Firstly, below 70 clutter points,

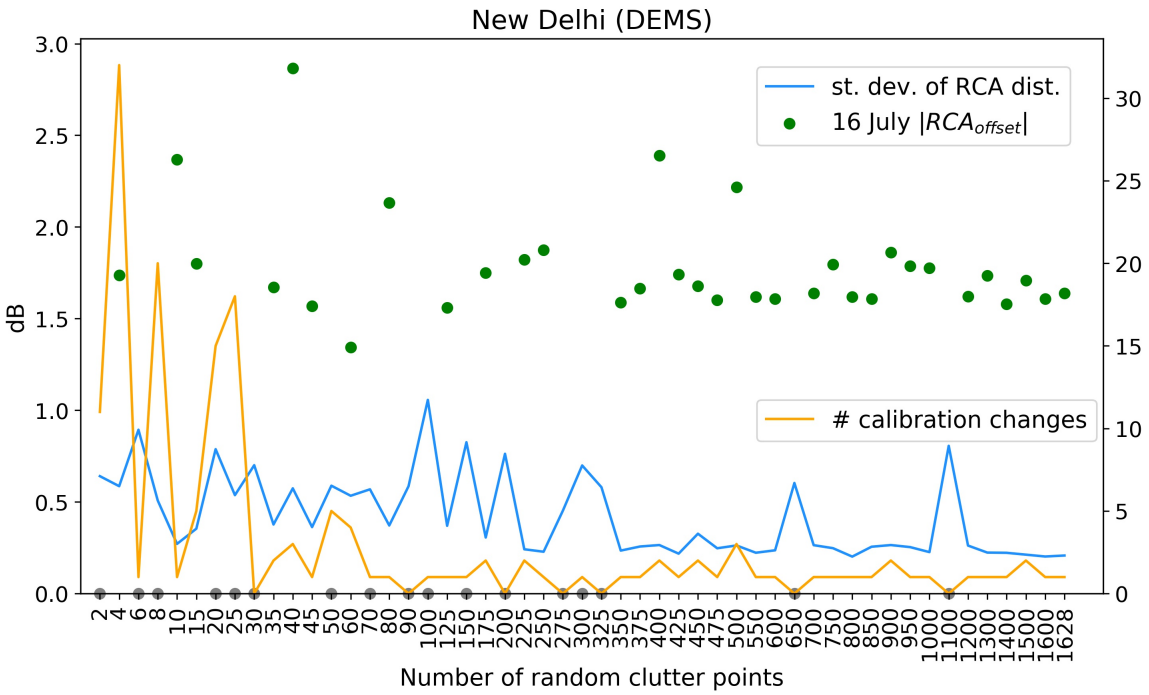

Figure 3.2: Sensitivity of the 2016 New Delhi relative calibration to the number of clutter points (randomly selected without replacement), up to the total number of 1628 pixels. The standard deviation of the seasonal RCA distribution (dB) corrected for any relative calibration changes is shown by the blue line, and the green circles represent the magnitude of the 16 July calibration change. Grey circles are plotted with a value of 0 dB where no 16 July calibration change is identified. The second y-axis (right-hand side) is the total number of calibration changes (day-to-day RCA change of $\geq$ 1 dB), shown by the yellow line.

systematic calibration changes – such as 16 July 2016 for New Delhi – are still frequently identified, with similar magnitudes of the calibration change compared to taking all 1628 points. Nonetheless, for small amounts of clutter, the major calibration changes are also most frequently unidentified. For greater amounts of clutter where no calibration change is noted (e.g., 650 and 1100 points), this appears to be a result of changes over consecutive days being less than 1 dB, but visually a clear calibration change has still occurred over several days. However, for small amounts of clutter, the variability in the clutter becomes large, meaning it becomes difficult to disentangle systematic calibration changes from unrelated variability in the clutter artefacts. As a result, the RCA when performed on small amounts of clutter is also more prone to identifying several calibration changes within a season that are not systematic when taking a larger amount of clutter. Clearly, some clutter artefacts are less robust than others. Therefore, the number of calibration changes and the standard deviation

of the RCA distribution after RCA corrections have been applied are rather stochastic below 50 clutter pixels, depending on the random pixels selected. Finally, considering all cases where the 16 July calibration change was identified, the standard deviation in the corrected RCA distribution is relatively lower (<0.4 dB) for more than approximately 100 clutter points. For the RCA process, lower variance in the clutter is desirable in order to identify the systematic calibration changes, and as long as the clutter is robust, even small amounts of clutter (e.g., 50 points) are sufficient. Therefore, Figure 3.2 suggests the strict thresholds of clutter being above 40 dBZ 95% of the time are justified, even if it means the amount of clutter is small.

Due to the aforementioned issues, or due to the placement of radars upon buildings so as to purposefully reduce clutter in the surrounding area, this may not always be possible with the constraints set here. Whilst it is important to choose only the most persistent clutter artefacts, a reduction in the clutter magnitude threshold from 40 dBZ to 30 dBZ is a possible solution here. This does however, begin to carry the risk that precipitation will impact even the 95th percentile of the clutter distribution. Alternatively, the frequency threshold can also be reduced (Figure 3.1b), e.g., to 50%, to increase the amount of clutter artefacts, as used by Wolff et al. (2015). This clutter will be less robust by definition and therefore introduce more noise into the RCA analysis. Here, if fewer than 100 clutter points are found on the initial pass, the magnitude threshold is reduced to 30 dBZ. Following this, the frequency threshold is reduced to 50%. If there are less than 50 clutter points after this relaxing of the constraints, RCA is not performed. Only Vishakhapatnam (VEVZ) obtains sufficient clutter in this manner, and RCA is not performed on the other 4 radars without total power data. Furthermore, Bhopal (VABP) had total power data missing for a large amount of files over the season, meaning RCA was also not possible for Bhopal. Dibrugarh (VEMN), despite having total power data available, did not exhibit enough clutter points even after the relaxing of the constraints. This resulted in RCA being successfully performed for 10 out of a total 16 radars. Fortunately, for the 6 radars where an RCA cannot be performed due to insufficient clutter, the next stage of absolute calibration can still be undertaken, but with less certainty in the stability.

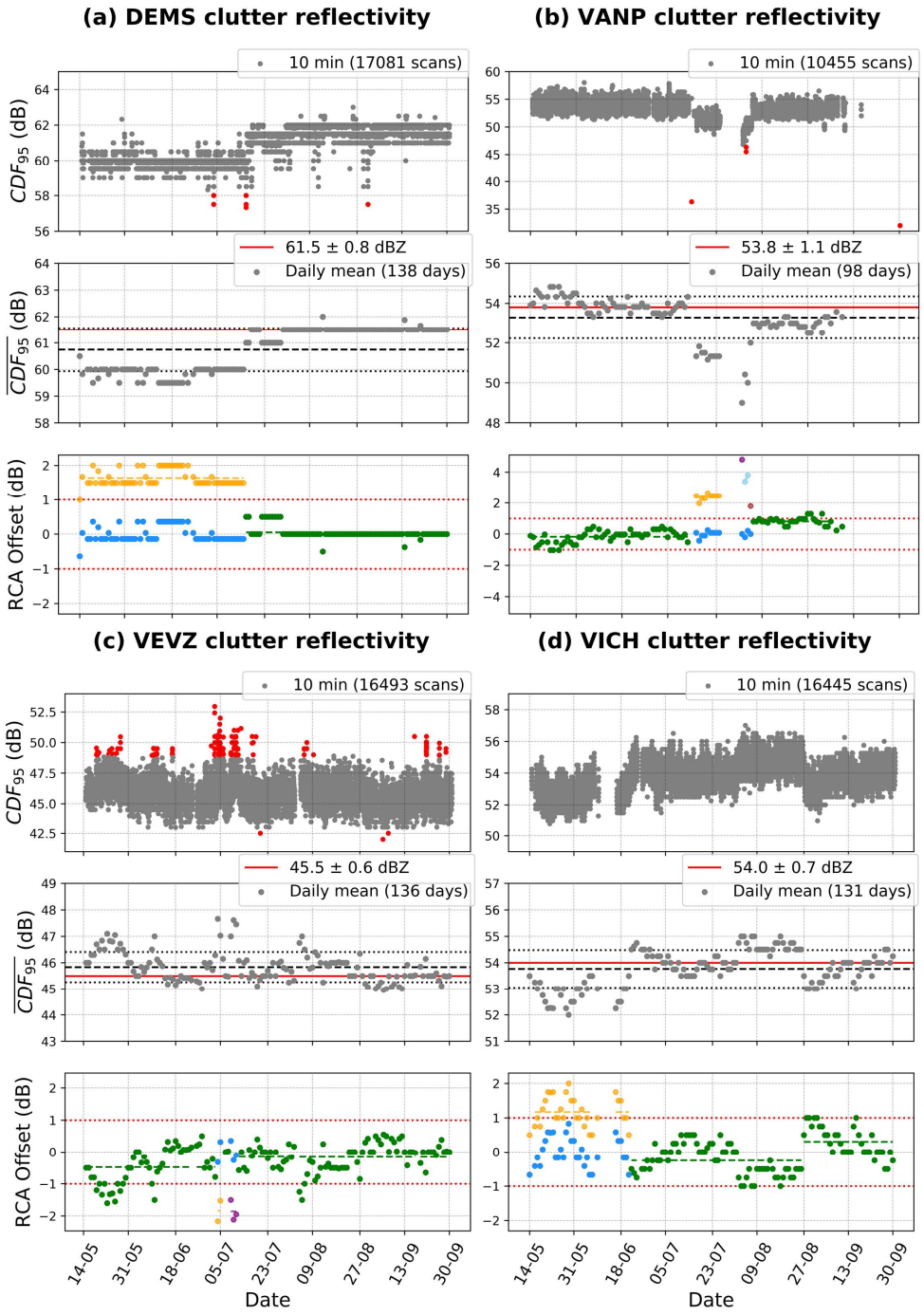

Figure 3.3: Clutter reflectivity and RCA offset values for (a) New Delhi, (b) Nagpur, (c) Vishakhapatnam, and (d) Patiala for the 2016 season. The top panel for each site is the 95th percentile of the clutter reflectivity for every radar volume, where values more than 3 standard deviations from the mean are coloured red. The middle panel is the clutter reflectivity averaged over each day, where the black dashed and dotted lines are the mean and mean ± 1 standard deviation respectively. The red solid line is the RCA baseline and its value is labelled. The bottom panel shows RCA offsets. Dashed lines show the mean RCA_{offset} of each time period, with time periods below the calibration threshold (1 dB) shown in green, and those above given a different colour. Time periods corrected to the baseline are shown in blue after correction for clarity. The red dotted lines show the ±1 dB correction threshold.

Out of these 10 radars, 4 sites are discovered that need an RCA offset applied to part of the season before absolute calibration (Figure 3.3). New Delhi (DEMS) exhibits the clearest calibration change within the 2016 season. The $\overline{CDF_{95}}$ increases suddenly by more than 1 dB from 16 to 17 July. The baseline is taken as the modal value of $\overline{CDF_{95}}$ over the season (61.5 dB; middle row of panel a). This means the RCA offset of all days up until 16 July is in excess of the correction threshold. As this is the only clear (± 1.0 dB) change in calibration, the mean of all daily RCA offsets up to and including 16 July is taken as the RCA offset to correct the entire period.

For Nagpur (VANP), Vishakhapatnam (VEVZ), and Patiala (VICH) there is more variability. Note that for Vishakhapatnam, this may be partly due to the relaxed constraints on defining clutter, and thus affirms the need for the strict clutter threshold values. Nagpur has several separate periods that require calibrating. The first is 11–19 July, with an average offset of 2.4 dB. Following a small period of missing data, this offset then increases to above 4 dB, which is a jump of over 1 dB. This means a new calibration period is defined for 27 July, and again for 28–29 July and 30 July respectively. Vishakhapatnam and Patiala also have several periods of time exceeding the correction threshold. However, not all of these points are corrected as the entire period of days before a 1.0 dB offset change (e.g., from 14 May to 28 June for VEVZ) does not exceed the calibration threshold. The opposite situation occurs for Patiala (VICH). The period of time 14 May to 21 June is corrected to the baseline despite many of these days experiencing offsets of a magnitude less than 1.0 dB. It should be noted that days with no RCA offset due to missing radar data are disregarded and the next available day should be compared to the last available day before the data gap. Finally, it is possible for day-to-day changes in RCA offsets to be consistently less than 1 dB but for the calibration offset to gradually increase in magnitude. To avoid large offsets not being corrected owing to this effect, any RCA offsets ≥ 1.5 dB (that are not already identified for correction following the procedure above) are automatically corrected to the baseline by the mean of its own offset and all consecutive points ≥ 0.5 dB from the baseline. The final RCA offsets and their dates are provided in Table 3.2.

Table 3.1: A list of calibration parameters applied to each radar for RCA and GPM volume matching respectively. Those radars without total power data are given a clutter threshold of 30 dBZ and a minimum fraction for clutter of 50%. However, only Vishakhapatnam (VEVZ) gains a sufficient number of clutter points in this manner.

Parameter	**Value**
Clutter threshold	40 dBZ
Min. Fraction for Clutter	95%
Max. Range for Clutter	15 km
Min. Clutter points	50
Min. Samples in Vol. match	10
Time gap	10* minutes
Min. radar reflec.	15 dBZ
Min. DPR reflec.	15 dBZ
Max. height	4 km
Max. radar reflec.	40 dBZ
Min. / Max. radar range	15 / 150 km
Correction threshold	1 dB

*For Mumbai and Jaipur, no volume match is obtained until the time gap is increased to 19 minutes, due to missing radar data.

3.3.2 GPM volume matching

The application of the GPM volume matching technique to the Indian Doppler radars was largely successful, as 14 out of 16 radars had volume matches available for DPR-ground radar comparison. However, Mumbai and Jaipur had no volume matches over the season using the parameters in Table 3.1, largely due to a relatively small number of radar scans over the season and the strict constraints applied on what constitutes a volume match. Similar to the RCA process, the final derived calibration offset can be very sensitive to the choice of parameters in Figure 3.1. Firstly, the maximum delay between a spaceborne and ground radar measurement is taken to be 600 seconds. This is chosen as it is the sampling frequency of the Indian Doppler radar scan cycles. As it takes approximately 7 minutes for each scan cycle to complete, the time halfway through each complete scan cycle is taken as the ground radar timestamp, as opposed to taking the start time. At least 10 satellite profiles inside the ground radar domain are required for comparison. Furthermore, in the tropics, the ice phase can be

ignored, owing to plentiful measurements in the liquid phase (below approximately 5 km). Additionally, samples of very high reflectivity (C-band > 40 dBZ, S-band > 50 dBZ) are excluded from the analysis due to undercorrection of attenuation at low levels as described in Warren et al. (2018). The minimum sensitivity of the ground radar out to the maximum range of 150 km must also be considered. For the Indian Doppler radars this is approximately 10 dBZ but varies per radar. Therefore, the same sensitivity as that of GPM (approx. 15 dBZ), is used.

When applying the volume matching technique, only radar reflectivities above 15 dBZ are thus considered. Warren et al. (2018) noted that the reflectivity differences obtained are very sensitive to this minimum threshold. This is because after correcting the radar reflectivities toward the DPR, many reflectivity samples that were not included within the original volume match become part of the radar reflectivity distribution. This effect is mitigated through an iterative procedure to reduce the variation between the radar and DPR reflectivity distributions (Protat et al., 2011; Warren et al., 2018; Louf et al., 2019b). After correcting the radar reflectivities following the first volume match, if the absolute reflectivity difference remains greater than the correction threshold of 1.0 dB, then the volume matching scheme is started again, and a new reflectivity difference is found. The two differences are then totalled to give the final calibration correction applied to the radar. This procedure is repeated until the reflectivity difference converges to within 1.0 dB. For the IMD radars, Dibrugarh (VEMN) required two iterations for two volume matches, and Patiala (VICH) required three iterations, also in the case of two volume matches. All other radars required a maximum of one iteration for the correction to converge.

The results for each radar are shown in Figure 3.4. There exists a wide range of calibration offsets (as high as 18.4 dB in Table 3.2), highlighting the necessity of performing this procedure. Broadly speaking, the calibration procedure does not improve the correlation between GPM and each radar. This is because the calibration technique is essentially a bias correction, and this is applied to each individual comparison point independently. However, it successfully reduces the root-mean square error and bias, centring the distribution near the 1:1 line. This is also achieved consistently across multiple volume matches for a site. Volume

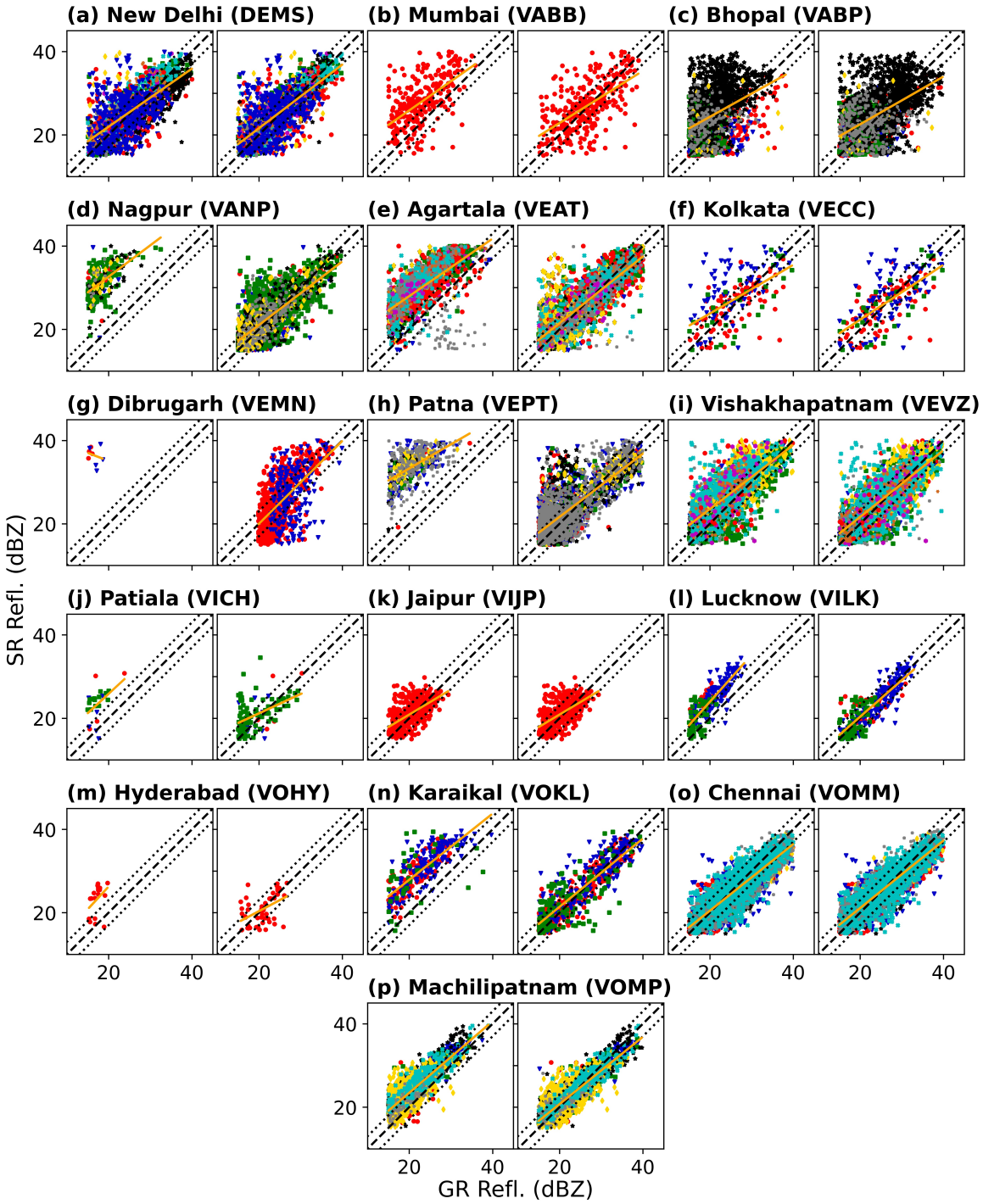

Figure 3.4: Scatter plots of ground radar reflectivity against GPM DPR reflectivity for each site (a–p), before calibration (left), and after calibration (right). Each colour marker represents a different volume match. The offset is applied to each volume match individually here. The yellow line is the line of best fit for the data in each case. The black dashed and dotted black lines represent the 1:1 line and a bias of ±1 dB respectively. Mumbai and Jaipur have just one volume match obtained by increasing the maximum time difference to 19 minutes in both cases.

match dates with many more samples tend to perform very well owing to a higher number of individual comparisons. Therefore, it is ideal to increase the minimum number of samples as high as possible whilst still obtaining a sufficient number of volume matches. Here, a minimum of 10 comparison samples was set due to the lack of volume matches, which is generously low.

The final GPM offset values in Table 3.2 are calculated by averaging the *total* offset from all volume matches for that site. Louf et al. (2019b) suggested that the average of each GPM offset may be weighted by the number of comparison samples in each volume match, but only small differences were noted compared to applying equal weights to each volume match, as we have done here. Furthermore, volume match offsets should be relatively consistent with one another, owing to the RCA process being conducted prior to the GPM volume matching. However, in some cases outliers in the distribution of volume match offsets may remain (e.g., because RCA was not performed or perhaps heavier rain rates that yield decreased accuracy).

3.3.3 Verification

Here, a simple verification against IMD synoptic surface (synop) data is undertaken, as an alternative source of rainfall information in the vicinity of many of the radar sites. These data provide point measurements of 3-hourly cumulative rainfall over India, with a 24-hour total taken at 03 UTC each day. Data are available for the first half of the INCOMPASS period from 15 May–15 July 2016. Radar-derived rainfall before and after calibration correction is compared directly to the synop data using the procedure below:

1. Synop readings within 100 km of the radar site are extracted. Only those synop readings with rainfall accumulations of at least 0.1 mm per 3 hour period are considered for comparison.

2. Radar reflectivities (prior to and following calibration adjustment) are transformed onto a 2-D Cartesian grid at a height of 2 km above ground level, with horizontal domain boundaries of 40–100 km from the radar location, and a horizontal resolution of 1 km,

Table 3.2: Results of the calibration for each radar site. First, the clear-sky day used for the RCA process and the number of identified clutter points are shown. The RCA offset is then given alongside the dates it corresponds to. Some sites have multiple RCA offsets. Next, the number of volume matches and the average calibration offset from those volume matches are given. In the right-most column, the minimum sensitivity of each radar at 100 km after any calibration corrections is shown.

Site	Clear-sky day	Clutter points	RCA offset(s) (dB)	Volume matches	GPM offset (dB)	Noise at 100 km (dB)
DEMS	15 May	2628	1.6 (14 May–15 Jul)	12	0.0	−5
VABB	15 May	1159	None	1†	5.1	2
VABP	23 Jul	1411	None	7	3.5	0
VANP	15 May	128	2.4 (11–19 Jul) 4.8 (27 Jul) 3.6 (28–29 Jul) 1.8 (30 Jul)	6	13.2	6
VEAT	16 May	196	None	19	6.5	−1
VECC	28 May	10*	n/a	3	1.2	2
VEMN	6 Jul	11*	n/a	2	18.4	13
VEPT	15 May	100	None	9	12.9	8
VEVZ	16 May	125	−1.9 (4–5 Jul) −1.9 (9–11 Jul)	10	2.4	0
VICH	28 Sep	231	1.2 (14 May–21 Jun)	3	13.3	4
VIJP	16 Sep	1372	None	1†	0.0	−5
VILK	26 Sep	589	None	3	4.2	3
VOHY	16 Jul	0*	n/a	1	5.6	−3
VOKL	30 Sep	2114	None	3	7.0	3
VOMM	15 May	9*	n/a	7	0.0	2
VOMP	15 May	0*	n/a	8	3.3	2

* Insufficient number of clutter points to perform RCA.
† Maximum time gap increased to 19 minutes to obtain single volume match.

following the method of Section 2.2. The chosen height of 2 km is safely above any clutter artefacts in the vicinity of the ground, but still closely represents surface rainfall owing to the lower troposphere in the tropical monsoon being very moist, such that there is minimal evaporation (e.g., Kumar et al., 2013a).

3. Spatial matching: The nearest radar pixel to the synop site is identified, and then all contiguous pixels to this closest pixel are also considered (using 4-connectivity), giving

a total of 5 radar pixels. Through trial and error, this small neighbourhood size was found to yield the most accurate verification in terms of root mean-square error. Inverse distance weighting is applied in order to average the reflectivity within this radius, such that those pixels closest to the synop site are weighted most strongly.

4. Reflectivity is converted to rainfall intensity using the Marshall-Palmer Z-R relationship ($Z = 200R^{1.6}$; Marshall and Palmer, 1948). Tests were performed on multiple Z-R relationships and they were found to result in no significant difference to the verification.

5. Temporal matching: The rainfall intensity from the radar is converted to depth for the 10 minute time resolution of each radar volume during the period of the synop reading (between 3 and 24 hours; considered individually). Finally, this is then scaled to the total number of 10-minute periods within the period of the synop reading, in order to account for frequent missing radar data. However, there must be a radar volume on average at least every 15 minutes (i.e., 75% of the the maximum number of radar volumes) in order for the comparison to be made. This is to avoid errors becoming too large as a result of this scaling.

Data were not available in the vicinity of every site, but the verification was performed successfully on 3 sites that all had large calibration corrections applied: Nagpur, Patna, and Patiala.

Significant improvements in the accuracy of radar-derived rainfall after calibration correction were found for all 3 sites. However, Nagpur obtained the largest sample of synop-radar comparison points, and is shown in Figure 3.5. Synop readings taken at 12 UTC and 03 UTC (9 hour and 24 hour accumulations respectively) provide enough comparisons to be shown here, and are designated different markers in Figure 3.5. Before calibration, the radar-derived rainfall is much too low compared to the synop rainfall. High values of rainfall from both synop sites within the radar domain register as very light rain or drizzle from the radar. After the 13.2 dB calibration offset is applied, the comparison points lie closer to the 1:1 line and the percentage error between synop and radar improves. For example, using Marshall-Palmer

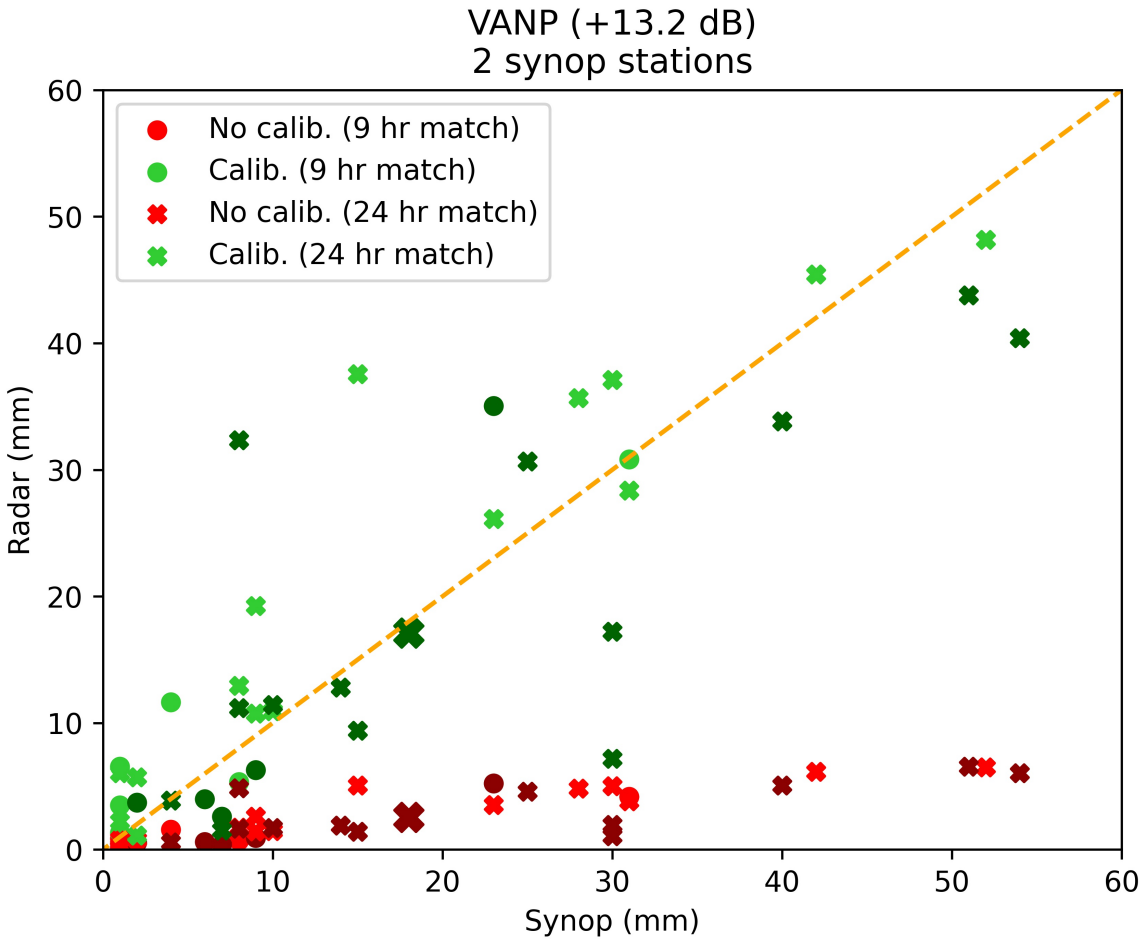

Figure 3.5: Scatter plot of synop rainfall (15 May–15 July) against radar-derived precipitation at the 2 km CAPPI level for Nagpur (VANP). The red markers are before calibration, and the green markers are after calibration correction. The different shades of green and red correspond to different synop locations, of which there are two in this case. Circles represent rainfall comparisons over 9 hours, and crosses over 24 hours. The orange dashed line is the 1:1 line. Only those synop readings equating to an average rainfall of at least 0.1 mm per 3 hour period are matched with the radar. 75% of the 10-minute radar volumes must be available over the period of the synop reading. Radar-derived rainfall is converted to depth and scaled by the total number of 10-minute periods within the period of the synop reading. The full procedure for this verification is described in the text. The two larger scatter markers are outlined as they are extracted in Figure 3.6 to visualise the verification in 2-D space.

($Z = 200R^{1.6}$), a 13.2 dB increase in reflectivity is a factor 21 increase in reflectivity in linear units, and so equates to a 6 × increase in rain-rate. Therefore, the impact of the calibration becomes even more evident at higher rainfall readings.

As 24-hour accumulations consider a longer time period, one might expect to see lower accuracy for these data points in Figure 3.5. However, the 24-hour comparisons still are much closer to the 1:1 line after calibration in Figure 3.5. As applying this large positive offset to

the radar increases the rainfall values by an order of magnitude, there is much greater spread in the distribution, and as a result the overall correlation does not change much. Nonetheless, the accuracy of the calibrated radar rainfall continues to be a vast improvement too at higher rainfall readings, confirming the necessity of applying this calibration offset before using the radar data for analysis.

In order to visualise what this calibration correction looks like in 2-D space, any individual comparison point from Figure 3.5 can be examined in closer detail as a map of rainfall, utilising the gridded GPM IMERG as an external observations-based comparison. Figure 3.6 shows a map representation of the larger comparison point in Figure 3.5, and values are total rainfall over a 24-hour period. The position of the synop station is shown by the red cross with its 24-hour rainfall depth labelled. Figure 3.6 makes it visually clear that the rainfall totals provided by the non-calibrated radar are much too low across the entire domain compared to GPM IMERG. After calibrating the Nagpur radar reflectivity, the magnitude of the rainfall totals compare much more favourably with observations, and this is reflected in the similar depths recorded at the synop site.

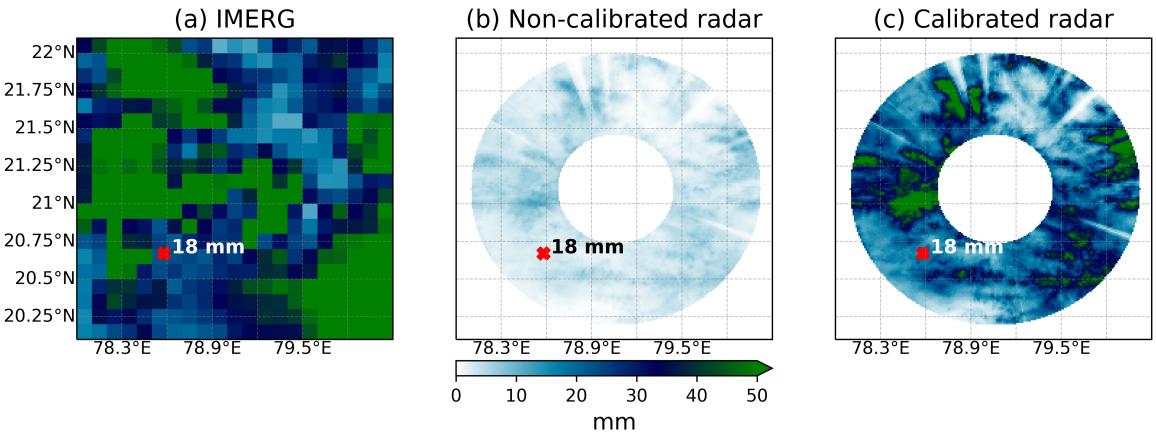

Figure 3.6: Rainfall-depths (mm) over a 24-hour period for (a) GPM IMERG on its native $0.1^\circ \times 0.1^\circ$ grid, centred on the radar site, (b) radar-derived rainfall (40–100 km from the radar site) at a height of 2 km before calibration correction, and (c) Same as panel (b) but after calibration correction. The location of the synop site is shown by the red cross, and its rainfall total over the 24-hour period labelled.

3.4 Discussion and conclusions

A robust 2-stage calibration process following Warren et al. (2018) and Louf et al. (2019b) has been applied to an operational network of Indian Doppler weather radars. Firstly, consistency in clutter fields within 15 km of each radar allowed for stability corrections to within an accuracy of 1.0 dB. This RCA process was successfully applied for 11 radars, but 5 of the radars did not have sufficient clutter for the radar calibration to be monitored in this way. Secondly, volume matching radar sweeps against the GPM DPR with a season of data allowed for a network of 16 radars to all be reliably calibrated against the same instrument, and is achieved for most radars to within an accuracy of 1 dB. The main advantage of this two-stage method is that – unlike traditional calibration methods – it is not reliant upon a robust and dense network of ground rainfall measurements within the radar domain. Furthermore, calibrating against the GPM DPR after the RCA process provides assurance that the radar is relatively calibrated over the season, allowing a single absolute offset correction to be applied.

The main shortcoming with the application of the procedure upon these Indian Doppler weather radars was a lack of clutter and volume matches over the season in several locations, contributing to less certainty in the calibration. More volume matches would be obtained with radar data that is more reliable and for a case-study spanning a longer period of time. Frequent precipitation is also required for volume matches to be useful. Nonetheless, it has been shown that accuracy should not be compromised for the purpose of obtaining more volume matches, and relaxation of the volume matching constraints here was left as a last resort if no matches were obtained. This is because the final calibration offset is considerably sensitive to the parameters in Table 3.1. Therefore, the parameters used should be considered carefully for each radar and its corresponding location, especially for radars with different properties and scanning strategies.

Finally, radar-derived rainfall at Nagpur before and after calibration correction was verified against ground synop rainfall measurements. Even at long time-scales (9 hours and 24 hours), clear improvements are seen post-calibration between ground measurements and radar-derived rainfall, for a broad range of rainfall totals. This verification clearly displays

the improvements that can be achieved with the RCA correction and GPM volume matching technique respectively, and stresses the importance of assessing the calibration of radars before their use in any application that relies upon accurate reflectivity measurements.

As this method utilises the ground clutter native to each radar, and the quasi-global overpasses of the GPM DPR, it has great potential as a semi-automated and widely applicable method that can be repeated each year to monitor calibration changes in operational radar networks, as well as for research-grade radars such as CPOL (Louf et al., 2019b). Furthermore, some potentially common difficulties encountered in executing this calibration procedure for radars have been outlined here, and as a result is more accessible for its future implementation, especially for heterogeneous operational radar networks.

For all analysis that follows using IMD radar reflectivities, the total calibration offsets as given in Table 3.2 are applied before any processing or analysis. This provides greater confidence in the identification and properties of convection for each site, and thus allows a fair and accurate comparison of storms from different radars across India.

Chapter 4

Temporal patterns in radar-observed convective cell development during the 2016 monsoon onset

4.1 Introduction

The timing of onset of the South Asian summer monsoon (hereafter referred to as monsoon) is notoriously difficult to forecast (e.g., Rao et al., 2019), with a standard deviation in the monsoon onset of around 8 days (Pai and Nair, 2009). This interannual variability in monsoon arrival and progression has significant ramifications for communities across India, who rely on monsoon rains to alleviate the pre-monsoon heat, as well as agricultural production (Gadgil and Gadgil, 2006).

As described in Chapter 1, the monsoon arrives in southern India (Kerala) on 1 June on average, before moving in a non-steady motion toward the north-west, reaching the far north-west border of India by 15 July (Pai et al., 2020; Volonté et al., 2020). Parker et al. (2016) noted the climatologically gradual withdrawal of dry air at around 400–700 hPa, originating in the desert north-west, associated with cumulus congestus clouds moistening the mid-levels during monsoon advance, thus resulting in the formation of more convection. In this way, the development of convection in successive regions during monsoon advance

and the associated withdrawal of dry mid-level air to the north-west drives the monsoon forwards, perpendicular to the low-level winds. Volonté et al. (2020) found this competition between retreating dry subtropical air and advancing moist tropical air (as detailed by Parker et al., 2016) to be a non-linear process, modulated through intraseasonal variability (active and break periods; Rajeevan et al., 2010) and the occurrence of synoptic-scale features such as a cyclonic circulation over the Arabian Sea or a monsoon depression in the Bay of Bengal. This results in periods of hiatus and forward jumps in the progression of the monsoon, and this non-steadiness has further consequences for predictability. Furthermore, monsoon onset at Kerala at the southern tip of India has substantial interannual variability: since 1970 the date of onset as stated by the India Meteorological Department (IMD) has fluctuated from as early as 19 May in 1990 to as late as 18 June in 1972. This interannual variability combined with the aforementioned non-steadiness of monsoon advance makes onset an inherently unpredictable phenomenon across India.

Whilst cloud development and the physical processes involved are crucial components of the monsoon, their representation in weather and climate models remains a challenge for both convection-permitting models and those with parameterised convection (ref. Section 1.1.4). The historical undersampling of monsoon clouds in observations is a limitation on constraining these models. Here, using IMD Doppler weather radar observations at 12 sites across the country, we assess the large-scale temporal patterns and local cloud fields associated with monsoon onset in 2016, compared to the increase in local rainfall.

Specifically, in this chapter we will focus on:

1. How do we identify convective cells using radars and how do we define monsoon onset (Section 4.2)?

2. What did monsoon advance look like in 2016 and what large-scale dynamical changes were associated with monsoon onset and progression (Section 4.3)?

3. What is the observed temporal pattern of radar-derived convective cell coverage in the days and weeks leading up to and following monsoon onset and how does this compare with precipitation? Furthermore, how does this differ by region (Section 4.4)?

4.2 Radar data and monsoon onset definition

4.2.1 Indian Doppler radar data

This chapter aims to build a spatial representation of how the monsoon onset presents itself in terms of convective development. In order to analyse any regional differences, we consider 12 Doppler radars (Table 4.1), forming part of the IMD operational radar network (ref. Section 1.2.2). Of the 16 radars with 2016 monsoon season data made available to INCOMPASS (Turner et al., 2020) and used in this thesis, 2 of these radars did not have data for June, thus not fully capturing the monsoon onset. A further 2 radars were missing substantial amounts of data from the days around monsoon onset in the region, and so were not analysed here. The 12 remaining radars are all S-band with the exception of New Delhi (C-band), and have a temporal sampling of 10 minutes between radar volume scans. All radars have similar beamwidths (0.93°–1.00°) and elevation angles (see Table 4.1), with similar or identical scanning strategies. There is some disparity in the gate size between different radars, varying between 250 m and 1000 m for Patna and Karaikal respectively. All radars were calibrated prior to analysis using clutter reflectivity and GPM DPR overpasses following Chapter 3.

Following the processing steps outlined in Section 2.2, a 3-D Cartesian grid of reflectivity data is constructed for each radar between 2 km and 16 km above the surface. Any storms penetrating above this level are set to a maximum of 16.5 km but may represent convective cells deeper than this. The horizontal resolution of the 3-D grid is 1 km $\times$ 1 km and information from the ten elevation scans is linearly interpolated (for each horizontal pixel) onto a 0.5 km vertical grid. Once the 3-D grid of reflectivity is obtained, the Steiner et al. (1995) convective/stratiform classification is implemented using the reconstructed reflectivity at 2 km height to identify convective pixels. A convective pixel at 2 km is assumed convective throughout the vertical profile, similarly to Kumar et al. (2013a).

Each Cartesian pixel for each radar volume scan is given an echo-top height (ETH) based on the maximum height of the 10 dBZ level for this chapter. This threshold is chosen to be as low as possible but above the minimum sensitivity of all radars at 100 km (see Table 4.1).

Table 4.1: Latitude and longitude coordinates for each radar site used in this work chapter, alongside gate size and the noise value of the radar at the outer edge of the 3-D domain (100 km) after calibration. The right-most column gives the date of monsoon onset in 2016 from the IMD monsoon progression isochrones.

Site name*	**Lat. (°N)**	**Lon. (°E)**	**Gate size (m)**	**Noise at 100 km (dB)**	**2016 onset date**
Karaikal	10.91	79.84	1000	3	8 June
Chennai	13.07	80.29	500	2	8 June
Machilipatnam	16.18	81.15	500	2	17 June
Vishakhapatnam	17.75	83.35	1000	0	17 June
Kolkata	22.57	88.35	500	2	17 June
Patna	25.58	85.09	250	8	19 June
Agartala	23.89	91.25	500	−1	14 June
Mumbai	18.90	72.81	300	2	20 June
Nagpur	21.10	79.06	500	6	19 June
Bhopal	23.24	77.42	500	0	21 June
New Delhi	28.59	77.22	300	−5	2 July
Patiala	30.36	76.45	500	4	2 July

*The elevation angles for all radars except Nagpur are 0.2°, 1.0°, 2.0°, 3.0°, 4.5°, 6.0°, 9.0°, 12.0°, 16.0°, and 21.0°. Nagpur's first elevation angle is 0.5°.

Finally, the cell-top height (CTH) is determined as the maximum ETH in a convective region, where any cell greater than 4 km^2 in size is considered for analysis. Here, we define cells with CTH $\geq$ 8 km above ground level as deep cells, representing the most potent convection. Deep cells are associated with high 2 km reflectivities (typically in excess of 30 dBZ, not shown). We also prescribe those cells with CTH $\geq$ 5 km and CTH $<$ 8 km as cumulus congestus cells, with 2 km reflectivities less than 30 dBZ (light rain), and CTH in the approximate region of the tropical monsoon freezing level. More information explaining the definitions of these storm modes is given in Chapter 5. Whilst we only consider a single season due to radar data availability, 2016 is considered a representative year for analysis, with 97% of average all-India rainfall and an onset data at Kerala on 8 June (7 days later than the climatological average, within one standard deviation; Pai and Nair, 2009).

4.2.2 Monsoon onset

The definition of monsoon onset at a particular location is not trivial. Difficulty stems from the need to avoid false monsoon onsets. For example, in 2016, south-eastern India saw record-breaking amounts of rainfall on 18 May due to Cyclonic Storm Roanu, but this was not associated with the monsoon regime. However, such storms can act to help advance the northern limit of the monsoon (Krishnamurti et al., 1981). Furthermore, it is a misconception to think there is no rain in a region prior to monsoon arrival with consistent rain after. For example, rain-shadow regions (such as south-eastern India, in the lee of the Western Ghat mountains) will often experience long dry spells following monsoon arrival. Due to the aforementioned non-steady nature of monsoon progression associated with day-to-day as well as intraseasonal variability and regional differences, it is a complex task to objectively define monsoon onset. Purely dynamical methods make sure that onset is associated with the monsoon synoptic regime (i.e., dominant westerly winds in the lower troposphere with easterly winds in the upper troposphere) but may define onset where there is little actual rain at the surface. Statistical methods rely on rainfall but are more prone to false onsets as a result. The IMD has historically used a blend of large-scale circulation features and measured rainfall to define monsoon onset and progression in a particular year (e.g., Pai and Nair, 2009). Recently, new objective criteria were released for the monsoon onset by the IMD (Pai et al., 2020). This method uses IMD gridded daily rainfall data (Rajeevan et al., 2010) to define onset at each $1^\circ \times 1^\circ$ pixel, in order to ensure rainfall in a location on the day of onset, with stricter criteria for certain regions depending on the local meteorology. Further details are provided in Pai et al. (2020). However, on investigation, even the new objective criteria were prone to early onset, especially for northern India.

Therefore, to define onset at each radar site, we compare the radar location against the IMD progression isochrones[1]. The requirement for the IMD isochrones is for two consecutive days with rainfall in excess of 2.5 mm for at least 60% of surrounding stations, given the depth of westerlies reach 600 hPa and the satellite-derived outgoing longwave radiation (OLR) is less

[1]IMD onset isochrones are available at https://reliefweb.int/sites/reliefweb.int/files/resources/20161010_pr_60.pdf

than 200 W m^{-2} in a surrounding grid-box. The IMD takes these criteria into consideration in a subjective manner to determine the onset date (Pai and Nair, 2009). The first date at which the exact radar location is level with or behind the progression line is taken as the monsoon onset date for that radar site. The date of monsoon onset for each site is shown in Table 4.1.

4.3 Large-scale drivers of cloud development at onset

Firstly, we consider the progression of the monsoon and its rainfall in 2016, and discuss the circulation changes associated with its advance. Figure 4.1 shows average daily rainfall totals from the GPM IMERG product (Huffman et al., 2020), alongside 850 hPa wind vectors from ERA5 (Hersbach et al., 2020), averaged over successive pentads (grouped 5-day periods) from mid-May to mid-July 2016. The spatial resolutions of GPM IMERG and ERA5 are 0.1° and 0.25° respectively.

In May the monsoon regime is yet to be established over India. Low-level winds are from the north-west over the land, resulting in dry air advection, and are weak in magnitude. Westerlies south of India gradually spread northwards, encompassing most of India by the end of May (Figure 4.1c). Over land (except the far south of India), these westerly winds weaken again in early June (Figure 4.1d) but continue to strengthen over the Arabian Sea (west of India). As a result, rainfall begins to build offshore from the western coast of India, as well as off the south-eastern coast. This brings monsoon onset to far south-eastern India in the first week of June. However, following this, a break period develops. We define a break period using rainfall over a central India zone (18–27°N, 73–82°E) and comparing to the climatological average for each day (Rajeevan et al., 2010 provides more details). Break periods are associated with decreased rainfall in the central India zone (and vice versa for active periods). These events can be instrumental in delaying the progression of the monsoon north-westwards (Rajeevan et al., 2010). The gradual movement of rainfall over western India from offshore to over land (e.g., Figures 4.1e and f) is associated with a clear increase in the strength of the westerly onshore winds (Fletcher et al., 2020). Over the Bay of Bengal (east of

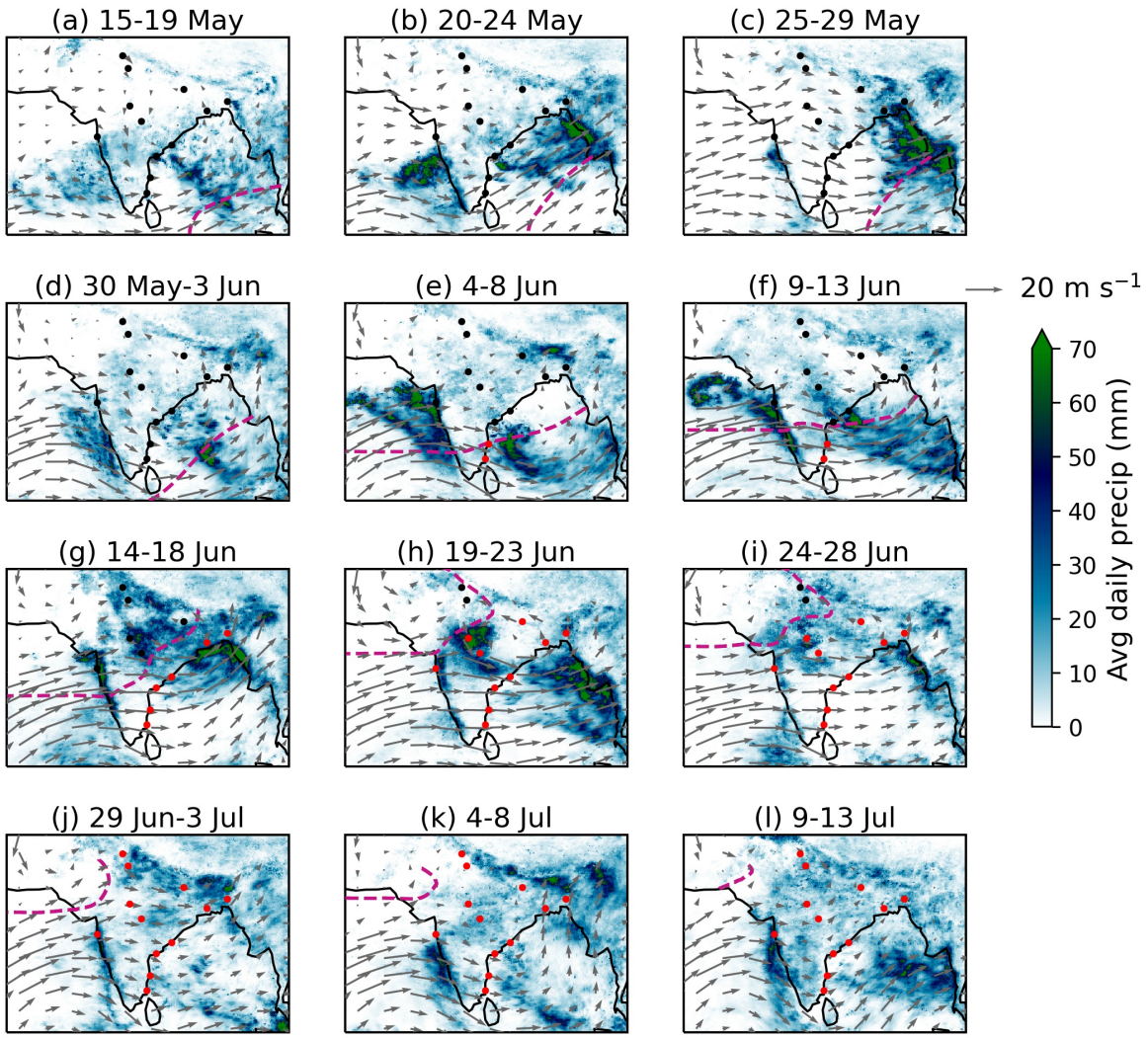

Figure 4.1: Pentads (5-day grouped periods) of GPM IMERG rainfall and ERA5 wind vectors at 850 hPa from 15 May until 13 July, near the climatological peak of the monsoon. The locations of the 12 radar sites used (see Table 4.1) are marked as black dots, and are coloured red from the first pentad at which monsoon onset occurs at that site. Both the rainfall and winds are plotted as daily means averaged over the respective pentad. The purple dashed line is the northern limit of the monsoon on the last day of each pentad from the official IMD isochrones. Winds are not shown in regions above 1.5 km elevation.

India), a northward-pushing wave packet associated with the Boreal Summer Intraseasonal Oscillation (BSISO) phases 2 and 3 (Kikuchi et al., 2012)[2] brings rainfall to much of north-eastern India by mid-June (Figure 4.1g), resulting in the formation of a monsoon depression, and monsoon onset in this region. In Figures 4.1g and h, the monsoon depression visibly tracks westwards in the 850 hPa wind field, resulting in monsoon onset across the remainder

[2]Daily BSISO phase data are available at http://iprc.soest.hawaii.edu/users/kazuyosh/ISO_index/data/BSISO_25-90bpfil.rt_pc.txt

of western and central India. Finally, in early July, New Delhi and Patiala in northern India experience monsoon onset as the westerly winds push sufficiently northwards. Note that New Delhi and Patiala saw significant rainfall earlier in June associated with the aforementioned monsoon depression, but this was followed by drier weather as low-level winds were still weak with a north-westerly component, and thus onset was not defined in these regions. By mid-July (Figures 4.1l), the monsoon regime is almost at its peak, with substantial and persistent precipitation over most of the country.

One major feature of the monsoon regime over South Asia is the establishment of the tropical easterly jet (TEJ). The TEJ is a thermal wind in the upper troposphere which forms in Boreal spring due to the developing north-to-south temperature gradient between the Tibetan Plateau and the equator. It continues to increase in strength until the end of June, and is responsible for the usual westward passage of monsoon depressions (e.g., Figures 4.1g and h), that can be instrumental in advancing the northern limit of the monsoon through synoptic forcing (Parker et al., 2016). Studying mid-level relative humidity and moisture flux (see Figure 4.2), in general we note the gradual retreat of dry mid-level air over north-western India throughout May and into June, as detailed by Parker et al. (2016). In late May (Figure 4.2c), drier air advects back into southern India which delays monsoon onset in Kerala. Into June, moisture then continues to build over most of India until the final pentad (near peak monsoon) associated with increasingly persistent convection. However, the north-western wedge of dry air is a spatially transient feature even well into the monsoon season, sometimes retreating back into neighbouring Pakistan, and sometimes pushing back south-eastward (e.g., Figures 4.2h and k). Intriguingly this seems to have little bearing on the monsoon advance into north-western India in 2016. New Delhi and Patiala experience monsoon onset in Figure 4.2j, associated with drier air once again encroaching from the north-west (see Figure 4.2j), but westerly winds do push north into the region at this time. This illustrates the complexities involved with predicting monsoon onset, due to the competing effects of advancing moist tropical air and dry subtropical air not always displaying a clear anti-correlation in a region.

Moisture flux vectors in Figure 4.2 are shown to elucidate the point that eastward moisture

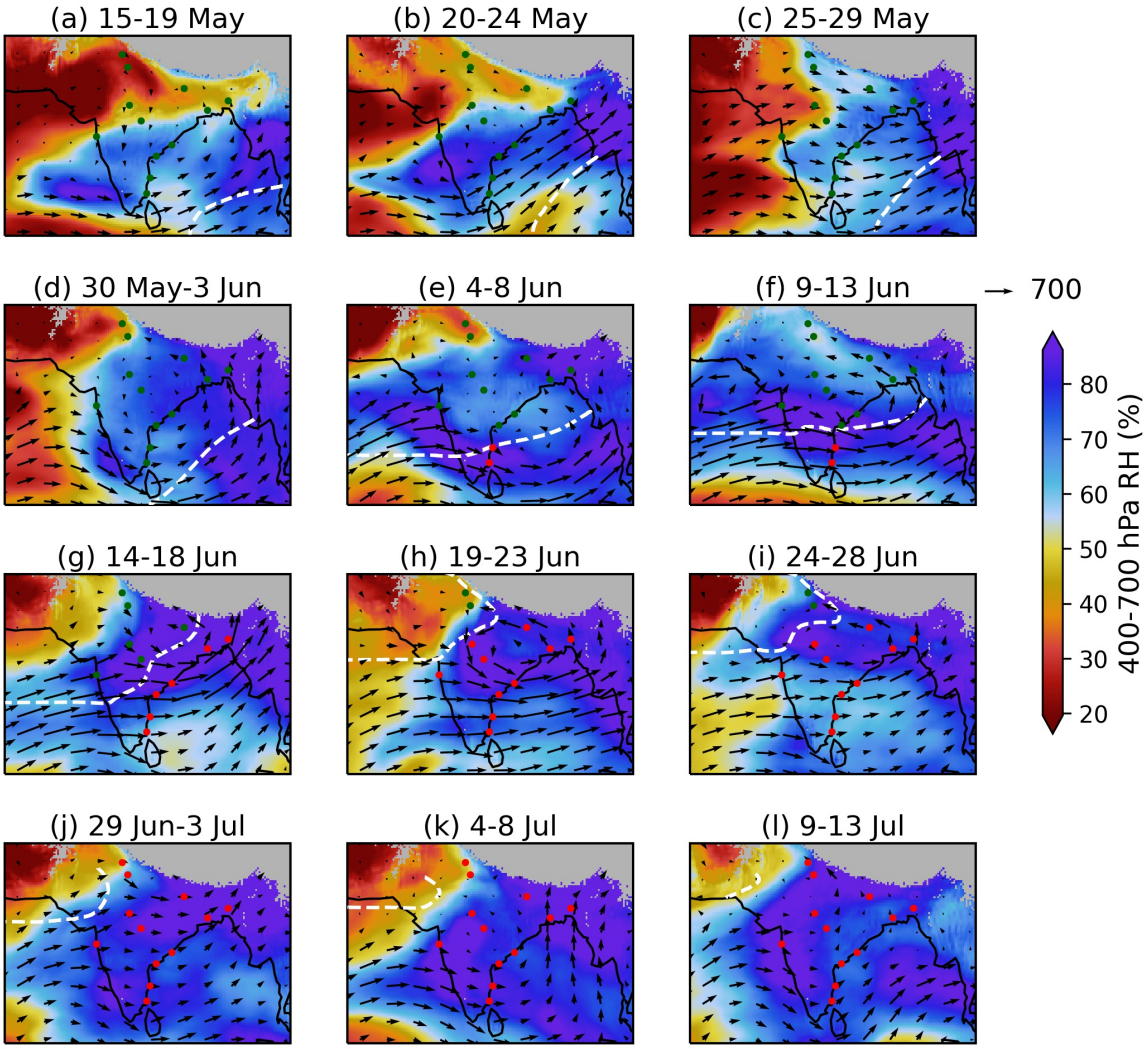

Figure 4.2: Same as Figure 4.1 but the colours show relative humidity averaged in the region 400–700 hPa, alongside vertically-integrated (surface to top-of-atmosphere) moisture flux vectors (kg m^{-1} s^{-1}, both from ERA5). The northern limit of the monsoon is the white dashed line, and sites are coloured green before monsoon onset arrives at that location. Areas more than 2 km above sea level are shaded grey.

flux and convergence of moisture occur both sides of the northern limit of the monsoon (white dashed line), especially over the ocean. This was also noted by Parker et al. (2016), and therefore shows that convergence of tropical moisture-laden air alone cannot explain monsoon advance. As a result, we can expect significant convection and associated rainfall for many regions in advance of monsoon onset at a given location. This raises the importance of the additional dynamical requirement of westerly winds in the lower troposphere when defining onset.

4.4 Temporal patterns in local cloud and precipitation during monsoon advance

We now turn our attention to the convection surrounding each radar site in Table 4.1, comparing with local rainfall measurements from IMD $1^\circ \times 1^\circ$ daily gridded rainfall data (Rajeevan et al., 2010), and study how these observations evolve during monsoon onset at each site. Figure 4.3 shows 5-day running means of local precipitation and convective area for deep (CTH $\geq$ 8 km) and cumulus congestus type cells (5 $\leq$ CTH $<$ 8 km). The vertical black dashed line represents the date of monsoon onset. We calculate Pearson correlation coefficients between precipitation and congestus/deep convective area, and these are labelled in Figure 4.3 for each site. There is a positive correlation between local rainfall and deep convective area for all sites (0.26 for New Delhi and 0.94 for Mumbai). Deep convective cells are usually responsible for most precipitation due to their larger average surface area and greater intensity. Two sites (Kolkata and New Delhi) show weaker correlations less than 0.5. Interestingly, both these sites show relatively higher correlations for congestus cell area. However, examining Figures 4.3e and k closely, the poor correlations stem from periods with a large amount of deep convection that is not reflected in the rainfall time series (e.g., Kolkata 25 June, New Delhi 8–15 July). This could be because not all deep convection at these sites is resulting in high precipitation at the surface. The area covered by congestus-type cells is significantly less compared to deep cells, resulting in a weaker correlation for most sites, but still is positively correlated with precipitation for all regions (as high as 0.92 in Mumbai). The strength of this correlation for Mumbai is likely associated with the predominance of shallow precipitating convection over the western coast of India (Utsav et al., 2017). It follows that an increase in deep cell coverage is usually associated with a smaller increase in congestus cell coverage. This suggests that at 5-day resolution, monsoon onset is associated with an approximately simultaneous increase in cells of multiple levels. This is in contrast to a progressive deepening of cells on this timescale, as one might infer from the Parker framework (Parker et al., 2016) of congestus convection moistening the mid-level troposphere, allowing deeper clouds to form as the monsoon arrives in a region.

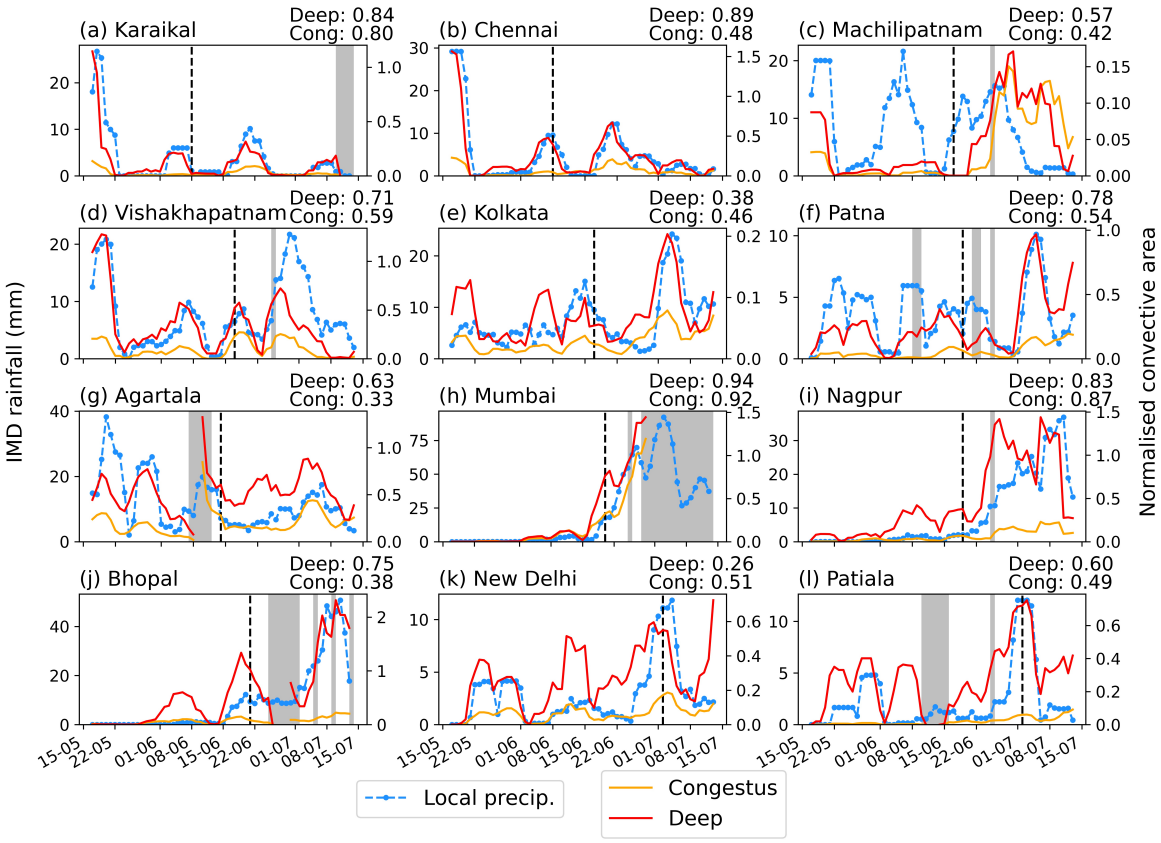

Figure 4.3: 5-day running means (centred on the date shown) of local precipitation from IMD $1° \times 1°$ gridded daily precipitation (spatially averaged for the nearest five grid boxes). Also shown is the daily sum of deep (CTH $\geq$ 8 km) and congestus (5 $\leq$ CTH $<$ 8 km) convective area for each day (normalised by the number of radar volume scans) at each site for when data are available. Pearson product–moment correlation coefficients of precipitation against deep and congestus cell area over the time series are labelled for each site in the top right corner. Grey shaded regions are days with zero radar volume scans for that site and are not included in the correlation. The vertical black dashed line represents the day of onset for that site, as given in Table 4.1.

We recall that onset is defined based on sufficiently low OLR (i.e., cold cloud tops associated with deep convection) and at least two consecutive days of 2.5 mm observed precipitation. Therefore, as one might expect, monsoon onset is associated with a defined peak in precipitation and cell coverage on or a few days prior to the IMD-defined monsoon onset date in Figure 4.3. However, it is immediately obvious that for most sites, there is a significant amount of convection prior to the monsoon, associated with pre-monsoon rainfall, making purely observations-based definitions of onset difficult. Some sites, such as Mumbai, Nagpur and Bhopal in central west and northern India, show a more pronounced increase in rainfall from pre- to post-monsoon. Other locations show a more complex picture with

significant amounts of pre-monsoon convection and rainfall. However, if a composite of several seasons of data could be considered, the temporal patterns in Figure 4.3 for these sites may become more meaningful. Nonetheless, the exact date of monsoon onset should not be taken too literally, owing to the high-frequency variability in rainfall associated with monsoon initiation. Furthermore, due to the definition of monsoon onset date being a hybrid of large-scale dynamical changes and measured rainfall, neither of these properties in isolation can be fully linked to the onset date. For example, some sites (e.g., Karaikal, Vishakhapatnam, Bhopal, New Delhi) show the maximum in deep cell coverage associated with onset at that location occurring a day or two in advance of the maximum in rainfall associated with onset. Intraseasonal variability associated with the BSISO is likely responsible for the high frequency variability in rainfall for most sites even after monsoon onset. South-eastern India, due to being in a rain shadow region, is prone to periods of near-zero convection and rainfall even after monsoon onset. In contrast, northern India experiences periods of plentiful convection pre-monsoon owing to active periods and monsoon depressions in June.

One interesting abnormality is the presence of significant early June (pre-onset) convection in Bhopal and Nagpur (Figures 4.3i and j) that is not associated with any substantial precipitation (Mumbai shows a similar signal though it is not quite as evident). However, pre-monsoon convection in other regions does result in rainfall. Further analysis with satellite data might be able to inform of the nature of this seemingly non-precipitating convection.

4.5 Conclusions

The progression of the South Asian summer monsoon is a complex and non-steady phenomenon (Volonté et al., 2020). As a result, it remains a relatively unpredictable area of meteorology, yet forecasts of monsoon onset in a particular region have importance for more than a billion people. Here, we have analysed the monsoon progression in 2016 from a large-scale perspective, and using a network of operational Doppler radars, analysed convective cell area in the weeks before and after monsoon onset at each respective location, comparing against local precipitation. The main conclusions from this chapter are as follows:

- Monsoon onset date is difficult to define objectively for specific locations. It is associated with an increase in westerly winds bringing moist tropical air, and the gradual retreat of dry mid-level air, as well as an increase in precipitation.

- The area covered by deep and congestus type cell populations correlates well with precipitation throughout monsoon onset for all sites, with only a few irregularities (e.g., Bhopal in early June). This shows that the rainfall is dominated by convective activity across all regions. Onset appears to be associated with a simultaneous increase in all types of cells as opposed to congestus gradually giving way to deep cells.

- Mumbai, Bhopal and Nagpur show a clear increase in the amount of convection and rainfall after monsoon onset in their respective regions.

- The complexities in the clarity of onset for most other sites may be a result of their local environment (e.g., south-eastern India rain shadow, northern India pre-monsoon rainfall from monsoon depressions).

The convective cell time series examined here have been shown to be linked to local precipitation as well as the large-scale environment that they are embedded within when considering 2016 alone. However, analysing these temporal patterns across multiple years would be valuable. It is a big effort to expand such observational studies to multiple years due to the large volume of data and amount of processing time it would require, but this would be very beneficial in building up a more robust climatological picture, if data were made available. Next, this thesis expands on this chapter by assessing the relationship between Indian monsoon convection and major timescales of variability during the entire 2016 monsoon season.

Chapter 5

2016 monsoon convection and its place in the large-scale circulation using Doppler radars

5.1 Introduction

The Indian summer monsoon (ISM) is responsible for one of the largest modes of seasonal variability in wind direction and precipitation seen worldwide, and supplies more than 80% of India's annual rainfall during the Boreal summer months of June to September (Turner et al., 2020). This fact, along with the vast, growing population across South Asia whose livelihoods depend upon monsoon rains, makes it one of the most active areas of research in the atmospheric sciences. It has been discussed in this thesis that the ISM is a complex phenomenon, exhibiting substantial variability on intraseasonal and interannual time scales (e.g., Krishnamurti and Bhalme, 1976), and monsoon forecasts remain a challenge as a result of this complexity. Rao et al. (2019) raised three areas of improvement required in numerical weather prediction (NWP) models for improved ISM forecasts: resolution, physics, and ocean coupling. Whilst substantial improvements have been made in recent years, meaningful forecast skill exists only out to four days (Turner et al., 2011; Durai and Roy Bhowmik, 2014; Rao et al., 2019). The representation of monsoon clouds in NWP models is one of the

most challenging physical aspects of the ISM due to complex and numerous sub-gridscale processes (Willetts et al., 2017). General circulation models (GCMs) used for forecasting have resolutions too large to explicitly capture convective processes, a crucial component of the monsoon. Errors due to parameterisation of deep convection in GCMs are quick to grow over time (e.g., Martin et al., 2010). A more detailed view of the monsoon circulation and underlying processes from observations is necessary to better comprehend the intimate coupling between the land surface, boundary layer, and cloud development (Turner et al., 2020). In this vein, this chapter presents an observation-driven analysis of the ISM's distinctive cloud regimes in relation to the large-scale environment over the entire 2016 monsoon season.

Large-scale variability in fields such as temperature, winds, and moisture content all directly affect cloud development. This study will explore cloud regimes and the large-scale environment in relation to three time scales of variability that play a primary role in the ISM. Firstly, monsoon propagation from the south-east to the north of India each year (and its retreat again later in the Boreal summer) is non-steady (Volonté et al., 2020) with substantial interannual variability in arrival times. Therefore, we investigate individual months during the monsoon season from May–September 2016, in order to represent large-scale variability associated with monsoon progression, the peak monsoon, and monsoon withdrawal. Secondly, systematic variation in convection exists as a result of active and break periods (Krishnamurti and Bhalme, 1976; Krishnamurthy and Shukla, 2000, 2007; Rajeevan et al., 2010), a key component of intraseasonal variability during the ISM. These occur as a manifestation of fluctuations in the Boreal summer intraseasonal oscillation, the northward movement of clouds and convection from the equator to the Indian monsoon region (e.g., Jiang et al., 2004), varying on 30–60 day time scales. Models have been found to lack sufficient variability on intraseasonal time scales over both land and ocean (Martin et al., 2017). Thirdly, monsoon clouds typically exhibit a strong signal on diurnal time scales associated with the solar cycle and heating of the surface (Yang and Slingo, 2001). However, the diurnal cycle is poorly modelled in the tropics, leading to underestimates in daily mean rainfall (Martin et al., 2017). Currently, there is limited understanding of the main

drivers of monsoon convection in different locations, and the relative importance of different factors such as local orography, proximity to the coast, prevailing wind direction, amongst others. Evidently, more observations of monsoon convection are required in order to better understand these relationships.

To observe monsoon storms here, 7 radars from the IMD operational weather radar network are used. The overarching aim for this study is to find the spatiotemporal characteristics of convective storms across India during the monsoon season in 2016, which coincides with the period of radar data available to us (15 May to 30 September 2016). As mentioned in previous chapters, the 2016 season is considered a representative year for analysis (June–September all-India rainfall was 97% of the long-term average). To summarise our approach, local radar-derived fields of CTH and near-surface reflectivity are calculated for the 7 radars across the entire 2016 monsoon season and statistically analysed. Patterns in these cells are interpreted over major time scales of variability during the ISM, encompassing the seasonal cycle, active and break events and the diurnal cycle in 2016. Finally, these patterns are related to the large-scale monsoon circulation, in order to assess large-scale patterns of cloud development.

The chapter is structured as follows: Section 5.2 explains how the radars are used to calculate CTH and describes any auxiliary datasets used; Section 5.3 presents the season-average cell statistics in the context of the large-scale environment; Section 5.4 assesses cell patterns during 2016 active and break periods; Section 5.5 examines the diurnal cycle in cell activity at each location, and investigates how it compares between land and ocean, and how it is modulated by monsoon progression and active-break spells through the season. Finally, the main conclusions of this study and key areas requiring future investigation are presented in Section 5.6.

5.2 Data and methods

5.2.1 Radar data

This study makes use of 139 days of reflectivity data (15 May to 30 September 2016) from 7 Indian Doppler Weather radars (see Figure 5.1a). Of the 17 radars available for analysis during this season, these 7 radars are chosen for analysis as they are all S-band (approx. 10 cm wavelength), and represent four distinct climate regions with different monsoon rainfall climatology and arrival dates. Furthermore, the minimum detectable signal at 100 km for all these radars is below 5 dBZ after calibration (ref. Table 5.1), allowing a lower (i.e., 5 dBZ) reflectivity threshold for calculating ETH (closer to that of Kumar et al., 2013a, who took a 0 dBZ threshold using CPOL). The south-east sites (Chennai, Machilipatnam) represent coastal India, and are outside the core monsoon circulation. Mumbai in western India represents the west coast and Western Ghats region. Northern India (Bhopal, Lucknow) represents inland regions within the core monsoon circulation. North-eastern India (Agartala, Kolkata) is a near-coastal region where the monsoon winds typically begin to curve back to the north (Figure 5.1b). Two radars per region were identified for analysis if possible, to allow comparison within each region. However, Mumbai was the only radar with data available on the west coast.

Following the procedure detailed in Section 2.2, a 3-D Cartesian grid of reflectivity data is constructed for each radar between 2 km and 16 km above the surface. The horizontal resolution of the grid is 1 km $\times$ 1 km and 0.5 km in the vertical.

5.2.2 Derivation of echo-top height and cell-top height

To calculate radar-derived ETH, a 5 dBZ threshold is used here. The choice of threshold must be greater than the noise level at 100 km (the outer-edge of our domain), as shown in the right-most column of Table 5.1. Specifically then, searching upwards from 2 km, the pixel nearest in value to 5 dBZ in the vertical column is taken as the ETH, with the condition that there must be retrievals greater than 5 dBZ at each 0.5 km level in the vertical column below

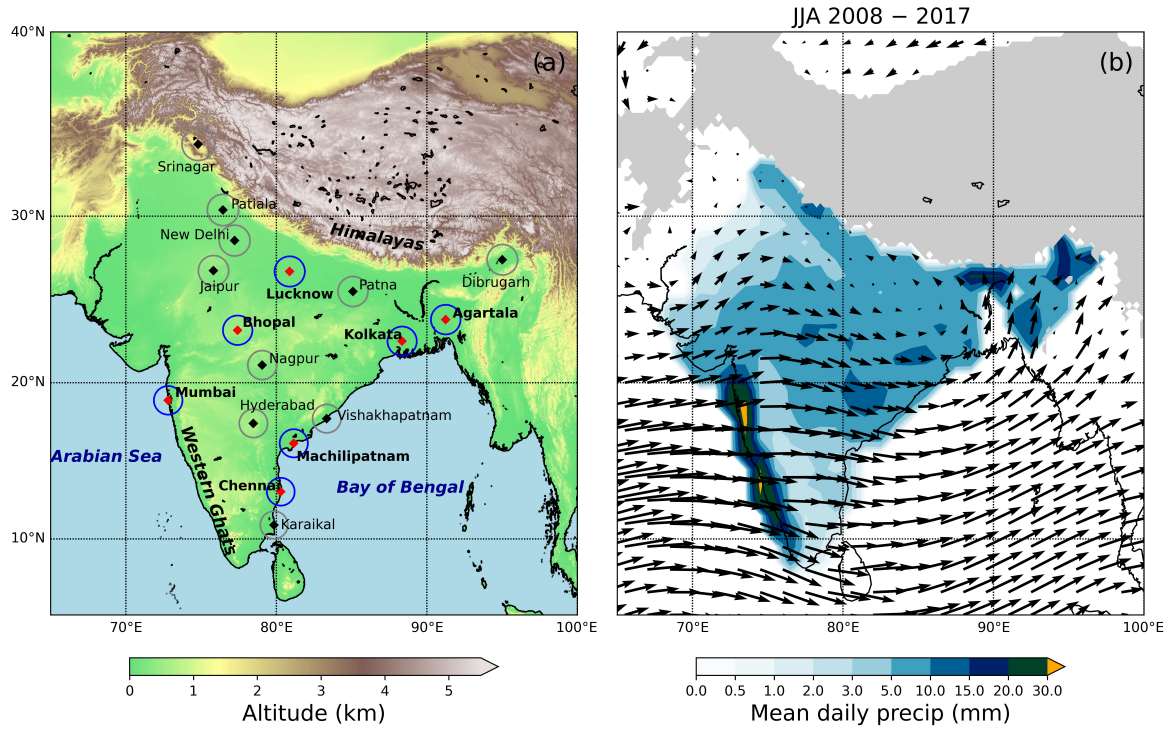

Figure 5.1: (a) Topographical map of India and surrounding regions, with some major features labelled. Also shown is the network of 17 Indian Meteorological Department Doppler weather radars made available to INCOMPASS, with diamond markers, and rings denoting 100 km range from the radar. The blue rings (with bold labels and red markers) are the 7 radars used in this study. The network has since been expanded further. (b) Recent climatological (2008–2017) precipitation (India only) and 850 hPa winds from IMD gridded data and ERA5 respectively. Regions above 1.5 km in altitude are shaded grey.

the ETH. As discussed in Chapter 2, the spatial gaps between sweeps may lead to under- and overestimates of ETH, especially further from the radar where the separations become greater, and for higher elevation angles. However, these errors are reasonably predictable for a given scan strategy and vary with ETH and as a function of distance from the radar. In Appendix A, we carry out further analysis using data from a research radar, featuring high vertical resolution, on how the bias varies with range for the Indian radar scan strategy. We find that for ETH below 10 km, the error is typically less than 1 km and the mean error is close to 0 km.

This level of accuracy is sufficient for the purpose of this work, firstly, because we aggregate our ETH into single cell-top height (CTH) values for each convective region and, secondly, because we are interested in the statistical variability of ETH averaged over a longer period of time. Such an approach has successfully been carried out in numerous studies for

the Australian monsoon using the Darwin CPOL radar (May and Ballinger, 2007; Kumar et al., 2013a; Jackson et al., 2018), which has similar gaps between elevation angles compared to the IMD radars. For the CPOL ETH estimates, Jackson et al. (2018) reported a statistically significant correlation with satellite-retrieved cloud top heights, demonstrating the suitability of using radar-derived ETHs for analysis of convection over a monsoon season. Finally, CTH is then calculated as the maximum ETH in a convective region, defined using the Steiner algorithm (ref. Section 2.2).

Radar-derived convective cell statistics for each of the seven sites analysed in this chapter can be found at Doyle et al. (2021c).

Table 5.1: Relevant specifications for the 7 Doppler radars used in this study, grouped by region. The noise at 100 km is the minimum detectable signal calculated using a random day of clear-sky data for each radar. A clear-sky day is simply determined as any day with no measured rainfall that is also persistently clear in infra-red satellite imagery.

Site*	Lat (°N)	Lon (°E)	Alt (m)	Gate size (m)	Beam width (°)	Noise at 100 km (dB)
Chennai (VOMM)	13.07	80.29	35	500	1.00	2
Machilipatnam (VOMP)	16.18	81.15	35	500	1.00	2
Bhopal (VABP)	23.24	77.42	570	500	0.93	0
Lucknow (VILK)	26.77	80.88	143	500	0.97	3
Agartala (VEAT)	23.89	91.25	35	500	0.93	−1
Kolkata (VECC)	22.57	88.35	35	500	1.00	2
Mumbai (VABB)	18.90	72.81	100	300	1.00	2

*Elevation angles for all radars are: 0.2°, 1.0°, 2.0°, 3.0°, 4.5°, 6.0°, 9.0°, 12.0°, 16.0°, and 21.0°.

5.2.3 Auxiliary datasets and method

The convective cell statistics presented are considered in the context of the local and large-scale meteorological state during the 2016 monsoon season. GPM IMERG (Huffman et al., 2020) – providing half-hourly robust precipitation estimates at 0.1° horizontal resolution – is used to visualise the large-scale precipitation field.

IMD gridded daily rainfall accumulations (Rajeevan et al., 2006), with $1° \times 1°$ spatial resolution, are used to designate active and break days in 2016 (and are also used in Figure 5.1b).

We follow the method of Rajeevan et al. (2010) with a few adjustments: June–September 2016 IMD gridded daily rainfall is compared to the recent climatological (2008–2017) rainfall, averaged across a central India zone (18–27°N, 73–82°E). A standardised rainfall anomaly is then calculated for each day, defined as the climatological average subtracted from the 2016 value, divided by the standard deviation of the climatological average. A difference between each day's standardised anomaly and the 2016 mean standardised anomaly that is greater than 0.7 defines an active day, and conversely a difference less than -0.7 defines a break day. Finally, an active/break day must be part of a set of 3 consecutive active/break days in order to be included in our statistics. The active and break days derived in this manner may not necessarily be part of true active and break periods, but instead more closely represent active and break spells with respect to the 2016 mean state, and their corresponding large-scale pattern changes. As a result, we identify a larger and more equal number of active and break days, lending itself to a more robust and fair comparison. The final active and break days used for this study are presented in Table 5.2. Handily, there are 32 active and 32 break days across the season (26% of the full sample in each case).

Table 5.2: 2016 Indian monsoon season active and break spells. The method used to obtain these dates is described in the text.

Date	Active/Break
1–3 June	Break
9–17 June	B
28–30 June	Active
2–7 July	A
9–13 July	A
20–26 July	B
2–4 August	A
12–14 August	B
19–21 August	A
3–12 September	B
14–17 September	A
21–28 September	A

ERA5 estimates of several atmospheric variables at multiple levels are also used to complement this analysis over the 2016 season (Hersbach et al., 2020). Owing to the hourly resolution of ERA5, the diurnal cycle can be explicitly determined. Finally, twice daily (00 UTC and 12 UTC) atmospheric soundings are available in the near vicinity (< 25 km) of all sites analysed here (ref. Section 2.3.3). In the case of both GPM IMERG and ERA5, when comparing fields at local radar sites, the average of all gridboxes with centroids in the 40–100 km radar domain is used.

5.3 Individual cell statistics

We start by examining the number of cells of different heights for each site, and relate these patterns to near-surface cell reflectivity. Table 5.3 shows the number of cells at each site and as an average per radar volume. Agartala has by far the largest number of cells, situated in the very convectively active north-eastern India region, with prevailing low-level winds originating from over the very moist Bay of Bengal (Figure 5.1b). Mumbai has noticeably fewer volumes over the season, owing to substantial periods of missing data during July and August in particular, and so should be analysed with more caution. Considering the ratio of number of cells to number of radar volumes as a measure of convective activity (fourth column of Table 5.3), Agartala is by far the most convectively active, then all other sites average approximately 3 cells per radar volume over the entire season.

The probability of cell occurrence in each 0.5 km CTH bin is shown in Figure 5.2a. There is consistency between all 7 sites in the shape of this function, with a peak in CTH at approximately 6–8 km, around or just a bit above the average freezing level during the monsoon (Harris Jr et al., 2000). The two northern India sites – Bhopal and Lucknow – have the maximum CTH occurrence at a greater height, as well as the highest proportion of very deep (CTH $\geq$ 12 km) cells. Several sites (Chennai, Machilipatnam, Bhopal, Lucknow) display the hint of a secondary peak in CTH at 12–13 km, associated with deep convection. However, this peak is not obvious, as Figure 5.2 is an average over the entire season, throughout which different cloud regimes, some dominated by shallower convection, will occur. Indeed, taking

Table 5.3: Total number of complete radar volumes, the number of cells (including CTH > 16 km), and average number of cells per radar volume for all 7 sites, grouped as in Table 5.1, from 15 May to 30 September 2016. We recall that Chennai and Machilipatnam are in coastal south-eastern India. Bhopal and Lucknow are located further inland in northern India. Agartala and Kolkata are near-coastal north-eastern India sites. Finally, Mumbai is on the western coast. The percentage of cells with CTH > 16 km is also shown. Note that with a radar volume of 10 minutes, if there were 0 missing scans through the season, the number of volumes would equate to 20016 scans.

Site	Volumes	Cells	Cells per Volume	CTH > 16 km (%)
Chennai (VOMM)	17839	51125	2.9	1.8
Machilipatnam (VOMP)	18589	46888	2.5	1.5
Bhopal (VABP)	13546	49059	3.6	4.4
Lucknow (VILK)	6914	19840	2.9	5.4
Agartala (VEAT)	14710	95741	6.5	1.4
Kolkata (VECC)	13018	31971	2.5	1.3
Mumbai (VABB)	3553	10365	2.9	0.1

especially convectively active weeks displays the secondary peak much more clearly (not shown). Evidence of such bimodality was also found during the Austral monsoon season at Darwin by Jackson et al. (2018), especially during the more active phases of the Madden-Julian Oscillation when mid-level moisture was found to be higher. Therefore, Figure 5.2a suggests the presence of at least 2 cumulus modes, one around the freezing level, and one in the upper troposphere. This will be explored in more detail later in this section.

Mumbai exhibits a larger proportion of shallow convection (CTH < 5 km), and a smaller proportion of deep convection relative to other sites. While the Mumbai data are predominantly unavailable from July, this is consistent with previous observational analysis for the region (e.g., Utsav et al., 2017). Das et al. (2017) found rain in the Western Ghats region to be dominated by shallow-convective systems (echo tops below the melting layer). Mid-tropospheric air from Mumbai radiosonde soundings in 2016 is found to be drier on average compared to the other regions (not shown), consistent with the findings of Kumar (2017). Das et al. (2017) also commented on the role of orography, showing that convective clouds over the Western Ghats precipitate out quickly owing to rapid collision-coalescence of cloud droplets due to orographic uplift.

The vertical wind profiles in Figure 5.2b show the presence of the tropical easterly jet (TEJ) upwards of 8 km, a major component of the large-scale monsoon circulation in Boreal summer (Krishnamurti and Bhalme, 1976). It forms as a result of the meridional temperature gradient between the subtropics and equatorial Indian Ocean in the upper troposphere. Mumbai and south-eastern India exhibit westerly or south-westerly winds in the low and mid-troposphere, with strong easterly winds associated with the TEJ in the upper troposphere. Interestingly, the transition to easterly at around 6–8 km above the surface is where the winds are weakest, and this is approximately the height of the modal CTH for these sites. The presence of stronger winds aloft associated with the TEJ may be an inhibiting factor for vertical cell growth, as the strong wind shear can spread cloud tops above 8 km (Sathiyamoorthy et al., 2004). This can act as one constraint on CTH, especially during peak monsoon months when the TEJ is strongest. For northern and north-eastern India, there is a deep layer of southerly winds in the lower and middle-troposphere, with a small amount of gradual backing of these winds with height. Wind speeds only begin to increase above 8 km, again above the modal peak in CTH for these sites. The increase in wind speed is more subtle for Lucknow (VILK), where weaker upper-level wind shear may contribute to the marginally higher proportion of very deep cells here ($\geq$ 12 km), due to less spreading of cloud tops.

As aforementioned, Figure 5.2a suggests the presence of multiple cumulus modes (preferential detrainment of cloud tops at certain levels), and we investigate this and its associated mechanisms in more detail here, by analysing the relationship between CTH, equivalent potential temperature (θ_e; Figure 5.2c) and near-surface reflectivity (Figure 5.3). This analysis is important because the different cumulus modes in Figure 5.2a are likely to have different characteristics and may interact with the large-scale environment in different ways. Firstly, Figure 5.3 shows that 2 km cell reflectivity is clearly a definitive indicator of CTH for all sites. More intense cells (higher 2 km reflectivities) typically have higher cell tops (and are greater in horizontal extent, not shown here). Reflectivity values of 20 dBZ indicate light rain ($<$ 1 mm hr^{-1}), 30 dBZ moderate rain ($>$ 1 mm hr^{-1}), and 40 dBZ heavy rain ($>$ 10 mm hr^{-1}) and so higher cells are also associated with heavier precipitation. Mumbai exhibits a higher average 2 km reflectivity for shallow CTH (27 dBZ at 4 km compared to 24 dBZ at 4 km

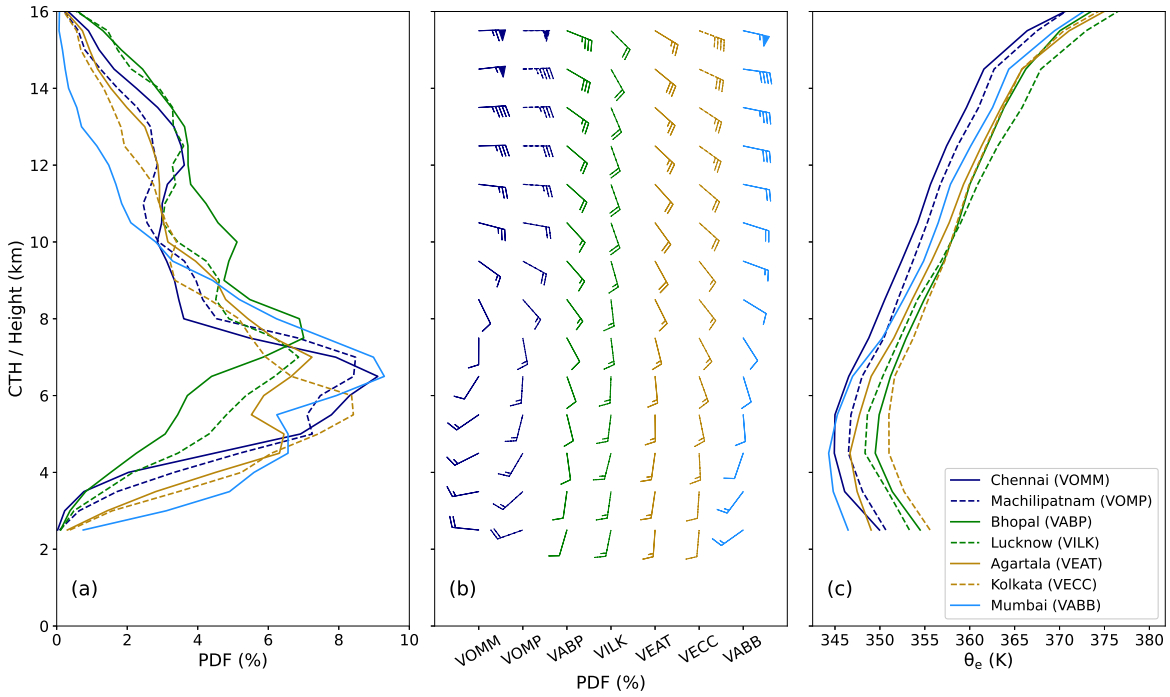

Figure 5.2: (a) Percentage of different CTHs for the 7 radars used in this study as shown in Figure 5.1, from 2.5 km above the surface, every 0.5 km in height, (b) wind barbs from local soundings every 1 km in height with barb increments denoting 5, 10 and 50 knots respectively and, (c) equivalent potential temperature (θ_e) every 1 km in height also from local soundings. Radars in different regions are grouped by colour. The PDF does not include CTH > 16 km (see Table 5.3).

for the composite of all sites), suggesting low cell tops are associated with heavier rainfall here. As discussed previously, this is a direct impact of the surrounding orography, which causes rapid collision-coalescence of raindrops in shallow convection. Although our Mumbai analysis is weighted towards May and June, these results are consistent with recent findings using both TRMM (Shige and Kummerow, 2016; Kumar and Bhat, 2017), and ground-based weather radars (Utsav et al., 2019). The ability for shallow convection (with warmer cloud tops) to produce high rainfall rates in this region has implications for conventional satellite rainfall algorithms which relate precipitation to cloud top brightness temperature (Shige and Kummerow, 2016). Studying Figure 5.3h, the shallowest cells are associated with very low reflectivity and have a broad reflectivity distribution, with large variance in the intensity of these shallow cells, as indicated by the 5–95 percentile range. For shallow cells, the variance of the composite is 35 dBZ as opposed to 7 dBZ for deep cells. As CTH increases there is initially a rapid rise in reflectivity until approximately 30 dBZ. At this point, CTH is on average

5–7 km, in the region of the freezing level (dashed blue line) and the modal CTH over the season. This is also the approximate region of maximum atmospheric stability (as shown by the minima in the vertical profiles of θ_e in Figure 5.2c), and is associated with a narrowing of the reflectivity distribution (scanning horizontally between the black dotted lines in Figure 5.3). The stable layer near the freezing level forms physically as a result of latent heat release due to precipitation freezing and melting processes (Posselt et al., 2008). Above this level, there is a smaller increase in reflectivity with CTH. Furthermore, around 12 km the temperature lapse rates (not shown) increase to quasi-dry adiabatic with remarkable consistency between all sites hinting at the regulatory and homogeneous influence of the large-scale monsoon pattern upon different regions in India. Around 10 km there is a small atmospheric layer of constant reflectivity with increased CTH for some of the sites (e.g., Bhopal, Lucknow, Mumbai). This is likely because clouds that penetrate to this level encounter considerable atmospheric instability associated with steep temperature lapse rates and shear-driven instability from the TEJ. Therefore, these cells can grow deeper without any significant increase in intensity.

Therefore, the convective modes identified from Figure 5.2a show distinct characteristics in terms of intensity and can be related to atmospheric stability. The first mode is shallow convection (CTH < 5 km), associated with highly variable, but on average low 2 km reflectivity (rapidly increasing with each 0.5 km CTH bin). The second mode represents cumulus congestus clouds (5–8 km). These cells are bounded by the maximum in atmospheric stability above the freezing level and so the 2 km average reflectivity values remain less than 35 dBZ. This is also visible as the modal peak in cells around this region for all sites (Figure 5.2a). The third mode (deep convection) penetrates above the region of stability associated with the freezing level ($\geq$ 8 km), and exhibits the most vigorous convection with average 2 km reflectivity values of approximately 35 dBZ. When referring to shallow, congestus, and deep convection throughout this study, we refer to these CTHs. These modes were also found by Kumar et al. (2013a) for Darwin in Austral summer (in addition to an overshooting top mode which we are unable to investigate here due to 3-D grid restrictions). However, our results in contrast show more of a continuous increase in mean 2 km reflectivity as CTH increases above the freezing level. This may stem from the spreading of cloud tops by the TEJ above

8 km, except for the largest and most intense cells. To summarise, for all sites, the statically stable layer around the freezing level (Figure 5.2c) acts as a constraining factor upon CTH, and this manifests itself as a reduction in the gradient of 2 km reflectivity around this level (Figure 5.3h). When discussing the cell patterns over the diurnal cycle in Section 5.5, we will consider the mean diurnal cycle of these separate convective modes as well.

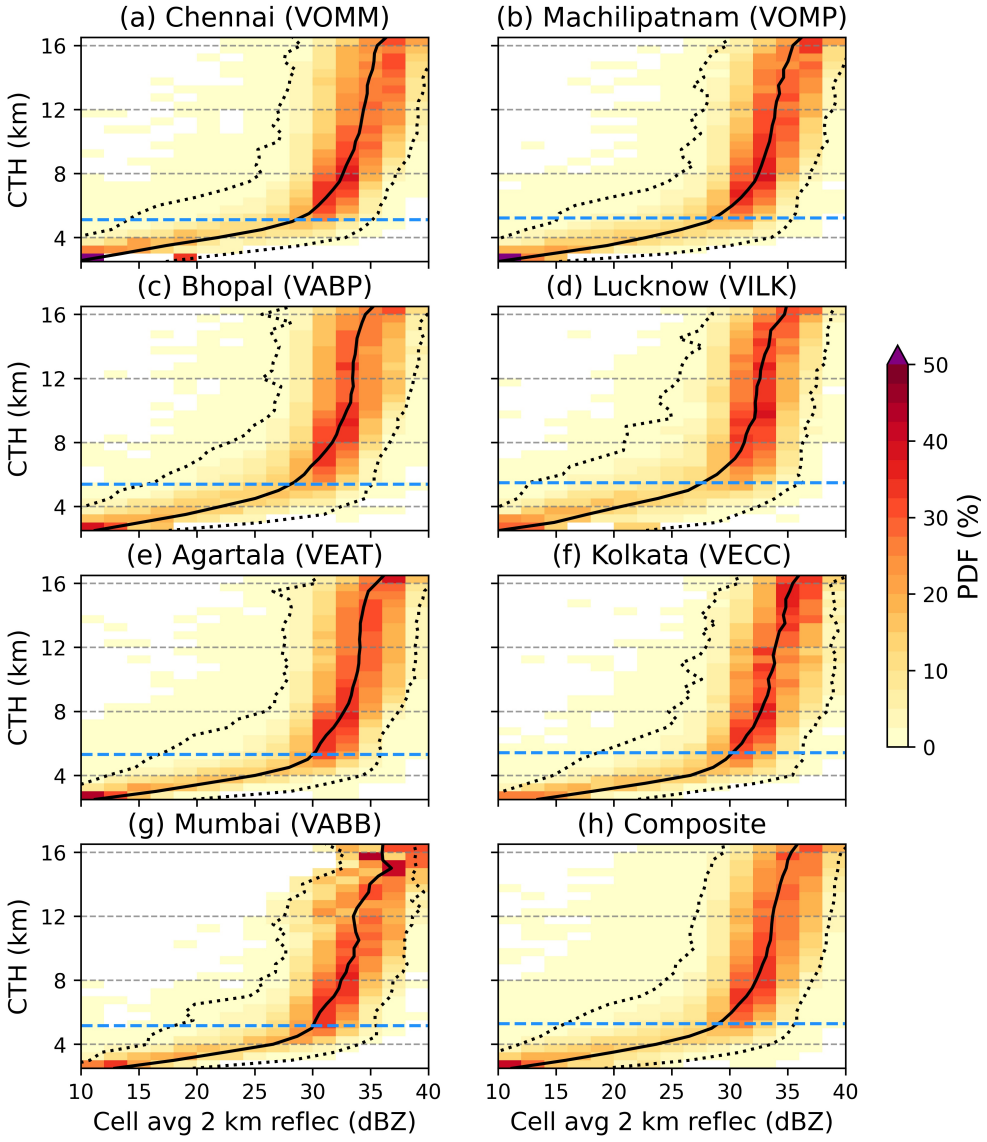

Figure 5.3: PDF of 2 km cell average reflectivity using a bin size of 2 dB and as a function of CTH (not including CTH > 16 km). (a) Chennai, (b) Machilipatnam, (c) Bhopal, (d) Lucknow, (e) Agartala, (f) Kolkata, (g) Mumbai, and (h) a composite of all sites. The black solid line is the mean reflectivity at each CTH, with dotted lines denoting the 5th and 95th percentiles. The dashed horizontal blue line is the height of the average freezing level from local radiosonde profiles.

5.4 Cell patterns over active and break periods

Active and break spells are the foremost manifestation of systematic intraseasonal variability during the ISM. These oscillations occur in most of the elements of the monsoon system, and are highly pronounced in monsoon cloudiness (Krishnamurti and Bhalme, 1976). Here, we analyse how the active and break spells in 2016 (Table 5.2) affect the height of convective cells in each region. Figure 5.4 displays the distributions of CTH for active and break periods at each site, alongside vertical profiles of horizontal wind and θ_e from soundings. Bhopal, Lucknow and Mumbai form part of the central India gridbox that is used here to monitor anomalous rainfall and active and break spells. As a result, we expect to see more frequent deep convection in active periods at these sites. Mumbai and Bhopal exhibit this most discernibly in both the mode and 90th percentile of the CTH distributions. This pattern of deeper convection is associated with a clear increase in θ_e for Mumbai and Bhopal, most starkly in the region of the freezing level, but indeed through a large part of the troposphere. Interestingly, Lucknow shows little difference between active and break CTH distributions, despite also displaying a clear increase in instability below 6 km. Potential causes for the similar distributions will be explored later in this section. The changes in the wind profiles for these locations between active and break periods are subtle at higher altitudes where the TEJ dominates. However, the winds nearer the surface are slightly stronger in magnitude for Bhopal and Mumbai, with different directional components suggesting the importance of lower tropospheric moisture advection for cumulus growth.

There is also little change between the CTH distributions of Agartala and Kolkata in north-eastern India (Figure 5.4e–f). Chennai and Machilipatnam also show no substantial change between active and break spells in the modal CTH. These four locations exhibit slight increases in instability in the freezing level region, but with small differences elsewhere, which suggests the importance of instability at upper levels as well as the freezing level for deep convective development. However, Chennai does exhibit a signal in active spells having more frequent deep convection, shown by the disparity in the 90th percentiles. For CTH < 8 km, the distributions are very similar however. The split in the distributions above

this level appears to be caused by an increase in the fraction of very deep cells (CTH ≥ 12 km) during active periods. It is important to recall that only convective cells are considered here. For example, Rao et al. (2016) found a higher occurrence and fraction of stratiform rain in active spells, due to the prevalence of large, organised storms such as mesoscale convective systems. This suggests that rainfall will not only be more intense but more long-lived, consistent with the typical longer lifetimes of stratiform rains (Steiner et al., 1995).

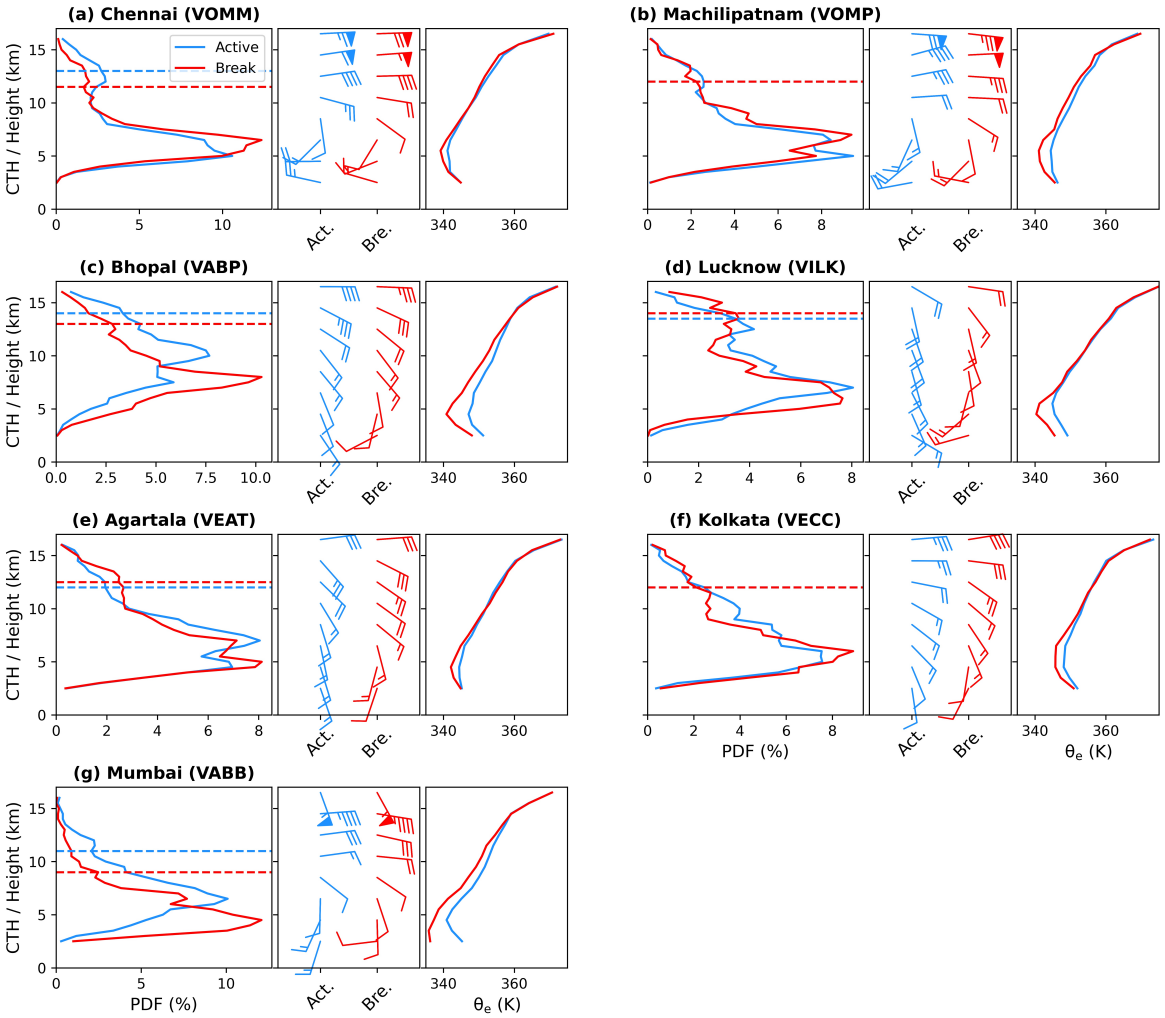

Figure 5.4: Same as Figure 5.2 but the CTH distributions, wind barbs, and θ_e profiles are shown separately for each site, where the blue lines/barbs are for all active days and red for all break days, as given in Table 5.2. The horizontal dashed blue and red lines show the 90th percentile in the distribution of CTH for active and break periods respectively.

Table 5.4 shows the numbers and proportions of cells in the different cumulus mode categories as defined in Section 5.3 for active and break periods in 2016: shallow convection, cumulus congestus, and deep convection. Between active and break periods, similar propor-

tions of cells in different modes are seen in Machilipatnam, Lucknow, Agartala, and Kolkata (consistent with Figure 5.4). An increase in the number of cells per radar volume from break to active periods occurs for all sites but Lucknow and Kolkata, where there is no or minimal change in this statistic. The increase in convection during active periods is most noticeable in Mumbai. Due to periods of unavailability in the data, Mumbai has 135 radar volumes during active periods mostly during 28–30 June, and partly 2–4 August and the September active spell dates. During break periods, there are 715 radar volumes mostly during the June break spell dates and partly 3–12 September. For break spells represented by the Mumbai radar, there is a large reduction in the proportion of shallow convection, and a 21% increase in the proportion of deep convection. In Bhopal, deeper convection is also more likely in active spells, with a reduction in the proportion of the congestus mode. Chennai sees a reduction in the likelihood of the cumulus congestus mode during active periods, and a higher likelihood of shallow and deep cells, though the total amount of convection per radar volume is only marginally higher.

Table 5.4: For each site, the number of cells in each cumulus mode category for 2016 active and break periods and the average number of cells per radar volume. The numbers in parentheses show the percentage of cells in that cumulus mode. Shallow mode (CTH < 5 km); congestus mode (5 ≤ CTH < 8 km); deep mode (CTH ≥ 8 km).

Site	Active/Break	Shallow	Congestus	Deep	Cells per Volume
Chennai (VOMM)	Break	806 (9)	5268 (61)	2615 (30)	2.1
	Active	1238 (13)	4754 (50)	3604 (38)	2.3
Machilipatnam (VOMP)	B	836 (13)	3045 (47)	2533 (39)	1.5
	A	2521 (16)	7451 (47)	5949 (37)	3.6
Bhopal (VABP)	B	477 (5)	3068 (35)	5151 (59)	2.2
	A	288 (2)	2374 (20)	9320 (78)	5.6
Lucknow (VILK)	B	241 (5)	1729 (39)	2433 (55)	2.4
	A	421 (8)	1768 (35)	2920 (57)	2.4
Agartala (VEAT)	B	4119 (18)	9005 (40)	9302 (41)	6.4
	A	3520 (18)	8260 (41)	8234 (41)	7.0
Kolkata (VECC)	B	1675 (20)	3609 (43)	3119 (37)	3.0
	A	1436 (17)	3248 (39)	3546 (43)	2.8
Mumbai (VABB)	B	708 (40)	802 (45)	276 (15)	2.5
	A	294 (15)	1000 (49)	731 (36)	15.0

We further analyse these statistical patterns in the context of the large-scale circulation so as to understand what dynamic component of active and break spells drives convective variability in different locations. Anomalies in IMERG rainfall, ERA5 winds, and relative humidity between 2016 active and break periods are shown in Figure 5.5, along with contours of average mean sea-level pressure (MSLP). The rainfall anomalies (Figure 5.5a–b) provide the closest relationship to CTH, with a narrow band of increased rainfall down the Western Ghats region and a larger swathe over central and northern India during the active spells. The effect of convective enhancement over the Western Ghats means this positive rainfall anomaly remains confined to the coastal region south of 18°N, despite anomalously strong westerly winds and high relative humidity extending further east (Figure 5.5c–d). This explains the lack of a definitive change in the distribution of CTH between active and break periods over south-eastern India (Figure 5.4). It is difficult to explain what may be causing the increase in deep convection in Chennai during active periods in 2016, and indeed how robust this feature is. At 26.8°N, Lucknow falls just north of the region of increased rainfall during active spells. Over central India there are relatively much stronger westerlies during active periods. These winds then start to curve back towards the north-west over the Bay of Bengal, and so Lucknow experiences south-easterly winds in the lower troposphere, as it is positioned north of the monsoon trough. This results in less rainfall than the region of potent westerlies further south. In the transition to break periods the monsoon trough moves northwards to the foot of the Himalayas (shown by the northward push in the MSLP pattern from Figure 5.5e to 5.5f.), bringing lower tropospheric westerlies further north to Lucknow. However, the background state is drier overall (Figure 5.5d), thus Lucknow exhibits no significant change in rainfall and the distribution of CTH. In north-eastern India, it is an even more complex picture, with small pockets of positive and negative rainfall anomalies in the region during 2016. To the east of Agartala (91.25°E) along the Bay of Bengal coast, there is a more definitive area of increased rainfall and higher relative humidity during break periods, associated with enhanced southerly winds from the Bay of Bengal. The lack of a clear active-break driven signal over north-eastern India is likely responsible for the similar percentages of different cumulus modes in this region between active and break periods (Table 5.4).

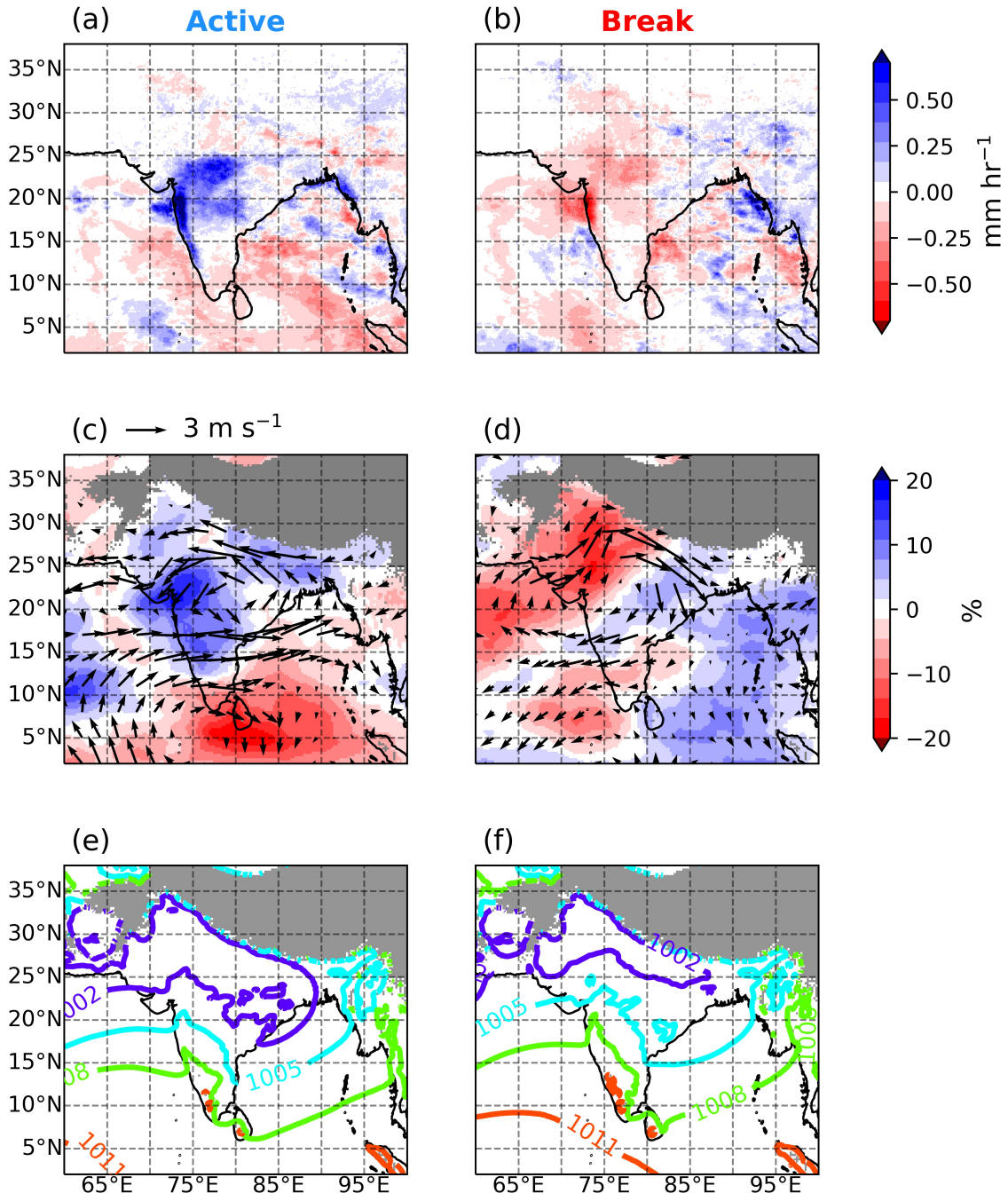

Figure 5.5: Large-scale patterns for the 32 active and 32 break days in 2016. (a–b) IMERG rainfall anomalies, relative to the entire season (c–d) 850 hPa relative humidity (colours) and wind vector anomalies, (e–f) contours of average mean sea-level pressure in units of hPa. Grey shaded regions in the centre and right columns are areas of topography over 1.5 km.

5.5 Cell patterns over the diurnal cycle

The diurnal cycle is intrinsic to convection, as well as the local meteorology and land surface features of the region, and so its monsoonal behaviour is important to understand. With time

continuous radar observations of 10-minute resolution, the diurnal cycle of convection is fully captured by the radar observations. Furthermore, Chennai, Machilipatnam and Mumbai radar domains include both coastal land and ocean areas (Figure 5.1), allowing an analysis of the diurnal cycle over these different surface types. Finally, we will then investigate how the diurnal cycle is modulated by the progression of the monsoon through the season, and the active and break periods discussed in Section 5.4.

5.5.1 Diurnal cycle cell statistics

The diurnal cycle of convective cells at every CTH bin is shown in Figure 5.6 with individual convective modes shown in Figure 5.7. Broadly speaking, observing the number of cells (at all CTH) through the day, we see distinct differences between the four different regions (and similarities within regions). Chennai and Machilipatnam display an overall night-time peak in the number of cells. Machilipatnam appears to show two peaks, one in the afternoon and a more prolonged peak overnight. We will see later how respective land and ocean convection contributes to this. IMERG rainfall (shown by the blue line in Figure 5.6 as a fraction of the daily total) exhibits a clear relationship with diurnal convective fraction, but most strongly with the more heavily precipitating deep convection. Assuming that convection dominates rainfall, we expect rainfall to be correlated with convective area (which is in itself correlated with the number of cells). More precisely, the rainfall appears to peak alongside the maximum in the number of deep cells (CTH $\geq$ 8 km, see Figure 5.7). As discussed in Section 5.3, deep convective cells are associated with higher 2 km reflectivity (and thus higher precipitation rates).

The effect of solar heating is clearly a larger source of influence for the inland sites Bhopal and Lucknow, with a convective peak in the afternoon and evening associated with maximum surface heating. Noticeably, IMERG rainfall is more constant through the day in comparison, although both sites exhibit an increase in rainfall into the evening a few hours after the peak in the number of cells, but well correlated with the peak in the fraction of deep convection (Figure 5.7c). Initially, there are a greater number of shallow and congestus cells associated

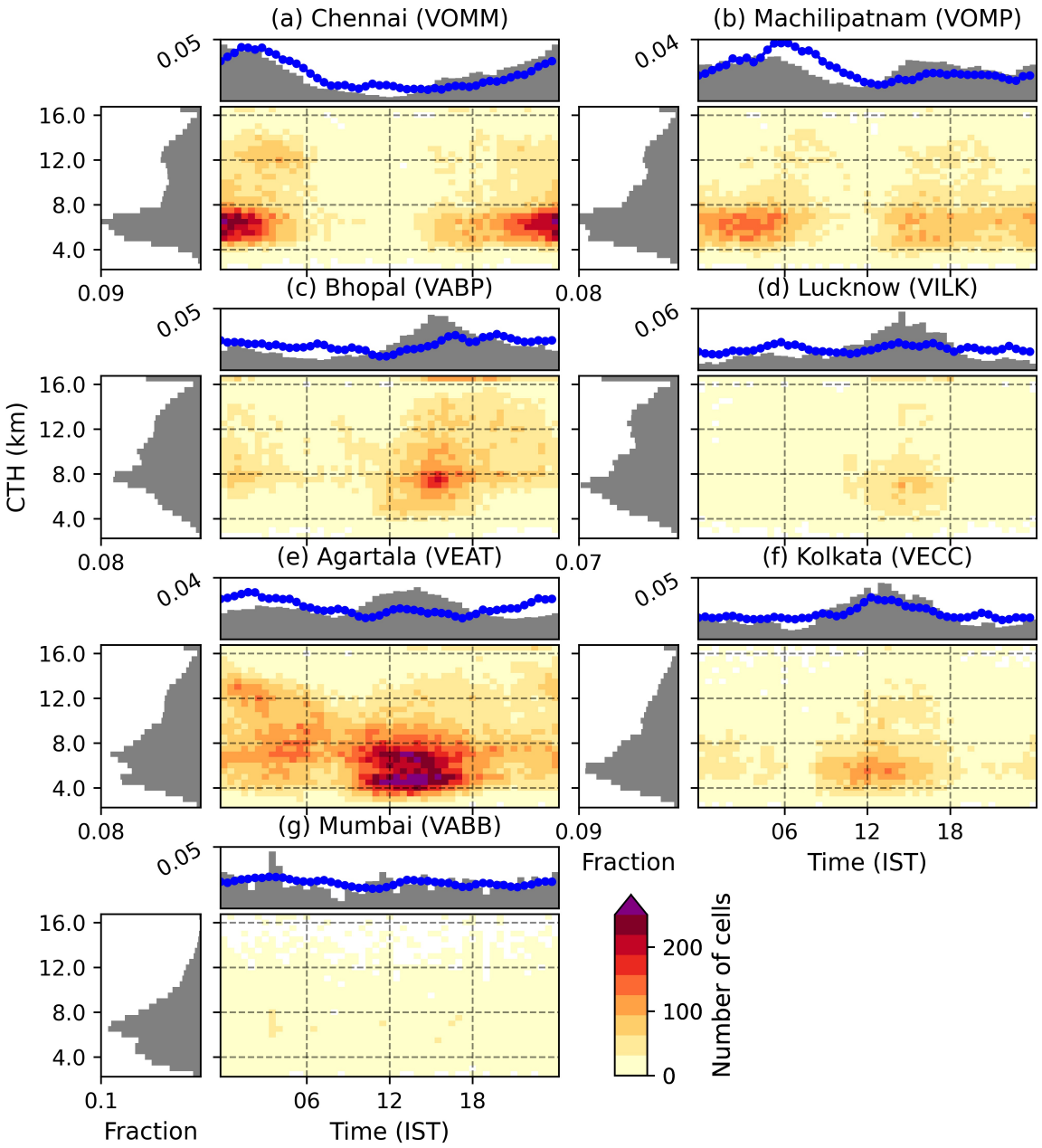

Figure 5.6: Number of cells as a function of the diurnal cycle (30-minute bins) and CTH, with histograms representing the probability density of cell occurrence across each axis for (a) Chennai (VOMM), (b) Machilipatnam (VOMP), (c) Bhopal (VABP), (d) Lucknow (VILK), (e) Agartala (VEAT), (f) Kolkata (VECC), and (g) Mumbai (VABB). Includes CTH > 16 km. IST = Indian Standard Time (UTC+5.30). Pixels with 0 cells are masked white. The blue dotted line is the normalised diurnal cycle in IMERG precipitation as a mean over each IMERG gridbox whose centroid lies in the 40–100 km radar domain.

with the afternoon peak in cell fraction. Some of these cells dissipate, and others grow and merge, meaning that as the number of cells decreases in the evening, the number of deep cells and the total area covered by convection nonetheless continues to increase for a few hours.

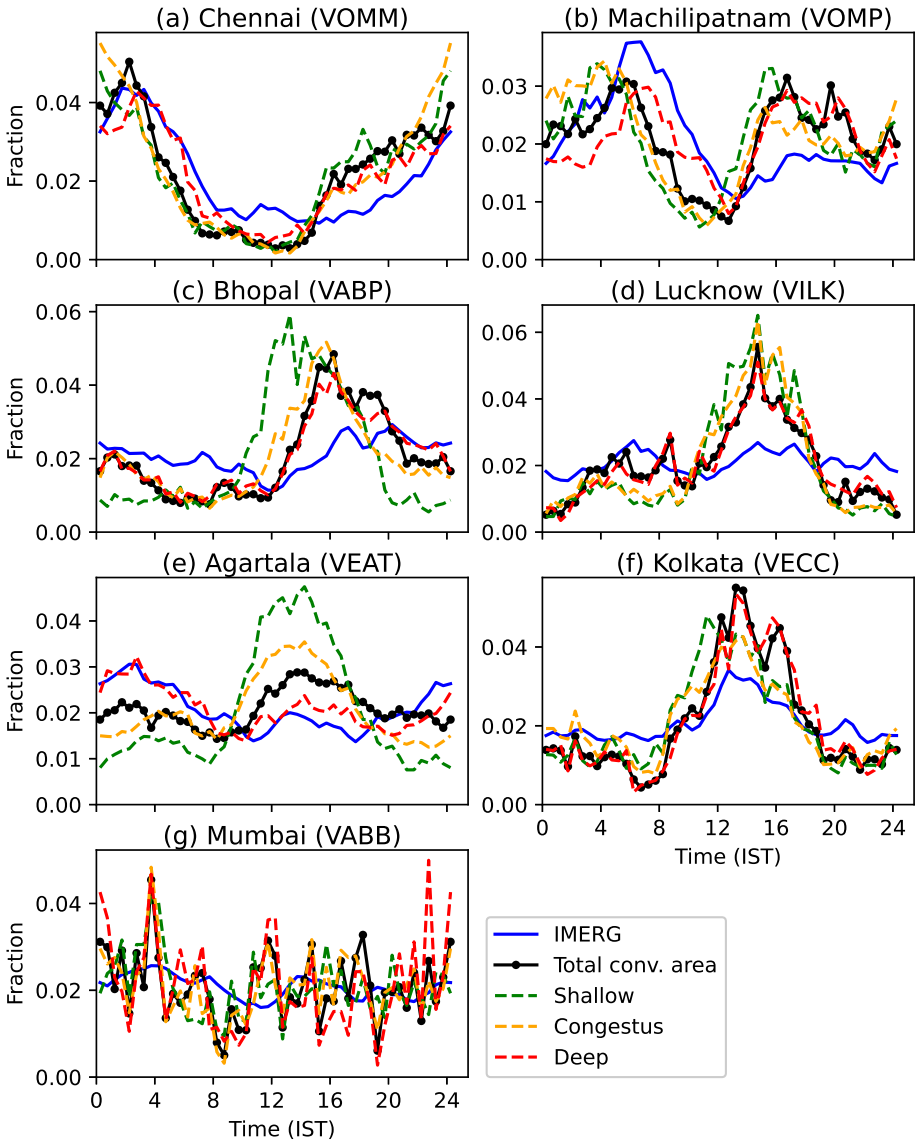

Figure 5.7: As Figure 5.6, but showing the normalised fraction of cells in different cumulus mode categories: shallow (CTH < 5 km); congestus (5 ≤ CTH < 8 km); deep (CTH ≥ 8 km). The black line is the total convective area normalised over the diurnal cycle, and IMERG rainfall is as in Figure 5.6.

North-eastern India sees its peak in total cell number around noon and early afternoon, however, Agartala especially is prone to convection at all times of day. This explains the much larger number of cells per radar volume shown in Table 5.3, with no real convectively inactive time of day. Consistently high low-level moisture from the Bay of Bengal likely contributes to this. Interestingly, the peak in Agartala rainfall actually occurs at night, the opposite time of day to the peak in cell number. Figure 5.6e and Figure 5.7e show a higher likelihood of deeper cells at night, whereas the daytime cells, whilst higher in number, are

typically shallower. This appears to be a fairly localised effect however, as it is not seen further south and west in Kolkata, which instead shows one clear peak centred at 2pm along with the peak in rainfall. Figure 5.7 shows that cells in north-eastern India (and also Chennai) appear to deepen more quickly than those over northern India and Machilipatnam, meaning rainfall peaks more closely alongside the peak in the number of cells. Mumbai shows no diurnal cycle in cell number or rainfall, bar the slight suggestion of a night-time and an afternoon peak. Although the Mumbai analysis is dominated by May and June, the study of Romatschke and Houze (2011) supports this result. They noted using Tropical Rainfall Measurement Mission data that over the western Indian coast, small and medium sized systems are present throughout the day, as the prevailing south-westerly moisture laden flow is lifted over orography. The prevalence of shallow convection here also moderates the daytime temperatures relative to northern India, meaning there is less of a surface heating contribution upon convective initiation.

5.5.2 Diurnal cycle over land and ocean

We look in more detail at Chennai, Machilipatnam and Mumbai by considering cells over land and ocean separately. These sites have the advantage of having nearly 50% of their domains over ocean, and 50% over land. For simplicity here, cells are judged to be land or ocean cells based off their centroids; 2–4% of (generally larger) storms straddle the coast. Firstly considering Chennai and Machilipatnam, Figures 5.8a–b show clearly that there is higher rainfall and a greater cell number at night and in the early morning over the ocean compared to land. This is also a consistent pattern for all three cumulus modes shown in Figure 5.9. Either cells are simply forming later into the night on average offshore, or there is advection of cells from onshore to offshore as the evening progresses. If we consider that the 1–6 km vertical wind shear in south-eastern India is typically quasi-westerly through the day, it largely supports the advection hypothesis. That is to say, cells that form over land in the evening move with the quasi-westerly offshore wind shear. This theory is further supported by the similar shapes and amplitudes of the cycles between land and ocean. This suggests the

spreading of the cloud tops over the ocean from coastal regions in the evening. This was also found for the Bay of Bengal by Yang and Slingo (2001). They suggested gravity waves and complex land-sea breeze effects as drivers of this process. On further study of Figure 5.8, there is a clear second peak in the height of cells (at about 13 km) over ocean, but not over land. The fact that deeper cells are more likely over ocean does not contradict the advection hypothesis. As cells move offshore in the night and early morning, they mature and thus grow in vertical extent. However, there are also plenty of shallower cells over the ocean, suggesting that convection also initiates over the ocean itself. Over land, both sites exhibit an initial afternoon peak in IMERG rainfall, followed by a slight dip, then a second night-time peak. Machilipatnam also displays this feature in the fraction of cells. This suggests in the average situation that cells continue to initiate over land for a period of time, with a slight lull around 9pm after the initial round of afternoon convection. After midnight, convection is hindered over land following large amounts of convection in the preceding hours, and so the diurnal cycle spreads out into the ocean (Yang and Slingo, 2001).

For Mumbai, the most discernible change in the diurnal cycle is that the afternoon peak in the fraction of land cells and rainfall is not seen over ocean, which instead has a peak at night or early morning, similar to south-eastern India. This suggests that land surface heating over Mumbai, whilst smaller than the other locations, still has a significant contribution to convection. We note, however, that our Mumbai analysis is biased towards the months of May and June with a small number of active period samples. However, the robustness of the interpretation of these results benefits from a similar number of radar volumes over the diurnal cycle (not shown). Also similarly to south-eastern India, Mumbai has a slightly higher fraction of deep cells over ocean compared to land, although this is not significant enough for a clear second peak in the CTH histogram. This may partly occur due to a smaller amount of collision-coalescence of raindrops over ocean away from the Western Ghat mountains, giving clouds a chance to grow more in vertical extent before precipitating out.

In Figure 5.9, the afternoon peak in convection over land for Chennai and Machilipatnam exhibits a clear time lag between shallow and deep storms. The morning peak over ocean for both these sites also shows that deep cells peak later into the night (and continue to

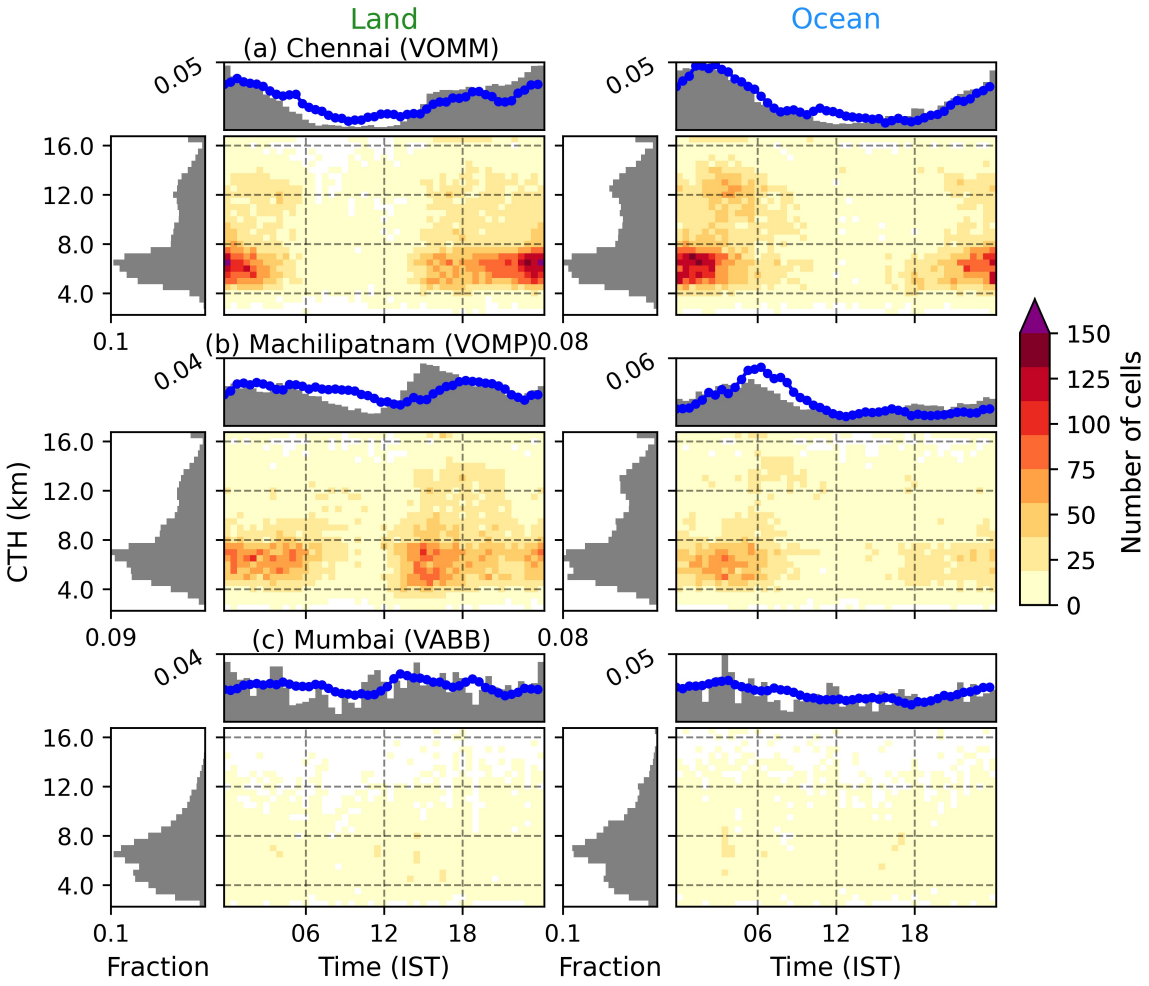

Figure 5.8: Same as Figure 5.6 but with separate plots for cells with their respective centroids over land and ocean. (a) Chennai, (b) Machilipatnam, (c) Mumbai. A land-ocean mask is also applied to IMERG rainfall.

be prevalent longer into the morning), although the transition from shallow to congestus is perhaps not as clear as over land. The diurnal fraction of the different cumulus modes over Mumbai is too noisy for useful interpretation here. Once more, precipitation is clearly most associated with the fraction of deep cells and total convective area over both land and ocean.

5.5.3 Diurnal cycle during monsoon progression

The diurnal cycle can vary over longer time scales, such as the progression of the monsoon itself. The normalised diurnal cycle in cell number is shown for each month individually (May–September) in Figure 5.10. Firstly, for all sites, the diurnal cycle is often least pro-

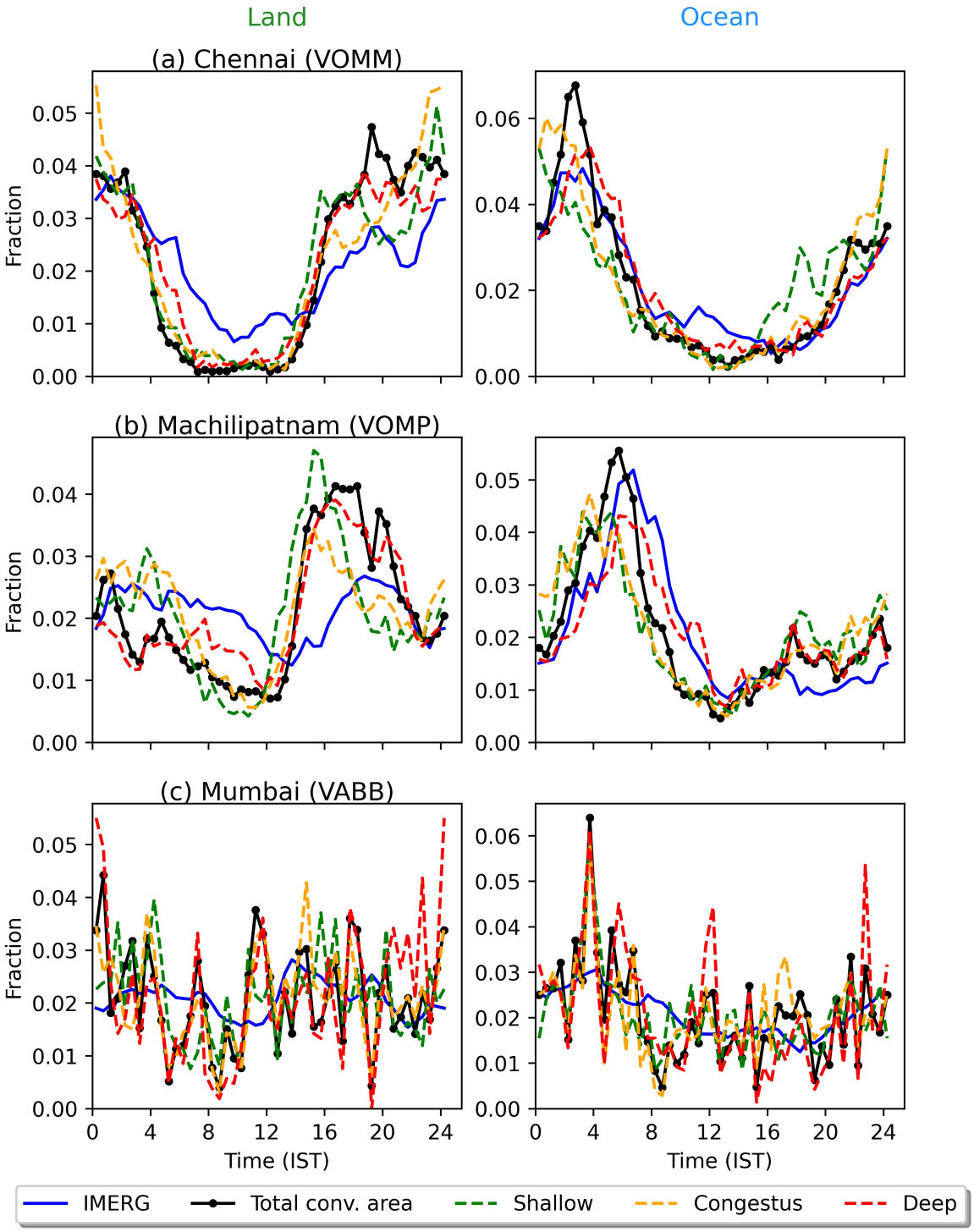

Figure 5.9: The diurnal cycle in the fraction of cells in different cumulus mode categories: shallow, congestus and deep, split into land and ocean segments for (a) Chennai, (b) Machilipatnam and (c) Mumbai. The black line is the total convective area normalised over the diurnal cycle, and IMERG rainfall is as in Figure 5.8.

nounced in May, as the monsoon regime is not yet established. Chennai shows a distinct night-time peak in the fraction of cells from June onwards. However, June also has the

highest likelihood of convection in the hours around midday, with very few cells around this time later in the season. The length of this daytime period of relative inactivity extends into September, by which point convection is rare between 8am and 2pm local time. As with Figure 5.6, Machilipatnam's diurnal cycle is more complex, exhibiting multiple peaks from June, most definitively one centred around 4am associated with ocean convection, and one around 4pm for land convection. However, a third peak around midnight seems to occur in June and September, although this is not very distinct in IMERG rainfall. The minimum occurs around noon from July through September, and in fact these latter three months match considerably. This suggests the progression of the monsoon at this stage has less effect on the diurnal cycle of south-eastern India.

Bhopal shows most clearly the arrival and retreat of the monsoon. In Bhopal and Lucknow the monsoon arrived on approximately 20 June (Ramesh, 2017). This is associated with a more pronounced diurnal cycle in May and June with a peak in the fraction of convection around 4pm and extending into the evening and night. However, during peak monsoon months (July and August), convection can occur any time of day, demonstrated by a shallower peak in the afternoon, and in fact the diurnal cycle in IMERG rainfall becomes hard to visually decipher. This suggests a moister background environment more conducive for convection and less reliance upon daytime surface heating. Into September, as the monsoon gradually retreats south again, convection is once again constrained into the afternoon hours, especially for Bhopal. The development of convection from shallow to deep before precipitating out is most pronounced in September (not shown). Bhopal shows this effect most clearly, possibly as a result of its inland location as well as the tropospheric drying associated with monsoon withdrawal, resulting in a necessary period of shallow and congestus convection to moisten the environment in advance of any deep convection. Bhopal convection also seems to dissipate more quickly into the evening compared to June. This suggests a greater reliance upon surface heating for the initiation of convection. A longer convectively inactive period is visible from approximately 4am to 11am for Bhopal in September. Lucknow displays comparatively more morning convection in September compared to Bhopal, with a minimum around midnight.

Agartala shows a night-time and a day-time peak in convective fraction from June to

August, with relative minima in between. We recall that the night-time peak in IMERG rainfall was found to stem from a higher proportion of deeper cells at night, with a tendency for cells during the day to be shallow and cumulus congestus type modes. The proportion of deep cells at night reduces into September, with all three convective modes then seeing their peak in the early afternoon (not shown). Kolkata has a peak in convective fraction centred around 2pm for all months from June, but with convective cells and rainfall evident at all times of day, especially during June and July.

5.5.4 Diurnal cycle during active and break periods

It is also of interest to consider whether active and break spells may modulate the diurnal cycles shown earlier in this section, in terms of phase and/or amplitude. Figure 5.11 displays the phase of the diurnal cycles as in Figure 5.6, but now subsampled over the active and break days in Table 5.2. Chennai shows no clear change in the amplitude or phase of its diurnal cycle between active and break periods. Further up the coast in Machilipatnam however, there are clearly more inactive periods of convection during a break spell than an active spell, such as during late morning. In an active spell, convection can occur all times of day (although still preferentially during the afternoon and night-time). Figure 5.12 shows the cycles in Figure 5.11 for each individual cumulus mode. During active periods, deep cells are most common from 3pm all the way through until around 7am as a single peak (Figure 5.12b). However, during break periods, these deep cells have a shallow peak at 4pm, followed by an evening lull, then a second, larger peak around midnight. Machilipatnam is systematically affected by active and break spells in this way, despite such a signal not being evident in the overall distribution of CTH in Figure 5.4. This suggests that cells in Machilipatnam that do occur are not on average less intense or deep during break periods, but are more dependent on the time of the day and thus less frequent, as shown in Table 5.4.

Turning our attention to northern India (Figure 5.11c–d), active periods display a higher fraction of convection during the night-time hours in Bhopal compared to break periods. Indeed, the diurnal maximum in the congestus mode during active periods is at night, whereas

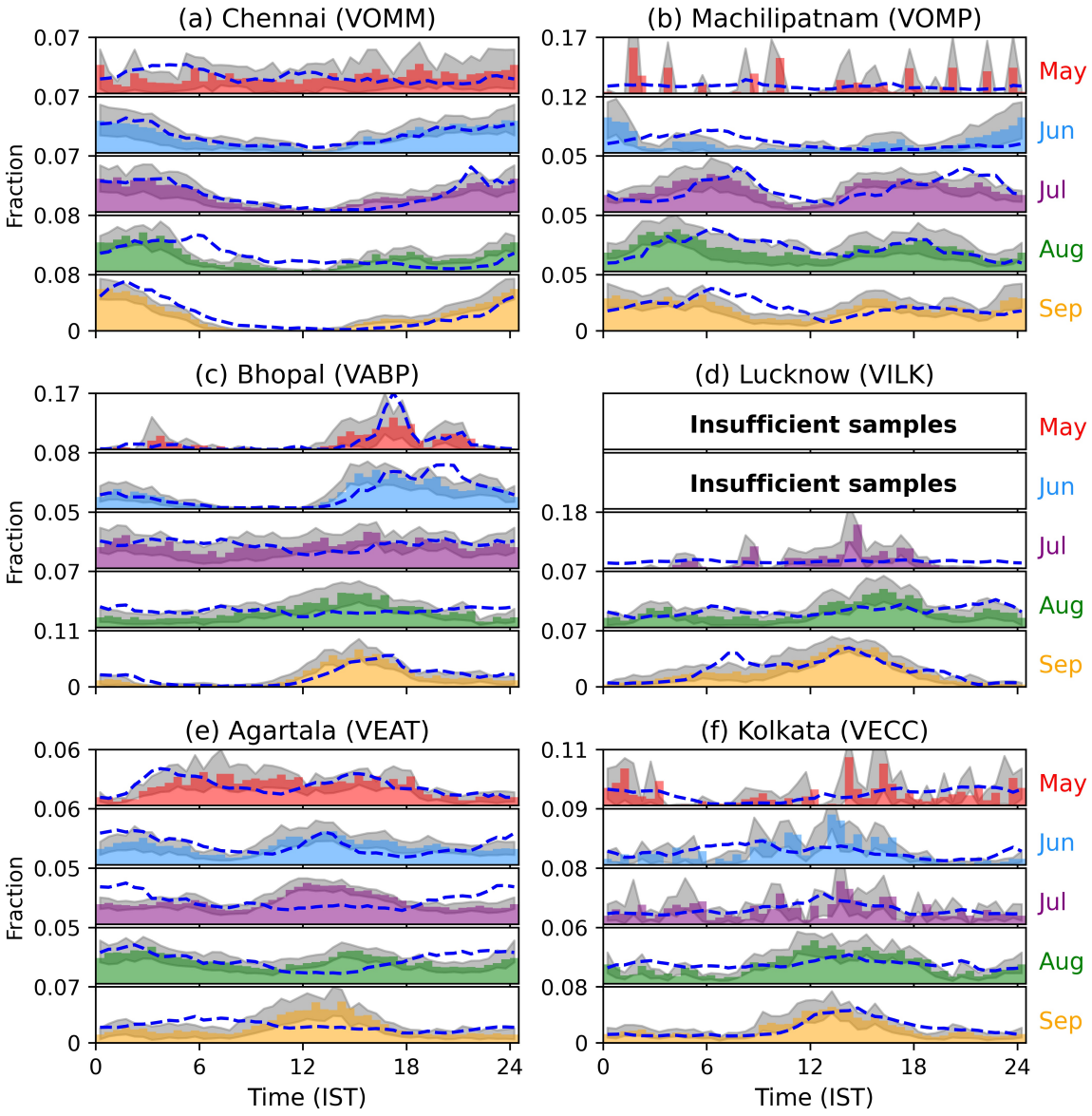

Figure 5.10: Diurnal cycle probability density histograms showing the number of convective cells subset by month for the same sites as in Figure 5.6, including CTH > 16 km. However, Mumbai is not shown here due to long periods of unavailable data, especially during July and August. The shaded region represents the variance in the sample as the bootstrap 10th and 90th percentiles. The equivalent average IMERG rainfall diurnal cycle for each month is shown by the blue dashed line. There must be at least 500 cells during the month or the diurnal cycle is not shown.

the peak in the deep mode is in the afternoon (Figure 5.12c). For Lucknow, break periods are associated with a higher fraction of cells in late evening and early morning, but active periods display a significantly higher fraction of late morning and afternoon convection. For both sites, there is a suggestion that the peak in normalised convection is slightly earlier in

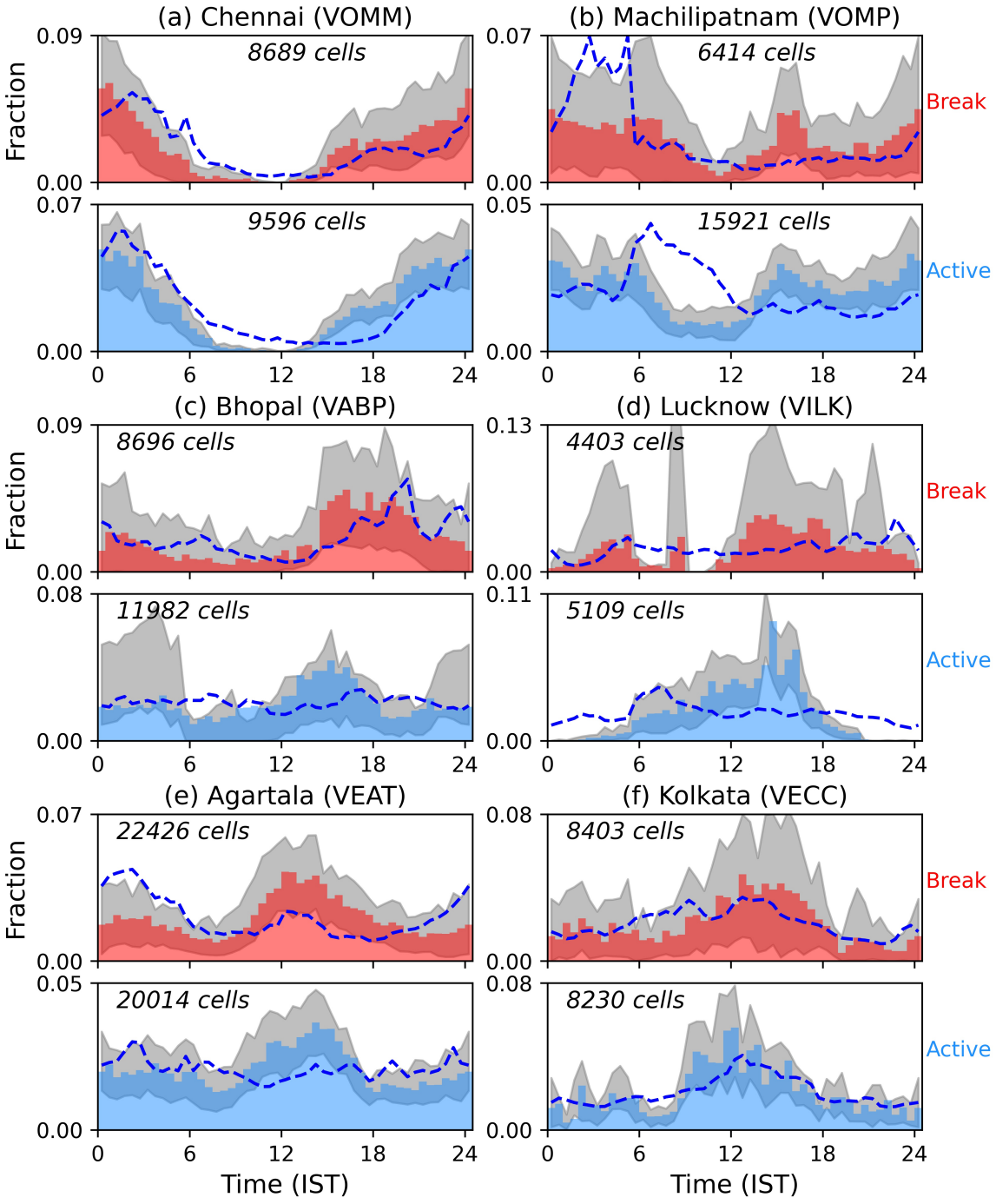

Figure 5.11: Same format as Figure 5.10 but shown for break (red) and active (blue) periods. Mumbai is again not shown owing to a lack of radar volumes during the active and break spells during July and August. The total number of cells at a site over respective break and active spells is labelled to give the reader an idea of sample size. The right-most column in Table 5.4 shows the number of cells per radar volume to give a measure of average activity.

the afternoon for active periods, with more of an evening peak for break periods. This likely occurs as a result of the active spell environment being more conducive for convection, such that convection initiates, deepens and intensifies more quickly in the afternoon. This effect is also supported by the IMERG rainfall for Bhopal, although it is less clear for Lucknow.

Lastly observing the respective diurnal cycles for north-eastern India, it is evident that convection can occur at all times of day during both active and break periods. For Agartala, there is a more distinct peak in cell fraction in the early afternoon during break periods, with less of a diurnal cycle in active periods, and an almost constant proportion of IMERG rainfall through the day. Figures 5.11c–e show large (weak) diurnal cycle amplitudes during break (active) periods. The lower relative humidity in these regions during break periods (Figure 5.5d) likely acts to constrain convection into the afternoon and evening hours, similarly to the September diurnal cycle in these regions. In contrast, during break periods, rainfall exhibits two peaks, one in the afternoon and a more significant one at night. For Kolkata, there is less of a visual difference on first inspection, however convection appears quicker to initiate around midday during active spells, and this peak is more well defined than the afternoon peak during break periods. The results in this section express the need for models to capture the interactions between large-scale regime changes (e.g., active/break periods, monsoon progression) and the local environment in different regions. In particular, the development of convection within the diurnal cycle is sensitive to background moisture associated with wind pattern changes in the lower troposphere, which models must resolve accurately to represent the diurnal cycle of convection. Field campaigns that prioritise high-resolution atmospheric observations, alongside longer periods of radar data availability, would in future allow the study of the diurnal cycle with relation to large-scale atmospheric conditions in more detail.

5.6 Conclusions

An understanding of ISM cloud development on large spatiotemporal scales is an important aspect of monsoon forecasting. This study has used 2016 monsoon season data from 7 IMD Doppler radars in order to analyse CTH in relation to near-surface reflectivity, with a focus

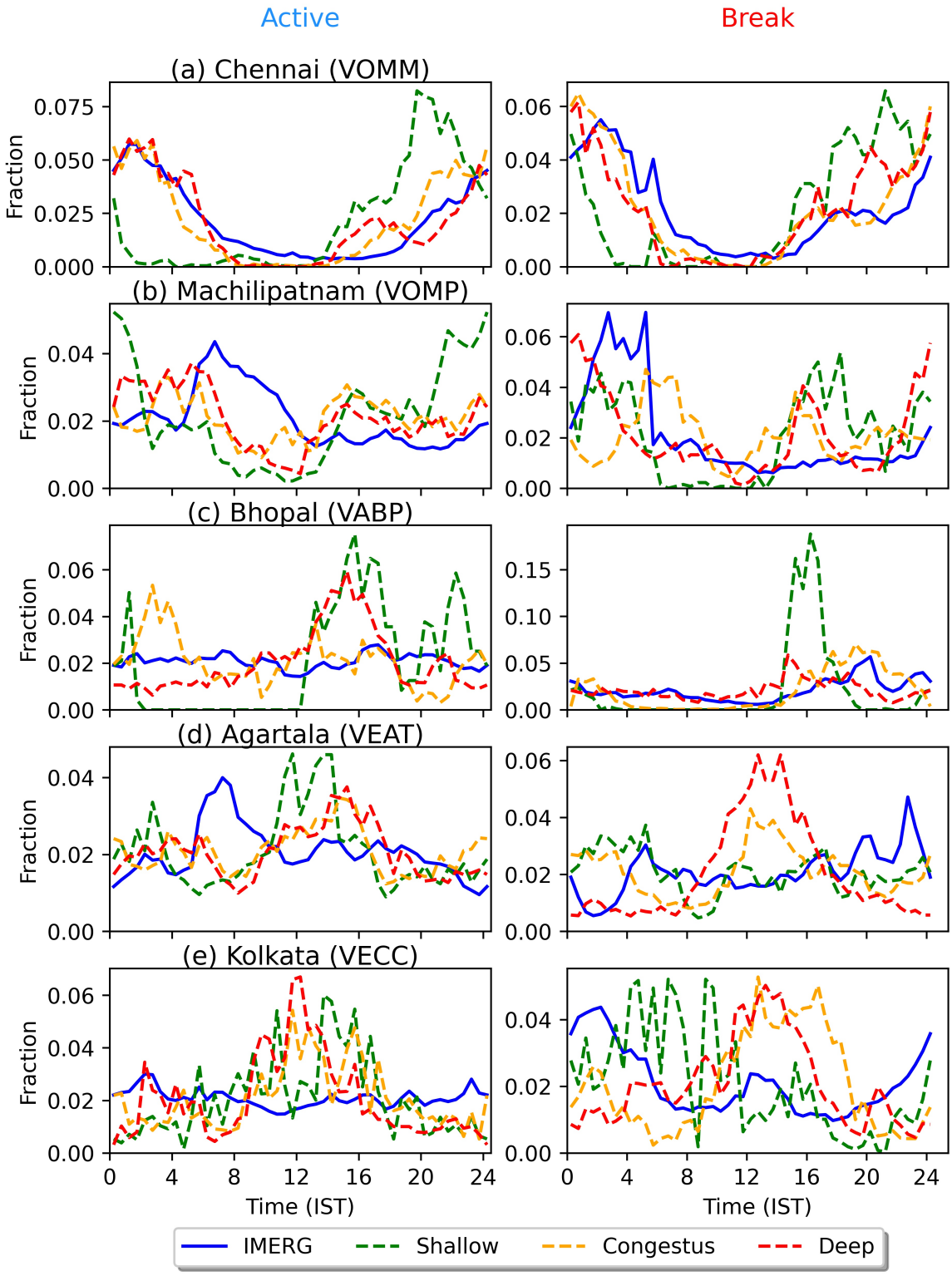

Figure 5.12: The diurnal cycle of different cumulus modes as in Figure 5.9 but shown for all cells during active periods (left column) and break periods (right column). (a) Chennai, (b) Machilipatnam, (c) Bhopal, (d) Agartala, and (e) Kolkata. Lucknow and Mumbai are not shown.

on active and break periods, the diurnal cycle, different months during the monsoon season, and location. Our main findings are as follows:

1. A season-average peak in CTH was found between 6 km and 8 km for all sites, just above the freezing level and region of maximum tropospheric stability.

2. The seasonal distribution of CTH suggests the presence of three distinct convective cumulus modes: shallow convection, cumulus congestus, and deep convection. Considering the season as a whole, cumulus congestus is the dominant mode. 2 km reflectivity was found to increase rapidly with CTH below the melting layer, and slowly above it.

3. There is less convection per radar volume during break periods compared to active periods for all sites. CTH is also lower on average for the 2016 break periods for Bhopal and Mumbai, spatially matched with the positive rainfall anomalies. Other sites display no definitive change in the respective CTH distributions. Low-level wind circulation and θ_e profile changes between active and break periods are an indicative driver of resultant variability in CTH, most notably the position and strength of increased westerly winds associated with the position of the monsoon trough.

4. All sites but Mumbai show a clear seasonally-averaged diurnal cycle in the number of cells, with differences between each climate region attributed to local and large-scale features of the atmosphere. The peak in rainfall tends to occur around or soon after the peak in the number of deep cells.

5. The phase of the diurnal cycle and average height of cells depends on the surface type being land or ocean for south-eastern India. Ocean cells exhibit more of an early morning peak in convection and have a higher proportion of deeper cells. Mumbai also shows more of an afternoon peak over land and an early morning peak over ocean, though the difference is more subtle.

6. The diurnal cycle is further modulated by the progression of the monsoon. During peak monsoon months (July and August), the diurnal cycle becomes less distinct for

most sites, with longer spells of convective inactivity pre and post-monsoon. This is most definitive for northern India.

7. Active and break periods also modulate the diurnal cycle in rainfall and cell number for several sites. Break spells tend to see convection preferentially at the more convectively active times of day, whereas active spells are associated with convection through the day (but still more frequent at certain times).

This research naturally points towards further investigation of ISM monsoon clouds and their place in the large-scale monsoon circulation. An analysis of the vertical structure of convective cells (i.e., in terms of reflectivity) associated with different large-scale regimes would be a useful next step. Similar analyses of the intricate relationship between cloud development and the wider monsoon circulation from a satellite or modelling standpoint could also further explore some of the patterns discussed here.

Our findings broadly agree with previous studies of multiple monsoon seasons using TRMM (e.g., Houze et al., 2007; Romatschke et al., 2010; Romatschke and Houze, 2011; Shige and Kummerow, 2016). Such agreement implies that the IMD weather radar data can successfully be used to study monsoon convection for individual years. The high temporal frequency and spatial resolution of the ground-based radars, as well as the planting of further radars since 2016 both in India (Roy et al., 2019), and recently Nepal (Talchabhadel et al., 2021), means they are valuable resources in the analysis of storm-scale and mesoscale phenomena for South Asia. The methodology presented here, including existing tools (e.g., Wradlib) developed using other radars (e.g., Kumar et al., 2013a) should prove useful to study convection over India, especially allowing comparison across different radar sites.

Finally, these findings emphasise the potential use of these radar data for nowcasting and NWP case-study evaluation. Improvements in the representation of convection in NWP simulations of the monsoon will come from establishing what the biases are in the occurrence and morphology of different convective modes and evaluating the causes of these biases. This study provides a useful benchmark for model verification; the expansion of the radar

network (Roy et al., 2019) and continued atmospheric sampling over time, will allow for deeper climatological questions to be investigated, such as the spatiotemporal variability of the convective modes. Furthermore, local capacity for model development – including at the Indian Institute for Tropical Meteorology and the National Centre for Medium Range Weather Forecasting (e.g., Jayakumar et al., 2017; Martin et al., 2020) – will allow for continual model evaluation programs and development to occur. In this vein, the next work chapter explores the use of these radars in convection-permitting model verification.

Chapter 6

Evaluating monsoon storm morphology in convection-permitting models with operational weather radars

6.1 Introduction

Numerical weather prediction (NWP) models over the South Asian region are of great importance for providing forecasts of extreme weather events, such as monsoon depressions, that are very hazardous to the population of India. As mentioned in previous chapters, the ISM is innately complex owing to the fact that it is a convectively driven phenomenon (e.g., Parker et al., 2016). Furthermore, atmospheric convection is predictable on timescales of only a few hours (e.g., Lorenz, 1969), and this provides a significant barrier in NWP skill, especially for global models that rely on parameterisations of convection. However, today's regional models operating at grid lengths on the order of 1 km make it possible for convection to be represented explicitly, with convective parameterisation turned off.

As discussed in Chapter 1, these so-called convection-permitting models have been found to greatly reduce biases in the timings, numbers and locations of storms during the Indian monsoon (e.g., Willetts et al., 2017). Nonetheless, Section 1.1.4 described how convection-permitting models are not exempt from their own errors, with a wet bias in the north and

north-east of India and a dry bias over the Western Ghats (Willetts et al., 2017). Furthermore, they struggle to represent the timing of monsoon onset (e.g., Sperber et al., 2013), suggesting that the non-linear feedbacks between local rainfall and the large-scale monsoon (Parker et al., 2016) are not represented well by these models. Such errors associated with simulated convection in NWP propagate and grow with time, and are a fundamental limitation in forecast skill. Furthermore, with continued model development, there may be systematic errors in modelled convection yet undiscovered. As a result, evaluating convection in NWP models against reliable observations has great potential for improving forecast skill over the Indian region. Willetts et al. (2017) utilised rainfall as observed by the tropical rainfall measuring mission (TRMM) satellite, at 0.25° spatial resolution. However, a limitation of satellite rainfall products is that small-scale convective features and low rainfall rates are typically not measured well (Huffman et al., 2007), and the grid lengths are substantially bigger than today's high-resolution models. In comparison, ground-based weather radars have the distinct advantage of operating at high-resolution (gate sizes typically less than 1 km with a range of elevations, depending on the scanning strategy), that allows for direct comparison against today's convection-permitting regional models.

Model development is a rapidly progressing field, with different resolutions and model schemes trialled regularly. The performance of models that run explicit convection has been found to be highly resolution-dependent (Weisman et al., 1997). Moreover, it has been shown that there is significant multi-scale variability in convection over India over a single monsoon season (Doyle et al., 2021b), and model performance may differ with large-scale regime changes, e.g., monsoon active and break periods (Krishnamurthy and Shukla, 2000). Resultingly, it is useful to be able to perform model evaluations on a more ad hoc basis, during different large-scale atmospheric regimes. Archived and quality-controlled operational radar data provide high-resolution observations that allow for repeated model evaluation with no additional planning.

Whilst the use of radar-derived rainfall products is long established, the use of 3-D hydrometeor information from operational radars for model evaluation is a rather recent concept, especially in the tropics, where arguably, there is the most potential for model

improvement. Stein et al. (2019) used a network of 11 C-band South African operational radars for model evaluation. Firstly, they compared radar-based rainfall estimates to satellite-derived products, and secondly, they utilised the multiple elevation scans in the radar to evaluate the vertical extent of statistical cloud properties such as reflectivity and size. This uncovered the real potential for examining cloud macrophysical biases between operational radars and models. Additionally, McBeath et al. (2013) and Stein et al. (2014) used model radar reflectivity to compare simulated and observed convective storms over the UK, avoiding the need for radar-derived rainfall estimates. There are inherent quality control challenges associated with the use of operational radars for building a climatology of convection and evaluation of models, such as data provision and outages, calibration errors, uncertainty in the empirical rain-reflectivity relationship, restricted domains, and typically slightly sparser horizontal and vertical resolutions compared to research-grade radars. These obstacles should be carefully considered and mitigated through thorough quality control where appropriate, for a robust model evaluation to be achieved. Nonetheless, there is a unique opportunity for calibrated operational radars to help inform how realistically high-resolution models simulate convection, on a range of climatological scales from the diurnal cycle to seasonal composites, as well as for individual case-studies.

As part of the INCOMPASS field campaign of 2016 (Turner et al., 2020), regional convection-permitting runs with the Met Office Unified Model (MetUM) were executed for a 3-week period during late June and early July 2016, simulating thousands of convective storms over the entire Indian region. These data overlap with the provision of observational data from a network of IMD radars described in Section 1.2.2. The two regional models used in this study operate at respective horizontal resolutions of 1.5 km and 4.4 km, and are described in more detail in Section 6.2. The 4.4 km model is at a resolution that compromises on explicit convection whilst allowing a relative saving on computational cost and running time compared to 1.5 km. This is because a model nominally represents scales approximately 4–6 times the grid length (Lean et al., 2008). Therefore, for a 4.4 km model, many important components of convection such as small updrafts on scales $< 10\ \mathrm{km}^2$ are not well-represented explicitly. However, for many applications such as domain-averaged rainfall, a 4.4 km model

generally performs well compared to satellite observations (e.g., Holloway et al., 2012), and would then be a more apt choice to run. Therefore, one aspect of this chapter is to assess whether we can reasonably evaluate the 4.4 km model against radar observations given the limitations of the model grid size for representing smaller storms, and also the restricted areal coverage provided by the radar observations. These model and radar data form the basis of this study. Doyle et al. (2021b) already showed that the IMD radars can be used to statistically monitor monsoon convection on major timescales of variability within a single season, and following this, these radars are used for model evaluation for the first time.

Therefore, the aim of this paper is to assess the utility of a network of ground-based weather radars for model evaluation during the ISM. In Section 6.2, we expound the required techniques and approaches for collocating models and radars in space and time. Section 6.3 shows how two convection-permitting models spatially represent convection over India. Section 6.4 then statistically compare the properties and morphology of modelled and observed convection in terms of storm heights, sizes, and intensities. Section 6.5 explores several potential microphysical and dynamical arguments for some of the more prominent major model biases, and general conclusions to this study are given in Section 6.6.

6.2 Data and methods

In this section, the ground-based weather radars and convection-permitting model runs used in this study are detailed. The processing performed upon the model data in order to obtain convective information on discrete vertical levels (for comparison with the IMD weather radars) is outlined.

Firstly, in order to interpret the analysed patterns of convection in the models and radars for each region, a selection of large-scale variables that represent both the model microphysics and the actual observational state are acquired. To do this we use ERA5 reanalysis (0.25°; Hersbach et al., 2020), and rainfall from GPM IMERG (0.1°; Huffman et al., 2020), as well as radiosonde soundings which are available twice daily in the vicinity of each radar site (freely available at `http://weather.uwyo.edu/upperair/sounding.html`). Further

information regarding these data is given in Section 2.3. The flight data used in Section 6.5 are detailed therein.

6.2.1 Ground-based Doppler weather radar network

Following the provision of 2016 monsoon season data from 17 radars after the INCOMPASS field campaign, this chapter uses 15 of these radars for model evaluation. The X-band radar at Srinagar is not considered following the reasons outlined in Section 2.1, and the Dibrugarh (VEMN) radar is not used owing to its location in the far north-east of India and due to its very large calibration offset as detailed in Chapter 3, along with a minimum sensitivity above 10 dBZ at a range of 100 km. For all other radars, we recall there is some inhomogeneity within the network in terms of spatial resolution and minimum sensitivity, and the number of complete radar volume scans also differs somewhat.

The procedural steps of Chapter 2 are then applied to each of these radars for every complete volume scan from 19 June–11 July 2016 inclusive to obtain a statistical array of convective storms at each site. The horizontal resolution of the grid is set to 1.5 km, equivalent to the 1.5 km model, and the vertical resolution is 0.5 km. As in previous chapters, the radar domain boundaries are set to a radius of 40 km and 100 km from the radar site respectively, forming a "doughnut" region for analysis. Given the noise values at the outer edge of the radar domains shown in Table 3.2, the ETH for each column is calculated as the height with a reflectivity echo nearest to 10 dBZ for this chapter, (assuming consecutive retrievals above 10 dBZ at every CAPPI level below it). This is safely above the minimum sensitivity of all 15 radars at 100 km. As previously, the CTH of each storm is then determined as the *maximum* echo-top height in each convective cell region. Whilst the CTH obtained using the 10 dBZ ETH threshold is biased low compared to the true (visual) cloud top, it nonetheless provides an informative measure of the relative heights of storms, as it has been demonstrated such reflectivity-derived ETHs are correlated with satellite-derived CTH (Jackson et al., 2018). Importantly, we recall that any convective cells not entirely contained within the restricted radar domain (40–100 km) are also removed to ensure only entire convective cells are being

sampled. Further details are provided in Chapter 2.

6.2.2 Convection-permitting model runs

Regional convection-permitting model runs were executed as part of the INCOMPASS project at 1.5 km and 4.4 km horizontal resolutions using the MetUM during late June and early July 2016. The domain boundaries of both simulations are 5–35°N, 50–100°E. The model is free-running with lateral boundary conditions provided from the global analysis using the MetUM (Walters et al., 2017) every 24 hours at 00 UTC, and is downscaled to 1.5 km or 4.4 km resolutions using the interpolated global model analysis flow fields (Martin et al., 2019). The global model runs fully compressible, non-hydrostatic, deep atmosphere dynamics at 17 km horizontal resolution and 70 vertical levels with a model lid at 80 km. The dynamics of both the driving global model and the limited-area models (LAMs) are based on Even Newer Dynamics for General Atmosphere Modelling of the Environment (END Game; Wood et al., 2014). The microphysics scheme is a single moment, bulk scheme following that of Wilson and Ballard (1999), with some adjustments since. The most relevant difference between the global Met UM and the LAMs is that convection is entirely explicit in the regional models, with a diagnostic cloud scheme (Smith, 1990) that diagnoses cloud fraction when the relative humidity exceeds a critical value. A more extensive summary of the differences between the global and regional models and model configurations are found in Stratton et al. (2018), who used a 4 km model, but the configurations apply to both LAMs here. Model variables are outputted every hour (running in forecast mode for each 24-hour period) on a latitude-longitude Arakawa C grid. Both LAMs have 80 model levels with a model lid at 38.5 km, employing terrain-height following coordinates using Charney-Phililips staggering. There are 56 levels below 16 km (the maximum height of our 3-D Cartesian grid of reflectivity) and 32 levels in the lowest 5 km, with a grid spacing increasing quadratically from 170 m at approximately 2 km to 590 m at approximately 16 km (Stratton et al., 2018). For model evaluation, the vertical grid is transformed to height above ground level using the model orography.

The LAM framework was initially executed for the whole 2016 season in Menon et al. (2021), and then executed over two case-study periods during the 2016 monsoon season with additional output diagnostics such as radar reflectivity, that we introduce later. The first case-study in late June includes a time of persistent heavy rainfall over the Western Ghats associated with an offshore trough, described using observations in Fletcher et al. (2020). The second in early July encompasses the occurrence of a monsoon depression (track shown in Figure 6.3). For both model resolutions, these case-studies overlap, resulting in a continuous period of 23 days from 19 June–11 July 2016 within which our analysis is performed.

6.2.3 Model radar reflectivity and processing

In order to produce a direct and rigorous comparison between model and radars, we use the radar reflectivity variable available in the models, derived from the MetUM microphysics (see appendices of McBeath et al., 2013; Stein et al., 2014). This avoids the need to convert observed radar reflectivity to hydrometeor concentration values, which relies upon empirical relationships calculated from particle-size distributions. The total radar reflectivity (Z_t) used in this study is calculated using a Rayleigh scattering and spherical particles assumption, which means reflectivity is proportional to mass squared. This assumption is valid in most circumstances for S-band radars, but in the case of very heavy rain or hail may start to break down for C-band radars. Z_t is defined as the linear sum of radar reflectivity associated with different hydrometeors (ice aggregates, crystals, graupel, rain, and liquid cloud), and is instantaneously derived every hour, and expressed in logarithmic dBZ units. This forward model of reflectivity does not consider attenuation or brightband effects that might influence real-world radar observations. Therefore, the model may exhibit larger reflectivities in very heavy rain and hail as opposed to those in attenuated radar observations. However, as we are primarily utilising S-band radars and observing convective regions, we assume differences between real-world observations and the model due to attenuation or brightband effects to be small.

As the model is run in forecast mode for each 24-hour period, the probability of misplaced

or incorrectly timed convective clouds is high, and thus the evaluation work that follows in later sections is statistical in nature over the entire period (or regimes within the entire period), as opposed to a like-for-like comparison at each time within a radar domain. That is to say, the chief aim of this study is to assess and interpret the macrophysical properties of convective cells that the model is producing compared to radar observations, in terms of height, size and intensity.

In order to best provide a fair like-for-like comparison between the model and observations, additional measures are implemented to spatially match the two data sources. For example, the vertical interpolation applied between radar sweeps in producing the CAPPIs smooths out any sharp reflectivity gradients associated with the bright band or cloud edges. However, in the model, the high-resolution native 3-D grid can simulate such gradients, and thus impact our interpretation of the vertical convective cell structure compared to the radars. Furthermore, the radar domain is limited in range compared to that of the models. Our solution to these discrepancies is to effectively mimic the radar scanning and re-gridding procedure in the model, by constructing CAPPIs of reflectivity for each height between 2 km and 16 km above ground level.

The steps involved in this are detailed below:

- Create a simulated radar at each ground-based weather radar site, extracting model reflectivity values between 40 km and 100 km from the site location.
- For each simulated radar, at each hourly output, we reconstruct scans at each elevation as follows.
- All points in the model 3-D grid situated within the beam for each elevation angle at each range are retrieved by the algorithm and the data is smoothed as a Gaussian weighted average as a function of the distance to the centre of the radar beam.
- From the reconstructed scans, CAPPIs are created in the same way as for the observations (Section 2.2.1).
- Linear interpolation is carried out in dBZ units (following Warren and Protat, 2019),

to reconstruct the vertical profiles onto a 0.5 km vertical grid

- The Steiner algorithm is used to locate convection, removing cells that intersect the 40 km or 100 km range ring from the simulated radar site.

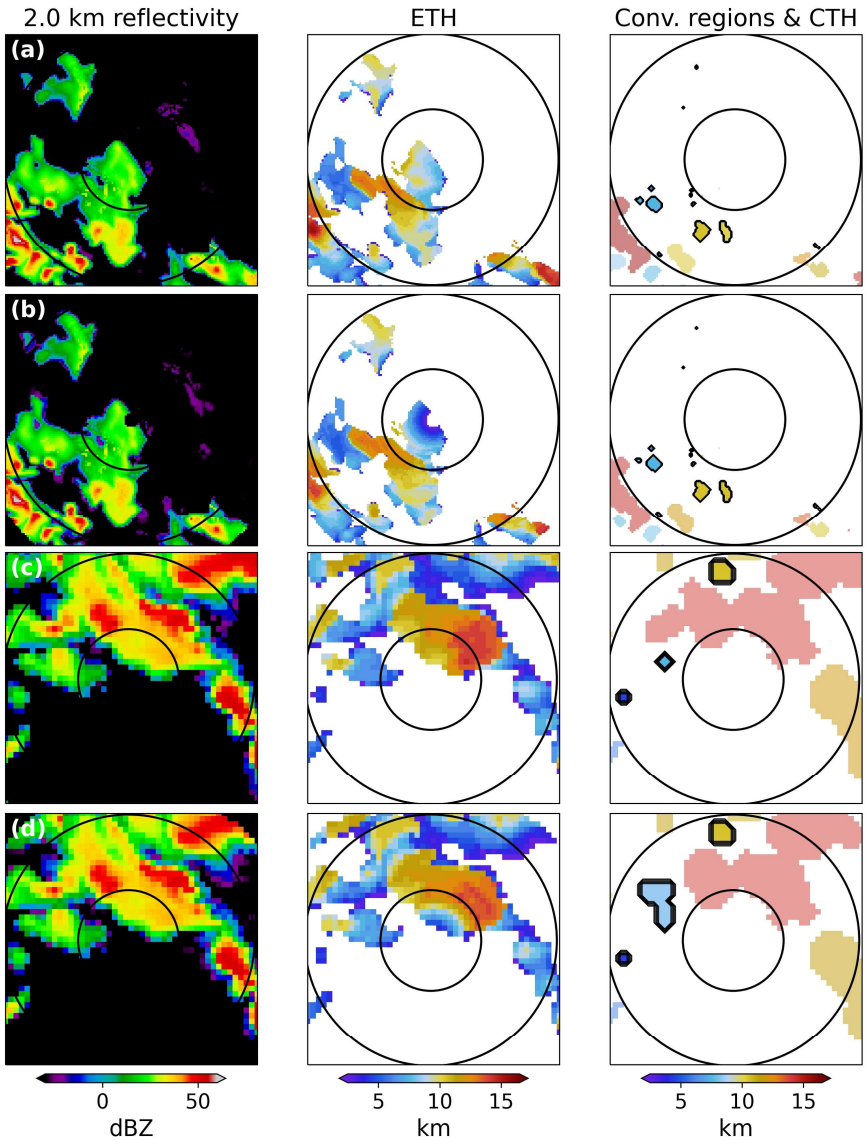

Figure 6.1: Example of a simulated radar region (collocated with the New Delhi radar) in the models on 3 July for (a) the 1.5 km LAM, (b) the 1.5 km LAM mimicking the radar scanning strategy, (c) the 4.4 km LAM, and (d) the 4.4 km LAM mimicking the radar scanning strategy. In each case, the left column is the maximum reflectivity (dBZ) in the vertical column for each pixel, the middle column is ETH (km) for every vertical column with a signal > 10 dBZ above 2 km, and the right column is the CTH for each storm (km) with black contours denoting the storm edges. Storms that are removed as they are not entirely contained within the simulated radar domain region are semi-transparent and their edges are not contoured.

As seen in Figure 6.1, the additional step of creating CAPPIs in the model makes only a small difference to the reflectivity and associated convective cell fields compared to taking the native 3-D grid within each doughnut region (i.e., proceeding to the vertical interpolation stage immediately after positioning each simulated radar). Nonetheless, some local differences can be noted in Figure 6.1. A slight reduction in the maximum reflectivity is seen for the transformed model data, resulting in a slight decrease in ETH. Secondly, following the application of the Steiner algorithm, convective objects are approximately equivalent, and given that ETH is aggregated over each object to give CTH, the latter does not differ much between the original model output and the radar-mimicking results. Thirdly, as seen in Figure 6.1, the locations and numbers of storms remains mostly identical between non-transformed and transformed data. However, the total sample size of storms identified using the transformed model data was found to be slightly smaller over the case study compared to the non-transformed data. This is likely because of the larger sampling gaps in the radar-mimicking data compared to the original high-resolution 3-D model grid. Although these aggregate characteristics appear similar, we find that the vertical profiles of reflectivity in the radar-mimicking results are slightly smoother, which compares more favourably to re-gridded radar observations (especially near the brightband region where the original model 3-D grid simulates a quasi-discontinuity in the reflectivity field with height). Overall, Figure 6.1 suggests that it is probably not necessary to go to this level of complexity for all evaluations of this nature. However, restricting the model data to be collocated with each radar domain is an important step for evaluation, as otherwise the model was found to be artificially biased towards modelling larger storms owing to the greater domain, and a fair comparison of storms was not possible. For this study, we use the transformed model data as we believe it provides the most robust comparison between model and radar, owing to the similar pre-processing of the respective data.

It is also important to note that the temporal sampling of the radars is every 10 minutes, as opposed to the hourly instantaneous readings of the model radar reflectivity diagnostic. Additionally, as previously mentioned, most radars are prone to periods of missing data. In order to mitigate this issue, especially longer periods of missing data for a particular radar,

only hourly model outputs where at least one radar volume from any site in that broader 'climate region' (ref. Figure 6.5) is available within the intervening hour period are included in the statistical evaluation.

Finally, the Steiner algorithm is run at at both 1.5 km and 4.4 km horizontal resolutions to compare to the model of the equivalent resolution. The same echo-top height threshold of 10 dBZ is applied across all model doughnuts to determine CTH, to match the same threshold applied to the IMD radars.

6.2.4 Additional methods

To represent the vertical profile of reflectivities in storms as an overall intensity, we use height-weighted reflectivity as defined by Kumar et al. (2016),

$$Z_{hwt} = \log_{10} \sum_{k} Z \cdot z_k \tag{6.1}$$

where Z is linear reflectivity (mm^6 m^{-3}) and z is the height at k km above ground level, thus weighting reflectivity more strongly at higher altitudes. Z_{hwt} is then converted back to logarithmic (dBZ) units. Z_{hwt} is a useful measure as it provides a single intensity-dependent value for each storm that can be related to other storm statistics such as CTH. Furthermore, it weights reflectivities at higher altitudes (associated with ice) more strongly, thus deep storms with strong updrafts have high values. For example, Kumar et al. (2016) noted that it is well-correlated with column-mean vertical velocity for Darwin, Australia. For Indian monsoon convection we also found Z_{hwt} to be highly correlated with the maximum reflectivity found in the vertical column (not shown).

Frequently throughout this chapter, storm heights are aggregated into three cumulus modes within the free troposphere following the analysis of radar-derived storm heights in Doyle et al. (2021b): shallow (CTH $<$ 5 km), congestus (5 $\leq$ CTH $<$ 8 km), and deep (CTH $\geq$ 8 km). In observations, shallow convection is associated with low near-surface reflectivities and light precipitation, congestus convection detrains in the freezing level region and is moderately intense, and deep convection pentetrates into the upper troposphere and is associated with

high near-surface reflectivities and heavy precipitation.

6.3 Representation of large-scale variability and convection in models

In this section, we explore the model independently of the radar observations. This is for several reasons. Firstly, before any evaluation is performed, it is important to ascertain the ability of the model to represent the large-scale conditions during the case-study period, as substantial errors here might displace convection and affect the radar-model comparison. Secondly, it is beneficial to investigate how the LAMs represent spatial variability in convection over India, compared to the large-scale synoptic situation during the period of the case-study, as well as with what we already know about spatial variability in convection during the Indian monsoon. This will build greater confidence in the forthcoming evaluation of the model. Thirdly, this exploration of the model provides an initial notion of the differences in performance between the two model resolutions. Finally, exploring simulated convection over the entire LAM region will help identify regions of similar convective characteristics during the period of interest.

6.3.1 Large-scale conditions during case study

Firstly, we assess how the model represents the large-scale conditions for the 19 June–11 July case-study period. Figures 6.2a–c show total precipitation and 850 hPa winds for both models and GPM IMERG/ERA5. The models evidently capture the large-scale situation well, with the highest rainfall totals in all cases seen over the Western Ghats and north-eastern India (also Bangladesh and Burma). High rainfall totals are also seen over northern and eastern portions of India, which as we will show shortly, is partly due to a monsoon depression in early July. Figures 6.2g–i show high 850 hPa relative humidity values over most of India associated with the monsoon, especially over the Western Ghats, with drier conditions in the far south-east and north-west of the country. Figure 6.2 also displays the biases in the

aforementioned fields. Noticeably, both LAMs are too dry compared to ERA5 at 850 hPa for much of inland India, but especially the north and north-west of the country. Coastal regions and much of north-eastern India exhibit smaller biases in relative humidity, and the surrounding seas are generally too moist in the model but for coastal southern and north-eastern India. The dry bias over north-western India is associated with a strong south-westerly wind anomaly, which appears to carry initially moist air from the Arabian Sea over the dry and hot regions of north-western India and Pakistan, lowering the relative humidity. The dipole in the northern India precipitation anomalies evident in Figures 6.2d–e likely results from errors in the positioning of a monsoon depression in the model, incident upon northern India in early July. The region bordering the Himalayas in northern India also appears to be too wet in both models, but with no clear corresponding signature in the relative humidity field. Dynamical differences between the two model resolutions are noticeably smaller, but the 1.5 km model has more onshore precipitation in the Western Ghats region, despite being marginally less humid.

For the evaluation work that follows, to maximise the available number of datapoints for similar conditions, compared to looking at 15 individual radar domains, we designate six climate-based subregions of India (Figure 6.3). These are defined from the precipitation, wind, and relative humidity fields shown in Figure 6.2, and are named after their positions within India.

R-SE represents the rain shadow and coastal south-eastern India region, positioned east of the elevated Western Ghats orography, and with low 850 hPa relative humidity. Four IMD radars are situated in this subregion. R-N experiences monsoon onset approximately halfway through the case-study period (Doyle et al., 2021a) and has less oceanic influence, and also exhibits lower humidity compared to most of India. R-C is the central and eastern region of India that experienced high levels of rainfall associated with the monsoon depression (track shown in Figure 6.3). This monsoon depression was especially active in producing precipitation in its south-western quadrant. R-W is the very convectively active region on the windward slopes of the Western Ghats mountains, with persistent moisture-laden westerly lower tropospheric wind shear. R-HIM is the region sandwiched between the monsoon

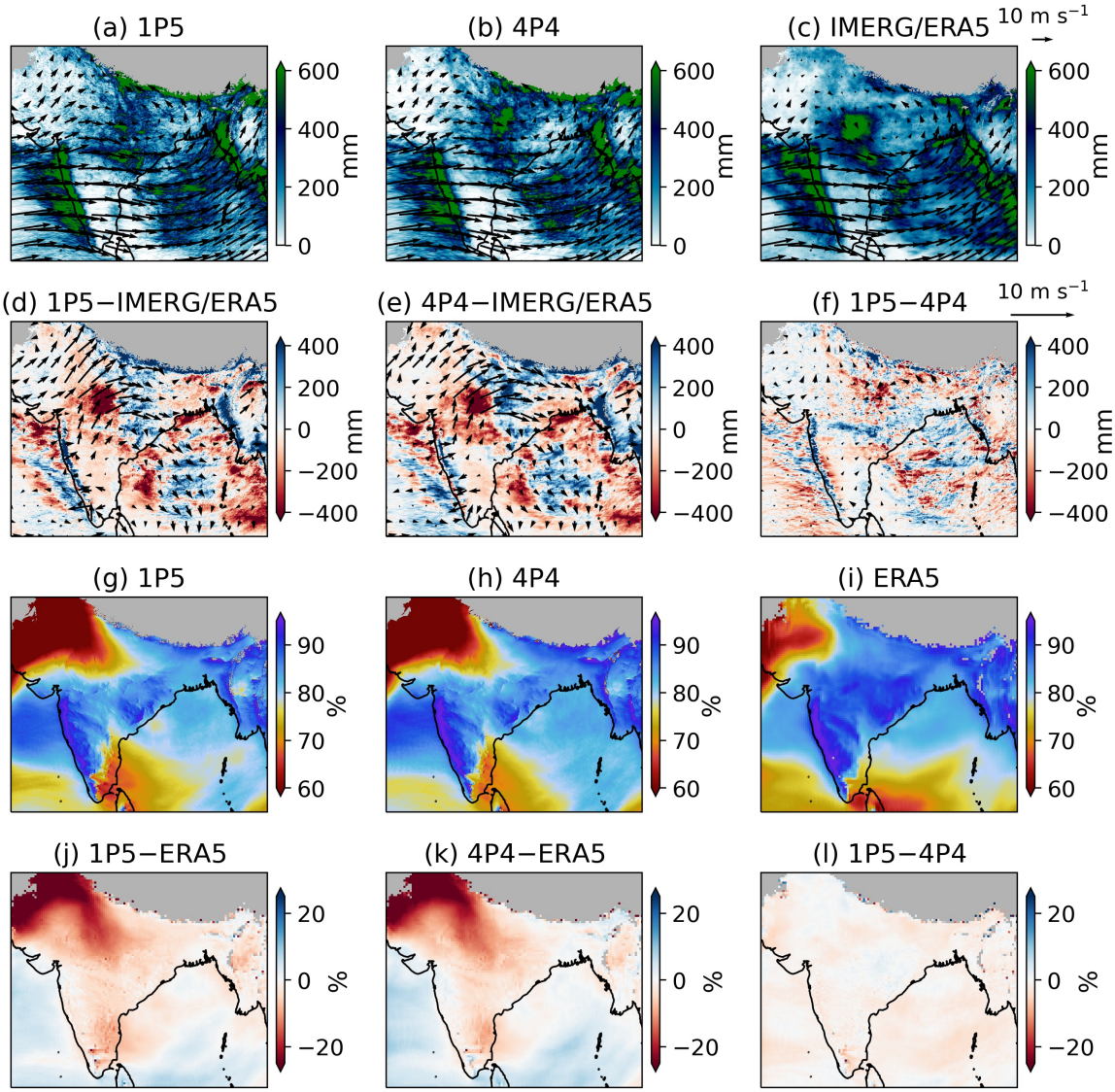

Figure 6.2: (a–f) Precipitation (GPM IMERG) and horizontal 850 hPa wind vectors (ERA5) for the 19 June–11 July case study period, with panels (a–c) showing total values, and (d–f) anomalies. (g–l) 850 hPa relative humidity (ERA5), with mean values shown in panels (g–i) and anomalies of these quantities in panels (j–l). (a,g) 1.5 km model and (d,j) 1.5 km model anomalies; (b,h) 4.4 km model and (e,k) 4.4 km model anomalies; (c,i) IMERG and ERA5; and (f,l) 1.5 km−4.4 km model anomalies. Model variables are smoothed onto the IMERG/ERA5 grid for comparison. In panels (i) and (l), the 1.5 km model is smoothed to the 4.4 km grid before subtraction. Regions above 1.5 km in elevation are shaded grey.

depression and the Himalayas mountain range, and is associated with two radars. It has relatively less oceanic influence and weak horizontal wind components in ERA5. Finally, R-NE is situated in north-eastern India, experiencing large amounts of rainfall and south-westerly winds from the Bay of Bengal.

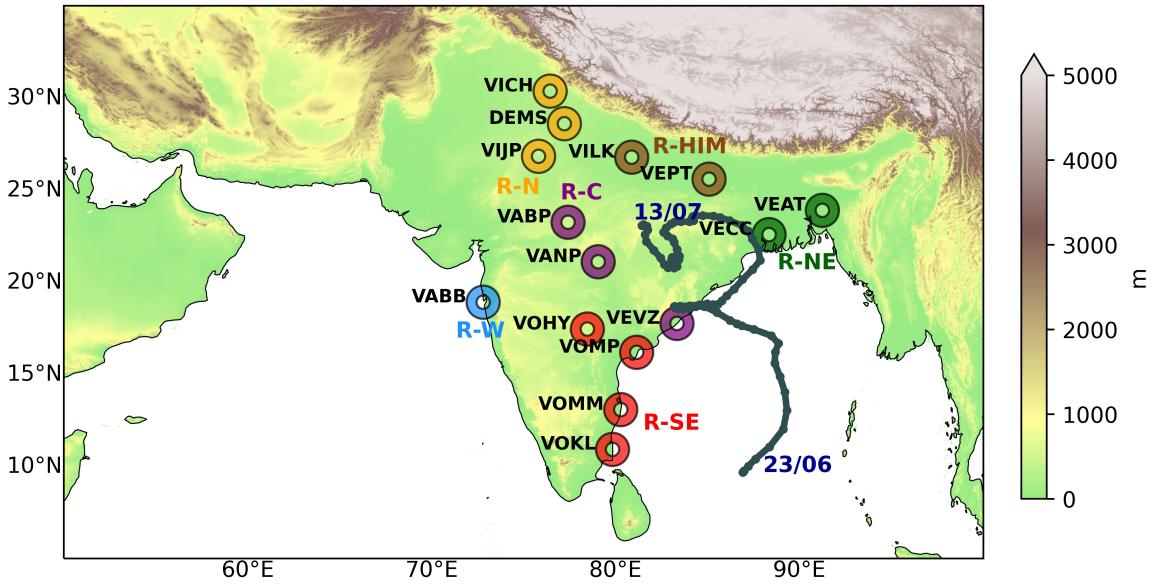

Figure 6.3: Topographic map of India and surrounding regions, showing the positions of the 15 IMD ground-based Doppler weather radar sites used in this study (filled regions representing a radius of 40–100 km from the radar). The site codes for each radar site are labelled. As explained in the text, each radar is coloured according to the subregion that it is incorporated within. The track of a monsoon depression, the effects of which were largely incident upon India during the first two weeks of July, is also shown in grey, with the genesis and lysis date labelled. The extent of the domain shown represents the boundary of the regional convection-permitting model runs.

These subregions are evidently then each associated with different large-scale conditions, and so it is important to explore how the model captures these regional differences in conditions, by studying vertical profiles of equivalent potential temperature (θ_e) and horizontal winds in each subregion compared to observations, and this is shown in Figure 6.4. Relatively smaller values of θ_e are associated with higher stability which might cause convection to be shallow more frequently.

For R-SE, R-C and R-W, the mean θ_e in the models is too low through most of the troposphere, suggesting more stable conditions. R-NE exhibits values of θ_e that are too low in the lower troposphere, but is more similar to soundings at upper levels. R-HIM displays only small differences in the vertical profiles of θ_e. R-N shows large spread in modelled θ_e with some very anomalously low values at Patiala in particular (the northernmost site in the region), positioned within the anomalously dry air shown in Figures 6.2j–k. However, at

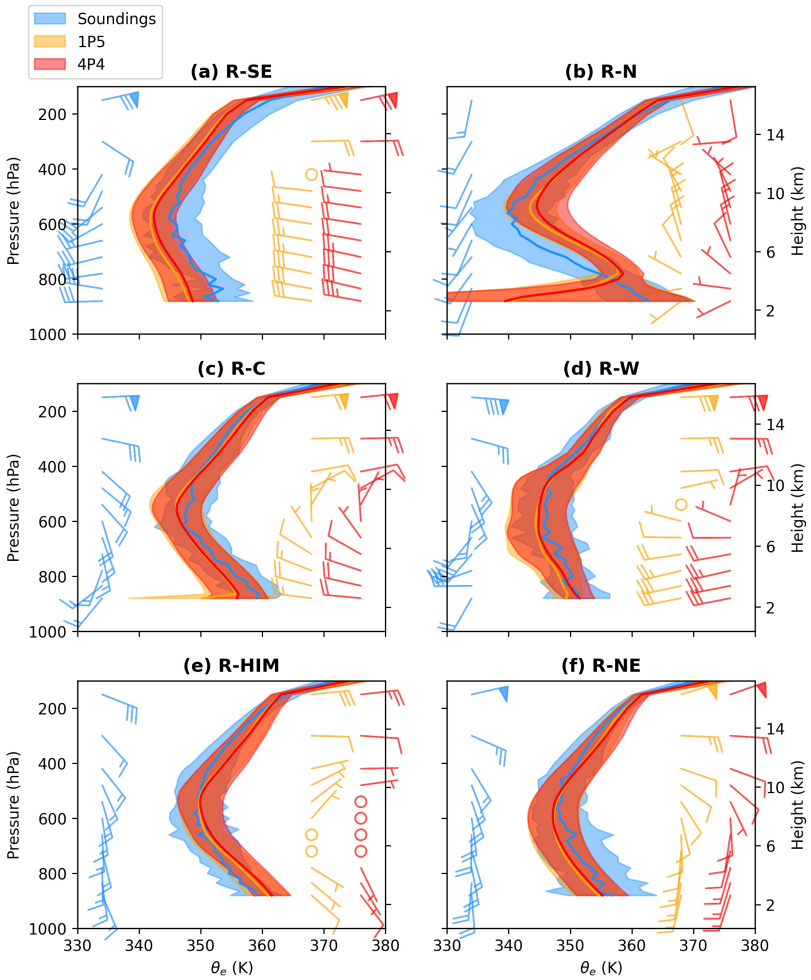

Figure 6.4: Vertical profiles of equivalent potential temperature (θ_e; units Kelvin) and horizontal winds for each subregion (a–f) for soundings (blue), and LAMs (1.5 km orange, 4.4 km red). Coloured shading represents the interquartile range. Horizontal winds are represented by wind barbs, where a half barb is 2 m s^{-1}, a full barb 4 m s^{-1}, and a flag 20 m s^{-1}. Vertical profiles of θ_e and horizontal winds are not shown below 900 hPa to avoid orographic interference.

mid-levels for R-N, both models have more instability than radiosonde observations, despite winds coming from the dry north and north-west instead of the moister south-west. This is possibly due to the air being significantly warmer in the model, despite the lower moisture content of the air. For all subregions, winds in the 400–700 hPa mid-troposphere region are often poorly represented in the model, with winds typically too weak and with large errors in direction compared to ERA5. This may well have an impact upon convective development in models, due to the importance of the moisture content of advected air as a key component of convective development. Nonetheless, the models overall represent the vertical atmospheric

profiles for each subregion well in Figure 6.4. The variability in θ_e is similar to that observed, and with the exception of below 800 hPa in the R-N region, is never displaced by more than 5 K from soundings in terms of the mean θ_e. Horizontal winds are also generally accurately simulated below 700 hPa and above 400 hPa. Therefore, by comparing the models to observations in this section, we have gained confidence in their ability to represent the large-scale conditions and thus, the embedded local convection.

6.3.2 Spatial patterns of convection in the model simulations

Figure 6.2 showed how the models represent fields of precipitation, horizontal winds, and relative humidity from a large-scale perspective. Following this, in Figure 6.5 we analyse a selection of convective statistics, placed onto a $1^\circ \times 1^\circ$ latitude-longitude grid for the 1.5 km and 4.4 km models respectively. Cells are identified as explained in Section 6.2.3 but ignoring the re-gridding to the radar grid and doughnut regions. Cell statistics contribute to the $1^\circ \times 1^\circ$ grid-box that matches their centroid location.

Figure 6.5 shows patterns of convection over different regions of India, broadly as expected from the large-scale conditions described above, combined with previous understanding of monsoon convection. We note the smaller cell numbers and CTHs associated with the rain shadow region of south-eastern India as well as north-western regions which had not yet experienced monsoon onset. Additionally, Figure 6.5 shows the predominance of shallow convection over much of the western coast despite high near-surface reflectivities (e.g., Utsav et al., 2017; Doyle et al., 2021b), the deeper storm heights over inland northern India (e.g., Doyle et al., 2021b), and the large amount of convection over north-eastern India due to its position in the monsoon trough region. We can see from the shallow (CTH < 5 km) cell frequencies that the Western Ghats region experiences the most shallow convection (for both resolutions, though comparatively less for the 4.4 km LAM), but is active in congestus and deep cumulus modes as well. Indeed, Figure 6.5 suggests that if a region is subject to significant activity in the shallow mode, it is likely to experience convection of all types. The converse, however, is not necessarily true, as deep storms are prevalent over many regions,

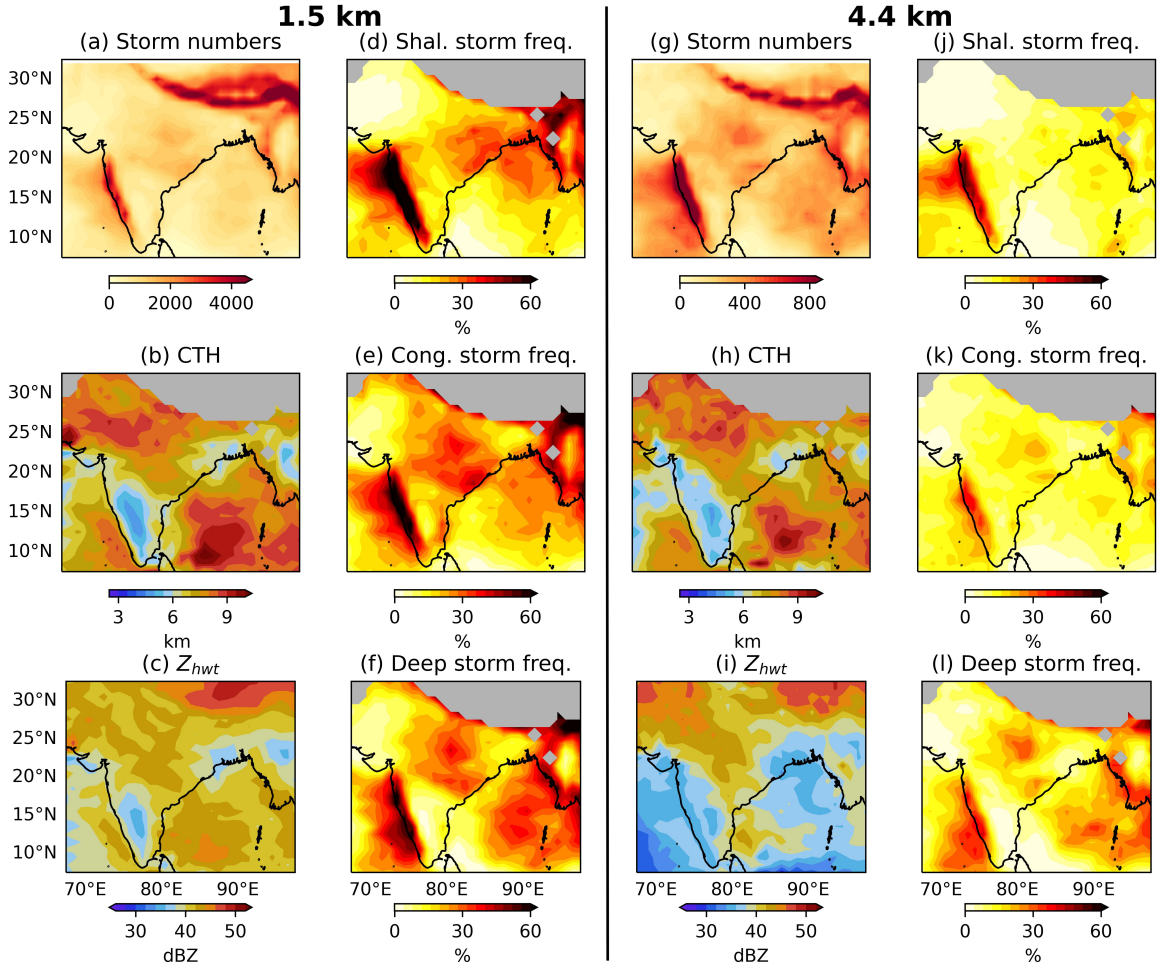

Figure 6.5: Convective cell statistics smoothed onto a $1^\circ \times 1^\circ$ grid over the Indian region, for storms consisting of at least four contiguous pixels. Shallow (CTH < 5 km), congestus ($5 \leq$ CTH < 8 km), and deep (CTH ≥ 8 km) storm frequencies are calculated as the number of occurrences in the model with at least one storm within the CTH bounds in that grid-box divided by the total number of hours in the model, then multiplied by 100 to obtain a percentage. (a) Number of storms for the 1.5 km model, (b) mean CTH, (c) mean of storm average Z_{hwt}, and (d–f) shallow congestus and deep storm frequencies respectively. Panels (g–l) show the equivalent information for the 4.4 km model.

especially the coastal Arabian Sea, Bay of Bengal, and northern India associated with the monsoon depression incident upon this case-study period (see track in Figure 6.3), without an associated swathe of shallow convection. An additional feature of interest is that both LAMs display shallow and congestus convection along the eastern coast (near Vishakhapatnam), but deeper convection is more prevalent inland nearer Bhopal and Nagpur.

The 4.4 km LAM displays similar patterns in the locations of convective activity. Shallow convection is still prevalent in the Western Ghats region (Figure 6.5j) but is much less frequent

in north-eastern India compared to the 1.5 km LAM. Instead, the region affected by the monsoon depression in early July is associated with mainly deeper storms in the 4.4 km LAM. CTH is generally very similar between the two models, with a few regions of lower CTHs in Figure 6.5h along India's west coast, especially further north. This is reflected too in the lower Z_{hwt} values in Figure 6.5i over the Western Ghats, Bay of Bengal, as well as much of the Arabian Sea, with a clear spatial correlation between CTH and Z_{hwt}. Overall, there are far fewer convective cells in the 4.4 km LAM, and we detail the reasons for this at the start of Section 6.4.

Comparing Figure 6.5 with the total precipitation in Figure 6.2 smoothed onto the same $1^\circ \times 1^\circ$ grid, we can take Pearson correlation co-efficients of each parameter of convection, i.e., a spatial correlation against model precipitation. The fraction of deep storms is highly correlated with model precipitation for both the 1.5 km and 4.4 km models (0.87 and 0.86 respectively). Congestus and shallow storm fractions, as well as the total number of storms, also exhibit correlations greater than 0.5 for both models. CTH and Z_{hwt} are strongly correlated with each other (0.85 and 0.54 for the 1.5 km and 4.4 km models respectively), but show less of a relationship with precipitation, exhibiting respective correlations of 0.13 and 0.41 for the 1.5 km model, and 0.24 and -0.09 for the 4.4 km model. This is probably because the statistical mean over the case study period of these quantities is not reflective of the number or areal extent of storms that are known to correlate more significantly with rainfall at the surface (e.g., Davies et al., 2013). The relationships between these convective statistics will now be explored in further detail in Section 6.4.

6.4 Evaluation of modelled convection with radars

We have now gained confidence in the ability of the model to simulate large-scale fields and convective environments that compare reasonably with observations and prior knowledge of the region. In this section, following the procedure of Section 6.2.3, (including the interpolation of model reflectivity to the radar sampling and the restriction to doughnut regions), we examine the model representation of convection in more detail by statistically

comparing it to patterns of convection observed by the IMD weather radars during the 23-day case study period.

Firstly, the number of volumes and sample sizes of different cumulus modes for each subregion is given for the two LAMs and radars run at 1.5 km and 4.4 km resolution respectively in Table 6.1. Due to the 10-minute resolution of the radars (albeit with frequent gaps for some sites), the number of overall radar volumes is larger. Tellingly, the number of shallow cells in the model is nonetheless of a comparable amount, and the proportion of convective storms that are shallow is indeed greater in both models compared to the radar observations. For R-N and R-C where deeper convection is more dominant in the radars, the models also have too high a proportion of congestus convection. This will be explored in further detail when examining convective cell heights below. Moreover, the sample sizes of the three cumulus modes for the 4.4 km model and radar grids are much smaller, especially for shallow convection and for R-W, where there is very limited data after 27 June.

The smaller sample sizes seen in Table 6.1 for the 4.4 km model and radar smoothed to 4.4 km resolution can be traced to two main effects. Firstly, the smallest storm a 4.4 km model can simulate is almost 20 km^2, i.e., one pixel. As explained previously, we do not consider storms made up of less than 4 pixels, as they may not represent robust convection and can dominate the statistics. Therefore, only storms with an area greater than 78 km^2 are able to be evaluated here, and this neglects a large proportion of storms of all types (about 80% of storms simulated by the 1.5 km LAM greater than 8 km^2 are smaller than 78 km^2), but especially the shallow mode that is usually associated with storms with smaller areal coverage (Doyle et al., 2021b). Secondly, merging of convective storms frequently occurs following implementation of the Steiner algorithm at this resolution. For example, this is visualised in the large storms in Figures 6.1c–d (right-most column) that intersect the minimum and maximum range rings, and occurs as a result of the 4.4 km resolution base CAPPI displaying fewer localised reflectivity minima that might separate convective features in the 1.5 km model and radars. This merging results in far fewer storms contained entirely within a 40–100 km radius of each radar site. Furthermore, the converse effect will also result in fewer storms, i.e., the 4.4 km model may miss or under-represent localised *maxima* in reflectivity.

Table 6.1: The total number of reflectivity volumes and the corresponding number of cells of the three different convective modes, with the percentage of total storms in each mode shown in parentheses. Only those model volumes corresponding to at least one radar volume in that region in the intervening hour period are included. Also, only storms with at least four contiguous pixels (classified as convective) are included. At 1.5 km resolution this equates to 9 km^2 and for 4.4 km resolution this equates to 78 km^2.

	1.5 km		**4.4 km**			**1.5 km**		**4.4 km**	
R-SE	Model	Radar	Model	Radar	**R-N**	Model	Radar	Model	Radar
Vols	2048	8223	2048	8223	Vols	1536	6081	1536	6081
Shal	1043 (29)	1118 (10)	112 (19)	13 (1)	Shal	417 (12)	655 (6)	20 (5)	17 (1)
Cong	1829 (51)	5983 (52)	308 (53)	538 (29)	Cong	1582 (47)	3896 (34)	187 (46)	328 (18)
Deep	683 (19)	4476 (39)	162 (28)	1281 (70)	Deep	1398 (41)	6954 (60)	197 (49)	1430 (81)
R-C	Model	Radar	Model	Radar	**R-W**	Model	Radar	Model	Radar
Vols	1530	6215	1530	6215	Vols	102	145	102	145
Shal	969 (21)	1277 (5)	65 (11)	27 (1)	Shal	223 (28)	169 (12)	28 (29)	4 (2)
Cong	1881 (41)	8542 (33)	269 (44)	709 (17)	Cong	256 (33)	755 (51)	31 (32)	82 (36)
Deep	1752 (38)	15802 (62)	271 (45)	3408 (82)	Deep	305 (39)	543 (37)	37 (39)	144 (63)
R-HIM	Model	Radar	Model	Radar	**R-NE**	Model	Radar	Model	Radar
Vols	832	2587	832	2587	Vols	1066	5604	1066	5604
Shal	551 (27)	775 (9)	42 (18)	20 (2)	Shal	1384 (46)	3353 (17)	126 (32)	80 (3)
Cong	662 (33)	2893 (34)	70 (29)	183 (15)	Cong	811 (27)	9135 (45)	150 (38)	867 (30)
Deep	808 (40)	4752 (56)	126 (53)	1015 (83)	Deep	790 (26)	7642 (38)	121 (30)	1990 (68)

As a result, the 'peakedness' criterium of the Steiner algorithm may not designate a region as convection as it is not sufficiently greater than the surrounding background reflectivity, whilst the same region is identified as convective at higher resolutions. Comparing the numbers of storms in Table 6.1 for the 4.4 km data to the 1.5 km data, this evidently has the greatest effect upon shallow cells, with the greatest reduction of storms for this cumulus mode. However, significant reductions in the sample size of all three cumulus modes are evident. The Steiner algorithm was originally tested by Steiner et al. (1995) for a 2 km grid, and this suggests

the need for some refining of this technique for coarser resolutions in particular, but such an analysis is beyond the scope of this work. For all these stated reasons, the 4.4 km model is not explored further in this study, with focus instead given to the evaluation of the 1.5 km model using the 1.5 km 3-D radar grid.

6.4.1 Cell-top height

We now compare distributions of CTH between the 1.5 km model (referred to simply as the LAM from henceforth) and radars for shallow, congestus, and deep cumulus modes (ref. Section 6.2.4). In particular, quantifying the areal coverage of different CTHs is important because of the strong relationship between the areal coverage of storms and precipitation depths. Figure 6.6 reveals that the LAM produces too much shallow convection (CTH<5 km) compared to radar observations across all six regions. The disparity in the amount of shallow convection is most clear for R-W and R-NE, where background moisture is very high due to prevailing onshore winds from the Arabian Sea and Bay of Bengal respectively. For the majority of regions, radar-observed convection has a greater area covered by deep cells, especially for Figures 6.6a–c. R-W (Figure 6.6d) shows the model overestimates areal coverage at most CTHs. The dashed lines (showing the medians of the respective cumulative distributions of CTH areal coverage) thus occur at the same value. Most distributions show considerable noise in the distributions due to the high-resolution vertical grid, and this is especially true for regions with small sample sizes (e.g., model for R-HIM and R-NE and both distributions for R-W). R-NE has a relatively more platykurtic distribution in the model, i.e., a flatter and broad-tailed distribution, with similar areal coverage associated with most CTHs, and so the maximum in areal coverage occurring at a higher CTH than that of the radar should not detract from the fact that the region still greatly overdoes the extent of shallow convection. Overall, R-HIM displays the most similar comparison between model and radar, but even here, the model overestimates the areal coverage of shallow convection.

Despite the consistent shallow convection bias for all six regions, the model clearly does capture regional differences in the statistical ensemble of CTH values. For example, R-N and

R-C display the largest amounts of deep convection in radar observations, and so relatively more areal coverage is provided by deeper storms in the model for these regions, compared to R-SE or R-NE.

Whilst these reflectivity-derived biases in convection between model and radar have not been explored before for India, it is known that the MetUM struggles to accurately represent clouds in the tropics, even at convection-permitting scales. Indeed, understanding of how turbulent and microphysical processes downscale to convection-permitting resolutions remains poorly understood (Prein et al., 2015). We explore the potential causes for these differences in convection in more detail in Section 6.5.

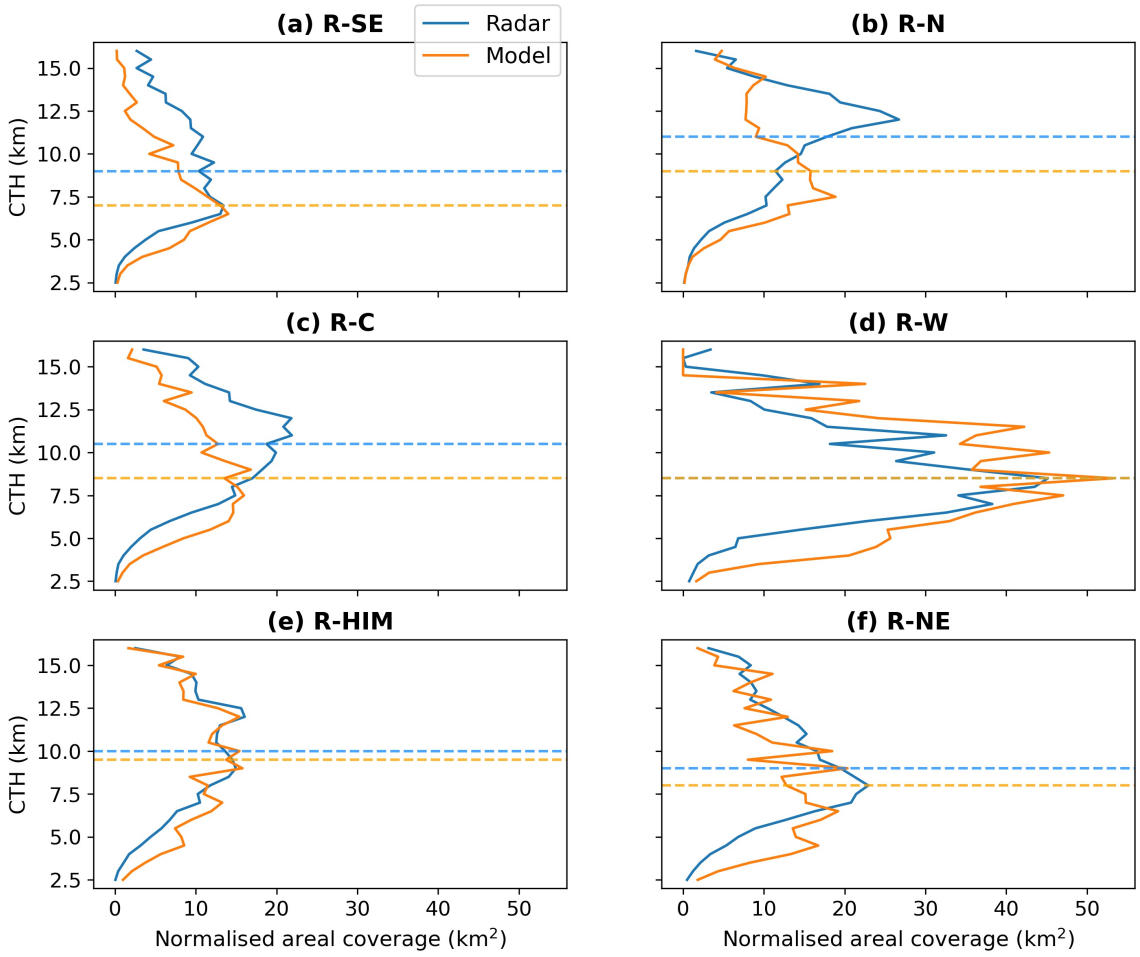

Figure 6.6: Total areal coverage of storms in each CTH bin (2.5–16.0 km), normalised by averaging over the total number of volumes, shown for each subregion as defined in Figure 6.3. The radar distributions are in blue and the 1.5 km LAM in orange. The median CTH bin (i.e., where lower and higher CTH have equivalent areal coverage) is shown by the horizontal dashed line of the corresponding colour. Only storms ≥ 9 km^2 are included, i.e., 4 pixels.

To summarise, Figure 6.6 either suggests that there is a higher proportion of shallower storms in the model, or that the shallower storms are greater in spatial extent in the model, or perhaps some combination of both effects. Table 6.1 already revealed the greater proportion of shallow convection in the 1.5 km LAM for all sites, and a greater proportion of congestus for R-N and R-C where storms are deeper on average. Therefore, we next investigate the model representations of storm size and intensity compared to observations.

6.4.2 Storm size and intensity

Here we examine the respective distributions of storm sizes in radars and models. The ubiquitous signal in Figure 6.7 is that the LAM simulates cells that are too large compared to observations for all three cumulus modes. This is especially evident for shallow cells (Figure 6.7a), where the radar storm sizes are constrained to values less than 32 km^2, but the model has storms of sizes up to around 128 km^2. Indeed, the model exhibits a second, albeit smaller peak around 64 km^2 for R-SE, R-W, R-NE, and perhaps R-HIM. This is further supported by the 25th percentile and median of size that are located at similar or identical magnitudes for radars and model. However, the 75th percentile of size is much greater in the model associated with this second peak. The exception is the R-N region, which shows similar distributions for shallow convection, but this is not the case for the congestus and deep modes.

This disparity in storm sizes means that not only is the model simulating relatively too much shallow convection, but that a proportion of this shallow convection is simulated at large sizes that don't occur in reality. As a result, the excess areal coverage of shallow convection in Figure 6.6 appears to be a combination of both these effects. Indeed, the two effects are also not likely to be mutually exclusive. The additional amounts of shallow convection in the model may well be associated with the ability for cells larger in area to be identified with shallow CTHs.

For congestus cells (Figure 6.7b), the model also produces too many large cells, but

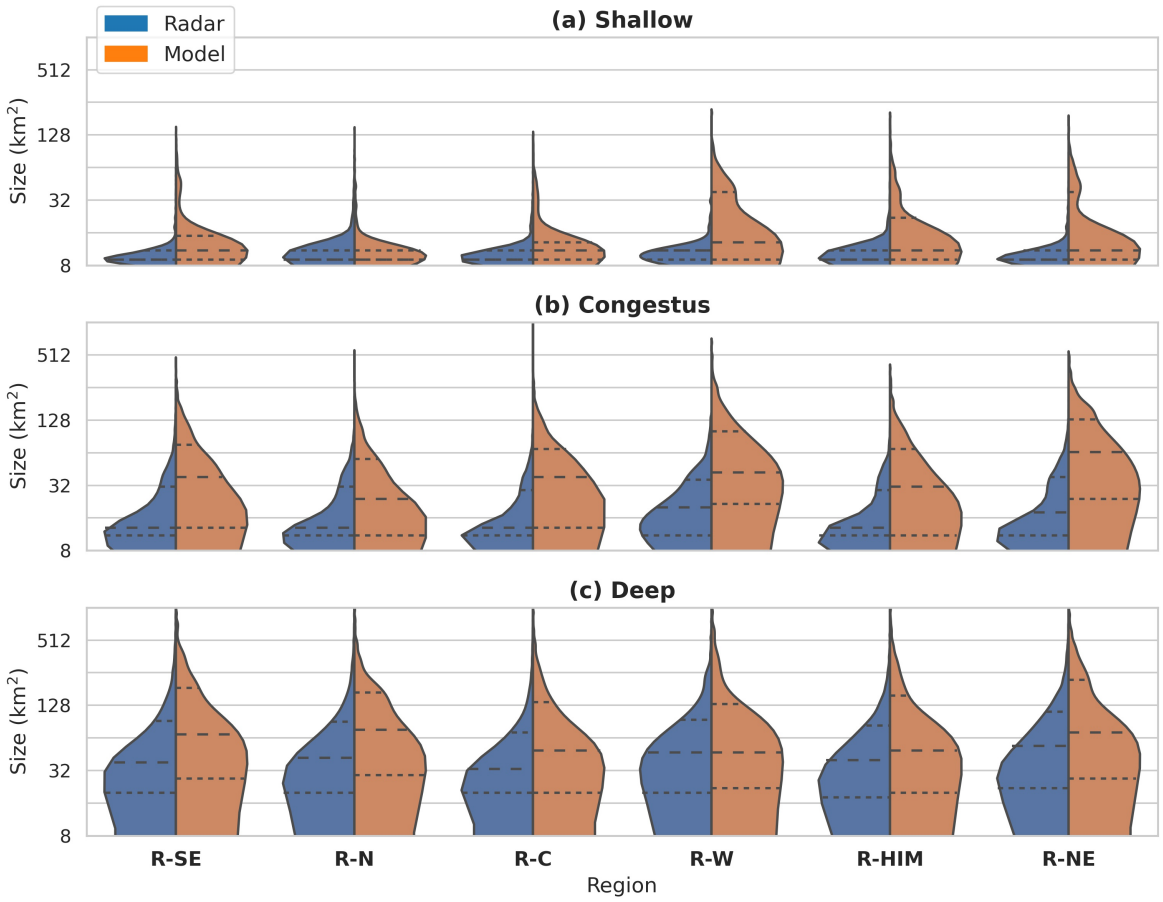

Figure 6.7: Split violin plots of storm size (km^2) for each region for (a) shallow, (b) congestus, and (c) deep storms, scaled to have the same width, irrespective of the number of storms. The radar distribution is blue and the model distribution is orange. The long dashed line in each violin is the median and the short dashed lines show the 25th and 75th percentiles. The y-axis is logarithmic.

now the entire distribution is shifted to greater sizes, especially for R-W and R-NE. Broadly speaking, the median size in the model congestus is similar in magnitude to the 75th percentile in the radar. Once more, a minority of cells in the model are larger than ever seen in radar observations. In fact, the radar congestus storm size distributions appear to compare more favourably with the shallow storms in the model.

For deeper convection (Figure 6.7c), we see that the model size distributions are more similar to that of the radars compared to shallow and congestus for all sites, but even in this case the model displays more cells with large storm areas > 256 km^2, and again the percentiles and medians of the deep cell distributions are shifted to higher values in the model. Despite

this, deep storms observed by radars cover a greater area on average as they are much more frequent. The reason why modelled storm sizes are larger on average is explored further later when discussing overall storm morphology (Section 6.4.3) and again in Section 6.5.

Given this information on the LAM producing too much shallow convection that is often wider than observed, we progress to explore how this manifests itself upon the intensity of the storm. Specifically here, we examine the relationship between storm area and height-weighted reflectivity (Z_{hwt}; ref. Section 6.2.4) for each cumulus mode for each region. We recall that Z_{hwt} is highly correlated with the maximum reflectivity in that column. Figure 6.8 displays the storm surface area and maximum height-weighted reflectivity for every storm, with blue dots for the radar (with a solid median line) and orange dots for the 1.5 km LAM (with a dashed median line).

For shallow storms (Figure 6.8a), the maximum Z_{hwt} for each storm area is similar between model and radars. As mentioned previously, there are more shallow storms at larger storm areas, but this has no clear related increase in intensity. This might be expected as Z_{hwt} has a strong positive spatial correlation with CTH (0.85), and so any significant increases in intensity here would mean the storm would likely no longer be a shallow type cell.

For congestus and deep storms (Figures 6.8b–c), we note the larger sample sizes of radar-derived storms, meaning for most storm areas, the total range of Z_{hwt} is larger for the radars. For storm areas approximately < 100 km^2, the model is contained within the total spread of the radar distribution. However, the model struggles for larger storm areas, producing maximum reflectivity columns that are too intense compared to those observed for deep convection. Simultaneously, at around 128–256 km^2 for congestus and deep storms, the LAM displays Z_{hwt} values that are unrealistically high for the storm size, with increasing separation between the radar and model medians. This is particularly noticeable for congestus storms in all six regions. Seemingly, the 1.5 km model is typically producing larger, deeper convection of congestus or deep types when the intensity is higher than is required in the real atmosphere.

It is also worth noting at this point that, despite the different large-scale dynamical conditions in these different regions during the case study period, the model errors in representing convection remain broadly consistent between different regions, suggesting that these errors

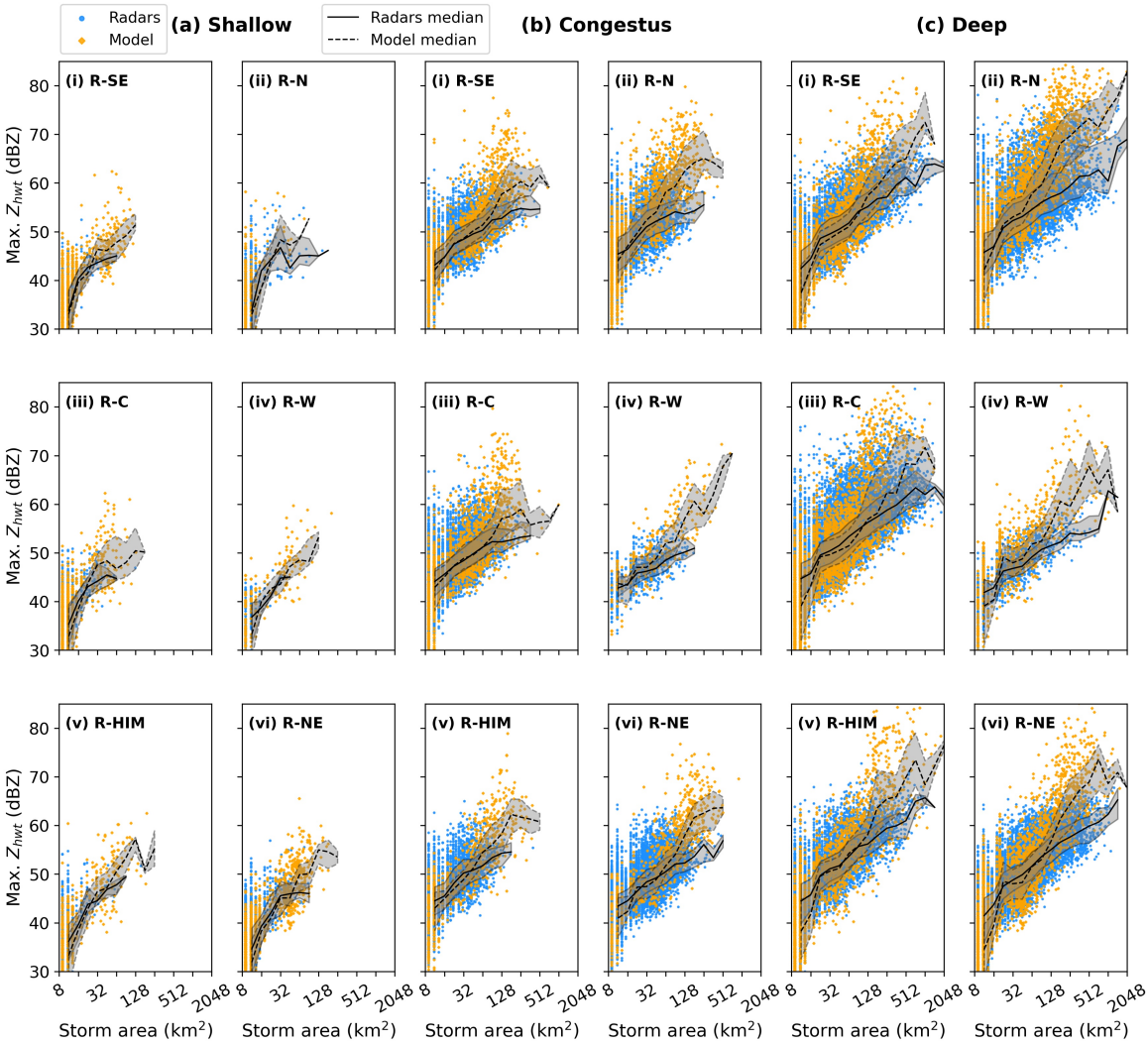

Figure 6.8: Scatter plots of storm maximum Z_{hwt} (height-weighted reflectivity) as a function of area (at 2 km height) of the storm for each sub-region (*i*–*vi*). (a) Shallow, (b) congestus, and (c) deep convection. Blue markers are radar observations and orange markers are modelled values for the 1.5 km LAM. The solid and dashed black lines show the median Z_{hwt} as a function of storm area for the radar and 1.5 km LAM respectively, with the grey shaded regions showing the corresponding interquartile ranges.

are relevant for all tropical monsoon convection irrespective of the background state during this case study period.

6.4.3 Cell morphology in model and radar

In this section, we investigate the vertical structure of storms in models and radars, with respect to their size and intensity investigated above. Given that we now know the model

produces too high a proportion of shallow storms, as well as too many large storms in area, we can try understand how this manifests itself in the vertical structure of the storm. Therefore, the morphology of convection in models and radars may also help us diagnose more precisely where the model is struggling to accurately represent the statistical ensemble of convective cells during the Indian monsoon.

To analyse the vertical structure (specifically the sizes) of storms, we note that the application of the Steiner algorithm in this instance is to find convection at the base CAPPI (i.e., 2 km), and then define all pixels directly above in the 3-D grid column as convective. However, this results in the vertical structure of storms being somewhat truncated at the edges, and ignores the stratiform component, including potential anvil cloud. Therefore, we utilise a neighbourhood search algorithm approach here, which radially expands each cell by up to 20 km, or until it reaches another (expanded) convective cell, whichever occurs first. The maximum value of 20 km was derived by trialling this algorithm on the 1.5 km model output – unrestricted by doughnut regions – and noting when the median morphology converged. For smaller values, cells would still be truncated, whereas for larger values, only few large storms will continue to expand, which do not contribute to the median. This suggests that the hydrometeor field associated with the original convective cell is fully contained within the expanded storms, which occurred for a neighbourhood size of 20 km. As a consequence of applying the neighbourhood search, we then consider the background stratiform rain region associated with each individual convective cell, for this part of the analysis.

Figure 6.9 shows the equivalent diameter of reflectivities $\geq$ 10 dBZ with height for model and radars. The equivalent diameter is defined as the diameter of a circle with area equivalent to the area of the expanded storm with reflectivities greater than the threshold (e.g., 10 dBZ here) at that height. For shallow convection, the model simulates storms to be too large at the near-surface level, consistent with the size distributions in Figure 6.7. The lapse rate of storm equivalent diameter is then steeper in the model compared to radar observations, with a lower median CTH of shallow storms despite the larger diameter storms. A similar effect is seen for congestus storms, and deep storms to a smaller extent, but most clearly in R-SE. It is possible to obtain non-zero diameter values slightly above 5 km for shallow storms (and

8 km for congestus) because the expanded storms may include stratiform pixels with values greater than 10 dBZ just above the actual CTH associated with the embedded convective cell.

For deeper storms, all sites show a maximum in median equivalent diameter around 2–4 km for congestus and 6–7 km for the deep mode. In contrast, the radar exhibits a maximum in median equivalent diameter at 2 km in both cases, which remains quasi-constant up to the level where the model maximum occurs, then decreases steadily with height. Furthermore, the model simulates storms that are consistently too large at and below the freezing level (< 6 km), despite the relatively low CTH in the model above this level. A particularly large difference in the diameter of deep storms can be seen for R-HIM. The vertical profile of model equivalent diameter for R-HIM is similar to that of other regions but the values observed by the radars in the R-HIM region are much smaller, but it is unclear why this is the case. Finally, we note the generally similar variability (i.e., the interquartile range) in the distributions of equivalent diameter at each height between radars and model, but for some sites the variability is clearly larger in the model doughnuts than the radars, despite the smaller sample sizes in the model. This reflects the broader range of storm sizes in the model. A larger interquartile range is expected for deep storms owing to the larger number of deep storms and broader range of cell heights, but the model again has too much variability for most sites, and especially for R-HIM where the aforementioned bias is also biggest.

Figure 6.9 thus shows a few further important model errors in the simulation of convection: Firstly, the median CTH of the expanded storms is lower for shallow and congestus storms than for radars, despite the larger sizes at the near-surface. Secondly, deep cells in particular bulge outwards up to around the freezing level or a bit higher, before quickly decreasing in diameter at upper levels. This maximum in diameter near the freezing level has been found before for the UK (Stein et al., 2014), West Africa during the monsoon (Stein et al., 2015b), and tropical South Africa (Stein et al., 2019). Stein et al. (2014) suggested that the sharp increase in width in the freezing level region is indicative of a large area of drizzle surrounding the storms, with no associated cloud-ice aloft, or small crystals with low reflectivities below 10 dBZ.

We reiterate that this section shows generally consistent model errors across the six

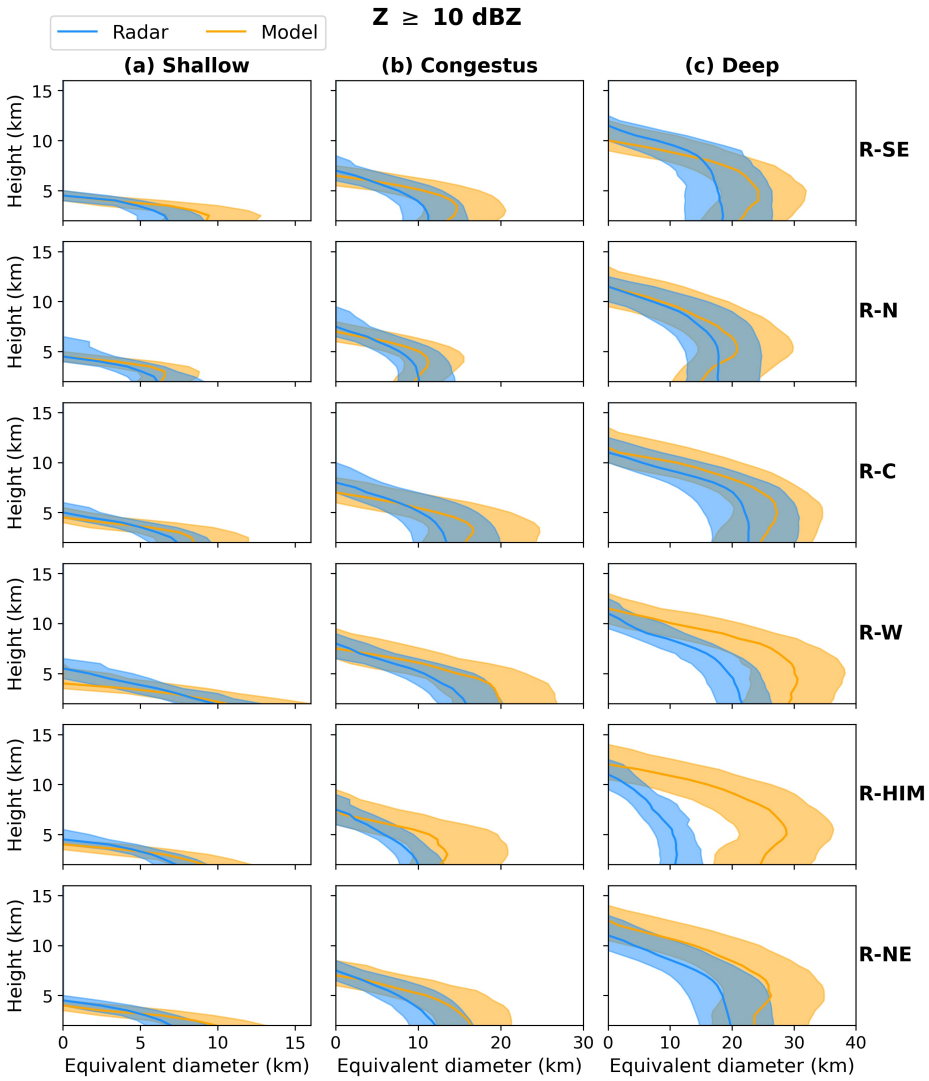

Figure 6.9: Median equivalent diameter ≥ 10 dBZ of the radar (blue line) and model (orange line) expanded storms with height for (a) shallow, (b) congestus, and (c) deep modes, for each labelled subregion. Note the x-axis scales for each column are not the same. The interquartile range of equivalent diameter is shown by the shaded regions of the corresponding colour.

different regions of India. Whilst regional differences occur, e.g., a deeper average population of storms in the R-N region, the model does detect these regional differences well, but the overall differences between the model and the radars as described thus far remain analogous, regardless of location. Therefore, to summarise the statistical information in this section, we take a composite of all six climate regions, encompassing all 15 doughnut domains for comparison (Figure 6.3), and explore the vertical profiles of size and intensity in the storms for the three cumulus modes. This is shown for all radars and collocated model doughnuts in

Figure 6.10.

We see that the model is too intense for all three cumulus modes, especially below and in the region of the freezing level. The convective core region also propagates higher for modelled deep convection in particular, with the 30 dBZ contour reaching 2–3 km higher in the model. We know from Figure 6.8 that the maximum intensity of the storm exhibits a strong relationship with the near-surface area of the storm, and so it is not unexpected to see that the larger model storm sizes are associated with greater core intensity.

Figure 6.10 also shows that the largest errors in the morphology of modelled convection are for the higher reflectivity contours. The 30 dBZ contour at 2 km is approximately a factor 1.5 times too large for deep and congestus storms, and the 20 dBZ contour for shallow storms is also about 1.5 times too large. Comparatively, the 10 dBZ contour is 1.2–1.3 times too large for all three storm modes. At the freezing level, this discrepancy increases, which we describe in further detail below. In particular, congestus convection has the largest error in its diameter, and is associated with reflectivity values over 40 dBZ that rarely occur in observations. The model producing storms that are a factor of 1.2–1.5 too wide (for the 10 dBZ countour) was also found by Stein et al. (2015a), and makes sense given that the smallest scales represented by a model are a factor of around 4–6 times the grid length (Lean et al., 2008).

Building on Figure 6.9, where we found that the cloud field expands in size in the lower troposphere up to the freezing level, we note that this occurs primarily for reflectivities less than 30 dBZ in modelled deep storms, with a smaller signal of this occurring too below 10 dBZ for congestus storms. This confirms that background drizzle with reflectivities below 30 dBZ surrounding the core storm could be responsible for this feature, and is clearly systematic amongst more than 3500 deep storm samples in the model. Expanding on this, we note that models do not simulate the brightband region, i.e., the gradual melting of ice to raindrops in the real atmosphere. Instead, the transition from ice to rain is an instantaneous transformation. This explanation would also apply for models of all resolutions, and indeed this feature was also found to occur for very high-resolution models of 200 m resolution by Stein et al. (2014), even though the overall storm diameters were more comparable to

those observed, which is an issue more directly related to the resolution as opposed to the microphysics.

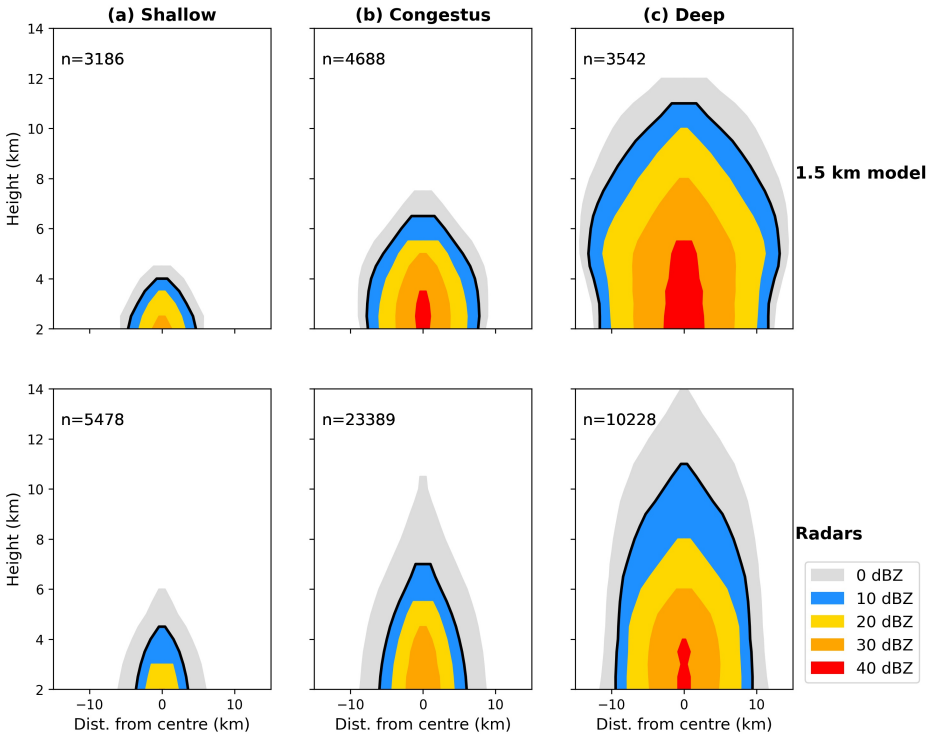

Figure 6.10: Storm morphology as a composite of all six regions, for model (top) and radar (bottom) subsampled for (a) shallow, (b) congestus, and (c) deep storms. The total storm numbers are labelled for each panel. The x-axis is the equivalent radius of the storm. The storm radius for each reflectivity threshold is then mirrored with the simplification that the storm region is symmetrical about its centroid. The black line shows the boundary of the 10 dBZ countour which portrays the CTH. Parts of the expanded storm below the 10 dBZ contour are below the minimum sensitivity of some radars and so this region is shaded light grey.

This section as a whole then serves to show three primary errors in the representation of convection in the 1.5 km resolution model, the latter two of which can be clearly seen in Figure 6.10. Firstly, the LAM is producing convection that is on average too shallow compared to radar observations for all regions (ref. Figure 6.6). Secondly, the LAM simulates storms that are too large and too intense for all types of convection. Thirdly, the LAM produces storms that are bulging outwards around the freezing level, compared to the steadily decreasing reflectivities upwards from 2 km seen more often in observations. These patterns are also found to be consistent across multiple climate regions of India during the period of the case

study. In order to try understand the existence of these errors, we delve into a two-day period of the case study below and evaluate these errors in convection in the model alongside INCOMPASS flight data.

6.5 Exploration of potential causes of biases in modelled convection

Now that we have revealed the ability to robustly evaluate regional high-resolution models with operational Indian ground-based weather radars, and discovered some areas where the model representation of convection systematically differs to that observed, it is important to delve into the potential reasons for the existence of these errors. In this section, we discuss several hypotheses with respect to the model errors, both microphysical and dynamical, and examine the convective and large-scale environment over the period of two INCOMPASS research flights on 2 July and 3 July 2016.

To investigate model errors in further detail, we compare high-resolution observations of atmospheric fields from radiosonde soundings and INCOMPASS flight data (ref. Turner et al., 2020) to modelled large-scale fields for the mornings of 2 July and 3 July over inland northern India (Figure 6.11). This case was chosen due to the existence of large amounts of convection in the region in both radars and models, associated with local monsoon onset around that time, as well as the existence of two research flights taking quasi-identical tracks on the respective mornings as shown in Figure 6.11. In both cases, the plane departed from Lucknow around mid-morning local time, passing just south of New Delhi, then changing its course south-west through Jaipur, before turning round west of Jaipur, and completing a similar path back towards the base at Lucknow. For the outbound portion, the plane would fly at high levels (around 6 km) and for the return portion it would fly lower (around 0.5 km above ground level) to sample the boundary layer. The plane on 3 July departed about an hour later compared to that of 2 July. The sampling frequency is every second whilst the flight is in operation.

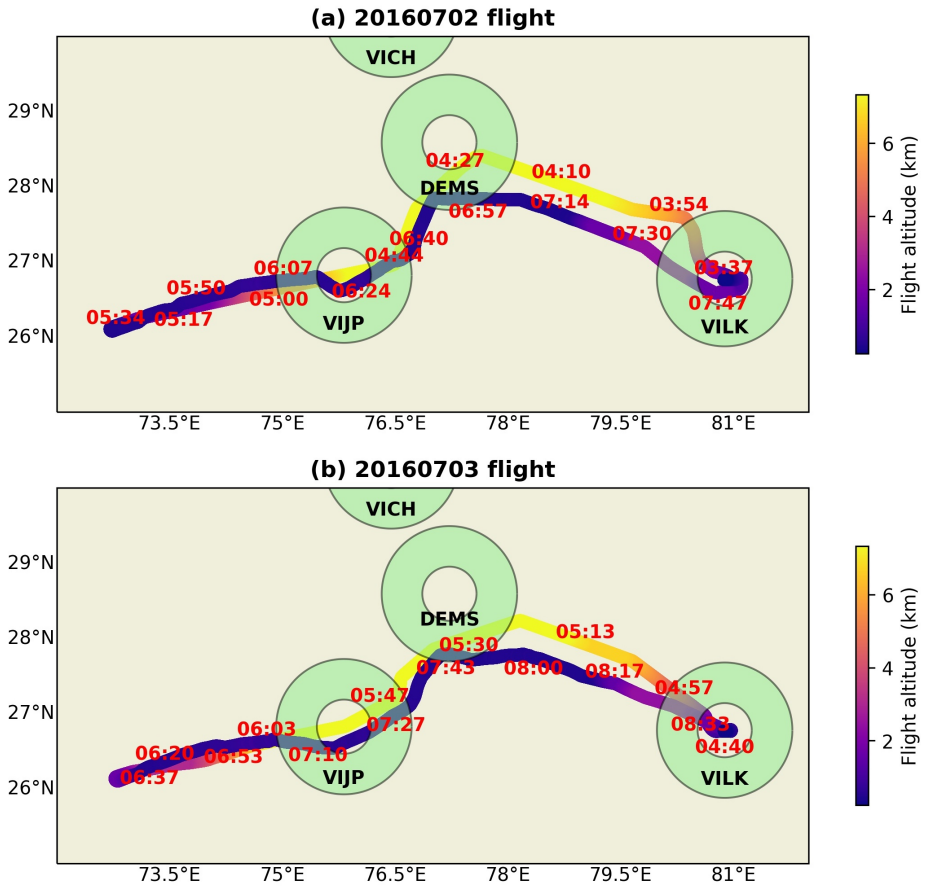

Figure 6.11: Flight tracks for the mornings of (a) 2 July (flight ID B969) and (b) 3 July (B970) 2016, as part of the INCOMPASS field campaign. Times in UTC are labelled in red (5:30 hours behind local time), and the colour of the track corresponds to the elevation of the flight. Radar site doughnut regions are labelled and filled between 40 km and 100 km radius from the position of the radar.

Firstly, we consider differences in convection between the model and radars specifically for the New Delhi (DEMS) region for 2–3 July. We note in Figure 6.12 that the model again underestimates the amount of deep convection that occurs in the region. In the model, 50% of storm coverage is provided by storms ≤ 9.5 km and for the radars this is 10.0 km. In fact, the model underestimates the areal coverage provided by almost all CTH, with a peak at 10.0 km, whereas the average of the radars peaks at much higher values for a CTH of 11.5 km. When taking the entire 23-day case study period, we note that the model typically simulates too much areal coverage associated with shallow and congestus convection. However, this includes periods of less convective activity. However, comparing Figure 6.12 to Figure 6.6b, we note the greater areal coverage in observations and model for the two-day period, as we

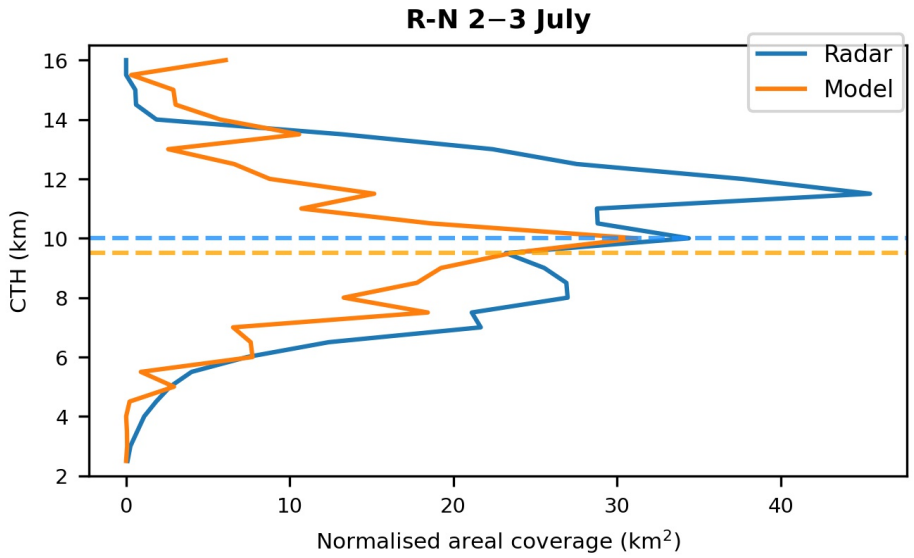

Figure 6.12: Same as Figure 6.6 but only the R-N region for 2–3 July 2016.

are including two days with very active local convection, and resultingly the model indeed produces very little shallow convection and a small amount of congestus, but nonetheless under-represents the amount of deep convection in observations. This suggests that whilst the model responds well to changes in the dynamics that lead to more frequent and/or deeper convection, it still preferentially detrains at lower heights than observed.

Studying the morphology of northern India convection for the 2–3 July in Figure 6.13, we note that similarly to the entire case study, congestus and deep convection in the model are found to have maximum areas near the freezing level, bulging outwards from 2 km height. For congestus storms this occurs for reflectivity contours 20 dBZ and below and for deep storms reflectivity contours 30 dBZ and below. For radars, congestus storms are at a maximum area at 2 km for all reflectivity contours. However, for deep storms, the overall radar storm diameter out to the 10 dBZ contour is approximately constant with height up to the freezing level, but the more intense reflectivity contours (30 dBZ and 40 dBZ) are at maximum heights higher in the storm. This suggests in the real atmosphere that the powerful updrafts associated with deep storms result in the transfer of the highest reflectivities in a storm system to higher altitudes where the hydrometeors are still liquid or perhaps with a contribution from hail. Conversely, the model 40 dBZ contour for deep storms is widest at

2 km height, despite the 10 dBZ contour being widest at 6 km. However, the width of the 40 dBZ contour is much wider than observations. Furthermore, the congestus storms in the model are also on average much more intense than the radars, but are associated with less of a storm diameter bias.

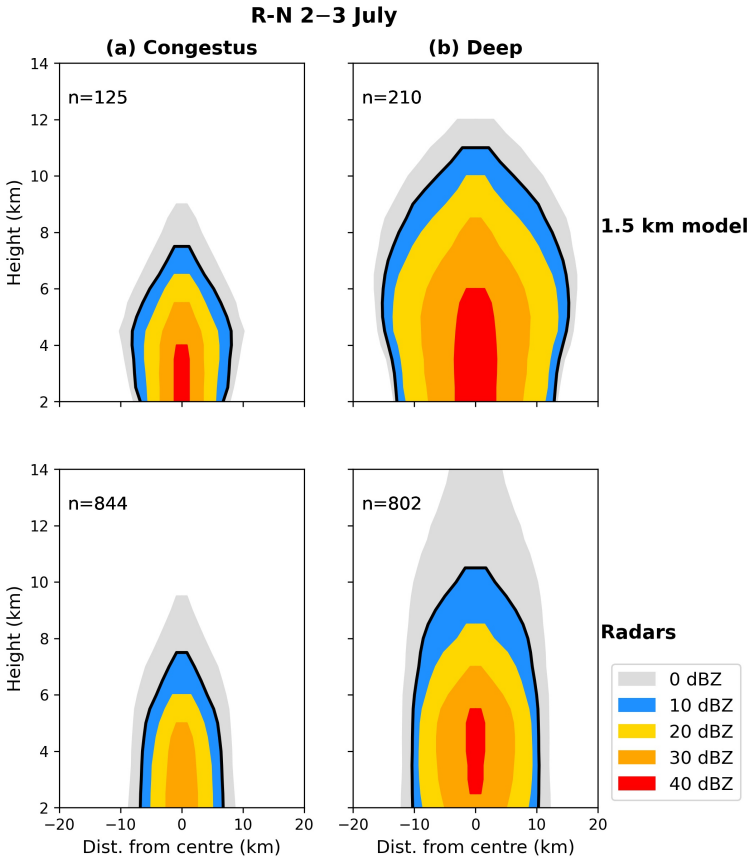

Figure 6.13: Same as Figure 6.10 but only the R-N region for 2–3 July 2016 for (a) congestus cells and (b) deep cells. Shallow cells are not shown due to small sample sizes.

Despite only being a small period of time and a limited spatial domain, these signals in Figure 6.13 are generally supported by the broader-scale evaluation performed across multiple regions of India earlier in this study. Given the deep storms in the model are also too wide for all reflectivity contours, the additional intensity associated with deep storms in the model may be part of why it evidently models too few deep storms that contributes to the much smaller areal coverage in the model shown in Figure 6.12.

Convection in particular presents a challenge for kilometre-scale simulations due to the broad range of hydrometeors with different radiative properties in convection, as a result of

mixed-phase processes. Indeed, errors in the the concentration of hydrometeors in clouds and associated radiative properties can have consequences upon the dynamics of clouds such as CTH and size, and thus associated precipitation (e.g., Fan et al., 2007). As the radar and model are compared at the same 1.5 km resolution within identical domains, and with the Steiner algorithm applied to both data, it is likely that some of these microphysical inaccuracies are contributing to the biases in modelled convection.

Finally, we return to the model representation of the large-scale dynamics and thermodynamics for this specific case-study. Local systematic errors in model dynamics can be difficult to identify but can result in persistent errors in convection. Below, we investigate high-resolution point observations from flight data taken during the INCOMPASS field campaign of 2016. We compare Lagrangian trajectories with ERA5 re-analysis and model fields at the closest time and grid-box to the flight's timestamp and coordinates.

Figure 6.14 shows large near-surface errors in dry bulb and dewpoint temperatures in the model compared to flight observations after 6am UTC. ERA5, which has assimilated observations that helps constrain it to the real-world, compares more favourably to the flight data, which aids our trust in the flight observations. The error in dry bulb temperature is close to +10 K on the downslope of the orography the flight passes over (mountain peak around 0600 UTC), with dewpoint temperatures also a few Kelvin too low at this point, leading to a much lower relative humidity than observed. The times associated with the largest errors in temperatures are collocated with the largest discrepancies in wind direction. The differences in dry bulb temperature are largest between approximately 0630 UTC and 0700 UTC. During this time, the flight observations and ERA5 show light and variable wind components, whereas the model shows stronger winds from the north-west, which advects air that is relatively dry and hot. Furthermore, the warm bias in dry bulb temperature is also noticeable, albeit not as significant, for the small section where the flight is at an altitude of approximately 2 km, again with stronger winds from the north-west in the model compared to observed. It is likely that these inaccuracies in the model are associated with the large dry bias over north-western India that protrudes into central and northern parts of India shown in Figure 6.2. This dry bias may then be improved by a better dynamical modelling of the

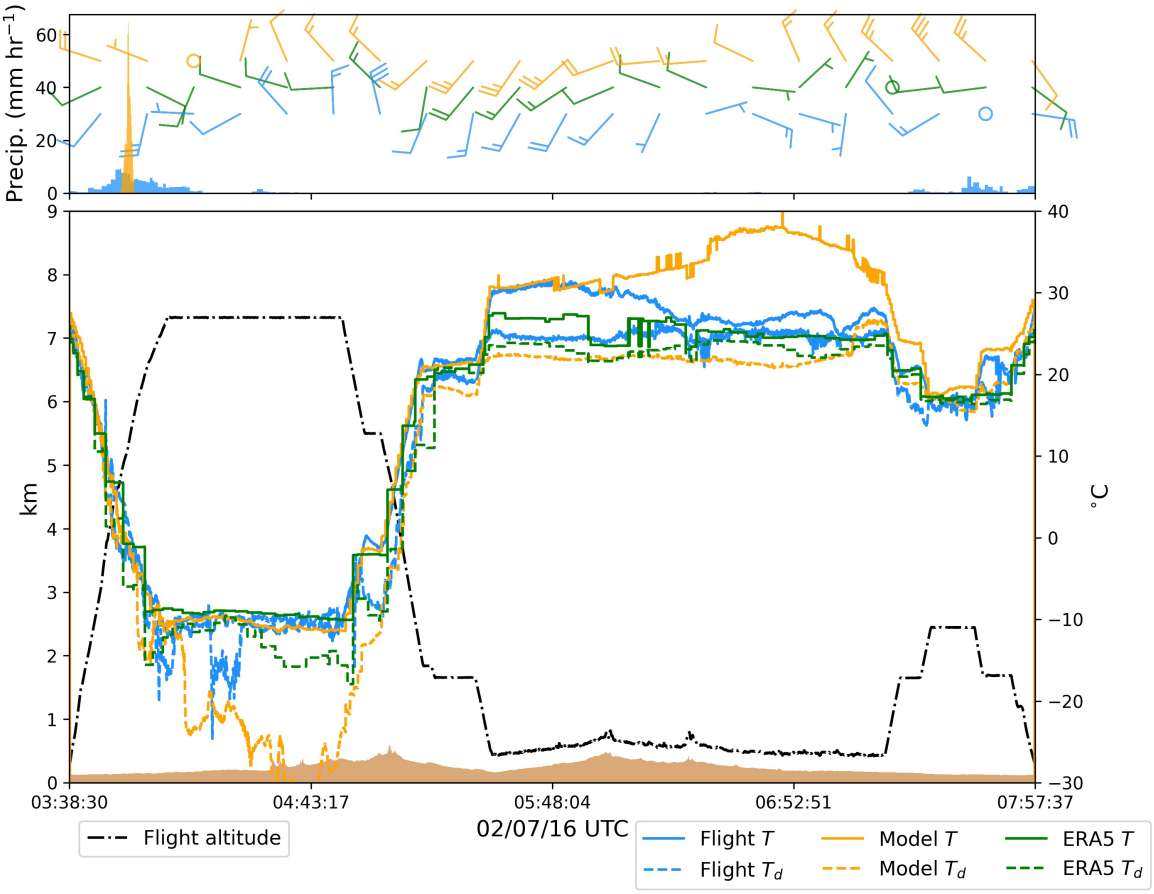

Figure 6.14: Lagrangian dynamical fields for the flight in Figure 6.11a on 2 July 2016 (flight ID B969), where the flight altitude in units of km is shown by the black line. Dry bulb and dewpoint temperatures (°C) sampling every second are extracted from the flight and compared against collocated fields for the 1.5 km model (orange) and ERA5 (green). The nearest grid-box in time and space for these data is used, with no interpolation or averaging performed. The top panel shows IMERG precipitation in blue and model precipitation in orange directly underneath the flight location. Wind barbs for horizontal winds at the flight level are also shown for the flight, ERA5, and the model. Half barb, 2 m s^{-1}; full barb, 4 m s^{-1}; flag, 20 m s^{-1}.

near-surface wind speed and direction. The signal at higher elevations (where the flight on its outbound portion is at approximately 7 km elevation) is noisier. This is partly because 7 km is no longer below the cloud base and so areas of cloud occurring in the data at this level will result in a large jump in dewpoint temperature and relative humidity, and vice versa. Dry bulb temperature exhibits no significant biases at this height however, with light winds from the west or north-west.

Intriguingly, Figure 6.15 shows broadly a very similar pattern the next day, though the

1.5 km model performs slightly better for a time around 0800 UTC compared to the previous day. However, for large portions of the near-surface portion of the flight, the dry bulb temperature is once again several Kelvin too high, and the dewpoint temperature slightly too low, compared to ERA5 and flight observations. At 2 km height, the dry bulb temperature is slightly too high again, akin to the previous day. The model winds this time are slightly more from the west as opposed to the north-west, but remain too strong in magnitude and lack accuracy compared to flight-observed winds. At 0800 UTC when the bias improves, the winds are more comparable, confirming the importance of accurate model simulations of the background flow. Model biases at a flight altitude of 7.5 km remain harder to interpret due to passages through cloud causing high variation in the dewpoint temperature. For an approximate 30-minute period up to 05:45 UTC, the dry bulb and dewpoint temperatures in the model seem to be too high by a few Kelvin, but this appears less systematic and did not occur during the flight on 2 July. Indeed, there appears to be no clear relationship between the bulging of cells around (or just a little below) this height in the model, and the dynamical and thermodynamical quantities shown here.

Precipitation in Figures 6.14 and 6.15 is shown to visualise the impact of errors in the representation of convection in the model on surface rainfall. Over both days, the models produce peaks in precipitation rate that are too sharp and intense (up to 60 mm hr^{-1}) compared to GPM IMERG, which is consistent with deep modelled storms being too intense on average, thus precipitating too heavily. Visualising the ensemble of storms in the region over the time of the flight (not shown), there is a large number of relatively small congestus or deep storms in the radar observations associated with cells embedded within larger stratiform regions of rain, that results in lower precipitation rate values and a broader distribution as the flight moves through the systems. In the model, the background near-surface reflectivity is typically higher, with larger regions above 40 dBZ. This results in the merging of many smaller cells in the model into intense, larger cells that are spaced further apart, resulting in short periods of high intensity rainfall from the perspective of the moving aircraft.

The main dynamical bias found in the model in this section relates to dry and hot air being advected from north-western India and Pakistan, and could partly explain the smaller areal

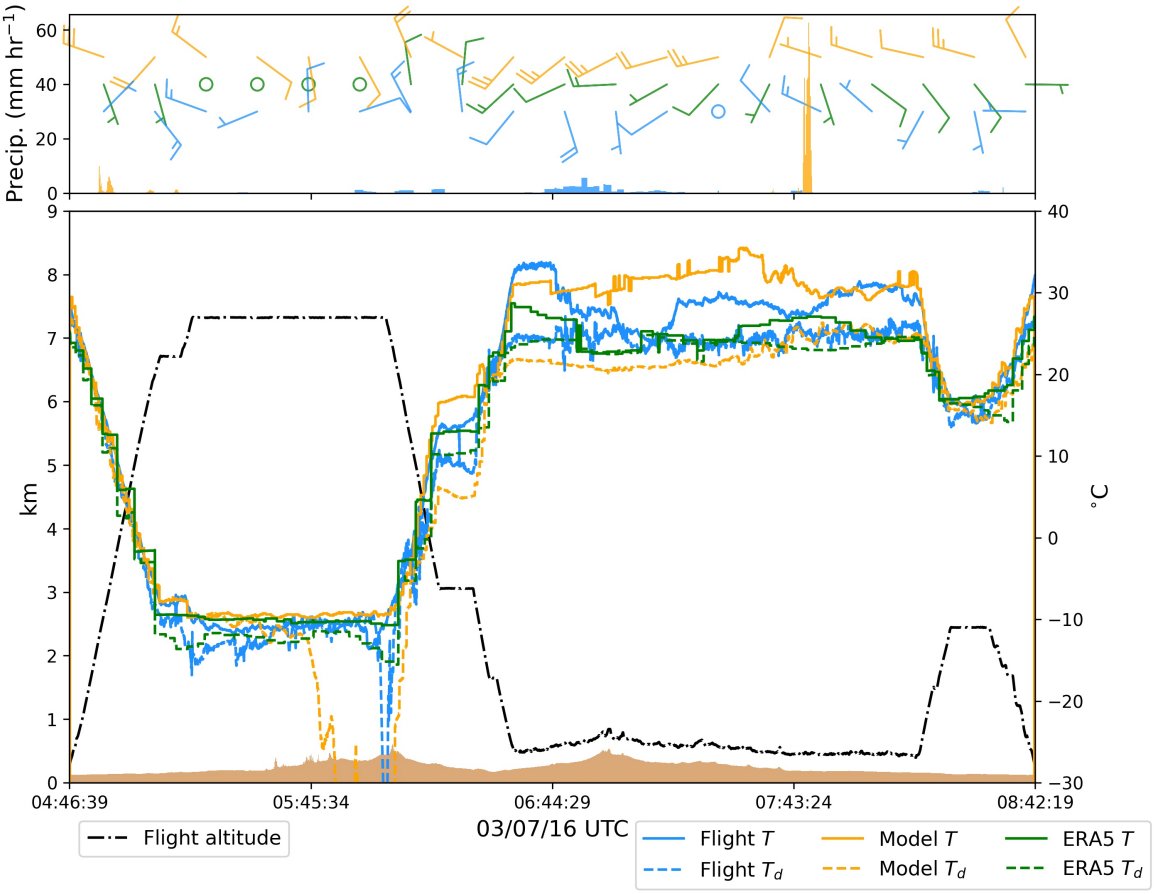

Figure 6.15: Same as Figure 6.14 but for the flight path on 3 July in Figure 6.11b (flight ID B970).

coverage of deep convection in the model compared to observations shown in Figure 6.12. However, as presented in Figure 6.13, modelled storms that are deep are larger and more intense. This is more difficult to explain with the errors in wind and temperatures shown here, and as discussed earlier in this section there are likely important microphysical aspects to this conundrum. However, Doyle et al. (2021b) explained how very moist conditions (e.g., over the Western Ghats) combined with orographic effects can lead to storms growing and 'raining out' (thus dissipating) more quickly. Therefore, drier conditions in the model over northern India may result in the opposite effect, i.e., larger storms with an intense core that develop less regularly. As discussed earlier, the larger storms in the model may also stem from merging of cells due to the greater background reflectivity associated with the wider storm system.

The northern India near-surface dry bias is one notable example of a dynamical bias that can impact upon modelled convection. Future work could expand this more comprehensively to further regions, using the full suite of INCOMPASS flight data available as well as alternative high-resolution data such as radiosonde soundings, in order to ascertain how much of an impact these biases have in different regions and their importance compared to inaccuracies in the microphysical processes in the model.

6.6 Discussion and conclusions

This study has navigated the intricate subject matter of evaluating a regional convection permitting model at 1.5 km resolution, using a network of 15 IMD operational ground-based weather radars for a 3-week period during the 2016 monsoon season. A novel approach is used to process model radar reflectivity, effectively mimicking the radar scanning strategy to create like-for-like comparable 3-D fields of reflectivity within each radar domain.

Models at both 1.5 km and 4.4 km resolutions were found to represent spatial variability in monsoon convection over India well. However, when evaluating the 4.4 km model for each radar doughnut region, the sample sizes are greatly reduced as we cannot reasonably represent storms smaller than 78 km^2 (or 4 pixels in area), which constitutes an especially high proportion of the shallow storm sample. Therefore, we focused on the 1.5 km model for evaluation. Several biases were found in the LAM when analysing different metrics for convection such as CTH, size and intensity. The model was found to not accurately capture the areal coverage associated with different CTHs, in particular typically simulating convection that was relatively too shallow compared to radar observations. This was traced to to there being both relatively too many shallower storms in the model as well as the shallower storms being larger in area. In fact, the model was typically dominated by shallow or congestus cells whereas the radars were dominated by deep cells in terms of this areal coverage. The fact that the LAM fails to represent properly the dominant mode of convection has potential ramifications for legitimate capturing of the convective development process. Furthermore, the shallow cells in the model exhibited cells with large areas and height-weighted reflectivities

(Z_{hwt}) that infrequently or never occurred in observations. Additionally, the model produces congestus and deep cells that bulge outwards around the freezing level, and are more intense than seen with radars for cells of the same cumulus mode.

Whilst significant dynamical biases were found to exist in the model, e.g., the warm and dry bias over northern India, they were not able to explain all the statistical differences found in modelled convection. Instead, many of the errors in convection in the LAM over India are comparable to those evaluated before for other regions (e.g., Lean et al., 2008; Stein et al., 2015a). For example, total radar reflectivity in high-resolution models has been found to be associated with anomalously high detrainment in the model in the freezing level region. Indeed, models with resolutions on the order of 1 km are still insufficient to fully capture turbulent processes associated with convective development.

Various studies have suggested that model turbulence schemes are a critical source of error for convection modelled at resolutions on the order of 1 km (e.g., Bryan et al., 2003). In order to explicitly capture turbulent processes more realistically, model resolutions on the order of 0.1 km would be required (Petch et al., 2002; Bryan et al., 2003). Further to this, Lean et al. (2008) speculated that shallow cells being too numerous may be related to the choice of dissipation in the turbulence scheme. Additionally, Stein et al. (2015a) and Stein et al. (2015b) showed that simulations on the order of 1 km underestimate the fraction of anvils with CTH above 12 km, due to ice water content being too low. Moreover, they noted that models consistently detrain close to the freezing level, which is too low compared to satellite observations. This detrainment was found to be even more abrupt in the original high-resolution model 3-D grid, but was mitigated by the radar-like scanning applied to the model here pre-evaluation. This preferential detrainment around the freezing level for simulated storms would explain our findings that modelled clouds bulge outwards up to the freezing level, and the underestimation of anvils explains the lack of areal coverage provided by deep convection in the model. Finally, the size and intensity of convection in the model is also overestimated as shown in Figure 6.13, which could be because of overactive hail in this version of the MetUM (Hawkness-Smith, personal communication). Further targeted sensitivity studies should examine these biases more closely by evaluating different model

microphysics schemes and their impact upon radar reflectivity and storm morphology.

It is encouraging that operational radars are evidently capable of showing robust (as in found before) errors in convection-permitting models, and this raises the profile of using operational radars for doing such evaluation work in multiple regions in the future. Nonetheless, great care must be taken at various steps in order to successfully evaluate models with operational radars, especially as it remains a novel approach for many tropical regions, where radars may differ in specification, even within operational radar networks. This study presents an applicable framework for achieving the required robustness that allows for future work in the area of model evaluation with radars, and indeed, future work can delve into the applications of these techniques by further assessing the physical reasons for biases in the regional models. Provision of operational radar data across the globe to the scientific community should be encouraged to allow evaluation studies to be performed more regularly, which will lead to further insight being gained in our understanding of clouds and storms in convection-permitting models, that are increasingly common and widely used in forecasts.

Chapter 7

Conclusions

The application of ground-based weather radars for determining the dynamical structure of convective cells has now long been recognised (e.g., Donaldson, 1961; Browning, 1978). The rapid rise in the number of operational weather radars, especially in tropical regions, is a much more recent development however, and these vast arrays of data offer significant (and largely untapped) potential for better understanding patterns of convection in tropical regions. One such network is that of the IMD Doppler weather radars (Viswanathan et al., 1997; Roy Bhowmik et al., 2011), of which 16 radars were used in this thesis. Much attention is now being placed on the use of radars for studying patterns in precipitation systems over India (Utsav et al., 2017; Morwal et al., 2018; Utsav et al., 2019; Doyle et al., 2021b; Jha et al., 2021; and others), as well as for the evaluation of high-resolution models in the UK and South Africa (McBeath et al., 2013; Keat et al., 2019; Stein et al., 2014, 2019).

The Indian summer monsoon (ISM) has profound socio-economic impacts upon the Indian region. It supplies more than 80% of India's annual rainfall to a growing population of more than a billion people. Nonetheless, medium-range forecasts of the ISM remain unreliable (Turner et al., 2020), and its representation in climate models exhibits large biases (e.g., Sperber et al., 2013). Improved process understanding may help reduce these errors (Turner et al., 2020). Indeed, the monsoon is known to be inherently complex due to multi-scale variability (Krishnamurti and Bhalme, 1976), and is also intrinsically linked to convection (Parker et al., 2016). Therefore, it is imperative to obtain further observations

and understanding of convection over the Indian region. Consequently, this thesis aspired to set out a robust and widely applicable method for identifying convection using a network of operational radars, and understand this convection better both in terms of its place in the large-scale circulation over India, and its representation in convection-permitting models. The following section summarises the major outcomes of this thesis pertaining to the three overarching research questions given in Chapter 1, and discusses the broader implications of the findings. The primary limitations of this work and suggestions for future work are considered.

7.1 Summary and discussion

7.1.1 Gaining robust observations of convection from Indian operational radars

To what extent can we develop a robust method toward using IMD weather radars for identifying convection and evaluating convection-permitting models?

Section 2.2 described the processing steps to identify convection from operational radars scanning in polar coordinates. Re-gridding of radar data onto regular height coordinates is not trivial, especially for operational radars with lower resolution. For the analysis of convection using radars, one must aim to eliminate – so far as possible – any range biases in re-gridded reflectivity that might impact upon ETH and CTH. These range biases show up as annular ring artefacts on a radar CAPPI mosaic, especially at higher altitudes where data is sparser. This is associated with many re-gridding tools simply selecting data from the nearest beam. To obtain more accurate estimates of reflectivity between radar beams, interpolation between beams is advised (e.g., Lakshmanan et al., 2013), and thus was performed here. By carrying out interpolation in two separate stages, artefacts were found to be further eliminated. Firstly, horizontal interpolation was performed for each (relevant) radar beam for each range from the radar. Secondly, vertical linear interpolation was then performed to place this data onto a 0.5 km height grid, as described in Chapter 2.

Accurate ETH estimates also rely on the radars being accurately calibrated. Chapter 3 detailed the calibration procedure performed upon the IMD radars. For several radar sites, there were large errors in reflectivity compared to the GPM DPR. These results illuminate the necessity of performing such a procedure prior to processing (i.e., re-gridding) and later analysis, especially for heterogeneous radar networks with different scanning properties, maintenance periods, hardware, and limited documentation. The methods of Warren et al. (2018) and Louf et al. (2019b) – combined in a so-called "integrated approach" – utilise the ground clutter native to each radar, and the quasi-global overpasses of the GPM DPR. Therefore, the overall procedure has great potential as a semi-automated and widely applicable method that can be repeated each year to monitor calibration changes in operational radar networks. A simple verification against synop rain gauges showed the improvements in the accuracy of radar-derived rainfall post-calibration are significant. Accuracy was achieved to within 1 dB, and this was also noted to result in small errors in ETH compared to the errors associated with resolution during re-gridding. Whilst accuracy to less than 1 dB is desirable for many applications of weather radars, e.g., for radar-derived rainfall and for the analysis of individual storm systems, it is sufficient for compositing statistical information on storms, as is undertaken in this thesis. Nonetheless, researchers involved in radar calibration (and other quality control procedures) should continue to focus on making such procedures more accessible to different scientific communities. Further thoughts regarding the capacity for different groups to perform such analyses using operational radar networks are provided as future work later in this chapter.

The techniques for radar quality control and processing, comprehensively described in Chapters 2 and 3, could act as a useful guide for those in future wishing to use these IMD radars or any other operational radar networks for analysis of storms. Much of the procedure described in Chapter 2 is already published within Doyle et al. (2021b) as a reference for the scientific community. The intention for the calibration procedure in Chapter 3 is to adapt it for publication in a technical journal such as *Atmospheric Measurement Techniques*. It is the first time this calibration strategy has been successfully applied to operational weather radars (including the IMD weather radars) and verified against synop rainfall observations.

7.1.2 Relationships between the large-scale and monsoon convection

What relationships exist between radar-derived convection, monsoon onset, and the large-scale circulation during the 2016 monsoon season across multiple regions of India?

Chapters 4 and 5 utilised the seasonal suite of radar-derived storm statistics in order to assess patterns of convection in relation to large-scale circulation changes associated with major timescales of variability. Chapter 4, published in the journal *Weather* (Doyle et al., 2021a), focused on the temporal patterns in convective development associated with the onset of the monsoon at 12 different radar sites. In particular, the findings of Chapter 4 were scrutinised with respect to the Parker hypothesis of onset being convectively-driven (Parker et al., 2016).

The 5-day running means of congestus and deep convective area for two months during May, June, and July at different radar sites showed high correlations with precipitation. As one might expect, this makes clear the importance of convective systems as the supplier of rainfall across India during monsoon onset. However, there was no visible pattern of congestus cells gradually being replaced by deeper cells in the days leading up to and following monsoon onset. Instead, a simultaneous increase in the areal coverage of all types of cells was noted. Furthermore, only a few sites (Mumbai, Bhopal, and Nagpur) showed clear increases in convection post-onset compared to pre-onset. Other sites showed significant amounts of variability in convection throughout the time series, albeit with a clear peak around the onset date.

The initial inference one can make here is that these findings are contradictory to the Parker hypothesis (and indeed the schematic of Figure 1.1 in Chapter 1). Indeed, some sites such as Patiala (an inland site in northern India) exhibited very little congestus areal coverage before monsoon onset but a large contribution from deep convection. For inland locations, the moister conditions that were found post-onset may be associated with more cumulus congestus, owing to the 'raining out' of storms due to rapid collision-coalescence of raindrops, a theory akin to that discussed for Mumbai (and the wider Western Ghats region) in Chapter 5. It is important to note that Parker et al. (2016) took a climatology

from radiosonde and rain gauge observations of over 30 years, compared to the one season of data here. The findings from Chapter 4 nonetheless raise further questions: On what scales might the heights of convection exhibit a gradual deepening associated with monsoon onset (e.g., zonal mean convection), if not the 5-day running means within radar domains described in Chapter 4? Further, does noise from local variability dominate the dynamically-induced convective signal of the ISM within individual years, and for what regions is this most evident? Such questions are relevant for the continued development of understanding in what explains monsoon advance. To achieve this, sampling over a greater number of years combined with more spatially complete observations of convection would be desirable. Convection-permitting model runs such as those in Chapter 6, but executed over an entire monsoon season or multiple monsoon seasons, could also aid the answering of these questions.

Chapter 5 expanded on Chapter 4 by studying temporal and spatial patterns of convection over the entire 2016 monsoon season, and is published in *JGR: Atmospheres* (Doyle et al., 2021b). Storms were found to exhibit clear patterns at seven different locations associated with intraseasonal variability, the diurnal cycle, and the calendar month, confirming that monsoon storm populations are embedded within the large-scale circulation. Specifically, a season-average peak in CTH was found just above the freezing level for all sites, and three cumulus modes were interpreted from the seasonal distribution of CTH: shallow, congestus, and deep cells, consistent with Johnson et al. (1996). Western and northern India sites showed clear variation in cell numbers and CTH associated with active and break periods, and all sites showed differences in the respective diurnal cycles associated with this intraseasonal variability. The diurnal cycle of convection was also modulated by surface type (land or ocean) and the progression of the monsoon (i.e., the calendar month).

The sensitivity of the diurnal cycle of convection (and rainfall) to these modes of variability was largely explained through the availability of moisture at each location associated with the airmass. The importance of the flow of moisture in regulating rainfall amounts has been noted for other tropical regions before, such as East Africa (Woodhams et al., 2019; Finney et al., 2020). Specifically, equivalent potential temperature (θ_e) was found to be a key variable for explaining the frequency and modal heights of convection. These results have

clear implications for forecasters who should pay particular attention to the availability of moisture in a region associated with large-scale regime changes.

This work emphasised the excellent potential for weather radars to improve understanding of convection in tropical regions. Additionally, the high-resolution observations from these radars can be used as a testbed in the subsequent evaluation of NWP models, as summarised below.

7.1.3 Evaluating high-resolution models with IMD operational radars

How well do convection-permitting models simulate different aspects of convection compared to radar observations during the 2016 ISM? What might explain specific biases in modelled convection?

Simulations of the ISM remain a considerable challenge to the modelling community, including GCMs (Sperber et al., 2013), and convection-permitting models (Willetts et al., 2017). The reasons for biases in high-resolution models with explicit convection remain poorly understood, with recent rapid development in such models emphasising the need to build capacity for process-based model evaluation. In Chapter 6, radar reflectivites from 15 IMD radars over India were used to perform a like-for-like evaluation of modelled radar reflectivity at a convection-permitting resolution of 1.5 km, for a period of 3 weeks during the peak 2016 monsoon season. Such an analysis had not (to the author's knowledge) previously been performed with these radars. From the reflectivity, different morphological properties of storms were objectively identified for six sub-regions of India. The 1.5 km model was found to simulate too much shallow convection compared to radars for all regions. Modelled convective storms were also shown to be frequently too wide and intense, with a maximum diameter around the freezing level, higher than observed.

Various potential microphysical and dynamical reasons for the aforementioned discrepancies between model and radars were discussed. Whilst significant dynamical biases were found to exist in the model, e.g., the warm and dry bias over northern India, they were not able to explain all the statistical differences found in modelled convection. Instead, many

of the errors in convection in the 1.5 km LAM over India were found to be comparable to those evaluated before for other regions at similar resolutions (e.g., Lean et al., 2008; Stein et al., 2015a). For example, total radar reflectivity in convection-permitting models has been found to be associated with anomalously high detrainment in the model at the freezing-level region (Stein et al., 2014).

It is encouraging that the IMD operational radars are evidently capable of showing robust errors in convection-permitting models, and this raises the profile of using operational radars for doing such evaluation work in multiple regions in the future. Nonetheless, great care had to be taken at various steps in order to successfully evaluate models with operational radars, especially as it remains a novel approach for many tropical regions, where radars may differ in specification, even within a given national operational radar network. However, this work demonstrated the usefulness of radar-based model evaluation for the Indian monsoon region, and indeed the novel approach of mimicking the radar scans in the model to eliminate sampling biases is broadly applicable to radar networks worldwide.

Further, this work has implications for forecasters, model developers, and researchers analysing NWP in the tropics. For forecasters and decision makers, more support should be given in understanding the limitations of convection-permitting models as well as their strengths from the scientific community. Whilst the improvement in models with explicit convection over GCMs using parameterisations are impressive and non-trivial, they are also now largely well-documented (e.g., Dirmeyer et al., 2012). Model developers and researchers should also focus on a more comprehensive understanding of the remaining errors associated with different convection-permitting models (i.e., different versions, microphysics schemes, and resolutions) if improvements are to be made. Evaluating these models would benefit greatly from the use of radar observations, as shown in this thesis. However, examining the potential causes of biases partly relies on good networking and sharing of model information within the broader research community, as well as provision of training to aid understanding of different model schemes. Targeted sensitivity studies may also yield progress in understanding the importance of different model schemes upon convection, such as land-surface configuration (Menon et al., 2021). Indeed, following the INCOMPASS field campaign, var-

ious model configurations are available for analysis during the 2016 monsoon season (Martin et al., 2020). The results in this chapter were initially written as a paper and could be submitted for publication in future as a follow-up to the INCOMPASS special collection (led by Turner and Bhat, 2020) in *The Quarterly Journal of the Royal Meteorological Society*.

7.2 Limitations and future work

7.2.1 Enhancing capability for use of weather radars for determining storm characteristics

This thesis has shown the great potential of radars for studying convection and as model evaluation tools. However, this full potential can only be realised if more radar data is made available, and secondly if the processing techniques are widely accessible. Of course, one cannot expect a seamless and fully archived global radar network any time soon, but several achievable improvements could be made to aid future scientific exploits, and are detailed below.

This thesis was limited by the amount of IMD radar data made available for this study, for a single monsoon season. Longer archived datasets – if made available – would allow for researchers to build a climatology of convection over the region using these radars, and analyse the impact of interannual variability, which was not able to be brought into this work. For India specifically, as alluded to in Chapter 1, a much larger suite of radar data is archived, but not publicly available. Periods of missing data were also substantial for some locations such as Mumbai, and this proved a significant limitation for the interpretation of some results, such as comparing the impact of intraseasonal variability on different radar sites.

As expressed in Chapter 1, the number of operational radars has continued to increase globally in recent years, especially in tropical regions. India is no exception to this trend, and it is not outside the realms of possibility that India may have quasi-seamless coverage from weather radars in the future. Therefore, if all this data (particularly the radar reflectivity) were archived and available for research, progress would be greatly accelerated. The sharing

of radar data between organisations is not yet possible for all regions due to national security challenges, but a steadily increasing number of weather services and institutions are now doing so (Saltikoff et al., 2019). In Europe, efforts have been made towards the sharing and standardisation of weather radar data, as part of the OPERA network, and similarly this has also been achieved in Australia (Soderholm et al., 2019). Radar network quality control and standardisation will allow for applications beyond meteorology as well, such as biodiversity monitoring (Shamoun-Baranes et al., 2022).

The second way to improve global capacity for research utilising operational radar networks is related to the wide array of processing techniques required, including radar reflectivity calibration. Further development of such calibration procedures and sharing of code to aid repeatability should be encouraged. This would increase confidence in comparisons (of reflectivity) between radar networks. Other processing techniques (e.g., construction of CAPPIs) can also be complex and time-consuming procedures, especially for lower-resolution radars as found in this thesis. Clearly, there is a need for a more universal and adaptable toolkit for the analysis of weather radar data that overcomes the inevitable heterogeneity between and even within radar networks. This would also allow for evaluation studies (such as that of Chapter 6) to be performed more regularly, which would yield significant benefits in the understanding of regional convection-permitting model skill.

7.2.2 Gaining a more detailed understanding of the importance of convection during the monsoon

There were several limitations associated with the analysis of the complex two-way relationship between monsoon convection and the large-scale. With the one season of data available, it was possible to ascertain how various aspects of convection were regulated by major timescales of variability. This meant the relationship was examined from the perspective of large-scale changes upon convection. However, it was difficult to assess this two-way relationship from the opposite direction, i.e., the impact of convection upon the monsoon circulation. This is also a key component of the Parker hypothesis, which describes the inter-

action between cumulus congestus moist convection gradually eroding mid-level dry air, thus helping establish monsoon winds carrying more moisture from the west. Therefore, a more comprehensive observational understanding of the impact of monsoon storms in different locations upon the large-scale would be a valuable next step toward further understanding of the dynamics of monsoon onset. However, such work relies on the provision of more data to aid in the robustness of the results and understand the variance involved in such relationships. Indeed, the physical mechanisms involved in the upscaling of convection impacting upon the large-scale are fundamentally less obvious than the downscaling of the large-scale upon local convection. Specific modelling case studies in addition to high-resolution observations might also help advance understanding in the impact of monsoon clouds upon the background circulation (e.g., Krishnamurti et al., 2012).

It would also be useful to approach the reasons for changing patterns in convection with more precision as to the specific meteorological drivers involved, and this is of clear benefit to model development. Specific hypotheses might help focus such work. For example, tropical convection is known to be sensitive to the advection of moisture associated with horizontal wind changes (Woodhams et al., 2019), but how, why, and to what extent is this the case? Furthermore, what timescales of variability are most definitive in explaining storm formation over different regions of India? In order to achieve this, future work might focus on the link between large-scale dynamics and local storms specifically for the Indian region, which is the local convective environment (Louf et al., 2019a), e.g., convective available potential energy (CAPE), convective inhibition (CIN), vertical moisture content, and vertical shear.

7.2.3 Performance of convection-permitting models during the monsoon

Convection-permitting models generally provide more accurate simulations of monsoon rainfall compared to GCMs (e.g., Willetts et al., 2017), however, they are not exempt from their own errors, as shown in Chapter 6. Nonetheless, this is just one model configuration, and whilst this showed the promise of radar-based evaluation for the region, clearly further config-

urations will need to be tested in order to understand the reasons for these biases. Specifically for the radar reflectivity parameter, the microphysics scheme requires further exploration, with communication of the key issues important between model developers and other researchers. Therefore, research in future should delve into the applications of radar-based evaluation by further assessing the physical reasons for biases in high-resolution models.

Further, in this thesis, the 4.4 km model was not evaluated owing to small sample sizes associated with radar domain size limitations and merging of storms. This of course is not a problem with the model per se, but a problem with the ability of the subsequent processing (e.g., re-gridding and the Steiner algorithm) to separate these convective features from each other. Therefore, future work might consider focusing on the performance of the Steiner algorithm (or alternative algorithms) at 4.4 km, (and indeed a broader range of resolutions). This would enable more research in the future on the effect of resolution on modelled convection over the region, specifically how the existing biases are modulated by changing grid length. Indeed, an important question to work towards is, what model is best to run for skilled forecasts over the region? Another potential avenue of future work is to take advantage of the ability for the model to record reflectivities far below the minimum sensitivity of operational weather radars. As such, these models may be used to aid understanding and interpretation of radar-derived storms, and the biases involved with different thresholds of ETH.

The diurnal cycle was also not investigated in Chapter 6 due to the short case study period. The diurnal cycle (driven by solar forcing) is a fundamental mode of variability in the atmosphere, so is an important component in understanding storm development over tropical regions such as India, and as such is the natural next step to further understanding of model performance over the region. Such analyses have been performed before (e.g., Johnson, 2011), but not in comparison to weather radar-derived convection.

Finally, it would be beneficial for radar meteorologists to continue exploring the empirical relationship between radar reflectivity and rainfall rate over the ISM region with calibrated IMD network radars. This will provide confidence in applying these evaluative techniques directly to radar-derived and modelled rainfall in the future.

7.3 Concluding remarks

This thesis has utilised an array of 16 radars from the IMD operational radar network to observe convective storms during the 2016 Indian monsoon, the first time this has been performed using this many network radars. A widely repeatable approach toward gaining robust and comprehensive output on storm characteristics was implemented, showing the impressive potential for these radars over India to be used in a research context.

The use of these operational radars has shown that convection is regulated by the large-scale circulation across India during the 2016 season, providing potential sources of predictability in understanding convective development. Following this, these radars were used to perform convection-permitting model evaluation, with modelled convective cells exhibiting several systematic biases in storm morphology, several found before for other regions, showing the potential for radars as model evaluation tools. This work then also has implications for model developers, as well as forecasters using high-resolution NWP products.

The potential of operational radar networks (especially in tropical regions) for such applications is gradually being recognised, but further efforts are needed to realise this potential and make such analyses widely employable. More sharing of radar data and processing techniques would allow for further exciting progress in key questions arising from this thesis, such as the upscaled impact of storms upon the large-scale, and the reasons for specific biases in convection-permitting models.

Appendix A

Error estimates for echo-top heights

The sampling strategy of operational weather radars leaves significant gaps, especially at higher elevation angles, which become greater as distance from the radar increases. For certain higher echo-top heights (ETHs) and at certain distances, the nearest IMD radar beam may be over- or undershooting the ETH by 2 km or more. Previous studies (e.g., Warren and Protat, 2019) have already demonstrated the merits of vertical interpolation between beams to estimate features such as ETH. Lakshmanan et al. (2013) used model simulations to estimate the error in 18 dBZ ETH and demonstrate that interpolation between beams provides an improved estimate compared to simply using the nearest beam. Jackson et al. (2018) evaluated ETH estimated from the CPOL radar against satellite-derived cloud-top heights. While they find that the radar estimates are biased low, there is a statistically significant correlation between the two data sets that justifies the use of ETH for statistical analysis of convective storms over longer periods of time.

Here, we provide further evidence to justify the use of ETH derived from the IMD radars. There is no observational estimate for the "true" ETH during the 2016 ISM. For instance, the number of overpasses from the GPM core observatory is insufficient to carry out this analysis, which furthermore relies on a suitably large number of convective cells. Instead, we demonstrate the range-dependence of these errors using data from the Chilbolton Advanced Meteorological Radar (CAMRa) in the UK. CAMRa is a 0.28°-beam S-band, dual-polarized Doppler radar. The narrow beam allows us to obtain an accurate estimate of the true ETH,

with the beam width reaching 450 m at 100 km range from the radar (see Figure A1, panel a, for an example). We use 2975 range-height indicator (RHI) scans performed through convective storms in southern England from 10 days during 2011–2019.

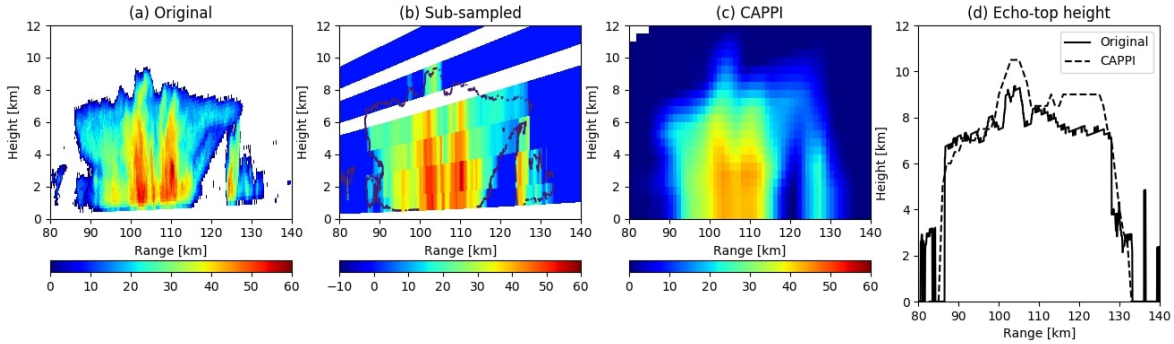

Figure A.1: Example of simulating a CAPPI reconstruction from an RHI from CAMRa. (a) The original RHI scan from CAMRa. (b) The same data smoothed to 1° in elevation and sub-sampled to the IMD radar elevation angles. (c) CAPPI reconstructed from the data in panel (b). (d) ETH estimated from the original RHI scan in panel (a) and the CAPPI in panel (c).

To simulate the ETH retrieval as obtained using the IMD radars, we first smooth the CAMRa RHIs to the IMD radar beam width and then sample the smoothed RHIs at the IMD radar elevations (see Figure A.1, panel b). Next, we re-grid the sub-sampled and smoothed RHI to a regular Cartesian grid of 1 km by 0.5 km, similar to the CAPPI reconstruction described in Section 2 (Figure A.1, panel c). Finally, ETH is determined at each 1 km in range as the height with reflectivity closest in value to 5 dBZ. Figure A.1 shows the results for a single CAMRa scan, including ETH in panel d. Clearly, the instantaneous error can be quite large, reaching more than 2 km in this example. It is also evident that the error depends strongly on where the radar beam is in relation to the true ETH, with errors closer to zero when the beam intersects the true ETH.

In Figure A.2, we show the bias as a function of distance from the radar and estimated ETH for all ETH estimates in the 2975 CAMRa RHI scans. Considering all ETH estimates, we find a statistically significant correlation between the true and estimated ETH of 0.93. The IMD radar scan strategy shows up very clearly in these statistics, as expected, with low bias where the radar beams intersect the true ETH. The bias is greater for those combinations of ETH and range where the beam separation is greater, although this might be exaggerated

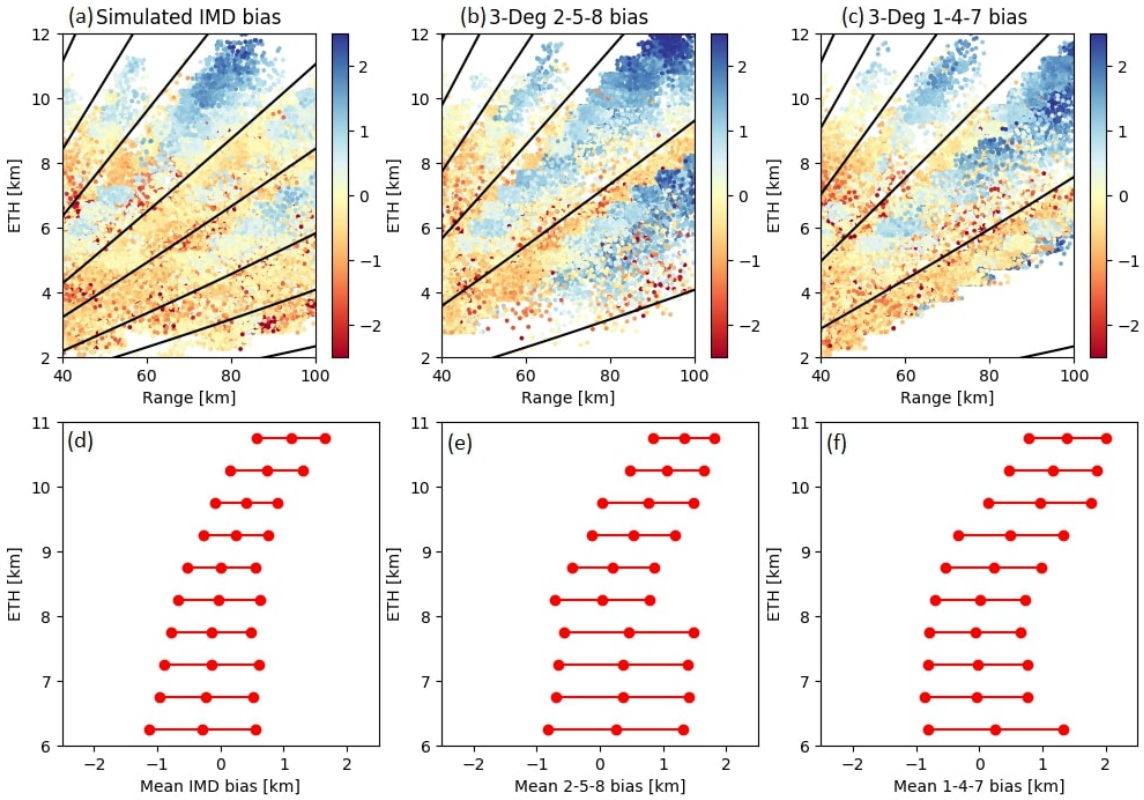

Figure A.2: Mean bias in km for ETH estimated by (a) simulating the IMD radar scan strategy using CAMRa RHIs (b) simulating a scan strategy with beams separated by 3° starting at 2° and (c) as in (b) but starting at 1°. Scattered points are randomly placed around their specific ETH (within 0.25 km) and range (within 0.5 km). Lines show the central location of the radar beams considered. Panels (d–f) show the mean bias and standard deviation variation with height for each of the three strategies considering ranges between 40–100 km, considering ETH between 6–11 km.

by the fact that ETH of 10 km and above were very rare in the CAMRa scans. To investigate the importance of beam separation further, we also simulate results using the CAMRa data but adopting a radar scan strategy with beam separation of 3° starting from either 2° or 1°. The resulting ETH from these simulations are shown in Figure A.2b and c respectively. The greater bias for combinations of ETH and range now also appear for ETH estimates below 9 km, which were frequently observed in these data. However, if we ignore the range-dependence of these results, we note that the mean bias for ETH estimates below 9 km is close to zero for both strategies. The mean bias increases to 1 km for ETH estimates above 9 km, but we postulate that this is due to the sparsity of true ETH above 9 km in the CAMRa data set.

This analysis demonstrates that the instantaneous errors in ETH estimation are generally of order 1 km, which is comparable to the vertical grid resolution we consider for our CAPPIs. The results show that the errors are greatest where the radar beams are far removed from the true ETH, but for a given ETH estimate the spatial and temporal mean bias is expected to be close to zero. The mean bias is most relevant to the results presented in this study for multiple reasons. Firstly, we consider ETH averaged over entire convective cells, i.e., cell-top height (CTH). Secondly, these convective cells may propagate throughout the domain so that any remaining bias in CTH will vary depending on where the cell is located in terms of range to the radar. Finally, the statistics presented in this study are averaged over multiple days so that if cells may be assumed to be spread across the radar domains, the mean bias in ETH will be close to zero.

Bibliography

Anagnostou, E. N., 2004: A convective/stratiform precipitation classification algorithm for volume scanning weather radar observations. *Meteorological Applications*, **11**, 291–300, https://doi.org/10.1017/S1350482704001409.

Arakawa, A., and W. H. Schubert, 1974: Interaction of a Cumulus Cloud Ensemble with the Large-Scale Environment, Part I. *Journal of Atmospheric Sciences*, **31**, 674–701, https://doi.org/10.1175/1520-0469(1974)031<0674:IOACCE>2.0.CO;2.

Asai, T., M. Yoshizaki, and K. Ishikawa, 1977: Some Results on an objective Analysis for Tracking Radar Echoes of Convective Clouds. *Journal of the Meteorological Society of Japan. Ser. II*, **55**, 553–558, https://doi.org/10.2151/jmsj1965.55.5_553.

Atlas, D., 1964: Instrumentation for Data Processing, Display, and Transmission. *Advances in Radar Meteorology*, 424–432.

Atlas, D., 2002: Radar Calibration: Some Simple Approaches. *Bulletin of the American Meteorological Society*, **83**, 1313–1316, https://doi.org/10.1175/1520-0477-83.9.1313.

Atlas, D., and S. C. Mossop, 1960: Calibration of a Weather Radar by Using a Standard Target. *Bulletin of the American Meteorological Society*, **41**, 377–382, https://doi.org/10.1175/1520-0477-41.7.377.

Battan, L., 1973: Instrumentation for Data Processing, Display, and Transmission. *Radar Observation of the Atmosphere*, 324.

Biggerstaff, M. I., and S. A. Listemaa, 2000: An Improved Scheme for Convective/Stratiform Echo Classification Using Radar Reflectivity. *Journal of Applied Meteorology*, **39**, 2129–2150, https://doi.org/10.1175/1520-0450(2001)040<2129:AISFCS>2.0.CO;2.

Biswas, S., and V. Chandrasekar, 2018: Cross-Validation of Observations between the GPM Dual-Frequency Precipitation Radar and Ground Based Dual-Polarization Radars. *Remote Sensing*, **10**, 1773, https://doi.org/10.3390/rs10111773.

Boardman, J. H., and P. L. Smith, 1974: a computer-generated "four dimensional" graphic display for weather radar data. *Bulletin of the American Meteorological Society*, **55**, 16–19, https://doi.org/10.1175/1520-0477(1974)055<0016:ACGDGD>2.0.CO;2.

Browning, K. A., 1978: Meteorological applications of radar. *Reports on Progress in Physics*, **41**, 761–806, https://doi.org/10.1088/0034-4885/41/5/003.

Bryan, G. H., J. C. Wyngaard, and J. M. Fritsch, 2003: Resolution Requirements for the Simulation of Deep Moist Convection. *Monthly Weather Review*, **131**, 2394–2416, https://doi.org/10.1175/1520-0493(2003)131<2394:RRFTSO>2.0.CO;2.

Cao, Q., Y. Hong, Y. Qi, Y. Wen, J. Zhang, J. J. Gourley, and L. Liao, 2013: Empirical conversion of the vertical profile of reflectivity from Ku-band to S-band frequency. *Journal of Geophysical Research: Atmospheres*, **118**, 1814–1825, https://doi.org/10.1002/jgrd.50138.

Casey, S. P., E. J. Fetzer, and B. H. Kahn, 2012: Revised identification of tropical oceanic cumulus congestus as viewed by CloudSat. *Atmospheric Chemistry and Physics*, **12**, 1587–1595, https://doi.org/10.5194/acp-12-1587-2012.

Charney, J. G., 1969: A Further Note on Large-Scale Motions in the Tropics. *Journal of Atmospheric Sciences*, **26**, 182–185, https://doi.org/10.1175/1520-0469(1969)026<0182:AFNOLS>2.0.CO;2.

Clark, P., N. Roberts, H. Lean, S. P. Ballard, and C. Charlton-Perez, 2016: Convection-permitting models: a step-change in rainfall forecasting. *Meteorological Applications*, **23**, 165–181, https://doi.org/10.1002/MET.1538.

Collis, S., A. Protat, and K.-S. Chung, 2010: The Effect of Radial Velocity Gridding Artifacts on Variationally Retrieved Vertical Velocities. *Journal of Atmospheric and Oceanic Technology*, **27**, 1239–1246, https://doi.org/10.1175/2010JTECHA1402.1.

Crook, J., C. Klein, S. Folwell, C. M. Taylor, D. J. Parker, R. Stratton, and T. Stein, 2019: Assessment of the Representation of West African Storm Lifecycles in Convection-Permitting Simulations. *Earth and Space Science*, **6**, 818–835, https://doi.org/10.1029/2018EA000491.

Da Silva, N. A., B. G. M. Webber, A. J. Matthews, M. M. Feist, T. H. M. Stein, C. E. Holloway, and M. F. A. B. Abdullah, 2021: Validation of GPM IMERG Extreme Precipitation in the Maritime Continent by Station and Radar Data. *Earth and Space Science*, **8**, e2021EA001 738, https://doi.org/10.1029/2021EA001738.

Das, S. K., M. Konwar, K. Chakravarty, and S. M. Deshpande, 2017: Raindrop size distribution of different cloud types over the Western Ghats using simultaneous measurements from Micro-Rain Radar and disdrometer. *Atmospheric Research*, **186**, 72–82, https://doi.org/10.1016/j.atmosres.2016.11.003.

Davies, L., and Coauthors, 2013: A single-column model ensemble approach applied to the TWP-ICE experiment. *Journal of Geophysical Research: Atmospheres*, **118**, 6544–6563, https://doi.org/10.1002/jgrd.50450.

Dirmeyer, P. A., and Coauthors, 2012: Simulating the diurnal cycle of rainfall in global climate models: Resolution versus parameterization. *Climate Dynamics*, **39**, 399–418, https://doi.org/10.1007/S00382-011-1127-9.

Dixon, M., and G. Wiener, 1993: TITAN: Thunderstorm identification, tracking, analysis, and nowcasting—A radar-based methodology. *Journal of Atmospheric and Oceanic Technology*, **10**, 785–797, https://doi.org/ https://doi.org/10.1175/1520-0426(1993)010<0785:TTITAA>2.0.CO;2.

Donaldson, R. J., 1961: Radar Reflectivity Profiles in Thunderstorms. *Journal of Atmospheric Sciences*, **18**, 292–305, https://doi.org/10.1175/1520-0469(1961)018<0292:RRPIT>2.0.CO;2.

Donaldson, R. J., 1964: A Demonstration of Antenna Beam Errors in Radar Reflectivity Patterns. *Journal of Applied Meteorology and Climatology*, **3**, 611–623, https://doi.org/10.1175/1520-0450(1964)003<0611:ADOABE>2.0.CO;2.

Doyle, A., T. Stein, and A. Turner, 2021a: Temporal patterns in radar-observed convective cell development during the 2016 monsoon onset. *Weather*, **76**, 180–184, https://doi.org/10.1002/wea.3969.

Doyle, A. J., T. H. M. Stein, and A. G. Turner, 2021b: 2016 Monsoon Convection and Its Place in the Large-Scale Circulation Using Doppler Radars. *Journal of Geophysical Research: Atmospheres*, **126**, https://doi.org/ 10.1029/2021jd035496.

Doyle, A. J., T. H. M. Stein, and A. G. Turner, 2021c: INCOMPASS: India Meteorology Department Doppler radar convective cell statistics v2. Centre for Environmental Data Analysis, http://dx.doi.org/10.5285/b28633ddc0f44d77a6aa81ad7bd66285.

Durai, V. R., and S. K. Roy Bhowmik, 2014: Prediction of Indian summer monsoon in short to medium range time scale with high resolution global forecast system (GFS) T574 and T382. *Climate Dynamics*, **42**, 1527–1551, https://doi.org/10.1007/s00382-013-1895-5.

East, T., and B. Dore, 1957: An electronic constant-altitude display. *Proceedings of 6th Weather Radar Conference*, American Meteorological Society, Boston, 325–330.

Fan, J., R. Zhang, G. Li, W.-K. Tao, and X. Li, 2007: Simulations of cumulus clouds using a spectral microphysics cloud-resolving model. *Journal of Geophysical Research: Atmospheres*, **112**, D04 201, https://doi.org/10.1029/2006JD007688.

Finney, D. L., J. H. Marsham, D. P. Walker, C. E. Birch, B. J. Woodhams, L. S. Jackson, and S. Hardy, 2020: The effect of westerlies on East African rainfall and the associated role of tropical cyclones and the Madden–Julian Oscillation. *Quarterly Journal of the Royal Meteorological Society*, **146**, 647–664, https://doi.org/10.1002/qj.3698.

Fletcher, J. K., and Coauthors, 2020: The dynamic and thermodynamic structure of the monsoon over southern India: New observations from the INCOMPASS IOP. *Quarterly Journal of the Royal Meteorological Society*, **146**, 2867–2890, https://doi.org/10.1002/qj.3439.

Flohn, H., 1968: Contributions to a Meteorology of the Tibetan Highlands. *Contributions to a Meteorology of the Tibetan Highlands*.

Fulton, R. A., J. P. Breidenbach, D.-J. Seo, D. A. Miller, and T. O'Bannon, 1998: The WSR-88D Rainfall Algorithm. *Weather and Forecasting*, **13**, 377–395, https://doi.org/10.1175/1520-0434(1998)013<0377:TWRA>2.0.CO;2.

Gadgil, S., 2018: The monsoon system: Land–sea breeze or the ITCZ? *Journal of Earth System Science*, **127**, 1–29, https://doi.org/10.1007/S12040-017-0916-X.

Gadgil, S., and S. Gadgil, 2006: The Indian Monsoon, GDP and Agriculture. Economic and Political Weekly, accessed: 2021-03-02, https://www.jstor.org/stable/4418949.

Goddard, J., J. Eastment, and M. Thurai, 1994: The Chilbolton Advanced Meteorological Radar: a tool for multidisciplinary atmospheric research. *Electronics & Communication Engineering Journal*, **6**, 77–86, https://doi.org/10.1049/ecej:19940205.

Goswami, B. N., and P. K. Xavier, 2003: Potential predictability and extended range prediction of Indian summer monsoon breaks. *Geophysical Research Letters*, **30**, 1966, https://doi.org/10.1029/2003GL017810.

Harris Jr, G. N., K. P. Bowman, and D.-B. Shin, 2000: Comparison of freezing-level altitudes from the NCEP reanalysis with TRMM precipitation radar brightband data. *Journal of Climate*, **13**, 4137–4148, https://doi.org/10.1175/1520-0442(2000)013<4137:COFLAF>2.0.CO;2.

Heistermann, M., S. Jacobi, and T. Pfaff, 2013: An open source library for processing weather radar data (wradlib). *Hydrology and Earth System Sciences*, **17**, 863, https://doi.org/https://doi.org/10.5194/hess-17-863-2013.

Helmus, J. J., and S. M. Collis, 2016: The Python ARM Radar Toolkit (Py-ART), a library for working with weather radar data in the Python programming language. *Journal of Open Research Software*, **4**, https://doi.org/https://doi.org/10.5334/jors.119.

Hersbach, H., and Coauthors, 2020: The ERA5 global reanalysis. *Quarterly Journal of the Royal Meteorological Society*, **146**, 1999–2049, https://doi.org/10.1002/qj.3803.

Hitschfeld, W., and J. S. Marshall, 1954: Effect of Attenuation on the Choice of Wavelength for Weather Detection by Radar. *Proceedings of the IRE*, **42**, 1165–1168, https://doi.org/10.1109/JRPROC.1954.274551.

Holloway, C. E., S. J. Woolnough, and G. M. S. Lister, 2012: Precipitation distributions for explicit versus parametrized convection in a large-domain high-resolution tropical case study. *Quarterly Journal of the Royal Meteorological Society*, **138**, 1692–1708, https://doi.org/10.1002/qj.1903.

Houze, R. A., D. C. Wilton, and B. F. Smull, 2007: Monsoon convection in the Himalayan region as seen by the TRMM Precipitation Radar. *Quarterly Journal of the Royal Meteorological Society*, **133**, 1389–1411, https://doi.org/10.1002/qj.106.

Huffman, G. J., D. T. Bolvin, E. J. Nelkin, and J. Tan, 2020: Integrated Multi-satellitE Retrievals for GPM (IMERG) Technical Documentation. NASA, accessed: 2021-03-02, https://docserver.gesdisc.eosdis.nasa.gov/public/project/GPM/IMERG_doc.06.pdf.

Huffman, G. J., and Coauthors, 2007: The TRMM Multisatellite Precipitation Analysis (TMPA): Quasi-Global, Multiyear, Combined-Sensor Precipitation Estimates at Fine Scales. *Journal of Hydrometeorology*, **8**, 38–55, https://doi.org/10.1175/JHM560.1.

Hunt, K., A. Turner, and R. Schiemann, 2022: Katabatic and convective processes drive two preferred peaks in the precipitation diurnal cycle over the Central Himalaya. *Quarterly Journal of the Royal Meteorological Society*, in review.

Jackson, R. C., S. M. Collis, V. Louf, A. Protat, and L. Majewski, 2018: A 17 year climatology of the macrophysical properties of convection in Darwin. *Atmospheric Chemistry and Physics*, **18**, 17 687–17 704, https://doi.org/10.5194/acp-18-17687-2018.

Jayakumar, A., S. J. Abel, A. G. Turner, S. Mohandas, J. Sethunadh, D. O'Sullivan, A. K. Mitra, and E. N. Rajagopal, 2020: Performance of the NCMRWF convection-permitting model during contrasting monsoon phases of the 2016 INCOMPASS field campaign. *Quarterly Journal of the Royal Meteorological Society*, **146**, 2928–2948, https://doi.org/10.1002/QJ.3689.

Jayakumar, A., J. Sethunadh, R. Rakhi, T. Arulalan, S. Mohandas, G. R. Iyengar, and E. N. Rajagopal, 2017: Behavior of predicted convective clouds and precipitation in the high-resolution Unified Model over the Indian summer monsoon region. *Earth and Space Science*, **4**, 303–313, https://doi.org/10.1002/2016EA000242.

Jha, A. K., S. K. Das, S. M. Deshpande, and U. V. Murali Krishna, 2021: Understanding the relationship of storm- to large-scale environment in the monsoon trough region: results inferred from long-term radar and reanalysis datasets. *Quarterly Journal of the Royal Meteorological Society*, 1–20, https://doi.org/10.1002/qj.4194.

Jiang, X., T. Li, and B. Wang, 2004: Structures and mechanisms of the northward propagating boreal summer intraseasonal oscillation. *Journal of Climate*, **17**, 1022–1039, https://doi.org/10.1175/1520-0442(2004)017<1022:SAMOTN>2.0.CO;2.

Johnson, R. H., 2011: Diurnal Cycle of Monsoon Convection. *The Global Monsoon System*, 257–276, https://doi.org/10.1142/9789814343411_0015.

Johnson, R. H., P. E. Ciesielski, and K. A. Hart, 1996: Tropical Inversions near the 0°C Level. *Journal of the Atmospheric Sciences*, https://doi.org/10.1175/1520-0469(1996)053<1838:TINTL>2.0.CO;2.

Johnson, R. H., T. M. Rickenbach, S. A. Rutledge, P. E. Ciesielski, and W. H. Schubert, 1999: Trimodal Characteristics of Tropical Convection. *Journal of Climate*, **12**, 2397–2418, https://doi.org/10.1175/1520-0442(1999)012<2397:TCOTC>2.0.CO;2.

Jones, T. R., and D. A. Randall, 2011: Quantifying the limits of convective parameterizations. *Journal of Geophysical Research: Atmospheres*, **116**, D08 210, https://doi.org/10.1029/2010JD014913.

Keat, W. J., and Coauthors, 2019: Convective initiation and storm life cycles in convection-permitting simulations of the Met Office Unified Model over South Africa. *Quarterly Journal of the Royal Meteorological Society*, **145**, 1323–1336, https://doi.org/10.1002/QJ.3487.

Keenan, T., K. Glasson, F. Cummings, T. S. Bird, J. Keeler, and J. Lutz, 1998: The BMRC/NCAR C-Band Polarimetric (C-POL) Radar System. *Journal of Atmospheric and Oceanic Technology*, **15**, 871–886, https://doi.org/10.1175/1520-0426(1998)015<0871:TBNCBP>2.0.CO;2.

Kendon, E. J., A. F. Prein, C. A. Senior, and A. Stirling, 2021: Challenges and outlook for convection-permitting climate modelling. *Philosophical Transactions of the Royal Society A: Mathematical, Physical and Engineering Sciences*, **379**, 20190 547, https://doi.org/10.1098/rsta.2019.0547.

Kikuchi, K., B. Wang, and Y. Kajikawa, 2012: Bimodal representation of the tropical intraseasonal oscillation. *Climate Dynamics*, **38**, 1989–2000, https://doi.org/10.1007/s00382-011-1159-1.

Koteswaram, P., 1958: The Easterly Jet Stream in the Tropics. *Tellus*, **10**, 43–57, https://doi.org/10.3402/TELLUSA.V10I1.9220.

Krishna Rao, P. R., 1961: Thunderstorms study in India. *MAUSAM*, **12**, 3–6, https://doi.org/10.54302/mausam.v12i1.4158.

Krishnamurthy, V., and J. Shukla, 2000: Intraseasonal and Interannual Variability of Rainfall over India. *Journal of Climate*, **13**, 4366–4377, https://doi.org/10.1175/1520-0442(2000)013<0001:IAIVOR>2.0.CO;2.

Krishnamurthy, V., and J. Shukla, 2007: Intraseasonal and Seasonally Persisting Patterns of Indian Monsoon Rainfall. *Journal of Climate*, **20**, 3–20, https://doi.org/10.1175/JCLI3981.1.

Krishnamurti, T. N., P. Ardanuy, Y. Ramanathan, and R. Pasch, 1981: On the Onset Vortex of the Summer Monsoon. *Mon. Wea. Rev.*, **109**, 344–363, https://doi.org/10.1175/1520-0493(1981)109<0344:OTOVOT>2.0.CO;2.

Krishnamurti, T. N., and H. Bhalme, 1976: Oscillations of a monsoon system. Part I. Observational aspects. *Journal of the Atmospheric Sciences*, **33**, 1937–1954, https://doi.org/10.1175/1520-0469(1976)033<1937:OOAMSP>2.0.CO;2.

Krishnamurti, T. N., A. Simon, A. Thomas, A. Mishra, D. Sikka, D. Niyogi, A. Chakraborty, and L. Li, 2012: Modeling of Forecast Sensitivity on the March of Monsoon Isochrones from Kerala to New Delhi: The First 25 Days. *Journal of the Atmospheric Sciences*, **69**, 2465–2487, https://doi.org/10.1175/JAS-D-11-0170.1.

Kumar, S., 2017: A 10-year climatology of vertical properties of most active convective clouds over the Indian regions using TRMM PR. *Theoretical and applied climatology*, **127**, 429–440, https://doi.org/10.1007/s00704-015-1641-5.

Kumar, S., and G. S. Bhat, 2017: Vertical structure of orographic precipitating clouds observed over south Asia during summer monsoon season. *Journal of Earth System Science*, **126**, 114, https://doi.org/10.1007/s12040-017-0897-9.

Kumar, V. V., C. Jakob, A. Protat, P. T. May, and L. Davies, 2013a: The four cumulus cloud modes and their progression during rainfall events: A C-band polarimetric radar perspective. *Journal of Geophysical Research: Atmospheres*, **118**, 8375–8389, https://doi.org/10.1002/jgrd.50640.

Kumar, V. V., A. Protat, C. Jakob, C. R. Williams, S. Rauniyar, G. L. Stephens, and P. T. May, 2016: The Estimation of Convective Mass Flux from Radar Reflectivities. *Journal of Applied Meteorology and Climatology*, **55**, 1239–1257, https://doi.org/10.1175/JAMC-D-15-0193.1.

Kumar, V. V., A. Protat, P. T. May, C. Jakob, G. Penide, S. Kumar, and L. Davies, 2013b: On the Effects of Large-Scale Environment and Surface Types on Convective Cloud Characteristics over Darwin, Australia. *Monthly Weather Review*, **141**, 1358–1374, https://doi.org/10.1175/MWR-D-12-00160.1.

Lakshmanan, V., K. Hondl, C. K. Potvin, and D. Preignitz, 2013: An improved method for estimating radar echo-top height. *Weather and Forecasting*, **28**, 481–488, https://doi.org/10.1175/WAF-D-12-00084.1.

Lean, H. W., P. A. Clark, M. Dixon, N. M. Roberts, A. Fitch, R. Forbes, and C. Halliwell, 2008: Characteristics of High-Resolution Versions of the Met Office Unified Model for Forecasting Convection over the United Kingdom. *Monthly Weather Review*, **136**, 3408–3424, https://doi.org/10.1175/2008MWR2332.1.

Levine, R. C., and A. G. Turner, 2012: Dependence of Indian monsoon rainfall on moisture fluxes across the Arabian Sea and the impact of coupled model sea surface temperature biases. *Climate Dynamics*, **38**, 2167–2190, https://doi.org/10.1007/S00382-011-1096-Z.

Levine, R. C., A. G. Turner, D. Marathayil, and G. M. Martin, 2013: The role of northern Arabian Sea surface temperature biases in CMIP5 model simulations and future projections of Indian summer monsoon rainfall. *Climate Dynamics*, **41**, 155–172, https://doi.org/10.1007/S00382-012-1656-X.

Li, C., and M. Yanai, 1996: The Onset and Interannual Variability of the Asian Summer Monsoon in Relation to Land–Sea Thermal Contrast. *Journal of Climate*, **9**, 358–375, https://doi.org/10.1175/1520-0442(1996)009<0358:TOAIVO>2.0.CO;2.

Lorenz, E. N., 1969: The predictability of a flow which possesses many scales of motion. *Tellus*, **21**, 289–307, https://doi.org/10.3402/tellusa.v21i3.10086.

Louf, V., C. Jakob, A. Protat, M. Bergemann, and S. Narsey, 2019a: The Relationship of Cloud Number and Size With Their Large-Scale Environment in Deep Tropical Convection. *Geophysical Research Letters*, **46**, 9203–9212, https://doi.org/10.1029/2019GL083964.

Louf, V., A. Protat, R. A. Warren, S. M. Collis, D. B. Wolff, S. Raunyiar, C. Jakob, and W. A. Petersen, 2019b: An Integrated Approach to Weather Radar Calibration and Monitoring Using Ground Clutter and Satellite Comparisons. *Journal of Atmospheric and Oceanic Technology*, **36**, 17–39, https://doi.org/10.1175/JTECH-D-18-0007.1.

Mahto, S. S., and V. Mishra, 2019: Does ERA-5 Outperform Other Reanalysis Products for Hydrologic Applications in India? *Journal of Geophysical Research: Atmospheres*, **124**, 9423–9441, https://doi.org/10.1029/2019JD031155.

Mapes, B. E., and P. Zuidema, 1996: Radiative-Dynamical Consequences of Dry Tongues in the Tropical Troposphere. *Journal of Atmospheric Sciences*, **53**, 620–638, https://doi.org/10.1175/1520-0469(1996)053<0620:RDCODT>2.0.CO;2.

Marshall, J., and W. Gordon, 1957: The constant-altitude presentation of radar weather patterns. *Proceedings of 6th Weather Radar Conference*, American Meteorological Society, Boston, 321–324.

Marshall, J. S., and W. M. K. Palmer, 1948: The Distribution of Raindrops with Size. *Journal of Meteorology*, **5**, 165–166, https://doi.org/10.1175/1520-0469(1948)005<0165:tdorws>2.0.co;2.

Martin, G. M., N. P. Klingaman, and A. F. Moise, 2017: Connecting spatial and temporal scales of tropical precipitation in observations and the MetUM-GA6. *Geoscientific Model Development*, **10**, 105–126, https://doi.org/10.5194/gmd-10-105-2017.

Martin, G. M., S. F. Milton, C. A. Senior, M. E. Brooks, S. Ineson, T. Reichler, and J. Kim, 2010: Analysis and reduction of systematic errors through a seamless approach to modeling weather and climate. *Journal of Climate*, **23**, 5933–5957, https://doi.org/10.1175/2010JCLI3541.1.

Martin, G. M., and Coauthors, 2019: Forecasting the monsoon on daily to seasonal time-scales in support of a field campaign. *Quarterly Journal of the Royal Meteorological Society*, **146**, 2906–2927, https://doi.org/10.1002/qj.3620.

Martin, G. M., and Coauthors, 2020: Forecasting the monsoon on daily to seasonal time-scales in support of a field campaign. *Quarterly Journal of the Royal Meteorological Society*, **146**, 2906–2927, https://doi.org/10.1002/qj.3620.

May, P. T., and A. Ballinger, 2007: The statistical characteristics of convective cells in a monsoon regime (Darwin, Northern Australia). *Monthly Weather Review*, **135**, 82–92, https://doi.org/10.1175/MWR3273.1.

McBeath, K., P. R. Field, and R. J. Cotton, 2013: Using operational weather radar to assess high-resolution numerical weather prediction over the British Isles for a cold air outbreak case-study. *Quarterly Journal of the Royal Meteorological Society*, **140**, 225–239, https://doi.org/10.1002/qj.2123.

Menon, A., A. G. Turner, G. M. Martin, and C. MacLachlan, 2018: Modelling the moistening of the free troposphere during the northwestward progression of Indian monsoon onset. *Quarterly Journal of the Royal Meteorological Society*, **144**, 1152–1168, https://doi.org/10.1002/qj.3281.

Menon, A., A. G. Turner, A. Volonté, C. M. Taylor, S. Webster, and G. Martin, 2021: The role of mid-tropospheric moistening and land-surface wetting in the progression of the 2016 Indian monsoon. *Quarterly Journal of the Royal Meteorological Society*, 1–23, https://doi.org/10.1002/qj.4183.

Molnar, P., W. R. Boos, and D. S. Battisti, 2010: Orographic Controls on Climate and Paleoclimate of Asia: Thermal and Mechanical Roles for the Tibetan Plateau. *Annual Review of Earth and Planetary Sciences*, **38**, 77–102, https://doi.org/10.1146/annurev-earth-040809-152456.

Morwal, S. B., S. G. Narkhedkar, B. Padmakumari, M. R. S., and J. R. Kulkarni, 2018: Characteristics of precipitating monsoon clouds over rain-shadow and drought-hit regions of India using radar. *Climate Dynamics*, **50**, 3571–3594, https://doi.org/https://doi.org/10.1007/s00382-017-3826-3.

Olauson, J., 2018: ERA5: The new champion of wind power modelling? *Renewable Energy*, **126**, 322–331, https://doi.org/10.1016/j.renene.2018.03.056.

Pai, D. S., A. Bandgar, S. Devi, and et al., 2020: CRS Research Report. New normal dates of onset/progress and withdrawal of southwest monsoon over India. IMD, accessed: 2021-03-02, https://internal.imd.gov.in/press_release/20200515_pr_804.pdf.

Pai, D. S., and R. M. Nair, 2009: Summer monsoon onset over Kerala: New definition and prediction. *Journal of Earth System Science*, **118**, 123–135, https://doi.org/10.1007/s12040-009-0020-y.

Parker, D. J., P. Willetts, C. Birch, A. G. Turner, J. H. Marsham, C. M. Taylor, S. Kolusu, and G. M. Martin, 2016: The interaction of moist convection and mid-level dry air in the advance of the onset of the Indian monsoon. *Quarterly Journal of the Royal Meteorological Society*, **142**, 2256–2272, https://doi.org/10.1002/qj.2815.

Petch, J. C., A. R. Brown, and M. E. Gray, 2002: The impact of horizontal resolution on the simulations of convective development over land. *Quarterly Journal of the Royal Meteorological Society*, **128**, 2031–2044, https://doi.org/10.1256/003590002320603511.

Peters, K., C. Jakob, L. Davies, B. Khouider, and A. J. Majda, 2013: Stochastic Behavior of Tropical Convection in Observations and a Multicloud Model. *Journal of the Atmospheric Sciences*, **70**, 3556–3575, https://doi.org/10.1175/JAS-D-13-031.1.

Portig, W. H., 1963: Thunderstorm frequency and amount of precipitation in the tropics, especially in the African and Indian monsoon regions. *Archiv für Meteorologie, Geophysik und Bioklimatologie, Serie B*, **13**, 21–35, https://doi.org/10.1007/BF02243785.

Posselt, D. J., S. C. van den Heever, and G. L. Stephens, 2008: Trimodal cloudiness and tropical stable layers in simulations of radiative convective equilibrium. *Geophysical Research Letters*, **35**, L08 802, https://doi.org/10.1029/2007GL033029.

Prakash, S., A. K. Mitra, A. AghaKouchak, Z. Liu, H. Norouzi, and D. Pai, 2018: A preliminary assessment of GPM-based multi-satellite precipitation estimates over a monsoon dominated region. *Journal of Hydrology*, **556**, 865–876, https://doi.org/10.1016/j.jhydrol.2016.01.029.

Prein, A. F., and Coauthors, 2015: A review on regional convection-permitting climate modeling: Demonstrations, prospects, and challenges. *Reviews of Geophysics*, **53**, 323–361, https://doi.org/10.1002/2014RG000475.

Probert-Jones, J. R., 1962: The radar equation in meteorology. *Quarterly Journal of the Royal Meteorological Society*, **88**, 485–495, https://doi.org/10.1002/qj.49708837810.

Protat, A., D. Bouniol, E. J. O'Connor, H. K. Baltink, J. Verlinde, and K. Widener, 2011: CloudSat as a Global Radar Calibrator. *Journal of Atmospheric and Oceanic Technology*, **28**, 445–452, https://doi.org/10.1175/2010JTECHA1443.1.

Qie, X., X. Wu, T. Yuan, J. Bian, and D. Lu, 2014: Comprehensive pattern of deep convective systems over the Tibetan Plateau-South Asian monsoon region based on TRMM data. *Journal of Climate*, **27**, 6612–6626, https://doi.org/10.1175/JCLI-D-14-00076.1.

Rajeevan, M., J. Bhate, J. Kale, and B. Lal, 2006: High resolution daily gridded rainfall data for the Indian region: analysis of break and active monsoon spells. *Current Science*, **91**, 296–306.

Rajeevan, M., S. Gadgil, and J. Bhate, 2010: Active and break spells of the Indian summer monsoon. *Journal of Earth System Science*, **119**, 229–247, https://doi.org/10.1007/s12040-010-0019-4.

Ramesh, K. J., 2017: Annual Report 2016. India Meteorological Department, accessed: 2020-07-03, https://metnet.imd.gov.in/imdnews/ar2016.pdf.

Rani, S. I., T. Arulalan, J. P. George, E. N. Rajagopal, R. Renshaw, A. Maycock, D. M. Barker, and M. Rajeevan, 2021: IMDAA: High-Resolution Satellite-Era Reanalysis for the Indian Monsoon Region. *Journal of Climate*, **34**, 5109–5133, https://doi.org/10.1175/JCLI-D-20-0412.1.

Rao, S. A., and Coauthors, 2019: Monsoon mission a targeted activity to improve monsoon prediction across scales. *Bulletin of the American Meteorological Society*, **100**, 2509–2532, https://doi.org/10.1175/BAMS-D-17-0330.1.

Rao, T. N., K. Saikranthi, B. Radhakrishna, and S. V. Bhaskara Rao, 2016: Differences in the climatological characteristics of precipitation between active and break spells of the Indian summer monsoon. *Journal of Climate*, **29**, 7797–7814, https://doi.org/10.1175/JCLI-D-16-0028.1.

Rinehart, R. E., 1978: On the Use of Ground Return Targets for Radar Reflectivity Factor Calibration Checks. *Journal of Applied Meteorology and Climatology*, **17**, 1342–1350, https://doi.org/10.1175/1520-0450(1978)017<1342:OTUOGR>2.0.CO;2.

Romatschke, U., and R. A. Houze, 2011: Characteristics of precipitating convective systems in the South Asian monsoon. *Journal of Hydrometeorology*, **12**, 3–26, https://doi.org/10.1175/2010JHM1289.1.

Romatschke, U., S. Medina, and R. A. Houze, 2010: Regional, seasonal, and diurnal variations of extreme convection in the South Asian region. *Journal of Climate*, **23**, 419–439, https://doi.org/10.1175/2009JCLI3140.1.

Rosenfeld, D., 1987: Objective Method for Analysis and Tracking of Convective Cells as Seen by Radar. *Journal of Atmospheric and Oceanic Technology*, **4**, 422–434, https://doi.org/10.1175/1520-0426(1987)004<0422:OMFAAT>2.0.CO;2.

Rosenfeld, D., E. Amitai, and D. B. Wolff, 1995: Classification of Rain Regimes by the Three-Dimensional Properties of Reflectivity Fields. *Journal of Applied Meteorology (1988-2005)*, **34**, 198–211.

Roy, S. S., M. Mohapatra, A. Tyagi, and S. K. Roy Bhowmik, 2019: A review of Nowcasting of convective weather over the Indian region. *MAUSAM*, **70**, 465–484.

Roy Bhowmik, S. K., and Coauthors, 2011: Processing of Indian Doppler Weather Radar data for mesoscale applications. *Meteorology and Atmospheric Physics*, **111**, 133–147, https://doi.org/10.1007/s00703-010-0120-x.

Saha, S. B., S. S. Roy, S. K. R. Bhowmik, and P. K. Kundu, 2014: Intra-seasonal variability of cloud amount over the Indian subcontinent during the monsoon season as observed by TRMM Precipitation Radar. *Geofizika*, **31**, 28–53, https://doi.org/10.15233/gfz.2014.31.2.

Saltikoff, E., and Coauthors, 2019: An Overview of Using Weather Radar for Climatological Studies: Successes Challenges, and Potential. *Bulletin of the American Meteorological Society*, **100**, 1739–1752, https://doi.org/10.1175/bams-d-18-0166.1.

Sathiyamoorthy, V., P. Pal, and P. Joshi, 2004: Influence of the upper-tropospheric wind shear upon cloud radiative forcing in the Asian monsoon region. *Journal of Climate*, **17**, 2725–2735, https://doi.org/10.1175/1520-0442(2004)017<2725:IOTUWS>2.0.CO;2.

Schneider, U., T. Fuchs, A. Meyer-Christoffer, and B. Rudolf, 2008: Global precipitation analysis products of the GPCC. *Global Precipitation Climatology Centre (GPCC), DWD, Internet Publikation*, **112**.

Schwaller, M. R., and K. R. Morris, 2011: A Ground Validation Network for the Global Precipitation Measurement Mission. *Journal of Atmospheric and Oceanic Technology*, **28**, 301–319, https://doi.org/10.1175/2010JTECHA1403.1.

Seliga, T. A., V. N. Bringi, and H. H. Al-Khatib, 1981: A Preliminary Study of Comparative Measurements of Rainfall Rate Using the Differential Reflectivity Radar Technique and a Raingage Network. *Journal of Applied Meteorology and Climatology*, **20**, 1362–1368, https://doi.org/10.1175/1520-0450(1981)020<1362:APSOCM>2.0.CO;2.

Serafin, R. J., 1990: Meteorological Radar. *Radar Handbook (Second Edition)*, 23.8–23.9.

Shamoun-Baranes, J., and Coauthors, 2022: Meteorological data policies needed to support biodiversity monitoring with weather radar. *Bulletin of the American Meteorological Society*, https://doi.org/10.1175/BAMS-D-21-0196.1.

Shige, S., and C. Kummerow, 2016: Precipitation-top heights of heavy orographic rainfall in the Asian monsoon region. *Journal of the Atmospheric Sciences*, **73**, 3009–3024, https://doi.org/10.1175/JAS-D-15-0271.1.

Silberstein, D. S., D. B. Wolff, D. A. Marks, D. Atlas, and J. L. Pippitt, 2008: Ground Clutter as a Monitor of Radar Stability at Kwajalein, RMI. *Journal of Atmospheric and Oceanic Technology*, **25**, 2037–2045, https://doi.org/10.1175/2008JTECHA1063.1.

Smith, J. A., D. J. Seo, M. L. Baeck, and M. D. Hudlow, 1996: An Intercomparison Study of NEXRAD Precipitation Estimates. *Water Resources Research*, **32**, 2035–2045, https://doi.org/10.1029/96WR00270.

Smith, P., K. Hardy, and K. Glover, 1974: Applications of radar to meteorological operations and research. *Proceedings of the IEEE*, **62**, 724–745, https://doi.org/10.1109/PROC.1974.9512.

Smith, R. N. B., 1990: A scheme for predicting layer clouds and their water content in a general circulation model. *Quarterly Journal of the Royal Meteorological Society*, **116**, 435–460, https://doi.org/10.1002/qj.49711649210.

Soderholm, J., A. Protat, and C. Jakob, 2019: Australian operational weather radar dataset. *National Computing Infrastructure*, NCI Data Catalogue, https://doi.org/10.25914/5cb686a8d9450.

Sperber, K., H. Annamalai, I.-S. Kang, A. Kitoh, A. Moise, A. Turner, B. Wang, and T. Zhou, 2013: The Asian summer monsoon: an intercomparison of CMIP5 vs. CMIP3 simulations of the late 20th century. *Climate Dynamics*, **41**, 2711–2744, https://doi.org/10.1007/s00382-012-1607-6.

Stein, T., R. Hogan, P. Clark, C. Halliwell, K. Hanley, H. Lean, J. Nicol, and R. Plant, 2015a: The DYMECS Project: A Statistical Approach for the Evaluation of Convective Storms in High-Resolution NWP Models. *Bulletin of the American Meteorological Society*, **96**.

Stein, T., and Coauthors, 2019: An evaluation of clouds and precipitation in convection-permitting forecasts for South Africa. *Weather and Forecasting*, **34**, 233–254, https://doi.org/https://doi.org/10.1175/WAF-D-18-0080.1.

Stein, T. H., D. J. Parker, R. J. Hogan, C. E. Birch, C. E. Holloway, G. M. Lister, J. H. Marsham, and S. J. Woolnough, 2015b: The representation of the West African monsoon vertical cloud structure in the Met Office Unified Model: an evaluation with CloudSat. *Quarterly Journal of the Royal Meteorological Society*, **141**, 3312–3324, https://doi.org/10.1002/QJ.2614.

Stein, T. H. M., R. W. Scovell, K. E. Hanley, H. W. Lean, and N. H. Marsden, 2020: The potential use of operational radar network data to evaluate the representation of convective storms in NWP models. *Quarterly Journal of the Royal Meteorological Society*, qj.3793, https://doi.org/10.1002/qj.3793.

Stein, T. H. M., and Coauthors, 2014: The Three-Dimensional Morphology of Simulated and Observed Convective Storms over Southern England. *Monthly Weather Review*, **142**, 3264–3283, https://doi.org/10.1175/MWR-D-13-00372.1.

Steiner, M., R. A. Houze, S. E. Yuter, M. Steiner, R. A. H. Jr., and S. E. Yuter, 1995: Climatological Characterization of Three-Dimensional Storm Structure from Operational Radar and Rain Gauge Data. *Journal of Applied Meteorology*, **34**, 1978–2007, https://doi.org/10.1175/1520-0450(1995)034<1978:CCOTDS>2.0.CO;2.

Stratton, R. A., and Coauthors, 2018: A Pan-African Convection-Permitting Regional Climate Simulation with the Met Office Unified Model: CP4-Africa. *Journal of Climate*, **31**, 3485–3508, https://doi.org/10.1175/jcli-d-17-0503.1.

Talchabhadel, R., and Coauthors, 2021: Weather radar in Nepal: opportunities and challenges in a mountainous region. *Weather*, **99**, 99–99, https://doi.org/10.1002/wea.3994.

Tan, J., G. J. Huffman, D. T. Bolvin, and E. J. Nelkin, 2019: Diurnal Cycle of IMERG V06 Precipitation. *Geophysical Research Letters*, **46**, 13,584–13,592, https://doi.org/10.1029/2019GL085395.

Taraphdar, S., P. Mukhopadhyay, and B. N. Goswami, 2010: Predictability of Indian summer monsoon weather during active and break phases using a high resolution regional model. *Geophysical Research Letters*, **37**, L21 812, https://doi.org/10.1029/2010GL044969.

Testud, J., E. L. Bouar, E. Obligis, and M. Ali-Mehenni, 2000: The Rain Profiling Algorithm Applied to Polarimetric Weather Radar. *Journal of Atmospheric and Oceanic Technology*, https://doi.org/10.1175/1520-0426(2000)017<0332:TRPAAT>2.0.CO;2.

Thurai, M., V. N. Bringi, and P. T. May, 2010: CPOL radar-derived drop size distribution statistics of stratiform and convective rain for two regimes in Darwin, Australia. *Journal of Atmospheric and Oceanic Technology*, **27**, 932–942, https://doi.org/10.1175/2010JTECHA1349.1.

Tokay, A., and D. A. Short, 1996: Evidence from Tropical Raindrop Spectra of the Origin of Rain from Stratiform versus Convective Clouds. *Journal of Applied Meteorology and Climatology*, **35**, 355–371, https://doi.org/10.1175/1520-0450(1996)035<0355:EFTRSO>2.0.CO;2.

Trenberth, K. E., D. P. Stepaniak, and J. M. Caron, 2000: The Global Monsoon as Seen through the Divergent Atmospheric Circulation. *Journal of Climate*, **13**, 3969–3993, https://doi.org/10.1175/1520-0442(2000)013<3969:TGMAST>2.0.CO;2.

Turner, A. G., and G. S. Bhat, 2020: Preface to the INCOMPASS Special Collection. *Quarterly Journal of the Royal Meteorological Society*, **146**, 2826–2827, https://doi.org/10.1002/qj.3889.

Turner, A. G., K. R. Sperber, J. Slingo, G. Meehl, C. R. Mechoso, M. Kimoto, and A. Giannini, 2011: Modelling Monsoons: Understanding and Predicting Current and Future Behaviour. *The Global Monsoon System: Research and Forecast (2nd Edition) (World Scientific Series on Asia-Pacific Weather and Climate)*, World Scientific, 421–454, https://doi.org/10.1142/9789814343411_0025.

Turner, A. G., and Coauthors, 2020: Interaction of Convective Organisation with Monsoon Precipitation, Atmosphere, Surface and Sea: the 2016 INCOMPASS field campaign in India. *Quarterly Journal of the Royal Meteorological Society*, qj.3633, https://doi.org/10.1002/qj.3633.

Ulbrich, C. W., and L. G. Lee, 1999: Rainfall Measurement Error by WSR-88D Radars due to Variations in Z–R Law Parameters and the Radar Constant. *Journal of Atmospheric and Oceanic Technology*, **16**, 1017–1024, https://doi.org/10.1175/1520-0426(1999)016<1017:RMEBWR>2.0.CO;2.

Utsav, B., S. M. Deshpande, S. K. Das, and G. Pandithurai, 2017: Statistical Characteristics of Convective Clouds over the Western Ghats Derived from Weather Radar Observations. *Journal of Geophysical Research: Atmospheres*, **122**, 10,050–10,076, https://doi.org/10.1002/2016JD026183.

Utsav, B., S. M. Deshpande, S. K. Das, G. Pandithurai, and D. Niyogi, 2019: Observed Vertical Structure of Convection During Dry and Wet Summer Monsoon Epochs Over the Western Ghats. *Journal of Geophysical Research: Atmospheres*, **124**, 2018JD028 960, https://doi.org/10.1029/2018JD028960.

Vaccarono, M., R. Bechini, C. V. Chandrasekar, R. Cremonini, and C. Cassardo, 2016: An integrated approach to monitoring the calibration stability of operational dual-polarization radars. *Atmospheric Measurement Techniques*, **9**, 5367–5383, https://doi.org/10.5194/amt-9-5367-2016.

Virts, K. S., and R. A. Houze, 2016: Seasonal and Intraseasonal Variability of Mesoscale Convective Systems over the South Asian Monsoon Region. *Journal of the Atmospheric Sciences*, **73**, 4753–4774, https://doi.org/10.1175/JAS-D-16-0022.1.

Viswanathan, G., R. Bhatia, V. Kamble, and S. Rao, 1997: Indian Doppler weather radar system-an overview. *IGARSS'97. 1997 IEEE International Geoscience and Remote Sensing Symposium Proceedings. Remote Sensing - A Scientific Vision for Sustainable Development*, Vol. 3, 1129–1131, https://doi.org/10.1109/IGARSS.1997.606373.

Vivekanandan, J., G. Zhang, S. M. Ellis, D. Rajopadhyaya, and S. K. Avery, 2003: Radar reflectivity calibration using differential propagation phase measurement. *Radio Science*, **38**, 8049, https://doi.org/10.1029/2002RS002676.

Volonté, A., A. Turner, and A. Menon, 2020: Airmass analysis of the processes driving the progression of the Indian summer monsoon. *Quarterly Journal of the Royal Meteorological Society*, qj.3700, https://doi.org/10.1002/qj.3700.

Walters, D., and Coauthors, 2017: The Met Office Unified Model Global Atmosphere 6.0/6.1 and JULES Global Land 6.0/6.1 configurations. *Geoscientific Model Development*, **10**, 1487–1520, https://doi.org/10.5194/gmd-10-1487-2017.

Warren, R. A., and A. Protat, 2019: Should interpolation of radar reflectivity be performed in Z or dBZ? *Journal of Atmospheric and Oceanic Technology*, JTECH–D–18–0183.1, https://doi.org/10.1175/JTECH-D-18-0183.1.

Warren, R. A., A. Protat, S. T. Siems, H. A. Ramsay, V. Louf, M. J. Manton, and T. A. Kane, 2018: Calibrating ground-based radars against TRMM and GPM. *Journal of Atmospheric and Oceanic Technology*, **35**, 323–346, https://doi.org/10.1175/JTECH-D-17-0128.1.

Webster, P. J., V. O. Magaña, T. N. Palmer, J. Shukla, R. A. Tomas, M. Yanai, and T. Yasunari, 1998: Monsoons: Processes, predictability, and the prospects for prediction. *Journal of Geophysical Research: Oceans*, **103**, 14,451–14,510, https://doi.org/10.1029/97JC02719.

Weisman, M. L., W. C. Skamarock, and J. B. Klemp, 1997: The Resolution Dependence of Explicitly Modeled Convective Systems. *Monthly Weather Review*, **125**, 527–548, https://doi.org/10.1175/1520-0493(1997)125<0527:TRDOEM>2.0.CO;2.

Willetts, P. D., J. H. Marsham, C. E. Birch, D. J. Parker, S. Webster, and J. Petch, 2017: Moist convection and its upscale effects in simulations of the Indian monsoon with explicit and parametrized convection. *Quarterly Journal of the Royal Meteorological Society*, **143**, 1073–1085, https://doi.org/10.1002/qj.2991.

Williams, S. D., 1961: Frequency of thunderstorms in South India. *MAUSAM*, **12**, 131–133, https://doi.org/10.54302/mausam.v12i1.4175.

Wilson, D. R., and S. P. Ballard, 1999: A microphysically based precipitation scheme for the UK meteorological office unified model. *Quarterly Journal of the Royal Meteorological Society*, **125**, 1607–1636, https://doi.org/10.1002/qj.49712555707.

Wolff, D. B., D. A. Marks, and W. A. Petersen, 2015: General Application of the Relative Calibration Adjustment (RCA) Technique for Monitoring and Correcting Radar Reflectivity Calibration. *Journal of Atmospheric and Oceanic Technology*, **32**, 496–506, https://doi.org/10.1175/JTECH-D-13-00185.1.

Wood, N., and Coauthors, 2014: An inherently mass-conserving semi-implicit semi-Lagrangian discretization of the deep-atmosphere global non-hydrostatic equations. *Quarterly Journal of the Royal Meteorological Society*, **140**, 1505–1520, https://doi.org/10.1002/qj.2235.

Woodhams, B. J., C. E. Birch, J. H. Marsham, T. P. Lane, C. L. Bain, and S. Webster, 2019: Identifying Key Controls on Storm Formation over the Lake Victoria Basin. *Monthly Weather Review*, **147**, 3365–3390, https://doi.org/10.1175/MWR-D-19-0069.1.

Wu, G., Y. Guan, Y. Liu, J. Yan, and J. Mao, 2012: Air-sea interaction and formation of the Asian summer monsoon onset vortex over the Bay of Bengal. *Climate Dynamics*, **38**, 261–279, https://doi.org/10.1007/S00382-010-0978-9.

Wu, G., and Coauthors, 2007: The Influence of Mechanical and Thermal Forcing by the Tibetan Plateau on Asian Climate. *Journal of Hydrometeorology*, **8**, 770–789, https://doi.org/10.1175/JHM609.1.

Xavier, P. K., C. Marzin, and B. N. Goswami, 2007: An objective definition of the Indian summer monsoon season and a new perspective on the ENSO–monsoon relationship. *Quarterly Journal of the Royal Meteorological Society*, **133**, 749–764, https://doi.org/10.1002/QJ.45.

Yang, G.-Y., and J. Slingo, 2001: The Diurnal Cycle in the Tropics. *Monthly Weather Review*, **129**, 784–801, https://doi.org/10.1175/1520-0493(2001)129<0784:TDCITT>2.0.CO;2.

Yatagai, A., K. Kamiguchi, O. Arakawa, A. Hamada, N. Yasutomi, and A. Kitoh, 2012: APHRODITE: Constructing a Long-Term Daily Gridded Precipitation Dataset for Asia Based on a Dense Network of Rain Gauges. *Bulletin of the American Meteorological Society*, **93**, 1401–1415, https://doi.org/10.1175/BAMS-D-11-00122.1.

Zhang, J., K. Howard, and J. J. Gourley, 2005: Constructing Three-Dimensional Multiple-Radar Reflectivity Mosaics: Examples of Convective Storms and Stratiform Rain Echoes. *Journal of Atmospheric and Oceanic Technology*, **22**, 30–42, https://doi.org/10.1175/JTECH-1689.1.